Title
Journey Before Destination: Understanding Quantum Dynamical Phenomena in Condensed Phases

Author
Schile, Addison

Publication Date
2021

Journey Before Destination: Understanding Quantum Dynamical Phenomena in Condensed Phases

by

Addison Jon Schile

A dissertation submitted in partial satisfaction of the

requirements for the degree of

Doctor of Philosophy

in

Chemistry

in the

Graduate Division

of the

University of California, Berkeley

Committee in charge:

Professor David T. Limmer, Chair
Professor Eran Rabani
Professor Joel E. Moore

Summer 2021

Journey Before Destination: Understanding Quantum Dynamical Phenomena in Condensed Phases

Abstract

Journey Before Destination: Understanding Quantum Dynamical Phenomena in Condensed Phases

by

Addison Jon Schile

Doctor of Philosophy in Chemistry

University of California, Berkeley

Professor David T. Limmer, Chair

The simplest picture of a chemical reaction through a reaction coordinate supposes a system begins as a set of reactants whose energy must fluctuate to overcome some activation barrier en route to the reacted products. These fluctuations are atypical in that they have large energy changes relative to the available thermal energy and thus reactions are exceedingly rare. Often, though, these reactions can occur after some initiation event, which removes this barrier and allows the reaction to freely proceed. Such is the case for photoinduced chemical reactions in which light-matter coupling instantaneously pumps energy into the system and serves as this initiator. These reactions are prevalent in all walks of the chemical sciences.The generic understanding of these reactions is, however, complicated by the many strongly-interacting degrees-of-freedom typically involved. Worse yet, these reactions, except in the most controlled of cases, mostly occur in condensed phase environments such as solvents, solid frameworks, or protein complexes, which dramatically increase the complexity of these dynamics while having important consequences on the reactions.

In this thesis we have applied the tools of nonequilibrium statistical mechanics to understand these photoinduced chemical reactions. These approaches rely on the accurate, but efficient treatment of multi-dimensional quantum systems through rigorous application of approximate theories consistent with fundamental thermodynamic relations. When satisfied, the resulting picture of the dynamics is numerically efficient and quantitatively accurate for many observables. Furthermore, path sampling approaches can be applied through the use of a quantum trajectory framework of the dynamics, which unravels the complex dynamics into a set of reduced simplified reaction coordinates. These techniques, as is demonstrated on model systems of photoinduced phenomena, can describe the complex dynamics and simulate the experimental observations of real condensed phase systems.

To Austin and Caitlin

Contents

Contents **ii**

1 Introduction **1**
1.1 Photoinduced Chemical Reactions 1
1.2 Outline 5

2 Theoretical Aspects of Condensed Phase Quantum Dynamics **6**
2.1 Quantum Dynamics of Closed Systems 6
2.2 Quantum Dynamics of Open Systems 14
2.3 Time-Dependent Response 29

3 Quantum Transition Path Sampling **35**
3.1 Introduction 35
3.2 Quantum Jump Path Ensembles 38
3.3 Conditioned Ensembles 43
3.4 Committor Analysis 50
3.5 Evaluation of Rate Constants 56
3.6 Conclusion 60

4 Hybrid Quantum Master Equations **62**
4.1 Introduction 62
4.2 Theory 64
4.3 Comparison with exact results 70
4.4 Application to Photoisomerization Quantum Yields 80
4.5 Conclusion 82

5 Azobenzene Photoisomerization **85**
5.1 Introduction 85
5.2 Hybrid Framework for Azobenzene Hamiltonian 86
5.3 Electronic Structure of Azobenzene 88
5.4 Developing a Minimal Model 97
5.5 Photoisomerization Dynamics 104

5.6 Conclusion 111

6 Two-Dimensional Electronic Vibrational Spectroscopy 113

6.1 Introduction 113

6.2 Theory 115

6.3 Static Signatures of Vibronic Coupling 124

6.4 Dynamical Signatures of Vibronic Coupling 127

6.5 Conclusion 133

A Details of the MCTDH Equations of Motion 135

B Choosing ω^* for Hybrid Quantum Master Equations 137

C Numerical Gradients of Generalized Coordinates 139

C.1 Transformation of Cartesian Gradients to Internal Coordinate Gradients . . 139

C.2 Numerical Procedure for Generating the Kinetic Energy 141

Bibliography 143

Acknowledgments

I have been incredibly fortunate to have encountered a number of people who supported me in obtaining my PhD that extends far beyond these past five years. I am forever indebted to these connections and would like to thank some specific people who have been particularly close.

I first must thank my advisor, David. As a newly-minted assistant professor it is no easy decision to let young (naive) graduate students like myself take on such challenging projects and I thank him for taking the chance on me—he has really opened my eyes to a broad view of chemistry and of science in general that has impacted my future career in more ways than imaginable. He has truly taught me how to think more concretely and holistically about scientific research that will undoubtedly serve me well in the future.

My first steps into theoretical chemistry were led by Ward Thompson. When I first ran into Ward I had just left the world of debate and he gracefully brought me into this new arena showing me the many wonders quantum and statistical mechanics research has to offer. Without his help I would likely not have landed at an institution like UC Berkeley and he forever has my gratitude.

Life during graduate school would have been far worse if it was not for the magnificent friends I have made along the way. I must first thank Jacqueline Shea who was a wonderful and supportive friend and showed me the joy of having a dog around. I hope her and Gracie enjoy many more years together. Carlos Mejuto Zaera is a brilliant scientist, excellent baker, and even better friend. I am grateful for all the times, intellectual discussions, recipes, and books we have shared these past few years and I hope to visit across the pond many times in the future. I also want to thank Jeffrey M. Epstein and Katie Klymko for their support and guidance as well as lunch companionship. I owe Eric Arsenault a special thank you for keeping me intellectually engaged during quarantine through collaboration and what has now become close friendship. I am excited to follow his assuredly successful career as it develops. Chloe Gao and Trevor Grand Pre have been amazing colleagues to join with and help start a new research group alongside David. I have really felt I have been able to learn from and confide in them. I wish them both the best in their careers. I am also thankful for the rest of the folks in the Limmer group—Aditya, Amael, Anthony, Avishek, Ben, Michelle, Mirza, Sam, Tom, and Yoon. I am glad we got to spend what time (long or short) we had learning and hanging together. I also must thank my close friends from my time at KU—Chase, Christian, Mason, Neil, and Will—with whom I have kept in touch despite the vast distance that separates us.

During what seems like a lifetime ago, I was a policy debater both in high school at Washburn Rural and in undergrad at KU. Through this activity I met many great minds such as Scott Harris and Brett Bricker who were early inspirations of my graduate school pursuits as well as excellent teachers of argumentation and logic. I also developed some friendships in Tim Ellis and Mark Wilkins who have remained close and supportive. I am extremely thankful to my high school debate coach Cindy Burgett who taught me more than anything how to be a (hopefully) good person.

I am also grateful for the love and support from my family. My parents, Steve and Lori, have been there for me in more ways than likely I or they know. I want to thank them especially for teaching me about exponents and algebra those many years back, which sparked my love of math and science and led me to my position today. My brother, Austin, and sister-in-law, Caitlin, have been so incredibly supportive throughout this time. Their love and warmth has helped me overcome some particularly difficult times and I am excited for our future together as a family. My brother especially has served as my inspiration for life in general. I hope to achieve his level of balance, passion, and happiness one day.

And finally, Vinnie, my boy, my pandemic pal, my partner-in-crime. As cheesy as this may sound you have really helped me pull through some dark times with your constant joy and energy. I could not be more thankful for you coming in my life and I only wish you could comprehend how much you mean to me. I suppose a big bone and a scratch on the butt will suffice.

Chapter 1

Introduction

> *"Highly organized research is guaranteed to produce nothing new."*
>
> — Frank Herbert [102]

1.1 Photoinduced Chemical Reactions

The interaction of light and matter induces a wide range of chemical and physical phenomena that arise in much of the natural world and in many of the major technological advances of the 20th and 21st centuries. By introducing additional energy that can flow throughout the system, light-matter interactions allow the detailed manipulation of material properties and chemical reactivity as exemplified through photoinduced chemical reactions. Rather than waiting for rare equilibrium fluctuations that take a reaction over an energy barrier, photochemical reactions give rise to unique chemistry by redistributing additional energy among the many degrees-of-freedom after light excitation.

Applications tied to such reactions are nearly limitless. Much of the natural world relies on light harvesting processes, such as photosynthesis,[79, 125, 210, 211] to efficiently generate energy for use in life cycles. In these processes light interacts with a photoexcitable complex and with high efficiency generates excited, mobile electrons that may move throughout the system for use in other reactions such as the creation of ATP. These processes can be analogously synthesized in the lab through so-called artificial photosynthesis to construct materials that harvest the power of the sun to efficiently and cleanly generate electricity.

Chemical reactions may also be directly dependent on light-matter interactions. From photoinitiated polymerization reactions[53] to photoinduced electron transfer reactions,[201, 276] photochemical reactions occupy a special cornerstone of chemistry itself, which is built on the details of electrons in chemical bonding. Through these wide variety of reactions photochemistry can be found throughout the natural world and can serve as a toolbox for chemical synthesis in the laboratory.[53]

Another class of photochemical reactions involve structural molecular transformations in what are known as photoisomerization reactions.[16, 223, 246, 275] In these reactions no chemical reaction occurs—there are no distinct changes in the chemical bonds—but a physical transformation is undergone from a molecule in a starting configuration to a rearranged state. These physical transformations can be used to perform work in microscopic systems, but are even found in biological contexts where human vision is dependent on the photoisomerization of a molecule.[223, 275]

While photoinduced chemical reactions are ubiquitous, general guiding principles that describe macroscopic properties of the reactions such as the timescale and yields through their mechanistic details remain elusive. In other words, what is the journey these systems take in going toward their destination? From the perspective of this thesis, there are three distinguishing features associated with these reactions that render our theoretical understanding of such processes a challenge: nonadiabatic effects, nonequilibrium phenomena, and nonmarkovian dynamics. Each of these unique aspects, which are described below, that occur during photoinduced processes not only introduce additional complexity into the dynamics, but are also largely dependent on the microscopic details of each individual system, which obfuscate the general principles that describe these reactions.

Nonadiabatic

A large portion of quantum chemistry research has focused on applications of the Born-Oppenheimer (BO) approximation, which underpins key concepts in chemical dynamics such as the potential energy surface. In this approximation, the total wavefunction can be written as a product of the nuclear wavefunction and an electronic wavefunction that is parametric on the nuclear coordinates. Dynamics of the nuclei evolve due to forces obtained from the potential energy surface, which is the resulting energy obtained from the time-independent Schrodinger equation of the BO Hamiltonian.

The electronic and nuclear degrees-of-freedom are uncoupled under the BO approximation and the dynamics of the system evolve in a *single* electronic state. Photoinduced reactions fundamentally violate this approximation—a wavepacket is prepared on an electronically excited state due to the light-matter interaction and the system eventually relaxes back down to the ground electronic state potentially through a number of other electronic states thus involving *multiple* electronic states.[138] In the absence of interactions with an external radiation field, transitions of the system from one electronic state to another are radiationless and must be induced by couplings between electronic states mediated by the nuclear coordinates. These couplings are referred to as nonadiabatic and represent an element of the dynamics that goes beyond the BO approximation. Additionally, the accurate calculation of these couplings through electronic structure programs can require immense computational resources—a challenge that is not specifically addressed in this thesis.

Nonadiabatic dynamics can complicate a simplistic description of photoinduced chemical processes through a few key effects. First, since the wavepacket evolves on multiple potential energy surfaces, the mechanism of photoinduced reactions can be rather complex. The forces acting on the nuclei can be dramatically different depending on the electronic state, which from a classical perspective means the reaction proceeds along a delicately balanced pathway along each potential energy surface with specific transitions between each electronic state. Compared to adiabatic processes, which proceed on a single potential energy surface, an expanded coordinate space that includes both nuclear and electronic degrees-of-freedom is required to describe nonadiabatic dynamical reaction pathways.

Another aspect of complex nonadiabatic dynamics are quantum mechanical interference effects.[215, 287] The system is described by a complex probability amplitude referred to as the wavefunction. Since the wavefunction is a probability amplitude rather than a probability density, observing the system in particular configurations depends on the phase information in the wavefunction. These considerations are particularly important when the wavepacket passes through conical intersections which are singular points in the nonadiabatic coupling in the nuclear configuration space due to degeneracies in the electronic energies. Depending on the way the system approaches and proceeds through the conical intersection, particular elements of the wavefunction can obtain phases that cause interference with other wavefunction elements and probabilistically restrict or guide the nuclear motion along certain pathways. These interference effects would otherwise be absent in a purely BO description.

Nonequilibrium

In any introductory chemistry course, one is immediately taught general principles of chemical reactions that relate equilibrium thermodynamics to kinetics. These relations such as the well-known Arrhenius law and Eyring's Transition State Theory rest on assumptions through which general mathematical expressions can be derived.[69] These assumptions suggest that chemical reactions proceed due to rare fluctuations that take a system from a set of configurations characterizing the reactant through a specific or set of specific configurations characterizing the transition state that are short-lived to the set of configurations characterizing the product of the reaction.[55] At the core of these assumptions is that the system is in thermal equilibrium when in its reactant or product configurations and that the necessary fluctuations that take the system through the transition state are rare due to a large energy barrier in the potential energy surface. In this picture, the rate of a chemical reaction can be decomposed into the probability for the system to fluctuate into the transition state configuration—which gives rates the Arrhenius temperature dependence—multiplied by the speed at which the system passes through the transition state.[44]

Photoinduced processes inherently break these equilibrium assumptions—light-matter interactions nearly instantaneously place the system in higher-energy electronic states and this additional energy can then be redistributed to nuclear degrees-of-freedom and the surrounding condensed environment. Often these processes are barrierless due to the additional energy that is initially pumped in, but can also be constrained by kinetic factors. Despite potential energy considerations that determine minimum energy pathways, pathways along more quickly fluctuating coordinates may be opened or the system can fall into kinetic traps that are inaccessible at thermal equilibrium. In this sense, the equilibrium picture of considering a probability times a speed, even if applicable, would be difficult to compute. The probability for particular fluctuations to occur that take the system along a reaction pathway are no longer dictated by equilibrium statistical mechanics, but are now determined by the kinetics of dynamics along competing fluctuating degrees-of-freedom.

Condensed phase environments further complicate the picture by expanding the relevant reaction coordinate space. Heightened fluctuations in the bath can dramatically change the typical configurations and reduced or implicit descriptions of the environment's influence on photoinduced reactions must appropriately account for these effects beyond the equilibrium description. At equilibrium, fluctuations are constrained by fundamental laws such as microscopic reversibility and detailed balance, however, out of equilibrium much more relaxed constraints are imposed.[52, 122] These relations determine the fluctuations that allow energy to be redistributed between the system and its surroundings and in general do not rigorously hold under certain approximations. Without proper description, important effects from this energy redistribution may be missed that determine the outcome of certain chemical reactions as encoded in macroscopic observables.

Nonmarkovian

Photoinduced reactions have often been observed to occur on an ultrafast (< 1 ps) timescale, which is in part due to the nonadiabatic and nonequilibrium effects. The degrees-of-freedom associated with condensed phase environments, however, move or relax on a timescale that is commensurate or slower than the ultrafast reaction dynamics. When these slower timescales have an important impact on the dynamics, we observe what are called nonmarkovian effects. Nonmarkovianity is the phenomena associated with after-effects that act on some system as a result of its previous dynamics. The consequence of nonmarkovianity is twofold. First, nonmarkovianity implies that there are additional degrees-of-freedom whose dynamics are important to the system dynamics.[193] These additional degrees-of-freedom are hence part of the reaction coordinate and complicate its description from a few-body picture to a many-body one.

The second consequence is that the idea of a transition state as a single configuration or set of configurations is no longer meaningful. At equilibrium, for example, a transition is often the configuration associated with a rare fluctuation along a slowly moving degree-of-freedom and once the transition state is reached, the reaction proceeds or fails with some probability or rate. With nonmarkovianity, the dynamics up to the point of the transition state are important. Supposing now an additional important slow degree-of-freedom, the transition state may now depend on how this other degree-of-freedom has fluctuated or will fluctuate along with the original reaction coordinate.[95, 183] In this manner, the transition state can be described by a configuration or set of configurations *and* the history of how it proceeded to that point.

1.2 Outline

As we have discussed, the challenges in theoretically describing photoinduced chemical reactions are associated with there being a large number of degrees-of-freedom, an importance of remaining faithful to fundamental physical laws, and a difficulty in elucidating the general principles of these reactions from the microscopic details. This thesis aims to address these challenges head on. In particular, the work described herein illustrates new theoretical and experimental tools that can be used for studying condensed phase photoinduced reactions and shows how these tools can be specifically applied.

This thesis is organized into five remaining chapters. In Chapter 2, the theoretical foundations upon which this thesis rests are outlined. These foundations cover the quantum mechanical theory of dynamics for molecular systems in condensed phase environments and the relation between such dynamics and experimental observations through spectroscopy. While the remaining chapters are relatively self-contained, this chapter serves as a useful reference for the subsequent work. Chapters 3 and 4 introduce new theoretical tools for simulating and analyzing the dynamics of condensed phase quantum systems. Problems associated with elucidating complicated reaction mechanisms in many-body systems are tackled with the methods proposed in Chapter 3 while efficient numerical techniques for simulating these systems are developed in 4.

These methods are then applied in two contexts. In Chapter 5 we show how the methods developed can be used to create model Hamiltonians for describing photoinduced chemical reactions, specifically the photoisomerization of azobenzene. Here it is illustrated how these new methods can lead to a dramatic reduction in the number of degrees-of-freedom needed to properly describe these reactions. Chapter 6 then showcases how these methods can be used to simulate spectroscopic observables and how a relatively new spectroscopy technique, two-dimesional electronic vibrational spectroscopy, can be used to obtain mechanistic insight in condensed phase photoinduced reactions, specifically, in light-harvesting complexes.

Chapter 2

Theoretical Aspects of Condensed Phase Quantum Dynamics

> *"When you play the game of thrones, you win or you die. There is no middle ground."*
>
> — Cersei Lannister [162]

In this chapter we outline the formalism, illustrate the methods, and derive the important equations that will serve as the theoretical foundation of this thesis. As this thesis concerns itself with the quantum dynamical phenomena of condensed phase systems, we will first discuss the basics of quantum molecular dynamics of closed systems that adequately describes gas-phase dynamics. This description will be followed by a discussion of dynamics of open quantum systems and quantum master equations, which can be applied to condensed phase systems. The final section will discuss connections between the underlying dynamics and experimental observations through the time-dependent response function formalism.

2.1 Quantum Dynamics of Closed Systems

When a system is completely isolated from its surroundings there is no exchange of energy, particles, or any other form of quantum information with an environment. In this instance, the system is considered to be closed and is entirely described by a wavefunction, $|\psi\rangle$. The energy of the system is an observable characterized by the Hamiltonian operator, H. Observable values of the energy are given by the eigenvalues of the Hamiltonian as encoded in the time-independent Schrödinger equation,

$$H|\psi\rangle = E|\psi\rangle, \tag{2.1}$$

with associated eigenvectors, which is a particular wavefunction. The average energy of the system, or average of any operator (replace H with some operator A in the following equation), is given by an inner product

$$\langle H \rangle = \langle \psi | H | \psi \rangle, \tag{2.2}$$

which is obtained experimentally by averaging over repeated measurements. The dynamics of the system is determined by the time-dependent Schrödinger equation,

$$\partial_t | \psi(t) \rangle = -\frac{i}{\hbar} H | \psi(t) \rangle, \tag{2.3}$$

where $\hbar$ is the reduced Planck constant. The time-dependent Schrödinger equation has the formal solution, for time-independent Hamiltonians,

$$|\psi(t)\rangle = e^{-iHt/\hbar} |\psi(0)\rangle \equiv U(t) |\psi(0)\rangle \tag{2.4}$$

where $U(t) = e^{-iHt/\hbar}$ is the propagator. The system is not generically in a particular eigenstate—of the Hamiltonian or any other Hermitian operator—but often exists in a superposition of states. In some suitable basis, this superposition is written as

$$|\psi\rangle = \sum_n c_n |n\rangle, \tag{2.5}$$

where $\{|n\rangle\}$ are the set of basis states and $\{c_n\}$ are the set of complex coefficients giving the amplitude of a particular basis state. When expanded in the energy eigenbasis—the set eigenvectors of the Hamiltonian $\{|n\rangle\}$ with eigenvalues $H|n\rangle = E_n|n\rangle$—the time-dependence of the wavefunction is built into the complex coefficients, that is,

$$|\psi(t)\rangle = \sum_n c_n(t) |n\rangle, \tag{2.6}$$

where $c_n(t) = e^{-iE_n t/\hbar} c_n(0)$.

While formally quite simple, these equations are of impractical use for describing real molecular systems. As will be explained below, finding solutions to either Eq. 2.1 or 2.3 is prohibitively expensive even for modern supercomputing architectures due to exponential computational scaling associated with representing the wavefunction of many-body systems. The remainder of this section is devoted to characterizing exact and approximate methods for computing the dynamics of such closed systems.

Nonadiabatic Effects

For much of the 20th century, major advancements in quantum chemistry utilized the adiabatic or Born-Oppenheimer (BO) approximation.[1] This approximation considers the *ab initio* molecular Hamiltonian

$$H = \sum_I \frac{\mathbf{P}_I^2}{2M_I} + \sum_i \frac{\mathbf{p}_i^2}{2m_i} + \sum_{i<j} V_{ee}(\mathbf{r}_{i,j}) + \sum_{i,I} V_{eN}(\mathbf{r}_{i,I}) + \sum_{I<J} V_{NN}(\mathbf{R}_{IJ}). \tag{2.7}$$

---

[1] Much of this discussion can be found in a number of textbooks. For an excellent introduction of the BO approximation and other topics in electronic structure theory we refer the reader to Ref. [245].

Here electron degrees-of-freedom are denoted in lower case and nuclei are denoted in upper case, M_I (m_i) is a nuclear (electron) mass, $\mathbf{P}_I$ ($\mathbf{p}_i$) is the nuclear (electron) momentum. The potential energy terms are given by the two-body Coloumb potentials of the electron-electron (ee), electron-nuclear (eN), and nuclear-nuclear (NN) interactions, which are all dependent on the distances (denoted by $\mathbf{r}$ or $\mathbf{R}$) between each particle.

The central tenet of the Born-Oppenheimer approximation is that the nuclei are massive relative to the electrons, that is for all I and i, $M_I \gg m_i$, and thus the electronic motion is instantaneous compared to nuclear motion. The approximate, Born-Oppenheimer, Hamiltonian is given by,

$$H_{BO} = \sum_i \frac{\mathbf{p}_i^2}{2m_i} + \sum_{i<j} V_{ee}(\mathbf{r}_{i,j}) + \sum_{i,I} V_{eN}(\mathbf{r}_{i,I}) + \sum_{I<J} V_{NN}(\mathbf{R}_{IJ}) \tag{2.8}$$

where the nuclear coordinates are now taken to be a vector of fixed c-numbers rather than quantum mechanical operators. The result is that the positions of the nuclei may be considered as parametric and the solution to the time-independent Schrödinger equation with H_{BO} gives adiabatic eigenstates that are products of an electronic and nuclear wavefunction (for the α eigenstate),

$$|\Psi_\alpha(\mathbf{r},\mathbf{R})\rangle = |\phi_\alpha(\mathbf{r};\mathbf{R})\rangle|\chi_\alpha(\mathbf{R})\rangle, \tag{2.9}$$

with eigenvalues $H_{BO}|\Psi_\alpha(\mathbf{r},\mathbf{R})\rangle = E_\alpha|\Psi_\alpha(\mathbf{r},\mathbf{R})\rangle$ where $|\phi_\alpha(\mathbf{r};\mathbf{R})\rangle$ is the electronic wavefunction, which is parametrically dependent on the nuclear coordinates and $|\chi_\alpha(\mathbf{R})\rangle$ is the nuclear wavefunction. These electronic eigenstates can be found independently at each value of the nuclear coordinates and the associated eigenenergies characterize the so-called potential energy surface from which the forces acting on the nuclei can be derived.

To see the effect of nonadiabatic dynamics—dynamics with the full Hamiltonian—it is useful to first consider dynamics of an adiabatic eigenstate, which is a typical initial condition of a system upon vertical excitation through light-matter interaction. In this case, we insert Eq. 2.8 and 2.9 into Eq. 2.3 and project out the nuclear wavefunction, from which we obtain

$$\partial_t|\phi_\alpha\rangle = -\frac{i}{\hbar}H_{BO}|\phi_\alpha\rangle, \tag{2.10}$$

with solution $|\phi_\alpha(t)\rangle = e^{-iE_\alpha t/\hbar}|\phi_\alpha(t)\rangle$. Taking the inner product of the time-dependent electronic wavefunction with another electronic eigenstate allows us to find the amplitude of finding the system in another electronic eigenstate at time t,

$$\langle\phi_\beta|\phi_\alpha(t)\rangle = \langle\phi_\beta|e^{-iE_\alpha t/\hbar}|\phi_\alpha(t)\rangle = e^{-iE_\alpha t/\hbar}\delta_{\alpha\beta}. \tag{2.11}$$

In other words, the system stays completely populated on a single electronic state throughout the course of its time evolution.

Now including the additional term from the nuclear kinetic energy not present in the BO Hamiltonian we have,

$$H|\Psi_\alpha(\mathbf{r},\mathbf{R})\rangle = \left(\sum_I \frac{\mathbf{P}_I^2}{2M_I} + H_{BO}\right)|\Psi_\alpha(\mathbf{r},\mathbf{R})\rangle = \left(\sum_I \frac{\mathbf{P}_I^2}{2M_I} + E_\alpha\right)|\Psi_\alpha(\mathbf{r},\mathbf{R})\rangle, \tag{2.12}$$

where we have used the fact that $|\Psi_\alpha(\mathbf{r},\mathbf{R})\rangle$ is an eigenstate of the BO Hamiltonian. Inserting the identity of the momentum operator

$$\sum_I \frac{\mathbf{P}_I^2}{2M_I} = -\sum_I \frac{\hbar^2}{2M_I}\frac{\partial^2}{\partial \mathbf{R}_I^2} \tag{2.13}$$

and applying it on the wavefunction gives us

$$\begin{aligned}
-\sum_I \frac{\hbar^2}{2M_I}\frac{\partial^2}{\partial \mathbf{R}_I^2}|\Psi_\alpha(\mathbf{r},\mathbf{R})\rangle &= -\sum_I \frac{\hbar^2}{2M_I}\frac{\partial^2}{\partial \mathbf{R}_I^2}|\phi_\alpha(\mathbf{r};\mathbf{R})\rangle|\chi_\alpha(\mathbf{R})\rangle \\
&= -\sum_I \frac{\hbar^2}{2M_I}|\phi_\alpha(\mathbf{r};\mathbf{R})\rangle\left(\frac{\partial^2}{\partial \mathbf{R}_I^2}|\chi_\alpha(\mathbf{R})\rangle\right) \\
&\quad -\sum_I \frac{\hbar^2}{M_I}\left(\frac{\partial}{\partial \mathbf{R}_I}|\phi_\alpha(\mathbf{r};\mathbf{R})\rangle\right)\left(\frac{\partial}{\partial \mathbf{R}_I}|\chi_\alpha(\mathbf{R})\rangle\right) \\
&\quad -\sum_I \frac{\hbar^2}{2M_I}\left(\frac{\partial^2}{\partial \mathbf{R}_I^2}|\phi_\alpha(\mathbf{r};\mathbf{R})\rangle\right)|\chi_\alpha(\mathbf{R})\rangle.
\end{aligned}\tag{2.14}$$

As we proceeded above, we will take an inner product of this term with a different BO eigenstate,

$$\begin{aligned}
-\sum_I \frac{\hbar^2}{2M_I}\langle\Psi_\beta(\mathbf{r},\mathbf{R})|\frac{\partial^2}{\partial \mathbf{R}_I^2}|\Psi_\alpha(\mathbf{r},\mathbf{R})\rangle &= -\sum_I \frac{\hbar^2}{2M_I}\delta_{\alpha\beta}\langle\chi_\beta(\mathbf{R})|\frac{\partial^2}{\partial \mathbf{R}_I^2}|\chi_\alpha(\mathbf{R})\rangle \\
&\quad -\sum_I \frac{\hbar^2}{M_I}\mathbf{d}_{I,\alpha\beta}(\mathbf{R})\langle\chi_\beta(\mathbf{R})|\frac{\partial}{\partial \mathbf{R}_I}|\chi_\alpha(\mathbf{R})\rangle \\
&\quad -\sum_I \frac{\hbar^2}{2M_I}g_{I,\alpha\beta}(\mathbf{R})\langle\chi_\beta(\mathbf{R})|\chi_\alpha(\mathbf{R})\rangle
\end{aligned}\tag{2.15}$$

where the first term is simply the nuclear kinetic energy and

$$\mathbf{d}_{I,\alpha\beta}(\mathbf{R}) = \langle\phi_\beta(\mathbf{r};\mathbf{R})|\frac{\partial}{\partial \mathbf{R}_I}|\phi_\alpha(\mathbf{r};\mathbf{R})\rangle \tag{2.16}$$

$$g_{I,\alpha\beta}(\mathbf{R}) = \langle\phi_\beta(\mathbf{r};\mathbf{R})|\frac{\partial^2}{\partial \mathbf{R}_I^2}|\phi_\alpha(\mathbf{r};\mathbf{R})\rangle. \tag{2.17}$$

Here we have defined two quantities $\mathbf{d}_{I,\alpha\beta}(\mathbf{R})$, which is the derivative or nonadiabatic coupling vector, and $g_{\alpha\beta}(\mathbf{R})$, which is the (scalar) diagonal BO correction. In many cases, the latter of these two is small and can be ignored, though some work has shown the importance of its inclusion in limited cases.[86, 164]

It can be shown through an application of the Hellman-Feynman theorem that the derivative coupling is equal to a scaled energy gradient,

$$\mathbf{d}_{I,\alpha\beta}(\mathbf{R}) = \frac{\langle\phi_\beta(\mathbf{r};\mathbf{R})|\frac{\partial H}{\partial \mathbf{R_I}}|\phi_\alpha(\mathbf{r};\mathbf{R})\rangle}{E_\beta - E_\alpha}. \tag{2.18}$$

As can be seen from this equation, the magnitude of the derivative coupling grows when the energy between two adiabatic states decreases. In many chemical reactions that proceed only along the ground state, this term remains small and can thus be ignored. In the case of photoinduced chemical reactions, the nuclear wavepacket moves along the excited state to regions where the ground state may be high in energy relative to its equilibrium position. In these instances, the adiabatic energies become close and may even go to zero at a conical intersection, in which case the derivative coupling terms becomes large and even singular. As this matrix element quantifies the rate of population transfer—which can be seen by including this term in Eq. 2.3 and working through the procedure of Eq. 2.11—fast population transfer from one adiabatic electronic state to another may occur in these regions of the potential energy and the dynamics will proceed in multiple electronic states.

Another dramatic effect from nonadiabatic dynamics is the so-called geometric phase.[287] The BO solution to the time-dependent Schrödinger equation can be rewritten as

$$|\phi_\alpha(\mathbf{r},t;\mathbf{R})\rangle = \exp\left[\int_0^t dt'\langle\phi_\alpha(\mathbf{r},t';\mathbf{R})|\partial_t|\phi_\alpha(\mathbf{r},t';\mathbf{R})\rangle\right]|\phi_\alpha(\mathbf{r},0;\mathbf{R})\rangle. \tag{2.19}$$

Here we will denote the phase accumulated throughout the dynamics as

$$\begin{aligned}\gamma &= \int_0^t dt'\langle\phi_\alpha(\mathbf{r},t';\mathbf{R})|\partial_{t'}|\phi_\alpha(\mathbf{r},t';\mathbf{R})\rangle \\ &= \int_0^t dt'\langle\phi_\alpha(\mathbf{r},t';\mathbf{R})|\frac{\partial}{\partial\mathbf{R}}|\phi_\alpha(\mathbf{r},t';\mathbf{R})\rangle\cdot\frac{\partial\mathbf{R}}{\partial t'} \\ &= \int_{\mathbf{R}_0}^{\mathbf{R}_t} B(\mathbf{R})\cdot d\mathbf{R} \end{aligned} \tag{2.20}$$

where

$$B(\mathbf{R}) = \langle\phi_\alpha(\mathbf{r},t';\mathbf{R})|\frac{\partial}{\partial\mathbf{R}}|\phi_\alpha(\mathbf{r},t';\mathbf{R})\rangle. \tag{2.21}$$

This phase, often referred to as the geometric or Berry phase, is thus a line integral over the nonadiabatic coupling vector. If we consider the line integral over a particular closed path and evaluate it using contour integration, it is nonzero only around singular points in the wavefunction, which are points of degeneracy in the adiabatic electronic states—in other words at conical intersections. Since the Berry phase is nonzero around conical intersections, the sign of the phase depends on the direction followed along the closed path. Hence a wavefunction as it is proceeding toward a conical intersection can interfere with itself depending on the direction with which components of the wavefunction go around the conical intersection. The accurate incorporation of these phase interference effects can have a dramatically large impact on the qualitative behavior of the dynamics of the system.[61, 214, 215]

Wavefunction Representations

So far we have considered adiabatic wavefunctions that are solutions to the time-independent Schrödinger equation with the BO Hamiltonian. Action of the full Hamiltonian on this representation, as we have seen above, induces couplings which may become large or even signular at particular nuclear configurations. An alternate representation that avoids these singularities is thus warranted and gives rise to the so-called diabatic representation. The diabatic states, $\{|\varphi_\alpha\rangle\}$, are position-independent, that is, they are electronic states that are unchanged by motion of the nuclear degrees-of-freedom and are states for which the derivative coupling is zero. To find the diabatic states, one must find a nuclear position-dependent unitary transformation that sets the derivative coupling to zero at all configurations.[138] In this sense, the nuclear kinetic energy operator becomes diagonal with respect to the diabatic electronic states, however, the diabatic electronic states are no longer orthogonal with respect to the potential and have nonzero couplings from that potential,

$$V_{\alpha\beta} = \langle\varphi_\alpha|V|\varphi_\beta\rangle, \tag{2.22}$$

which are referred to as the diabatic couplings. The procedure to find the diabatic states is unique when the adiabatic and diabatic bases are complete, however, this is impossible to achieve in practice.[138] There are thus a number of procedures that seek to compute an approximate unitary transformation that minimizes the derivative coupling in a suitably large basis of diabatic states.[14, 207, 208, 281]

Once an appropriate diabatic representation has been found an ansatz for the wavefunction must be imposed for efficient numerical calculations. The simplest approach for an ansatz is to assume a direct product basis, in which the wavefunction is expanded in products of one-dimensional basis functions.[138] The minimal direct product wavefunction is given by a Hartree product

$$|\Psi\rangle = |\varphi\rangle \prod_{m=1}^{N} |\chi_m\rangle, \tag{2.23}$$

where φ denotes the electronic wavefunction and $\{|\chi_m\rangle\}$ are the wavefunctions of the N nuclear degrees-of-freedom. As this Hartree product contains an expansion of each one-dimensional wavefunction with a single basis function it can be said to be minimally entangled. Nonadiabatic quantum dynamical phenomena, as we have previously discussed, induces entanglement by coupling different basis functions. Going beyond the Hartree product we can include products of superpositions of each one-dimensional wavefunction,

$$|\Psi\rangle = \left(\sum_\alpha c_\alpha|\varphi_\alpha\rangle\right) \prod_{m=1}^{N} \sum_j c_{\alpha,j_m}|\chi_{j_m}\rangle, \tag{2.24}$$

where $\{c_\alpha, c_{\alpha,j_m}\}$ are the complex coefficients describing that superposition. Put more compactly, this wavefunction has the form

$$|\Psi\rangle = \sum_\alpha \sum_{j_1,j_2,\ldots,j_N} A_{\alpha,j_1,j_2,\ldots,j_N}|\varphi_\alpha\rangle \prod_{m=1}^{N} |\chi_{j_m}\rangle, \tag{2.25}$$

where $A_{\alpha,j_1,j_2,\ldots,j_N}$ is the $(N+1)-$dimensional coefficient tensor, which is a product of all the one-dimensional coefficients

$$A_{\alpha,j_1,j_2,\ldots,j_N} = c_\alpha \prod_{m=1}^{N} c_{\alpha j_m} \tag{2.26}$$

Here we have invoked a form of the wavefunction in which its constituent basis functions are time-independent with time-dependent coefficients. The equation of motion for this wavefunction is given by the time-dependent Schrödinger equation for the coefficients

$$\dot{A}_{\alpha,j_1,j_2,\ldots,j_N}(t) = -\frac{i}{\hbar} \sum_{\beta,k_1,k_2,\ldots,k_N} H^{\alpha,j_1,j_2,\ldots,j_N}_{\beta,k_1,k_2,\ldots,k_N} A_{\beta,k_1,k_2,\ldots,k_N}(t) \tag{2.27}$$

with the Hamiltonian matrix elements given by

$$H^{\alpha,j_1,j_2,\ldots,j_N}_{\beta,k_1,k_2,\ldots,k_N} = \left(\langle\varphi_\alpha| \prod_{m=1}^{N} \langle\chi_{j_m}|\right) H \left(|\varphi_\beta\rangle \prod_{m=1}^{N} |\chi_{k_m}\rangle\right). \tag{2.28}$$

The matrix elements of the Hamiltonian can either be precomputed at the beginning of a calculation and then stored in memory or, for large systems, may be computed on-the-fly so as not to incur steep memory costs. In either case, a preferable choice of the time-independent basis functions are those that converge in the number of basis functions quickly and have analytical forms for the matrix elements. One such choice that fits these requirements is the discrete variable representation (DVR) basis.[157] A DVR basis is a complete basis that diagonalizes the position operator with eigenvalues representing the location of the basis functions on the one-dimensional grid. Thus matrix elements for any potential energy operator, which are functions of the position operators, are also diagonal and can be evaluated by simply computing the value of the potential at the grid point. An additional benefit of the DVR basis is the analytical form for the kinetic energy operator, which is often tridiagonal depending on the particular DVR basis employed. Since the DVR basis represents operators in a sparse way, sparse linear algebra techniques, such as Krylov subspace methods,[188] can be used to dramatically speed up and reduce the memory requirements of such calculations.

Multiconfigurational Time-Dependent Hartree Theory

While the direct product form of the wavefunction is conceptually simple, it is only practically useful for systems of a few degrees-of-freedom at most due to exponential computational scaling of the wavefunction with the number of degrees-of-freedom. To see this scaling we assume a system with N degrees-of-freedom that requires n basis functions per degree-of-freedom. The memory requirements then scale as n^N and thus as N grows we encounter the so-called curse of dimensionality.

An alternative approach to the direct product representation is the Multiconfigurational Time-Dependent Hartree (MCTDH) method.[18] The MCTDH wavefunction is given by

$$|\Psi(t)\rangle = \sum_{\alpha} \sum_{j_1,j_2,\dots,j_N} A_{\alpha,j_1,j_2,\dots,j_N}(t)|\varphi_\alpha\rangle \prod_{m=1}^{N} |\phi^{m}_{\alpha,j_m}(t)\rangle, \tag{2.29}$$

where $|\varphi_\alpha\rangle$ is the electronic wavefunction, $A_{\alpha,j_1,j_2,\dots,j_N}(t)$, is the coefficient tensor, and the nuclear degrees-of-freedom are now represented by single particle functions $|\phi^{m}_{\alpha,j_m}(t)\rangle$. This approach relies on two key differences to the direct product representation. The first difference is that the wavefunction is expanded in a basis of time-dependent functions, the single particle functions (SPFs). These SPFs are typically represented by an expansion of a time-independent basis, the primitive basis functions (PBFs), as in the aforementioned direct product approach,

$$|\phi^{m}_{\alpha,j_m}(t)\rangle = \sum_{p} c_{\alpha,j_m,p}(t)|\chi_{j_m}\rangle. \tag{2.30}$$

The coefficient tensor is still time-dependent, but the time-dependence of the basis functions adds additional complexity to the total wavefunction offering a more compact and thus lower memory representation at the cost of having a more complex equation of motion. Since the SPFs can optimally represent the wavefunction locally rather than relying on a global basis, fewer of them are required and the memory requirements of the coefficient tensor are significantly reduced. Considering a wavefunction that requires p SPFs per mode where $p < n$, the memory savings to the coefficient tensor is $(n/p)^N$. As the number of degrees-of-freedom grows, the curse of dimensionality remains, but scales at a lower rate than the direct product representation.

The second difference is that these basis functions can be, although it is not always used in practice, multidimensional in that they represent multiple degrees-of-freedom in the total wavefunction. This technique is referred to as mode-combination and is essentially a direct product basis expansion for multiple modes, but combined into a single set of SPFs. As the direct product basis is limited to a few degrees-of-freedom due to the scaling of the coefficient tensor, the mode combination technique reduces the scaling of the coefficient tensor by placing additional memory requirments into the SPFs. When utilized efficiently, this approach allows MCTDH to treat tens of degrees-of-freedom going well beyond the capabilities of the direct product approach.

The equation of motion for the MCTDH wavefunction is found by applying the Dirac-Frenkel variational principle[58, 74, 199] ($\hbar = 1$ throughout the remainder of this subsection),

$$\langle \delta\Psi | H - i\partial_t | \Psi \rangle = 0, \tag{2.31}$$

where $|\delta\Psi\rangle$ is an infinitesimal variation of the wavefunction. By adopting a particular gauge condition

$$i\langle \phi^{m,\beta}_{j_m}(t) | \dot{\phi}^{m,\alpha}_{k_m}(t) \rangle = 0 \tag{2.32}$$

we obtain two coupled equations of motion for the coefficients and the SPFs, respectively,

$$i\dot{A}_J(t) = \sum_K \langle \Phi_J(t)|H|\Phi_K(t)\rangle A_K(t) \tag{2.33}$$

$$i|\dot{\phi}^m_{\alpha,j}(t)\rangle = (1 - P^{(m)}_\alpha) \sum_{\beta,k,l} (\rho^{-1}_{m,\alpha})_{jk} \langle H\rangle^{(m)}_{\alpha\beta,kl} |\phi^m_{\beta,l}(t)\rangle, \tag{2.34}$$

where J and L are composite indices capturing all the previously listed indices and $|\Phi_J(t)\rangle$ represents a product of all the SPFs in composite index J. A detailed explanation of all the terms is rather involved and is thus detailed explicitly in Appendix A.

One additional consequence of using time-dependent basis functions is that the corresponding matrix elements—with respect to the SPFs specifically—cannot be precomputed and stored in memory for rapid application like in Eq. 2.27 and must be computed on-the-fly. For computational efficiency, it is thus imperative to impose a sum-of-products form of the Hamiltonian. Considering a general many-body expansion of the Hamiltonian we obtain the sum-of-products form

$$H = \sum_r^s d_r h_r^{(\mathrm{el})} \prod_{m=1}^N h_r^{(m)} \tag{2.35}$$

where d_r is the coefficient for the rth term and $h_r^{(m)}$ is an operator that acts on the mth mode, which can include the electronic states, (el). With this form, each one-body operator can act independently on the SPFs and efficient tensor contraction algorithms can be utilized to calculate the final matrix elements.

A final comment about the MCTDH method is that the wavefunction ansatz still, as was previously mentioned, scales exponentially with the number of degrees-of-freedom, albeit at a slower rate than the direct product form. An extension of MCTDH, which goes beyond the scope of this thesis, generalizes the mode combination concept and recursively applies the MCTDH ansatz to groups of degrees-of-freedom, called the multilayer variant or ML-MCTDH.[270, 274] This ansatz and subsequent equations of motion scales polynomially with the number of degrees-of-freedom and has the capacity to represent hundreds and even thousands of degrees-of-freedom with model Hamiltonians (see for example Ref. [271] in which the authors performed a calculation with 100,000 degrees-of-freedom).

2.2 Quantum Dynamics of Open Systems

In the previous section, we considered isolated systems and methods for simulating their dynamics. These strategies are appropriate for treating gas-phase systems or systems of small clusters where the number of degrees-of-freedom remain limited. Condensed phases, however, contain many degrees-of-freedom from an accompanying solvent, solid, or potential interfaces and representing every degree-of-freedom, even with advanced numerical techniques, is computationally intractable. Treating these sorts of systems with a closed systems approach also formally prevents the correct description of condensed phase phenomena such as thermalization due to dissipation and dephasing.

Fortunately, even though condensed phases dramatically increase the size and complexity of the system, we are often only interested in some small relevant subsystem. This subsystem can exchange energy and particles with its surrounding environment and it is thus considered open. We will formally consider condensed phases as characterized by a Hamiltonian of the form,

$$H = H_S + H_B + H_{SB}, \tag{2.36}$$

where H_S is the Hamiltonian of the relevant system, H_B is the Hamiltonian of the bath, and H_{SB} describes their interaction that allows exchange of energy and particles. The bath is typically taken to be a set of degrees-of-freedom whose fluctuations obey Gaussian statistics and thus are described by a set of harmonic oscillators,

$$H_B = \sum_k \frac{\omega_k}{2}(p_k^2 + q_k^2), \tag{2.37}$$

with linear interactions with the system

$$H_{SB} = S \sum_k c_k q_k. \tag{2.38}$$

Here $\{(p_k, q_k)\}$ are the set of dimensionless momenta and positions[2] of the bath, S is some operator that acts on the system through which the system is coupled to the bath, and $\{c_k\}$ are the set of coupling coefficients encoding the strength of coupling between the system and each mode of the bath. While we will consider the case of a single bath, the generalization to multiple, uncorrelated baths is straightforward due to the separability in the Hamiltonian. These coupling coefficients are characterized by the spectral density,

$$J(\omega) = \frac{\pi}{2} \sum_k c_k^2 \delta(\omega - \omega_k). \tag{2.39}$$

Since the number of degrees-of-freedom in the bath is significantly larger than in the system, its energy spectrum is accordingly more dense and thus this spectral density is often taken to have some continuous functional form, which will be discussed in later chapters.

Mixed States and Density Matrices

As we have discussed, the wavefunction can be written as a linear combination of basis functions,

$$|\psi\rangle = \sum_n c_n |n\rangle \tag{2.40}$$

---

[2] One could also use mass-weighted coordinates, which is achieved by the change of variables $p_k \to \sqrt{\frac{1}{\omega_k m_k}} p_k$ and $q_k \to \sqrt{m_k \omega_k} q_k$. Under this transformation the spectral density also changes to $J(\omega) = \frac{\pi}{2} \sum_k \frac{c_k^2}{m_k \omega_k} \delta(\omega - \omega_k)$

and with complex coefficients c_n. Since the coefficients are complex, they have an associated phase, which when taking expectation values of operators through a measurement

$$\langle A\rangle = \langle\psi|A|\psi\rangle = \sum_{nm} c_n c_m^* A_{mn} \tag{2.41}$$

it becomes clear that the phase relationship between these coefficients is important. When the system can be described by a wavefunction in this form, it is assumed that we have a scheme under which we can measure both the amplitude and phase components of the complex coefficients. When this is the case, we can equivalently describe the state of the system as a density matrix, which is an outer product of wavefunction, given by

$$\rho = |\psi\rangle\langle\psi| = \sum_{nm} c_n c_m^* |n\rangle\langle m|. \tag{2.42}$$

By comparing Eq. 2.41 and 2.42 it is clear that expectation values are given by

$$\langle A\rangle = \mathrm{Tr}\{\rho A\}, \tag{2.43}$$

which is a trace of the product of the density matrix and operator of the observable. When the density matrix is written as an outer product of a single wavefunction, our system is said to be in a pure state and importantly the density matrix can be diagonalized and with a single eigenvalue that is 1 and the rest 0.

More often is the case in which we cannot measure the entirety of the wavefunction, that is we cannot determine both the amplitudes and phases of all the coefficients, due to incomplete information or an insufficient experimental technology. We still, however, have access to expectation values of observables, but measured over a statistical mixture of pure states,

$$\langle A\rangle = \mathbb{E}_{|\psi\rangle}[\langle\psi|A|\psi\rangle] = \sum_{nm} \mathbb{E}_{c_n c_m}[c_n c_m^*] A_{mn}, \tag{2.44}$$

where $\mathbb{E}_x$ is the expectation value over the random variable x. As we mentioned above, a pure state has a particular phase relationship between all the coefficients and thus they are correlated random variables, $\mathbb{E}_{c_n c_m}[c_n c_m^*] \neq \mathbb{E}_{c_n}[c_n]\mathbb{E}_{c_m}[c_m^*]$. We can then define a density matrix, which is an average of pure state outer products

$$\rho = \mathbb{E}_{|\psi\rangle}[|\psi\rangle\langle\psi|] = \sum_{nm} \mathbb{E}_{c_n c_m}[c_n c_m^*]|n\rangle\langle m|. \tag{2.45}$$

Again by comparing Eq. 2.44 and 2.45, we see that Eq. 2.43 is satisfied without change. In this case, diagaonlizing the density matrix gives more than one nonzero eigenvalue and thus our system is said to be in a mixed state.

A tempting picture to use instead would be an expectation value of pure state wavefunctions,

$$|\Psi\rangle = \mathbb{E}_{|\psi\rangle}[|\psi\rangle] = \sum_{n} \mathbb{E}_{c_n}[c_n]|n\rangle. \tag{2.46}$$

This picture, however, does not give the correct expectation value of our operator

$$\langle\Psi|A|\Psi\rangle = \sum_{nm} \mathbb{E}_{c_n}[c_n]\mathbb{E}_{c_m}[c_m^*]A_{mn} \neq \langle A\rangle, \tag{2.47}$$

hence only the density matrix is capable of characterizing the statistical uncertainty in the measurement of pure states. Such uncertainty arises in the condensed phase—a massive increase in the number of degrees-of-freedom and thus accessible states as well as a lack of detailed control inhibits our ability to measure with any certain the pure state of the system characterized by the coefficients' amplitudes and phases. Thus we see that the density matrix is the most natural object with which to describe the state and dynamics of a condensed phase system.

The time evolution of the density matrix is obtained by considering the time evolution of a wavefunction. Writing the density matrix as a statistical ensemble of pure state outer products—which can always be found by working in a suitable basis that diagonalizes the density matrix—the time evolution is clearly given by,

$$\begin{aligned}\rho(t) &= \sum_n p_n|\psi_n(t)\rangle\langle\psi_n(t)| \\ &= \sum_n p_n U(t)|\psi_n(0)\rangle\langle\psi_n(0)|U^\dagger(t) \\ &= U(t)\rho(0)U^\dagger(t) \end{aligned}\tag{2.48}$$

By differentiating this equation with respect to t we obtain an equation of motion for the density matrix given by the Liouville-von Neumann equation,

$$\partial_t\rho(t) = -\frac{i}{\hbar}[H,\rho(t)] \equiv -i\mathcal{L}\rho(t), \tag{2.49}$$

where $\mathcal{L}\cdot = \hbar^{-1}[H,\cdot]$ is referred to as the generator of the dynamics. Since H is written in a separable form in Eq. 2.36, the generator is also separable,

$$\mathcal{L} = \mathcal{L}_S + \mathcal{L}_B + \mathcal{L}_{SB}. \tag{2.50}$$

Throughout this section we will also consider general Hamiltonians that can be written as a zeroth-order Hamiltonian, H_0 plus some external perturbation, V, (note the similarities between the system-bath Hamiltonian above) in the form

$$H = H_0 + V. \tag{2.51}$$

It will often be convenient to work in the frame of reference of H_0, which is given by the Dirac or interaction picture. This reference is define by the transformations to operators A and wavefunctions $|\psi(t)\rangle$ as

$$A_I(t) = e^{iH_0t/\hbar}Ae^{iH_0t/\hbar} \tag{2.52}$$

$$|\psi_I(t)\rangle = e^{iH_0t/\hbar}|\psi(t)\rangle = e^{iH_0t/\hbar}e^{-iHt/\hbar}|\psi(0)\rangle, \tag{2.53}$$

where the subscript I will be used to denote the interaction representation. The density matrix, being an operator, is written in the interaction picture as

$$\rho_I(t) = e^{iH_0 t/\hbar}\rho(t)e^{-iH_0 t/\hbar}, \tag{2.54}$$

which upon differentiation gives the following equation of motion,[3]

$$\partial_t \rho_I(t) = -\frac{i}{\hbar}[V_I(t), \rho_I(t)] \equiv -i\mathcal{L}_V(t)\rho_I(t). \tag{2.55}$$

This equation has the solution,

$$\rho_I(t) = \rho_I(0) - i\int_0^t ds\mathcal{L}_V(s)\rho_I(s), \tag{2.56}$$

which is obtained by the method of separation of variables. This equation can be expanded through iteration, that is by plugging the right-hand side into itself we obtain

$$\rho_I(t) = \rho_I(0) - i\int_0^t ds\mathcal{L}_V(s)\rho_I(0) - \int_0^t ds\int_0^s ds'\mathcal{L}_V(s)\mathcal{L}_V(s')\rho_I(s'), \tag{2.57}$$

after a single iteration. Performing this iteration an infinite number of times we obtain the so-called Dyson series,

$$\rho_I(t) = \left\{1 + \sum_{n=1}^{\infty}(-i)^n\int_0^t ds\int_0^s ds_1\cdots\int_0^{s_{n-1}} ds_n\mathcal{L}_V(s)\mathcal{L}_V(s_1)\cdots\mathcal{L}_V(s_n)\right\}\rho_I(0), \tag{2.58}$$

which defines the propagator denoted by

$$G(t,t_0) = \exp_+\left\{-i\int_{t_0}^t ds\mathcal{L}_V(s)\right\}. \tag{2.59}$$

Here we have used a shorthand for the series expansion where the subscript on the exponential refers to the chronological time-ordering of the integrals in the series. This propagator may also be found by Taylor-series-expanding the full exponential and then reordering and summing the terms such that the time-ordering relation in Eq. 2.58 is satisfied. The backward propagator (reversed in time), which will also be of use, follows the anti-chronological time-ordering and is denoted by

$$\tilde{G}(t,t_0) = \exp_-\left\{i\int_{t_0}^t ds\mathcal{L}_V(s)\right\}. \tag{2.60}$$

---

[3] Interestingly, this equation of motion is different by a sign for the equation of motion of any other operator in the interaction picture due to the underlying time-dependence of $\rho(t)$ in the Schrödinger picture.

Projection Operators and Reduced Dynamics

So far in this section, we have alluded to the idea of describing a reduced subsystem of interest that can interact with its surroundings. Here we consider the mathematical techniques through which we achieve this construction. In particular, we utilize the projection operator formalism in which we reduce the dimensionality of the Hilbert space by projecting out the subspace of the environment. This construction is achieved by defining a system projection operator, $\mathcal{P}$, that acts on the full density matrix ρ. This operator is a bounded linear operator with eigenvalues 0 or 1 and is idempotent, $\mathcal{P}^2 = \mathcal{P}$. The projection operator for the environment or irrelevant part is defined as the complement to $\mathcal{P}$, $\mathcal{Q} = 1 - \mathcal{P}$, which can be easily shown to also satisfy the properties of a projection operator. These projection operators are thus said to be complete.

The specific projection operator we shall henceforth use is given by

$$\mathcal{P}\cdot = \mathrm{Tr}_B\{\cdot\}\rho_B^{\mathrm{eq}}, \tag{2.61}$$

where ρ_B^{eq} is the thermal density matrix of the bath degrees-of-freedom given by

$$\rho_B^{\mathrm{eq}} = \frac{e^{-\beta H_B}}{\mathrm{Tr}_B\{e^{-\beta H_B}\}} \tag{2.62}$$

where $\beta = 1/k_B T$ with T the temperature and k_B Boltzmann's constant. This projection operator effectively traces out the bath degrees-of-freedom and is idempotent,

$$\begin{aligned}\mathcal{P}^2 A &= \mathrm{Tr}_B\{\mathrm{Tr}_B\{A\}\rho_B^{\mathrm{eq}}\}\rho_B^{\mathrm{eq}} \\ &= \mathrm{Tr}_B\{A\}\mathrm{Tr}_B\{\rho_B^{\mathrm{eq}}\}\rho_B^{\mathrm{eq}} \\ &= \mathcal{P}A.\end{aligned} \tag{2.63}$$

With this projection operator, we can then define the reduced density matrix, $\sigma(t)$,

$$\mathcal{P}\rho(t) = \sigma(t)\rho_B^{\mathrm{eq}}, \tag{2.64}$$

which is the kronecker product of the density matrix characterizing the state of the system degrees-of-freedom and the bath equilibrium density matrix.

We shall make use of our projection operators by inserting the identity into Eq. 2.55

$$\partial_t(\mathcal{P}+\mathcal{Q})\rho_I(t) = -i(\mathcal{P}+\mathcal{Q})\mathcal{L}_V(t)(\mathcal{P}+\mathcal{Q})\rho_I(t) \tag{2.65}$$

Due to the complementarity of the projection operators, the equation of motion can be separated into a set of coupled equations of motion

$$\partial_t\mathcal{P}\rho_I(t) = -i\mathcal{P}\mathcal{L}_V(t)(\mathcal{P}+\mathcal{Q})\rho_I(t) \tag{2.66}$$

$$\partial_t\mathcal{Q}\rho_I(t) = -i\mathcal{Q}\mathcal{L}_V(t)(\mathcal{P}+\mathcal{Q})\rho_I(t), \tag{2.67}$$

which describe the time-evolution of the system and bath subspaces, respectively.

The solution of the bath projected density matrix can be found through the means of the Green's function method

$$\mathcal{Q}\rho_I(t) = \mathcal{G}(t,0)\mathcal{Q}\rho(0) - i\int_0^t d\tau \mathcal{G}(t,\tau)\mathcal{Q}\mathcal{L}_V(\tau)\mathcal{P}\rho_I(\tau) \tag{2.68}$$

where

$$\mathcal{G}(t,t_0) = \exp_+\left\{-i\int_{t_0}^t ds \mathcal{Q}\mathcal{L}_V(s)\right\}. \tag{2.69}$$

By differentiating with respect to t it can be easily shown that this equation satisfies Eq. 2.67. Substituting Eq. 2.68 into Eq. 2.66 gives the Nakajima-Zwanzig-Mori equation[174, 179, 296]

$$\partial_t\mathcal{P}\rho_I(t) = -i\mathcal{P}\mathcal{L}_V(t)\mathcal{P}\rho_I(t) - \int_0^t d\tau \mathcal{P}\mathcal{L}_V(t)\mathcal{G}(t,\tau)\mathcal{Q}\mathcal{L}_V(\tau)\mathcal{P}\rho_I(\tau) - i\mathcal{P}\mathcal{L}_V(t)\mathcal{G}(t,0)\mathcal{Q}\rho_I(0). \tag{2.70}$$

Before proceeding further, it is informative to understand each piece of Eq. 2.70. The first term, which is the full dynamics of the projected density matrix projected onto the reduced subsystem. Since the density matrix is "pre-projected" before action of the generator, any bath and system-bath coupling terms, due to the choice of projector in Eq. 2.61, are zero and we are left with the dynamics of the subsystem without the presence of a bath. The final term represents a force that acts on the system from any initial correlations between the system and bath in the density matrix. In the context of photoinduced reactions, the system and bath are typically uncorrelated due to weak coupling without instantaneous excitation energy and hence we often assume $\rho(0) = \sigma(0)\rho_B^{\mathrm{eq}}$. In this case, the final terms is exactly zero.

The second term often generates the source of most difficulty in simulations with this formalism and thus warrants a deeper discussion. Qualitatively this term represents the effect of considering an initial interaction between the system and bath ($\mathcal{P}\rho_I(\tau)$), propagation of that correlation in the bath subspace up to time t ($\mathcal{G}(t,\tau)\mathcal{Q}$), and then the interaction between the two subspaces projected onto the system at time t ($\mathcal{P}\mathcal{L}_V(t)$). This term thus constitutes a "reaction-field effect" and the integral represents a sum over all contributions from times before t. This effect characterizes the memory of correlations—a measure of the correlation time length—between the system and bath and is often referred to as the memory kernel.

The Nakajima-Zwanzig-Mori equation derived here is given in the so-called time-convolution (TC) form in that the second term in Eq. 2.70 is a convolution integral. There has been much progress in the development of numerical algorithms for computing the dynamics in this form,[49, 133, 234] but we will work with the Tokuyama–Mori time-convolutionless (TCL) or time-local form.[258] In this formulation, we use the backward propagator

$$\rho_I(t_0) = \tilde{G}(t,t_0)\rho_I(t) \tag{2.71}$$

and substitute this relation into Eq. 2.68 such that the right-hand side only depends on $\rho_I(t)$ and no previous time information about the state is required

$$\mathcal{Q}\rho_I(t) = \mathcal{G}(t,0)\mathcal{Q}\rho_I(0) - i\int_0^t d\tau \mathcal{G}(t,\tau)\mathcal{Q}\mathcal{L}_V(\tau)\mathcal{P}\tilde{G}(t,\tau)(\mathcal{P}+\mathcal{Q})\rho_I(t). \tag{2.72}$$

We define the following quantity, the self-energy,

$$\Sigma(t) = -i\int_0^t d\tau \mathcal{G}(t,\tau)\mathcal{Q}\mathcal{L}_V(\tau)\mathcal{P}\tilde{G}(t,\tau), \tag{2.73}$$

which upon insertion into Eq. 2.72 and rearranging to isolate $\mathcal{Q}\rho_I(t)$ gives

$$\mathcal{Q}\rho_I(t) = [1-\Sigma(t)]^{-1}\mathcal{G}(t,0)\mathcal{Q}\rho_I(0) + [1-\Sigma(t)]^{-1}\Sigma(t)\mathcal{P}\rho_I(t). \tag{2.74}$$

This equation can then be inserted into Eq. 2.66 to give the TCL counterpart of the Nakajima-Zwanzig-Mori equation[45, 235]

$$\partial_t\mathcal{P}\rho_I(t) = -i\mathcal{P}\mathcal{L}_V(t)[1-\Sigma(t)]^{-1}\mathcal{P}\rho_I(t) - i\mathcal{P}\mathcal{L}_V(t)[1-\Sigma(t)]^{-1}\mathcal{G}(t,0)\mathcal{Q}\rho_I(0). \tag{2.75}$$

This equation can be compactly written as

$$\partial_t\mathcal{P}\rho_I(t) = K(t)\mathcal{P}\rho_I(t) + I(t)\mathcal{Q}\rho_I(0) \tag{2.76}$$

where

$$K(t) = -i\mathcal{P}\mathcal{L}_V(t)[1-\Sigma(t)]^{-1}\mathcal{P} \tag{2.77}$$

$$I(t) = -i\mathcal{P}\mathcal{L}_V(t)[1-\Sigma(t)]^{-1}\mathcal{G}(t,0). \tag{2.78}$$

We will refer to these terms as the TCL kernel and inhomogeneous term, respectively.

Weak Coupling and Markovian Limits—the Redfield Equation

Up to this point we have made no approximations and Eq. 2.70 and 2.76 are the exact equations of motion for the reduced density matrix. If we consider a system-bath interaction as the external perturbation we can write it as a scaled quantity

$$V = H_{SB} = \zeta\tilde{H}_{SB} \tag{2.79}$$

where ζ is a dimensionless parameter that quantifies that scale of this Hamiltonian from which we also obtain the scaled interaction-picture generator

$$\mathcal{L}_V(t) = \zeta\tilde{\mathcal{L}}_V(t). \tag{2.80}$$

In the case where the system and bath are weakly coupled we have $\zeta \ll 1$ and we can expand the TCL kernel in powers of ζ

$$K(t) = \sum_{n=1}^{\infty}\zeta^n K_n(t). \tag{2.81}$$

Here, as we previously discussed, we have taken the inhomogenous term in Eq. 2.76 to be zero. We can likewise expand the self-energy term in a geometric series

$$[1 - \Sigma(t)]^{-1} = \sum_{n=0}^{\infty} \Sigma^n(t), \tag{2.82}$$

which is guaranteed to be convergent when ζ is small as we are considering here. Taking also the lowest orders of the propagators, $\mathcal{G}(t,\tau) \approx 1$ and $\tilde{G}(t,\tau) \approx 1$, we have for the lowest-order terms in the kernel expansion,

$$K_1(t) = -i\mathcal{P}\tilde{\mathcal{L}}_V(t) \tag{2.83}$$

$$K_2(t) = -\int_0^t d\tau \mathcal{P}\tilde{\mathcal{L}}_V(t) Q \tilde{\mathcal{L}}_V(\tau)\mathcal{P}. \tag{2.84}$$

We can use our definitions for the for the interaction generator and projection operators to evaluate these kernels. The first-order term is

$$\begin{aligned} K_1(t)\mathcal{P}\rho_I(t) &= -i\mathrm{Tr}_B\{\tilde{\mathcal{L}}_V(t)\sigma_I(t)\rho_B^{\mathrm{eq}}\}\rho_B^{\mathrm{eq}} \\ &= -i\tilde{\mathcal{L}}_V^S(t)\sigma_I(t)\rho_B^{\mathrm{eq}}\mathrm{Tr}_B\{\tilde{\mathcal{L}}_V^B(t)\rho_B^{\mathrm{eq}}\}. \end{aligned} \tag{2.85}$$

The interaction generator can be written as a kronecker product of its system and bath components, $\tilde{\mathcal{L}}_V(t) = \tilde{\mathcal{L}}_V^S(t) \otimes \tilde{\mathcal{L}}_V^B(t)$, which allows us to evaluate the partial trace of the bath

$$\mathrm{Tr}_B\{\tilde{\mathcal{L}}_V^B(t)\rho_B^{\mathrm{eq}}\} = \sum_k c_k \mathrm{Tr}_B\{q_{k,I}(t)\rho_B^{\mathrm{eq}}\} = 0. \tag{2.86}$$

The second term follows along similar reasoning,

$$\begin{aligned} K_2(t)\mathcal{P}\rho_I(t) &= -\int_0^t d\tau \mathrm{Tr}_B\{\tilde{\mathcal{L}}_V(t) Q \tilde{\mathcal{L}}_V(\tau)\sigma_I(t)\rho_B^{\mathrm{eq}}\} \\ &= -\int_0^t d\tau \mathrm{Tr}_B\{\tilde{\mathcal{L}}_V(t)\tilde{\mathcal{L}}_V(\tau)\sigma_I(t)\rho_B^{\mathrm{eq}}\} \end{aligned} \tag{2.87}$$

where we have used the identity $\mathcal{Q} = 1 - \mathcal{P}$ and Eq. 2.86 to eliminate the resulting $\mathcal{P}$ term via Eq. 2.86. By explicitly acting $\mathcal{P}$ on the left-hand side of Eq. 2.76, multiplying by the inverse of ρ_B^{eq} on both sides, and reabsorbing the dimensionless parameter ζ into the generators we obtain

$$\begin{aligned} \partial_t \sigma_I(t) &= -\int_0^t d\tau \mathrm{Tr}_B\{\mathcal{L}_V(t)\mathcal{L}_V(\tau)\sigma_I(t)\rho_B^{\mathrm{eq}}\} \\ &= -\frac{1}{\hbar^2}\int_0^t d\tau \mathrm{Tr}_B\{[H_{SB,I}(t), [H_{SB,I}(\tau), \sigma_I(t)\rho_B^{\mathrm{eq}}]]\} \\ &= -\frac{1}{\hbar^2}\int_0^t d\tau [S_I(t), S_I(\tau)\sigma_I(t)]C(t-\tau) + [\sigma_I(t)S_I(\tau), S_I(t)]C^*(t-\tau) \end{aligned} \tag{2.88}$$

where we have defined the bath correlation function

$$\begin{aligned} C(t) &= \sum_{kl} c_k c_l \mathrm{Tr}_B \left\{ q_{k,I}(t) q_{l,I}(0) \rho_B^{\mathrm{eq}} \right\} \\ &= \sum_{k} c_k^2 \mathrm{Tr}_B \left\{ q_{k,I}(t) q_{k,I}(0) \rho_B^{\mathrm{eq}} \right\}, \end{aligned} \tag{2.89}$$

and in the last line we have used the fact that the bath modes are uncorrelated harmonic oscillators.

Up to this point we have been working in the interaction picture. Upon transforming back to the Schrödinger picture we have two sources of time-dependence in the equation of motion

$$\begin{aligned} \partial_t \sigma(t) &= \partial_t \left(e^{-iH_S t/\hbar} \sigma_I(t) e^{iH_S t/\hbar} \right) \\ &= -\frac{i}{\hbar}[H_S, \sigma(t)] + e^{-iH_S t/\hbar} (\partial_t \sigma_I(t)) e^{iH_S t/\hbar} \end{aligned} \tag{2.90}$$

Substituting in Eq. 2.88 and using some simplifying notation for the zeroth-order system propagators, $U_t = e^{-iH_S t/\hbar}$, gives

$$\begin{aligned} \partial_t \sigma(t) = -\frac{i}{\hbar}[H_S, \sigma(t)] - \frac{1}{\hbar^2} \int_0^t d\tau U_t [S_I(t), S_I(\tau)\sigma_I(t)] U_t^\dagger C(t-\tau) \\ + U_t [\sigma_I(t) S_I(\tau), S_I(t)] U_t^\dagger C^*(t-\tau). \end{aligned} \tag{2.91}$$

Inserting the expressions for the interaction picture operators and density matrix gives[4]

$$\begin{aligned} \partial_t \sigma(t) = -\frac{i}{\hbar}[H_S, \sigma(t)] - \frac{1}{\hbar^2} \int_0^t d\tau [S, S_I(t-\tau)\sigma(t)] C(t-\tau) \\ + [\sigma(t) S_I(t-\tau), S] C^*(t-\tau). \end{aligned} \tag{2.92}$$

As the only integrated time-dependence is found in one of the system-bath coupling operators, we can incorporate the scalar dependence from the bath correlation function into that operator only, which we define as the "dressed" system-bath coupling operators

$$\tilde{S}(t) \equiv S_I(t) C(t) \tag{2.93}$$

$$\tilde{S}^*(t) \equiv S_I(t) C^*(t), \tag{2.94}$$

and transforming the integration variable $\tau \to t - \tau$ we obtain the time-dependent Redfield or TCL2 equation

$$\partial_t \sigma(t) = -\frac{i}{\hbar}[H_S, \sigma(t)] - \frac{1}{\hbar^2} \int_0^t d\tau [S, \tilde{S}(\tau)\sigma(t)] + [\sigma(t)\tilde{S}^*(\tau), S]. \tag{2.95}$$

---

[4] This expression can be easily found by expanding out the commutators and working through the simple operator mechanics, *i.e.*, $U_t U_t^\dagger = 1$ and $U_t U_\tau^\dagger = U_{t-\tau}$.

The matrix elements of the dressed system-bath coupling operators can be found in the energy eigenbasis

$$\tilde{S}(t) = \sum_{jk} e^{i\omega_{jk}t} S_{jk} C(t) |j\rangle\langle k| \tag{2.96}$$

where $H|j\rangle = E_j|j\rangle$ and $\omega_{jk} = \hbar^{-1}(E_j - E_k)$. The bath correlation function can also be found using the same technique and is a ubiquitous result in the theory of open quantum systems, so we shall go through it step-by-step,

$$\begin{aligned} C(t) &= \sum_k c_k^2 \mathrm{Tr}_B \left\{ q_{k,I}(t) q_{k,I}(0) \rho_B^{\mathrm{eq}} \right\} \\ &= \sum_k c_k^2 \sum_m \langle m| e^{iH_{B,k}t} q_k e^{-iH_{B,k}t} q_k \rho_B^{\mathrm{eq}} |m\rangle \\ &= \sum_k c_k^2 \sum_m \frac{p_n}{2} \langle m| (e^{i\omega_k t} a_k^\dagger + e^{-i\omega_k t} a_k)(a_k^\dagger + a_k) |m\rangle \\ &= \sum_k c_k^2 \sum_m p_m [e^{i\omega_k t} \langle m| a_k^\dagger a_k |m\rangle + e^{-i\omega_k t} \langle m| a_k a_k^\dagger |m\rangle] \\ &= \sum_k \frac{c_k^2}{2} [e^{i\omega_k t} n(\omega_k) + e^{-i\omega_k t}(n(\omega_k) - 1)] \\ &= \sum_k \frac{c_k^2}{2} [(2n(\omega_k) + 1)\cos(\omega_k t) - i \sin(\omega_k t)]. \end{aligned} \tag{2.97}$$

In the 3rd line we have used the identity for the position operator of a harmonic oscillator in terms of its creation, $a_k^\dagger$, and annihilation, a_k, operators and the 5th line we have used the Bose-Einstein distrubtion for the thermal expectation value of the number operator, $n(\omega_k) = \sum_m p_m \langle m| a_k^\dagger a_k |m\rangle$ with the commutation relation of bosons $[a_k, a_k^\dagger] = 1$, which has the functional form $n(\omega) = (e^{\beta\hbar\omega} - 1)^{-1}$. We can now insert the identity for the spectral density

$$\begin{aligned} C(t) &= \sum_k \frac{c_k^2}{2} [(2n(\omega_k) + 1)\cos(\omega_k t) - i \sin(\omega_k t)] \\ &= \frac{1}{\pi} \int_0^\infty d\omega \frac{\pi}{2} \sum_k c_k^2 \delta(\omega - \omega_k) [(2n(\omega) + 1)\cos(\omega t) - i \sin(\omega t)] \\ &= \frac{1}{\pi} \int_0^\infty d\omega J(\omega) [(2n(\omega) + 1)\cos(\omega t) - i \sin(\omega t)]. \end{aligned} \tag{2.98}$$

Often this relation will be equivalently given as[5]

$$C(t) = \frac{1}{\pi} \int_0^\infty d\omega J(\omega) [\coth(\beta\hbar\omega/2)\cos(\omega t) - i \sin(\omega t)], \tag{2.99}$$

---

[5] In the encouraging words of a famous Bill Nye segment, "Try it!"

but importantly provides a direct relation between the bath correlation function, which encodes the system-bath coupling, to its power spectrum, which is a measurable quantity through various forms of spectroscopy.[176, 182]

Another useful approximation beyond just the weak system-bath coupling approximation can be made. If the bath relaxes to its thermal distribution on a timescale that is much faster than the system, $C(t) \sim e^{-\omega t}$ where $\omega \gg \omega_{jk}$ for all j, k, then we can assume that the time, t, in the integral of Eq. 2.95 can be taken to infinity, which underpins the Markovian approximation. The dressed system-bath coupling operators under this approximation are given by element-wise multiplication of the Fourier-Laplace transforms of the bath correlation function and the system-bath coupling operator,

$$\begin{aligned}\tilde{S} &= \sum_{jk} S_{jk}|j\rangle\langle k| \int_0^\infty d\tau e^{i\omega_{jk}\tau} C(\tau) \\ &= \sum_{jk} \tilde{C}(\omega_{jk}) S_{jk}|j\rangle\langle k| \end{aligned} \tag{2.100}$$

which can in some cases be evaluated analytically, but is often found numerically. The resulting equation of motion can be written by substituting Eq. 2.100 into Eq. 2.95, which is referred to as the Redfield equation distinct from the time-dependent Redfield equation, which we refer to as TCL2 throughout this thesis.

Secular Approximation—the Lindblad Equation

The TCL2 and Redfield equations offer simple theories that work well in the weak-coupling and Markovian regimes of open quantum systems dynamics. Both theories, however, suffer from the drawback that neither equations of motion satisfy the complete positivity property of a physical dynamical generator. Complete positivity is satisfied when the density matrix obtained from the dynamics is a physical density matrix, that is, $\{\sigma(t)\} = 1$ and $\sigma_{jj}(t) \geq 0$ for all j. The first of these requirements, trace-preservation, is satisfied by TCL2 and Redfield theory, however, the latter, positivity, is not in general satisfied. Violations of positivity are statements of negative probability of finding the system in a particular state. Since this is an unphysical result—probabilities must be nonneagtive—we will explore an additional approximation that rectifies this problem.

If we consider the system-bath coupling operator to be written in the energy eigenbasis, we can write it as a sum of operators with elements matching particular frequency, ϵ, that is[123, 268]

$$S = \sum_{\epsilon} S(\epsilon) \tag{2.101}$$

where

$$S(\epsilon) = \sum_{jk \text{ s.t. } \omega_{jk} = \epsilon} S_{jk}|j\rangle\langle k|. \tag{2.102}$$

In this projected basis, the dressed system-bath coupling operator is then scaled by the Fourier-Laplace transform of the bath correlation function at its particular frequency, $\tilde{S}(\epsilon) = \tilde{C}(\epsilon)S(\epsilon)$. In this case, it is more useful to work in the interaction picture where the projected operators obtain time-dependence through

$$S_I(t,\epsilon) = e^{i\epsilon t}S(\epsilon). \tag{2.103}$$

Transforming the Redfield equation into the interaction picture and substituting in Eqs. 2.101 and 2.103 we obtain

$$\partial_t\sigma_I(t) = -\frac{1}{\hbar^2}\sum_{\epsilon\epsilon'} e^{i(\epsilon+\epsilon')t}\left(\tilde{C}(\epsilon')[S(\epsilon),\tilde{S}(\epsilon')\sigma_I(t)] + \tilde{C}(-\epsilon')[\tilde{S}^*(\epsilon')\sigma_I(t),S(\epsilon)]\right). \tag{2.104}$$

The secular approximation concerns itself with the oscillatory terms due to $e^{i(\epsilon+\epsilon')t}$ in the previous equation relative to the decoherence and relaxation timescales set by $\tilde{C}(\epsilon)$. If the timescale of these system oscillations, $\tau_s = |\epsilon+\epsilon'|^{-1}$, is significantly shorter the timescale of the system-bath coupling interaction—an approximation that is often satisfied when $\zeta \ll 1$—then and term in which $\epsilon' \neq -\epsilon$ cycle averages to zero over the timescale of a single system-bath coupling interaction.[123, 268] The resulting master equation is given by

$$\partial_t\sigma_I(t) = -\frac{1}{\hbar^2}\sum_{\epsilon}\tilde{C}(\epsilon)[S(\epsilon),S(\epsilon)\sigma_I(t)] + \tilde{C}(-\epsilon)[S(\epsilon)\sigma_I(t),S(\epsilon)], \tag{2.105}$$

which can be simplified to

$$\partial_t\sigma_I(t) = \frac{1}{\hbar^2}\sum_{\epsilon}\frac{1}{2}\tilde{C}(\epsilon)[2S(\epsilon)\sigma_I(t)S(\epsilon) - \{S^\dagger(\epsilon)S(\epsilon),\sigma_I(t)\}]. \tag{2.106}$$

Transforming back to the Schrödinger picture and substituting $\Gamma_\epsilon = \tilde{C}(\epsilon)/\hbar^2$ we obtain the Gorini-Kossakowski-Sudarshan-Lindblad (GKSL)[6] master equation[158, 93]

$$\partial_t\sigma(t) = -\frac{i}{\hbar}[H_S,\sigma(t)] + \sum_{\epsilon}\Gamma_\epsilon\left(S_\epsilon\sigma(t)S_\epsilon^\dagger - \frac{1}{2}\{S_\epsilon^\dagger S_\epsilon,\sigma(t)\}\right). \tag{2.107}$$

It has been shown that this master equation has the Dynamical Semigroup property, which means it generates a trace-preserving and completely-positive dynamics,[158, 93] which will be of relevance throughout this thesis, particularly in Chapter 3.

Stochastic Unravelling

The weak coupling quantum master equation framework encoded in the Lindblad equation dramatically reduces the number of degrees-of-freedom of a system interacting with

---

[6] This equation is often in the literature referred to as the Lindblad equation or Lindbladian a moniker which we adopt throughout this thesis.

a condensed phase environment, however, due to strongly interacting system degrees-of-freedom through, *e.g.*, nonadiabatic effects a substantial number of degrees-of-freedom may be required to yet describe the system. For a direct product basis, we found that the computational resources scaled exponentially with the number of degrees-of-freedom for a wavefunction. As a density matrix is fundamentally an outer product of wavefunctions, the computational resources scale exponentially in *twice* the number of degrees-of-freedom, which dramatically increases the computational cost even for small systems. Furthermore, algorithms that rely on compact representations of the density matrix—*i.e.*, a corresponding MCTDH for density matrices—exist,[200] but are lacking in development relative to their wavefunction counterparts.

A workaround to this issue is provided through the stochastic unraveling of the density matrix, which simulates the density matrix through Monte Carlo sampling of wavefunction "trajectories". Consider the following stochastic differential equation, which is the stochastic unraveling of the Lindblad master equation,[7]

$$d|\psi(t)\rangle = -\frac{i}{\hbar}H_{\text{eff}}|\psi(t)\rangle dt + \sum_n \left(\frac{\sqrt{\Gamma_n}L_n}{\langle\psi(t)|\Gamma_n L_n^\dagger L_n|\psi(t)\rangle} - 1\right)|\psi(t)\rangle dN_n, \tag{2.108}$$

where $|\psi(t)\rangle$ is the (electron and nuclear) wavefunction of the system at time t. The first term in Eq. 2.108 represents coherent, deterministic dynamics with the effective Hamiltonian, H_{eff},

$$H_{\text{eff}} = H_S - \frac{i}{2}\sum_n \Gamma_n L_n^\dagger L_n, \tag{2.109}$$

which adds to the original Hermitian operator, H_S, an anti-Hermitian term due to the coupling with the bath through the operators L_n and their adjoints, $L_n^\dagger$. The L_n operators, include both dissipative and dephasing actions of the bath and Γ_n are the associated bare rates of those actions. The second term in Eq. 2.108 is a Poisson jump process reflecting projective actions of the bath with statistics $dN_n = 0, 1$ and $dN_n^2 = dN_n$ and rates for each L_n corresponding to the quantum expectation, $\Gamma_n\langle\psi(t)|L_n^\dagger L_n|\psi(t)\rangle$.

This equation implies that during the time evolution of a trajectory over some increment dt the system has one of two choices. The system can proceed along an uninterrupted deterministic pathway given by the unitary dynamics of the system Hamiltonian in the absence of an environment. Alternatively, the system can interact with its weakly coupled environment through the jump operators. As this interaction occurs stochastically, the probability of a jump occuring over the interval is given by

$$p_{\text{jump}}(dt) = dt\sum_n \Gamma_n\langle\psi(t)|L_n^\dagger L_n|\psi(t)\rangle \tag{2.110}$$

---

[7] Here we have replaced the index ϵ with n and the operators S_ϵ with L_n to note a more general case than that of Eq. 2.107, which was taken from first principles with a microscopic model. Often a Lindlbad master equation is imposed phenomenologically and the rates and jump operators are not defined with respect to the energy eigenbasis.

and the probability of the nth jump occurring is given by the nth term in the sum.

The jump probability distribution can be sampled through Monte Carlo procedures where at each discrete time one of the two pathways is randomly chosen according to the probability of the jump occurring. This algorithm however is only accurate to order dt and is practically inefficient. A more efficient algorithm is given by a Gillespie-like algorithm, which is described in Algorithm 1. A key difference in this algorithm is that rather than sampling the jump probability distribution, the Gillespie algorithm samples the waiting time distribution. As the bath is weakly interacting with the system in this framework, the jumps are somewhat rare and most of the simulation time can be spent performing an efficient wavefunction propagation—by efficient matrix vector based algorithms or MCTDH propagation—with intermittent checks on the conditions for a jump occurring.

Algorithm 1: Gillespie-like algorithm for computing a trajectory with the quantum jump stochastic differential equation.

```
Result: A sequence of wavefunctions $\{|\psi(t)\rangle\}$ that gives a trajectory realization.
Initialize with a wavefunction $|\psi(0)\rangle$, set a time step $dt$, and a draw random
  number, $r$, from the uniform distribution [0,1];
while $t < t_{obs}$ do
    reset $dt$ to original value;
    while $t < t + dt$ do
        propagate $|\psi(t)\rangle$ into a trial wavefunction $|\tilde{\psi}(t + dt)\rangle$ under action of $H_{\text{eff}}$;
        if $\langle\tilde{\psi}(t + dt)|\tilde{\psi}(t + dt)\rangle < r$ then
            using linear or logarithmic bisection, find $\tau$, such that $t \leq \tau \leq t + dt$
            satisfying the condition $\langle\tilde{\psi}(\tau)|\tilde{\psi}(\tau)\rangle = r$;
            draw a new uniform random number $r_j$;
            compute jump probabilities for each jump operator with associated rate
            $p_n = \Gamma_n\langle\tilde{\psi}(\tau)|L_n^\dagger L_n|\tilde{\psi}(\tau)\rangle$;
            find first $n$ that satisfies $r_j < \frac{\sum_{m=1}^{n+1} p_m}{\sum_m p_m}$;
            set $\tau \to t$;
            set $\frac{\Gamma_n L_n|\tilde{\psi}(t+dt)\rangle}{p_n} \to |\psi(t)\rangle$;
            set $t + dt - \tau \to dt$;
        else
            set $t + dt \to t$;
            set $|\tilde{\psi}(t + dt)\rangle \to |\psi(t)\rangle$;
            add $\frac{|\tilde{\psi}(t+dt)\rangle}{\sqrt{\langle\tilde{\psi}(t+dt)|\tilde{\psi}(t+dt)\rangle}}$ to the sequence of wavefunctions
        end
    end
end
```

Stochastic unraveling procedures are, however, not unique in that the only conditions required to satisfy an unraveling are that the average over trajectories reproduces the density matrix, which can be done in a number of ways. Another common unraveling is given by the quantum state diffusion equation[89, 90, 91]

$$\begin{aligned} d|\psi(t)\rangle = &-\frac{i}{\hbar}(H_S - i\hbar\sum_n \Gamma_n L_n^\dagger L_n)|\psi(t)\rangle dt \\ &+ \sum_n \Gamma_n \left(2\langle L_n\rangle L_n - \langle L_n^\dagger\rangle\langle L_n\rangle\right)|\psi(t)\rangle dt \\ &+ \sum_n (L_n - \langle L_n\rangle)|\psi(t)\rangle dW_n(t) \end{aligned} \tag{2.111}$$

Here the stochastic variable, $dW(t)$ undergoes a Wiener process with Gaussian white noise statistics and represents a system-bath interaction that is continuous in time rather than discrete. Relations to various experimental setups in atomic physics can be drawn between these two unravelings (see Ref. [192]), but such a discussion goes beyond the scope of this thesis.

Another advantage of the stochastic unraveling, as will be outline in Chapter 3, is the ability to probe deeper statistics than just the mean in the ensemble of the density matrix. By simulating individual trajectories not only can the mean, but also can the higher-order moments that encode the fluctuations of the dynamics be calculated through the stochastic unraveling framework.

2.3 Time-Dependent Response

Throughout this chapter we have considered the equations that underpin the quantum dynamics of systems in condensed phases. Knowledge of the dynamics is practically useful because it enables us to draw theoretical connections to experimental observations. One such set of observations is the way in which a system responds to some perturbation. Experimental measurements are often performed in this manner—a field is generated that causes the system to change and this change is probed through further interactions with the generated field or detection of the changes to the field. The theoretical formalism describing these phenomena will now be outlined.

Here we consider perturbations of the form,

$$V = -f(t)A, \tag{2.112}$$

where $f(t)$ is some time-dependent scalar function and A is an operator. Using the interaction picture formalism discussed in Sec. 2.2, we can rewrite the time-dependent density matrix in a Dyson series as a sum of nth-order density matrices

$$\rho_I(t) = \sum_{n=0}^{\infty} \rho_I^{(n)}(t), \tag{2.113}$$

where

$$\rho_I^{(0)}(t) = \rho(0) \tag{2.114}$$

$$\rho_I^{(n)}(t) = (-i)^n \int_0^t ds \cdots \int_0^{s_{n-1}} ds_n \mathcal{L}_V(s) \cdots \mathcal{L}_V(s_n)\rho(0). \tag{2.115}$$

As we are interested in observing the dynamical behavior of the system after some perturbation, we are interested in understanding the changes in the properties of the system through observable quantities associated with operators, *e.g.*, B,

$$\langle \delta B(t) \rangle = \langle B(t) \rangle - \langle B \rangle_0, \tag{2.116}$$

where the brackets denote the quantum mechanical expectation value of an observable $\langle \cdot \rangle = \mathrm{Tr}\{\cdot \rho\}$. If we take our initial condition to be the thermal equilibrium state of the unperturbed Hamiltonian,

$$\begin{aligned} \rho_I(0) &= \rho^{\mathrm{eq}} \\ &= \frac{e^{-\beta H_0}}{\mathrm{Tr} e^{-\beta H_0}} \end{aligned} \tag{2.117}$$

and substitute the Dyson expansion for the density matrix then our quantum mechanical expectation values become equilibrium expectation values $\langle \cdot \rangle \to \langle \cdot \rangle_{\mathrm{eq}}$ and we obtain a similar expansion in the response of the expectation value

$$\langle \delta B(t) \rangle = \sum_n (-i)^n \int_0^t ds \cdots \int_0^{s_{n-1}} ds_n \langle B_I(t) \mathcal{L}_V(s) \cdots \mathcal{L}_V(s_n) \rho^{\mathrm{eq}} \rangle \tag{2.118}$$

$$\equiv \sum_n \langle \delta B^{(n)}(t) \rangle_{\mathrm{eq}}. \tag{2.119}$$

Understanding the behavior of these terms at various orders is the foundation on which we will develop a theory of response.

Quantum Linear Response Theory

If we suppose the propagator can be written as a reduced propagator scaled by some dimensionless parameter,

$$\mathcal{L}_V(s) = \zeta \tilde{\mathcal{L}}_V(s) \tag{2.120}$$

we can then reduce the terms in Eq. 2.118 based on perturbative arguments when $\zeta \ll 1$. Specifically, truncating this expansion at linear order gives

$$\begin{aligned}\langle \delta B(t)\rangle &\approx -i\int_0^t ds\langle B_I(t)\mathcal{L}_V(s)\rangle_{\text{eq}} + \mathcal{O}(\zeta^2)\\ &= -\frac{i}{\hbar}\int_0^t ds\text{Tr}\{B_I(t)[V_I(s),\rho^{\text{eq}}]\}\\ &= \frac{i}{\hbar}\int_0^t dsf(s)\text{Tr}\{[B_I(t),A_I(s)]\rho^{\text{eq}}\}\\ &= \frac{i}{\hbar}\int_0^t dsf(s)\text{Tr}\{[B_I(t-s),A]\rho^{\text{eq}}\} \qquad (2.121)\end{aligned}$$

where we have used the cyclic permutation invariance property of the trace in the last line to incorporate the time-dependence of A into B. We will define the so-called response function[43, 141] as

$$R(t) = \begin{cases} \frac{i}{\hbar}\langle [B_I(t),A]\rangle_{\text{eq}} & t>0\\ 0 & t<0,\end{cases} \qquad (2.122)$$

through which it is clear that

$$\langle \delta B(t)\rangle = \int_0^t dsf(s)R(t-s). \qquad (2.123)$$

This result is the foundation of quantum linear response theory and it states that the time-dependent response of some observable out of its equilibrium state can be related, through a convolution integral, to a time correlation function at equilibrium. In other words, the dynamics of a system out of equilibrium, to linear order, are entirely encoded in the fluctuations and time-correlations at equilibrium in accordance with Onsager's regression hypothesis.

It will also be useful to consider the frequency spectrum of the response function, which is obtained via Fourier transform

$$\chi(\omega) = \int_{-\infty}^{\infty} dte^{i\omega t}R(t), \qquad (2.124)$$

which we refer to as the susceptibility. A further simplification which is of use is considering the response of the observable to which the external field is coupled. In this case the response function is given as a difference in autocorrelation functions

$$R(t) = \frac{i}{\hbar}\Theta(t)\left(\langle A_I(t)A\rangle_{\text{eq}} - \langle AA_I(t)\rangle_{\text{eq}}\right), \qquad (2.125)$$

where $\Theta(t)$ is the Heaviside step function. Due to our strict adherence to quantum mechanics, the two autocorrelation functions can be related to one another through the detailed balance relation

$$\frac{C(\omega)}{C(-\omega)} = e^{\beta\hbar\omega}, \qquad (2.126)$$

where

$$C(\omega) = \int_{-\infty}^{\infty} dte^{i\omega t}\langle A_I(t)A\rangle_{\text{eq}}. \tag{2.127}$$

Using this result we can also obtain the Fluctuation Dissipation Theorem,[36, 141] which relates the power spectrum of the time-dependent observable to the susceptibility

$$S_A(\omega) = 2\hbar[n(\omega) + +1]\text{Im}\chi(\omega), \tag{2.128}$$

where $n(\omega) = (e^{\beta\hbar\omega} - 1)^{-1}$ is the Bose-Einstein distribution. One may note the striking similarity between the general results presented here and those found in Sec. 2.2. This similarity is to be expected as the weak-coupling quantum master equation relates the dynamics of the system to the interactions between the system and environment through a response theory of the environment.

Linear Spectroscopy

As we alluded to earlier, a utility in the response theory is in relating the dynamics to experimental observations, one such example coming from spectroscopy. In spectroscopy, we consider an external perturbation of the form[176, 182]

$$V = -\mathcal{E}(t)\mu \tag{2.129}$$

where $\mathcal{E}(t)$ is some oscillating electric field from a light source and μ is the molecular dipole moment operator. This form assumes both a weak-coupling approximation for the interaction between the light and matter in the system as well as a long-wavelength approximation of the light relative to the length of the molecular system. The quantity of interest in spectroscopy is the absorption coefficient

$$\kappa = \frac{\partial_t E}{I}, \tag{2.130}$$

which is the ratio the rate of energy absorbed by the system, $\partial_t E$, and the intensity of incident light, I. We can write down the energy absorption rate as[43]

$$\partial_t E = -\frac{1}{T}\int_0^T dt \frac{\partial\mathcal{E}(t)}{\partial t}\langle\mu(t)\rangle, \tag{2.131}$$

where the integral is a cycle average taken over a period of oscillation of the magnetic field.

Since we are interested in a time-dependent average of some observable as it responds to a weakly interacting external perturbation, the quantum linear response theory naturally applies. Inserting our linear response expansion for $\langle\mu(t)\rangle$ in Eq. 2.131 we obtain

$$\partial_t E = -\frac{1}{T}\int_0^T dt \frac{\partial\mathcal{E}(t)}{\partial t}\left[\langle\mu\rangle_{\text{eq}} + \int_0^\infty d\tau R_\mu(\tau)\mathcal{E}(t-\tau)\right] \tag{2.132}$$

with the response function, $R\mu(\tau) = -i\langle[\mu_I(\tau), \mu]\rangle/\hbar$. For simplicity we assume a monochromatic light source from which the electric field has the following form

$$\mathcal{E}(t) = \frac{1}{2}\left[\mathcal{E}_0 e^{i\omega t} + \mathcal{E}_0^* e^{-i\omega t}\right], \tag{2.133}$$

with $\mathcal{E}_0$ the amplitude of the electric field. By inserting Eq. 2.133 into Eq. 2.132 and performing the integral over a period of the light-field, $T = 2\pi/\omega$, we obtain

$$\begin{aligned}\partial_t E &= \frac{i}{4}\omega|\mathcal{E}_0|^2[\chi_\mu(-\omega) - \chi_\mu(\omega)] \\ &= \frac{\omega}{2}|\mathcal{E}_0|^2 \mathrm{Im}\chi_\mu(\omega)\end{aligned} \tag{2.134}$$

where we have denoted the susceptibility as $\chi_\mu(\omega)$. Dividing this by the intensity of the light source, $I = c|\mathcal{E}_0|^2/8\pi$, then gives the linear absorption coefficient as

$$\kappa(\omega) = \frac{4\pi\omega}{c}\mathrm{Im}\chi_\mu(\omega). \tag{2.135}$$

It should come as no surprise based on the results of the previous section that the absorption coefficient has a similar form to the FDT as it is a measurement of the power spectrum of the time-dependent energy expectation due to some external perturbation.

Nonlinear Spectroscopy

Linear spectroscopy provides a route measuring the system through its response from a single interaction with the light-matter coupling field. Advances in spectroscopy have led to numerous experimental techniques generally referred to as multidimensional or nonlinear spectroscopy, which utilize multiple light-matter interactions—through a carefully chosen sequence of light pulses—to obtain additional information beyond that which linear spectroscopy can show. The theoretical formalism for describing such experiments follows similarly to that of linear spectroscopy, but goes beyond the linear response approximation. In particular, the time-dependent quantity of interest is the energy absorption as obtained from the change in the net polarizaiton of the system,

$$\langle \delta P(t)\rangle = \mathrm{Tr}\{\mu_I(t)\rho_I(t)\}, \tag{2.136}$$

which can be expanded to give

$$\langle \delta P^{(n)}(t)\rangle = \int_0^\infty d\tau_n \cdots \int_0^\infty d\tau_1 R_\mu^{(n)}(\tau_n, \ldots, \tau_1) E_1(t - \tau_n - \cdots - \tau_1) \cdots E_n(t - \tau_n), \tag{2.137}$$

where we have introduced the nth order response function

$$\begin{aligned}R_\mu^{(n)}(\tau_n, \ldots, \tau_1) = &\left(\frac{i}{\hbar}\right)^n \Theta(\tau_1)\cdots\Theta(\tau_n) \\ &\times \langle[\cdots[\mu_I(\tau_1 + \cdots + \tau_n), \mu_I(\tau_1 + \cdots + \tau_{n-1})], \cdots], \mu_I(0)]\rangle_{\mathrm{eq}}.\end{aligned} \tag{2.138}$$

The measured absorption is still obtained through the, now nonlinear, susceptibility, but the additional light-matter interactions demand some interpretation as they relate to the experiments.

The 2nd-order response function will contain, for example, the following terms

$$\begin{gathered}\langle \mu_I(\tau_1+\tau_2)\mu_I(\tau_1)\mu_I(0)\rangle \\ \langle \mu_I(\tau_1)\mu_I(\tau_1+\tau_2)\mu_I(0)\rangle.\end{gathered}$$

Recalling the definition of the interaction picture operators it is clear that the dipole operators will induce transitions between eigenstates that will then oscillate at different relative phases between the two terms. Additional complexity can be accounted for by considering also the wavevector dependence of the electric field and dipole operators. These additional phase relationships show how different experimental setups can selectively probe various signals while eliminating noise from others. While the details of these considerations are left for thorough discussion elsewhere (see Ref. [176] for a detailed theoretical description of nonlinear spectroscopy), we note that these additional complexities encode more information about the system and hence are in part why nonlinear spectroscopy is so elucidating.

Chapter 3

Quantum Transition Path Sampling

"And so, does the destination matter? Or is it the path we take? I declare that no accomplishment has substance nearly as great as the road used to achieve it. We are not creatures of destinations. It is the journey that shapes us. Our callused feet, our backs strong from carrying the weight of our travels, our eyes open with the fresh delight of experiences lived."

— Nohadon [217]

3.1 Introduction

Understanding the dynamics of quantum systems in condensed phases is an active area of research across physics and chemistry [71, 115, 121, 175]. Advances in time-resolved spectroscopies, such as pump-probe transient absorption and coherent two-dimensional spectroscopy, have made it possible to measure dynamics on ultrafast timescales, [63, 140, 172, 185] but require sophisticated simulation methodologies to help interpret and unravel the microscopic motions probed [72, 111]. In this chapter, we demonstrate how the Transition Path Sampling (TPS)[26, 55] framework can be used effectively for studying the dynamics

---

This chapter is based on work that has been published in *The Journal of Chemical Physics* [222] of nonadiabatic quantum systems. We do this by taking advantage of a stochastic trajectory representation of a detailed-balance-preserving quantum master equation, which allows for the generation of a trajectory ensemble whose statistics and correlations can be studied. We show how the use of path ensembles can elucidate dynamical mechanisms directly using a generalization of committor analysis [26, 55, 190] for coherent dynamics. Additionally, we show how TPS can be used to compute rate constants for rare dynamical events without assuming a specific mechanism or postulating a relevant reaction coordinate using path ensemble free energies [26, 55]. While the current framework is restricted to quantum jump dynamics, the perspective is general and the tools are generalizable to other open quantum dynamics [173, 269].

Nonadiabatic open quantum systems display a wide variety of chemical physics, from excitonic behavior in chromophoric systems[115, 121] to conical intersections[60, 98] and span a number of time, energy, and length scales[265]. This vast range of scales makes developing computational techniques for studying nonadiabatic dynamics difficult. The break down of the Born-Oppenheimer approximation necessitates that the dynamical evolution of the system is based on Schrödinger's equation, while the surrounding environment necessary to accurately describe dissipation makes its straightforward application intractable due to the exponential scaling with system size. Thus, most numerical techniques are developed to treat a few degrees of freedom quantum mechanically, resolving discrete electronic states or wavepackets, while the other degrees of freedom are treated with path integrals[260], or approximately semi-classically[19, 169], with mixed quantum-classical dynamics[129, 163, 264], or with reduced density matrix equations[132, 168, 173].

Independent of the computational technique, the prevailing perspective for studying such nonadiabatic open quantum dynamics relies on computing and analyzing the average dynamics that a few tagged degrees of freedom undergo when the rest of the system has been integrated out. This is sometimes done implicitly, by focusing on average populations even though the surroundings are represented molecularly, as is done with semiclassical methods [27, 149, 260, 264]. Often, however, this is done explicitly, as in methods that construct an equation of motion for the average behavior of the system directly, as in quantum master equation approaches [20, 22, 98, 116, 132, 251]. While this dimensionality reduction can be illuminating, it does result in a loss of information, as the fluctuations about the average dynamical behavior can encode important correlations. For example, understanding the mechanism of a rare dynamical event with information on just the average trajectory of the system is difficult. Most often a mechanism is inferred by varying a parameter of the system and noting the subsequent change in the rate. Instead of noting the response to a parameter, this same information exists in principle in the ensemble of trajectories, or dynamical fluctuations of the system, at a fixed value of a parameter. In static systems this is just a statement of the fluctuation-dissipation relation, but such statements can be extended to codify the relation between fluctuations and response in dynamical systems far from equilibrium [230, 263]. Indeed in classical systems, trajectory ensemble techniques have resulted in methods like Transition Path Sampling[26, 55] to sample rare dynamical events and generalizations of reaction coordinates and transitions state to complex systems [26, 55, 109, 190]. This has enabled the study of mechanisms of rare events in a wide variety of systems and settings [23, 85, 84, 130].

The application of trajectory ensembles to quantum dynamics, however, has not been as successful as in classical dynamics. Central to this failure is the difficulty in generating meaningful trajectories for open quantum systems. For many trajectory-based methods, the dynamics are reliable only for very short times due either to approximations that fail to accurately represent the back-reaction of the bath onto the system and consequently violate detailed balance [128] or because of the dynamical sign problem and exponential complexity of exact system-bath dynamics. Alternatively, path integral methods such as recent extensions to Ring Polymer Molecular Dynamics[97] that incorporate non-adiabatic effects[6, 165, 206, 239, 249] can recover the correct equilibrium statistics, and could be used to generate quantum trajectory ensembles in cases where they are also faithful to the quantum dynamics. Efforts to use practical methods such as surface hopping with trajectory ensembles have been proposed [233] though their reliability is questionable, as the form of the stationary distribution is unknown, making deriving acceptance criteria difficult. Recent work to identify an incompressible phase space structure for the density matrix of an open quantum system in the presence of quenched disorder holds significant promise [59].

In cases where the system and bath are weakly coupled however, the stochastic unraveling method from quantum optics as applied to quantum master equations supplies a means to identify quantum trajectories[31, 192]. In this method, a deterministic density matrix equation is converted to an average over stochastically evolved wavefunctions. Provided a microscopic model of the system bath interaction, the stochastic evolution be can developed. Such quantum trajectories are observable in simple systems using weak measurements [177]. A significant amount of work has been done using quantum jump trajectories in driven systems and under steady-state conditions, which have revealed the potential for dynamical phase transitions [13, 81], correlated dynamics [146], and localization [150]. Here we adopt this perspective and develop it with the motivation to study rare reactive events in nonadiabatic and quantum coherent dynamics. As this method is derived from a quantum master equation formalism, its dynamics obey detailed balance, and so its statistical fluctuations encode accurate information on the bath fluctuations that result in rare reactive events. While the bath is not represented in molecular detail, the fluctuations it imposes on the systems dynamics are directly observable.

The remainder of this chapter is outlined in five sections. In the following section, the trajectory formalism is introduced and the formulation of path ensembles and a scheme to sample them with TPS is developed. This path ensemble formalism is then applied to three different model systems: first to a three-level chromophoric system to show how path ensembles can be used to sample correlations in trajectories directly (Sec. 3.3), then to a proton-coupled electron transfer model in which the quantum committor distribution is utilized (Sec. 3.4), and finally to a system exhibiting rare barrier crossing to show the efficiency of TPS to compute a rate constant with no mechanistic assumptions (Sec. 3.5). Some final conclusions and thoughts for future work are presented in Sec. 3.6.

3.2 Quantum Jump Path Ensembles

In this section we develop a reactive path ensemble formalism for stochastic quantum jump dynamics[32]. Specifically, we consider the reduced dynamics of a subset of degrees of freedom, the system, embedded in an environment with an infinite number of degrees of freedom, the bath, and focus our discussion to instances where those reduced dynamics are Markovian and weakly coupled to the environment. For concreteness we will consider Hamiltonians in the full Hilbert space, H, partitioned into three terms,

$$H = H_S + H_B + H_{SB}, \tag{3.1}$$

where H_S is the system Hamiltonian, H_B is the bath Hamiltonian, and H_{SB} is the system-bath coupling term. Throughout, we will take H_{SB} as a sum of Kronecker products of linear operators in the system and bath Hilbert spaces,

$$H_{SB} = \sum_i \sum_n c_{n,i} S_i \otimes B_{n,i}, \tag{3.2}$$

where s_i is a system operator, and $B_{n,i}$ the corresponding bath operator. The coefficient $c_{n,i}$ relates the local system-bath coupling strength and in the case where the bath is harmonic, it is convenient to introduce the spectral density,

$$J_i(\omega) = \frac{\pi}{2} \sum_n c_{n,i}^2 \delta(\omega - \omega_n). \tag{3.3}$$

as the weighted sum of the system-bath coupling strengths and density of states at bath frequency ω_n. The spectral density can be inferred from linear absorption measurements [182] or computed from atomistic simulations. [148].

Stochastic Wavefunctions from Quantum Jumps

Provided the Markovian, weak coupling, and secular assumptions, trajectories traced out by the system degrees of freedom consist of periods of coherent evolution punctuated by abrupt changes in the state of the system, reflecting the instantaneous action of the bath. These trajectories represent physical realizations of a piecewise deterministic stochastic process in a projective Hilbert space[31] and provide a theoretical description of quantum jump observations in experiments. [92, 284] The time evolution for a wavefunction in the system Hilbert space over a quantum jump trajectory is given by the stochastic equation of motion,

$$d|\psi_t\rangle = -\frac{i}{\hbar} H_{\text{eff}} |\psi_t\rangle dt + \sum_n \left(\frac{\sqrt{\Gamma}_n L_n}{\langle \psi_t | \Gamma_n L_n^\dagger L_n | \psi_t \rangle} - 1 \right) |\psi_t\rangle dN_n, \tag{3.4}$$

where $|\psi_t\rangle$ is the wavefunction of the system at time t and $\hbar$ is Planck's constant divided by 2π. The first term in Eq. 3.4 represents coherent, deterministic dynamics with the effective

Hamiltonian, H_{eff},

$$H_{\mathrm{eff}} = H_S - \frac{i}{2}\sum_n \Gamma_n L_n^\dagger L_n, \tag{3.5}$$

which adds to the original Hermitian operator, H_S, an anti-Hermitian term due to the coupling with the bath through the operators L_n and their adjoints, $\hat{L}_n^\dagger$. The L_n operators, include both dissipative and dephasing actions of the bath and Γ_n are the associated bare rates of those actions. The second term in Eq. 3.4 is a Poisson jump process reflecting projective actions of the bath with statistics $dN_n = 0, 1$ and $dN_n^2 = dN_n$ and rates for each L_n corresponding to the quantum expectation, $\Gamma_n \langle\psi_t|L_n^\dagger L_n|\psi_t\rangle$.

When averaged over a large number of realizations Eq. 3.4 returns a master equation describing the probability flow of the Poisson stochastic process, which is of Lindblad form[158, 93],

$$\partial_t \sigma(t) = -\frac{i}{\hbar}[H_S, \sigma(t)] + \sum_n \Gamma_n \left(L_n \sigma(t) L_n^\dagger - \frac{1}{2}\{L_n^\dagger L_n, \sigma(t)\} \right), \tag{3.6}$$

where $\partial_t \sigma(t)$ is the time derivative of the reduced density matrix, σ, and $[\cdot,\cdot]$ is the commutator and $\{\cdot,\cdot\}$ the anti-commutator. Because the system and bath are weakly coupled, each stochastic trajectory is independent and the density matrix is obtainable from the stochastic wavefunctions by $\sigma(t) = \langle|\psi_t\rangle\langle\psi_t|\rangle$ where the brackets denote an average over the Poisson random noise. This master equation is known to form a dynamical semigroup, so that the equation of motion conserves the norm and positivity of the reduced density matrix.[32, 93, 158] The semigroup property is vital for a trajectory analysis as it ensures each trajectory has physical meaning and can be experimentally realized.[30] Stochastic equations of motion have been previously developed for a number of quantum master equations[135, 137], however, the representation often gives unphysical trajectories stemming from the underlying master equation's failure to form a dynamical semigroup. Additionally, stochastic unraveling has the algorithmic benefit of reduced scaling in propagating wavefunctions compared to propagating density matrices[194], which takes the overall scaling in terms of the number of system states N from $\mathcal{O}(N^3)$ to $\mathcal{O}(MN^2)$ where M is the number of trajectories required to converge the density matrix.

The operators, L_n, are identified as Lindblad operators and can be obtained directly from the original system-bath coupling operators[123, 268] of a microscopic model provided non-secular terms that couple populations and coherences are negligible[15]. In this case, it will be most convenient to represent the Lindblad operators in the energy eigenbasis, denoted L_{ij}, and are given by

$$L_{ij} = \mathcal{P}_{ij} S \tag{3.7}$$

where $\mathcal{P}_{ij}$ is an operator that projects out the ij elements of the system-bath coupling operator in the energy eigenbasis, *i.e.*, $\mathcal{P}_{ij} s = S_{ij}|\phi_i\rangle\langle\phi_j|$, where $|\phi_i\rangle$ is the ith energy eigenfunction of H_S. The associated rates in the energy eigenbasis, Γ_{ij}, are given by the Fourier-Laplace transform of the bath correlation function

$$\Gamma_{ij} = \int_0^\infty dt\, e^{-i\omega_{ij}t} \langle B(t)B(0)\rangle_{\mathrm{eq}}, \tag{3.8}$$

where $\langle \cdots \rangle_{\mathrm{eq}}$ is a thermal average and $\omega_{ij} = (E_i - E_j)/\hbar$ where $E_i\,(E_j)$ is the ith (jth) eigenvalue of H_S [182]. By the fluctuation-dissipation theorem for quantum time-correlation functions, these rates thus obey detailed balance,

$$\frac{\Gamma_{ij}}{\Gamma_{ji}} = e^{\beta\hbar\omega_{ij}}, \tag{3.9}$$

where $\beta = 1/k_{\mathrm{B}}T$ is inverse temperature, T, times Boltzmann's constant, k_{B}. This ensures that in the long time limit, the density matrix is given by a Gibbs state, $\sigma = \sum_i e^{-\beta E_i} |\phi_i\rangle\langle\phi_i|$. The Lindblad operators for nonzero frequencies, which are non-diagonal, are associated with population transfer while the zero frequency Lindblad operators, which are diagonal, are the dephasing operators [32].

Reactive Path Ensembles

Provided the stochastic equation of motion for the system wavefunction, we can define an ensemble of trajectories parameterized by a trajectory length t_{obs}. This follows closely previous work considering the spacetime thermodynamics of quantum jump processes [81]. We define a sequence of wavefunctions visited over the observation time, $\Psi(t_{\mathrm{obs}}) = \{|\psi_0\rangle, |\psi_{\Delta t}\rangle, \ldots, |\psi_{t_{\mathrm{obs}}}\rangle\}$ and the probability of observing that sequence, $P[\Psi(t_{\mathrm{obs}})]$, is given by

$$P[\Psi(t_{\mathrm{obs}})] \propto p_0(|\psi_0\rangle) \prod_{t=0}^{t_{\mathrm{obs}}-\Delta t} u(|\psi_t\rangle \to |\psi_{t+\Delta t}\rangle), \tag{3.10}$$

where $p_0(|\psi_0\rangle)$ is the probability of observing the initial wavefunction and $u(|\psi_t\rangle \to |\psi_{t+\Delta t}\rangle)$ are the transition probabilities for each interval of time Δt. The transition probabilities represent the probability of waiting times between jumps multiplied by the probability for each jump,

$$u(|\psi_t\rangle \to |\psi_{t+\Delta t}\rangle) = 1 - \frac{\langle\psi_t|\Gamma_n L_n^\dagger L_n|\psi_t\rangle}{r(|\psi_t\rangle)} e^{-r(|\psi_t\rangle)\Delta t} \tag{3.11}$$

where $r(|\psi_t\rangle)$ is the waiting time probability between jumps

$$r(|\psi_t\rangle) = \langle\psi_t| \sum_n \Gamma_n L_n^\dagger L_n |\psi_t\rangle, \tag{3.12}$$

and the ratio in front of the exponential is the probabilty to make a jump due to the action of the nth Lindblad operator, both of which follow directly from Eq. 3.4. These transition probabilities have been shown to obey a differential Chapman-Kolmogorov equation and yield a Markovian stochastic process in the projective Hilbert space. [31]

We define the normalization of the path ensemble as the path partition function $Z(t_{\mathrm{obs}})$, which is obtained by integrating over all paths

$$Z(t_{\mathrm{obs}}) = \int \mathcal{D}[\Psi(t_{\mathrm{obs}})]P[\Psi(t_{\mathrm{obs}})], \tag{3.13}$$

from which is clear that stochastic unraveling samples a real-time path integral, with probability measure $\mathcal{D}[\Psi(t_{\mathrm{obs}})]$ for realizations over the Poisson random noise. The absence of a dynamical sign problem is due to the Markovian and weak system-bath coupling approximations. Observable quantities can be computed directly by averaging the time-dependent expectation value over the ensemble of trajectories

$$\langle \mathcal{O}(t) \rangle = \int \mathcal{D}[\Psi(t_{\mathrm{obs}})]P[\Psi(t_{\mathrm{obs}})]\langle \psi_t | \mathcal{O} | \psi_t \rangle \tag{3.14}$$

where the usual quantum operator expectation value at time $t \leq t_{obs}$ is averaged over the stochastic paths, denoted with $\langle \ldots \rangle$. As a result of the detailed balance condition in Eq. 3.9, the trajectories obeys microscopic reversibility as codified by the Crooks Fluctuation Theorem[52]. This result implies both the Jarzsynski equality[122] and the correct physical interpretation to the flow of energy into and out of the system through heat and work[104, 105].

While Eq. 3.10 denotes the total path probability, it is possible to only consider those trajectories that undergo a rare, or reactive event. To do this we define the probability of observing a rare event, $P_{AB}[\Psi(t_{\mathrm{obs}})]$, in which the system begins in some quantum state A at time 0 and ends in some other quantum state B, at t_{obs},

$$P_{AB}[\Psi(t_{\mathrm{obs}})] \propto P[\Psi(t_{\mathrm{obs}})]\langle \psi_0 | h_A | \psi_0 \rangle \langle \psi_{t_{\mathrm{obs}}} | h_B | \psi_{t_{\mathrm{obs}}} \rangle, \tag{3.15}$$

where $h_{A(B)}$ is a projection operator for state A (B). The normalization of the path probability, $Z_{AB}(t_{\mathrm{obs}})$, and observables in this conditioned ensemble are computed as,

$$Z_{AB}(t_{\mathrm{obs}}) = \int D[\Psi(t_{\mathrm{obs}})]P[\Psi(t_{\mathrm{obs}})]\langle \psi_0 | h_A | \psi_0 \rangle \langle \psi_{t_{\mathrm{obs}}} | h_B | \psi_{t_{\mathrm{obs}}} \rangle \tag{3.16}$$

and,

$$\langle \mathcal{O}(t) \rangle_{AB} = \int \mathcal{D}[\Psi(t_{\mathrm{obs}})]P_{AB}[\Psi(t_{\mathrm{obs}})]\langle \psi_t | \mathcal{O} | \psi_t \rangle, \tag{3.17}$$

analogously as in the unconditioned path emsemble, and we adopt the subscript AB on the brackets to denote an average in the reactive path ensemble. Here the semigroup property is requisite due to the dependence of the normalization on the physicality of individual trajectories. Though we specifically consider path ensembles conditioned on reactive events, this formalism is general, and can be used for conditioning on time extensive quantities as done with the s-ensemble and related techniques [33].

If the probability of observing the transition form A to B in the unconstrained ensemble, $P[\Psi(t_{\mathrm{obs}})]$, is small, then accurately determining expectation values in the reactive path ensemble through brute force sampling will be difficult. One means to overcome such sampling problems is to use Transition path sampling (TPS) algorithms to sample $P_{AB}[\Psi(t_{\mathrm{obs}})]$ directly[26, 55]. Typically the most efficient Monte Carlo move for reactive path spaces is the so-called "shooting move"[55]. Shooting moves generate new trial trajectories by re-integrating the equation of motion forward and backward from some uniformly chosen intermediate time along the trajectory. If the integration of the trial trajectory uses the same equation of motion as that which defines the desired path ensemble, and the Monte Carlo procedure uses a symmetric change in the configuration about the intermediate time, the acceptance ratio is

$$P_{\mathrm{acc}}[\Psi^o \to \Psi^n] = \min\left\{1, \langle\psi_0^n|h_A|\psi_0^n\rangle\langle\psi_{t_{\mathrm{obs}}}^n|h_B|\psi_{t_{\mathrm{obs}}}^n\rangle\right\} \tag{3.18}$$

where Ψ^o and Ψ^n are the old and new trajectories with their arguments suppressed for compactness, P_{acc} is the acceptance probability for the Monte Carlo move, and the projection operators are evaluated at the end points of the new trajectory. Since the equation of motion for the quantum jump trajectory is stochastic, one-sided shooting can be done in order to increase the acceptance probability [55]. Here only the bias from the conditioning functional of $P_{AB}[\Psi(t_{\mathrm{obs}})]$ appears due to the symmetry in the Monte Carlo moves.

Rate Constants

Much like in the classical path ensemble formalism, a rate constant can be computed by a time derivative of the side-side correlation function, $C_{AB}(t)$,[44]

$$k(t) = \frac{d}{dt}C_{AB}(t) \tag{3.19}$$

where

$$C_{AB}(t) = \frac{\langle h_A[\psi_0]h_B[\psi_t]\rangle}{\langle h_A[\psi_0]\rangle}\,, \tag{3.20}$$

which is the conditional probability of the system being in state B at time t, given the system started in state A at time $t = 0$. With the identification of the ensemble averages in Eq. 3.20 as conditioned path partition functions it follows directly just as it does with classical path ensembles[55] that the rate constant is a time-derivative of a ratio of these conditioned path partition functions

$$k(t) = \frac{d}{dt}\frac{Z_{AB}(t)}{Z_A(t)}, \tag{3.21}$$

where

$$Z_A(t_{\mathrm{obs}}) = \int D[\Psi(t_{\mathrm{obs}})]P[\Psi(t_{\mathrm{obs}})]\langle\psi_0|h_A|\psi_0\rangle \tag{3.22}$$

is the reactant path partition function. The ratio of partition functions is computable by thermodynamic integration. By rewriting the ratio as an integral,

$$\ln \frac{Z_{AB}}{Z_A} = \int_0^B d\lambda \left(\frac{\partial \ln Z_{A\lambda}}{\partial \lambda} \right) \tag{3.23}$$

the rate is identical to the reversible work to "stretch" the ensemble of trajectories from the reactant to product regions. While thermodynamic integration is one means to compute this reversible work, any other free energy method could be use analogously. To this end, umbrella sampling can be used to constrain trajectories beginning in region A to end in overlapping intermediate regions λ in the interval ranging from A to B and constructing a "path free energy" in this coordinate. Because the rate has been constructed as a ratio of path partition functions or likewise a difference of path free energies, the calculation is independent of path taken along the thermodynamic integration, hence *a priori* knowledge of the reaction coordinate is unnecessary. The rate constant can then be computed either directly from the ratio of path partition functions or by computing the time-derivative. In the former case, one uses the identity at some steady-state time,

$$k = \frac{1}{t_{\mathrm{obs}}} \frac{Z_{AB}(t_{\mathrm{obs}})}{Z_A(t_{\mathrm{obs}})}. \tag{3.24}$$

valid for t_{obs} intermediate to the molecular timescale of a transition, τ_{mol}, and the reaction timescale, $1/k$, ($\tau_{\mathrm{mol}} < t_{\mathrm{obs}} \ll 1/k$) The rate constant is thus directly proportional to the ratio of path partition functions in this steady-state by the inverse of the steady-state time. Alternatively, the time derivative of this path partition function ratio can be computed by which the ratio is computed at a number of times and the slope, in the steady-state regime, is precisely the rate constant.

3.3 Conditioned Ensembles

In this section, we illustrate the utility of conditioned path ensembles for gaining mechanistic insight in open quantum dynamics. In particular, we show how conditioned ensembles build in correlations that elucidate the mechanistic details of specific rare events. Our work focuses on energy transfer dynamics in a donor-bridge-acceptor (DBA) system, schematically shown in Fig. 3.1(a). This system was recently considered by Jang and co-workers who applied a novel quantum master equation, termed the polaron-transformed quantum master equation (PQME)[118, 120], to a model three-level chromophoric system coupled to a bath[119]. Depending on the strength of the coupling to the bath, the energy transport between the donor and acceptor states could follow from either a superexchange mechanism, in which an excitation initially localized on the donor state is transferred coherently to the acceptor state, or from a sequential hopping mechanism, in which the excitation is transferred incoherently through a barrier-crossing-like event to reach the acceptor state after passing through the intermediate bridge state. By increasing the coupling strength between the system and bath, one can observe a smooth transition between these mechanisms, which gives rise to an overall turnover in the rate of charge transfer.

The PQME method is able to treat a broad range of the system-bath coupling strength by making use of a small polaron transform to the original system bath model. This transformation incorporates the bath modes into the system Hamiltonian through a reorganization energy, which changes the site energies, and hopping integrals, which dampen the electronic coupling terms in the system Hamiltonian exponentially as the system-bath coupling strength increases. After the application of the small polaron transform, the system Hamiltonian becomes,

$$H_S = \sum_l \epsilon_l |l\rangle\langle l| + \sum_{l \neq l'} V_{ll'} |l\rangle\langle l'|. \tag{3.25}$$

where $l = D, B, A$, labels the donor, bridge and acceptor sites, ϵ_l are the site energies reduced by the reorganization energy, and $V_{ll'}$ are the inter-site couplings that are dressed by the polaron transform. In this model there are nonzero inter-site couplings between $D - B$ and $B - A$, but no direct coupling between $D - A$. A consequence of the polaron transform is that the form of $V_{ll'}$ depends on the system-bath coupling

$$V_{ll'} = v_{ll'} e^{-\eta \lambda_r^2} \tag{3.26}$$

where $v_{ll'}$ are the bare inter-site couplings and are multiplied by an exponentially small term in the system-bath coupling strength, η, with temperature dependent prefactor

$$\lambda_r^2 = \frac{\pi}{\eta} \int d\omega \, J(\omega) \coth(\beta \hbar \omega / 2) \tag{3.27}$$

which is a thermally weighted integral over the spectral density. Following Jang and coworkers,[119] the spectral density is, using the convention of Eq. 3.3, taken to be of ohmic form

$$J(\omega) = \frac{2}{\pi} \frac{\eta}{3!} \frac{\omega}{\omega_c^2} e^{-\omega/\omega_c}, \tag{3.28}$$

where ω_c is the bath cutoff frequency. In principle, an inhomogeneous term arising from initial correlations between the system and bath modifies the system hamiltonian in a time dependent manner. However for the conditions we consider its effect is negligible, so we do not consider it in the following.

The resultant PQME is a weak-coupling master equation for the quasiparticle small polaron, interacting with the deformed environment, where the residual off-diagonal coupling to the bath is treated perturbatively [118]. In order to put the PQME into a quantum jump form, we must make two additional approximations to the equations of motion. First, we ignore non-secular terms that couple populations from coherences in the energy eigenbasis. Second, while the PQME is a time-local equation, it is non-Markovian in that the rates of transitions induced by the bath are time-dependent. In principle the Lindblad operators in

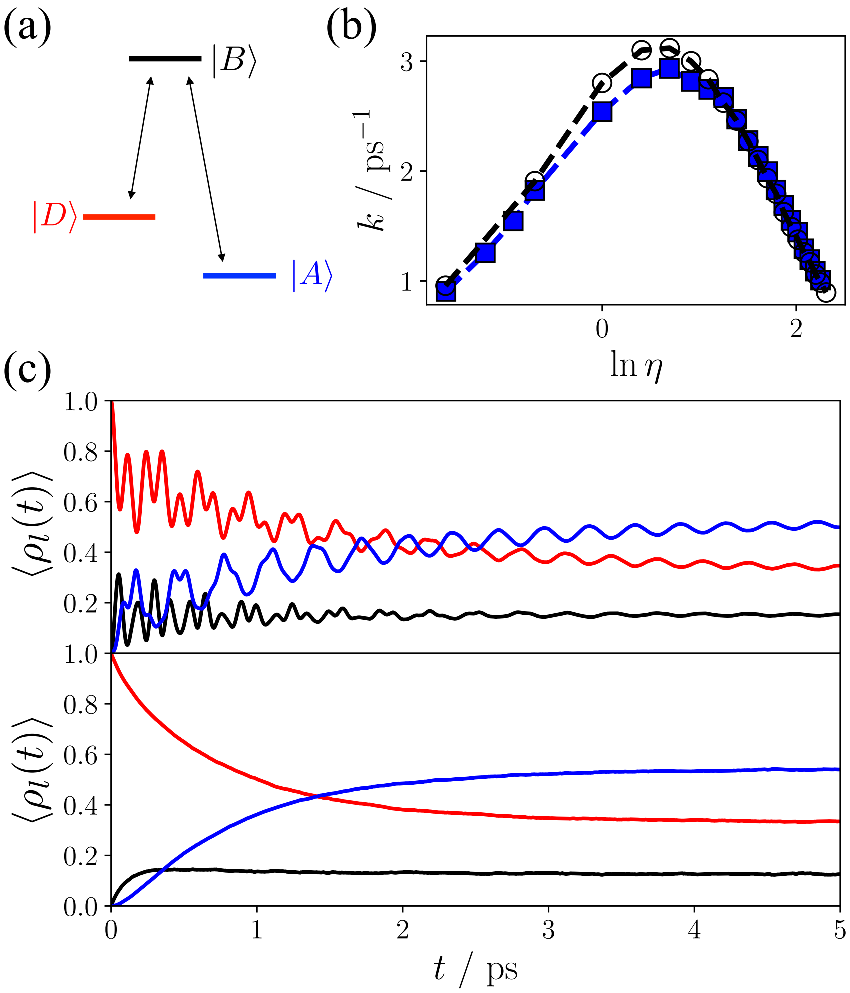

Figure 3.1: Energy transfer dynamics in the DBA model. a) Schematic energy levels used in the study. b) Donor to acceptor energy transfer rate constants as a function of system-bath coupling, η, for the full PQME (open circles) and for the Lindblad PQME (blue squares). c) Population dynamics are shown for the donor (red), bridge (black), and acceptor (blue) sites for $\eta = 0.2$ (top panel) and $\eta = 9.0$ (bottom panel).

the quantum jump equation can take time dependent forms, and as long as the rates are strictly positive the complete positivity of the density matrix will be preserved. However, we make a Markovian approximation and neglect this time-dependence.

Given these approximations, we can construct Lindblad operators from the elements of a time-independent Redfield-like tensor. As the rates of these operators obey detailed balance, it is most convent to express them in the energy eigenbasis. For population transfer between each pair of energy eigenstates, the Lindblad operators are

$$L_{ij} = |\phi_i\rangle\langle\phi_j|, \quad \Gamma_{ij} = \mathcal{R}_{iijj} \tag{3.29}$$

and the single dephasing operator is

$$L_{\mathrm{d}} = \sum_i \sqrt{\mathcal{R}_{iiii}} |\phi_i\rangle\langle\phi_i| \tag{3.30}$$

where we have absorbed the dephasing rate into the dephasing operator, and so have $\Gamma_{\mathrm{d}} = 1$. The elements of the Redfield-like tensor follow directly from Jang *et al.*, and in the energy eigenbasis are,

$$\mathcal{R}_{iijj} = \frac{1}{\hbar^2} \sum_{l \neq l'} \sum_{m \neq m'} J_{ll'} J_{mm'} \mathcal{F}^{ii,jj}_{ll',mm'} \tag{3.31}$$

whose kernel in our Markovian approximation is

$$\mathcal{F}^{ii,jj}_{ll',mm'} = \int_0^\infty dt \left(1 - e^{-\mathcal{K}_{ll',mm'}(t)}\right) \left(S^{ij,jj}_{ll',mm'} - \sum_{j'} S^{ij,j'j'}_{mm',ll'} \right) + \text{h.c.}, \tag{3.32}$$

where $\mathcal{K}_{ll',mm'}(t) = (\delta_{lm} + \delta_{l'm'} - \delta_{lm'} - \delta_{l'm})C(t)$ and δ_{lm} is the Kronecker delta. The correlation function $C(t)$ is given by

$$C(t) = \int_0^\infty d\omega J(\omega)[\coth(\beta\hbar\omega/2)\cos(\omega t) - i\sin(\omega t)]$$

and the overlap factors, $S^{ii,jj}_{ll',mm'}$, coming from the change from the site to energy eigenbasis are given by

$$S^{ij,j'j'}_{ll',mm'} = \langle\phi_i|m\rangle\langle m'|\phi_{j'}\rangle\langle\phi_{j'}|l\rangle\langle l'|\phi_j\rangle$$

and we employ h.c. to refer to the Hermitian conjugate of the product of the previous terms in Eq. 3.32.

Throughout we will use $\epsilon_B - \epsilon_D = 200$ cm^{-1}, $\epsilon_B - \epsilon_A = 200$ cm^{-1}, $j_{BD} = j_{BA} = 100$ cm^{-1}, and $\omega_c = 200$ cm^{-1}. With this equation of motion, and these parameters, we consider the dynamics of the system initially prepared in the donor state, $|D\rangle$. The donor state is energetically unfavored, and so relaxation mediated by the bath will lead to population transfer to the acceptor states. For the inter-site coupling strengths considered, the energy eigenstates are primarily localized on specific sites, becoming exactly commensurate in the limit of large system bath coupling strength, η. For simplicity, we will label the energy eigenstates by $|\phi_l\rangle$, for the state primarily supported on site l, and the corresponding state in the site basis with $|l\rangle$.

Though the Lindbladization procedure described above invokes both the Markovian and secular approximation, the dynamics show quantitative agreement with the original simulations of Jang et. al.[119] The rate constants computed from population dynamics, shown in

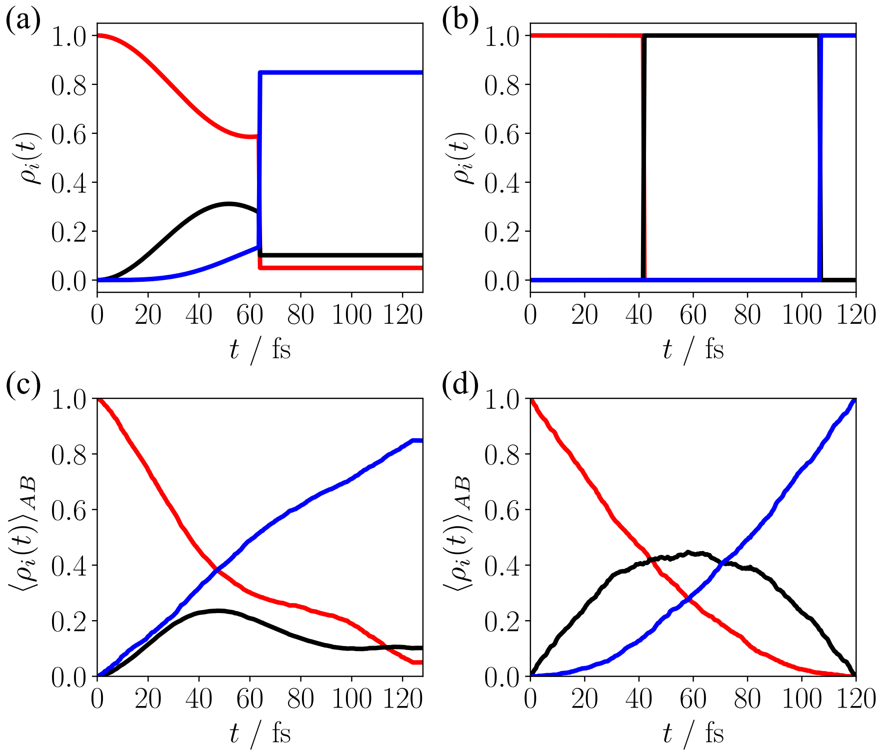

Figure 3.2: Population dynamics in the reactive ensemble. Representative stochastic trajectories for the donor (red), bridge (black), and acceptor (blue) populations are shown for (a) for $\eta = 0.2$ and (b) for $\eta = 9.0$ and averaged populations are shown in (c) for $\eta = 0.2$ and (d) for $\eta = 9.0$.

Fig. 3.1(b), are accurate across the whole range of system-bath coupling strengths exhibiting a maximum rate at $\eta = 2$, which agrees with the full PQME result. Example population dynamics computed from, an unconditioned ensemble, $\langle\rho_l(t)\rangle$, where ρ_l is the population operator, $\rho_l = |l\rangle\langle l|$ for site $l = (D, B, A)$, exhibit the same qualitative changes from coherent dynamics at weak system-bath coupling to hopping dynamics at strong system-bath coupling. These results were accomplished with 40,000 trajectories for each η. As was noted in early applications of the PQME method, [118] non-Markovian effects from the perspective of the non-transformed system Hamiltonian are treated in the system Hamiltonian to some degree by the PQME method due to incorporation of the bath modes from the small polaron transform. The deviation near the maximum stems from the secular approximation, which decouples additional transfer from coherences to the populations and slightly reduces the overall rate.

To study the mechanism of charge transport through trajectory analysis, we consider ensembles of trajectories conditioned on observing the system in the donor state at $t = 0$

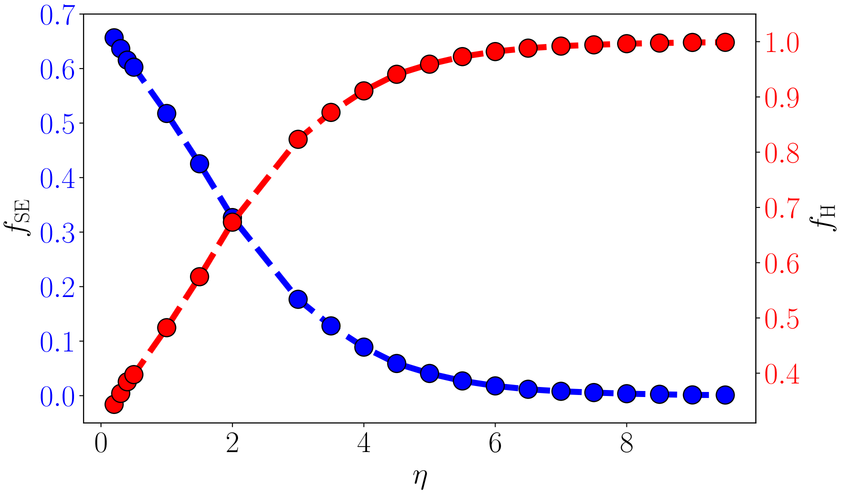

Figure 3.3: The average number of mechanistic jumps per trajectory are shown as a function of η. The average number of superexchange jumps (dashed blue curve with blue circles) have values on the left y-axis and the average number of hopping jump sequences (dashed red curve with red circles) have values on the right y-axis.

and in acceptor eigenstates at $t = t_{\mathrm{obs}}$. These conditioned probabilities are computed in a reactive path ensemble with initial and final states given by the projectors

$$h_A = |D\rangle\langle D| \quad \text{and} \quad h_B = |\phi_A\rangle\langle\phi_A| \tag{3.33}$$

so that the system begins in the donor state, which is a superposition of energy eigenstates, undergoes dephasing and dissipation through the action of the bath, and ends in an energy eigenstate mostly localized in the acceptor state. Additionally, we take $t_{\mathrm{obs}} = 120$ fs, which is much shorter than the time for population decay from the donor state on average, as shown in Fig. 3.1(c), but long enough that the system builds up population in the acceptor eigenstate with high probability.

Figures 3.2(a) and (b) show example quantum jump trajectories for $\eta = 0.2$ and $\eta = 9.0$, respectively. At weak coupling, the individual trajectories begin by undergoing Hamiltonian evolution with populations that are nearly identical to those in the unconditioned ensemble. After this initial delocalization through coherent dynamics, the system undergoes a quantum jump, which transfers population instantaneously between the eigenstates and gives rise to the decoherence apparent at long times in the averaged populations. Trajectories in the strong coupling regime are starkly different exhibiting no coherent evolution, due to the smaller inter-site coupling, and with quantum jumps transferring populations between the eigenstates. In the average populations, these quantum jumps result in exponential population transfer averaged populations, due to the exponential waiting time for the jump to occur. The short t_{obs} consists largely of trajectories that have made donor-to-acceptor eigenstate transitions, but no reverse acceptor-to-donor transitions.

The conditioned populations for $\eta = 0.2$ and $\eta = 9.0$ are shown in Fig. 3.2(c) and (d), respectively. In the weak coupling regime, where the superexchange mechanism dominates the transitions, the conditioned populations show a near direct transfer between the donor and acceptor states, while the dynamics in the bridge population remain nearly invariant to the conditioning relative to the unconditioned dynamics. At early times, the populations in the donor and bridge states rise at the same rate, and opposite to that of the acceptor states, which suggests that in this conditioned ensemble of trajectories the transfer follows the superexchange mechanism. In the strong coupling regime, where the hopping mechanism dominates, the conditioned populations show a sharp rise in the bridge state population followed by an increase in the acceptor state population. At short times the slopes now of the donor and bridge states are opposite one another, and at later times the slopes of the bridge and acceptor states are opposite. These features suggest that these trajectories primarily undergo hopping dynamics.

To verify this interpretation of the dynamics, we can directly resolve the bath operation that results in transfer from the donor to acceptor states in the individual quantum jump trajectories. Specifically, superexhange trajectories are those in which the Lindblad operator that acts to localize the population on the acceptor eigenstate is either L_{DA} or L_{BA} with no other population transfer jump occurring prior to these jumps. Using these operations ensures that transitions are made directly to the acceptor eigenstate either from the donor eigenstate or from the bridge eigenstate after coherent transfer of population to the bridge state. Hopping trajectories are similarly characterized with a Lindblad operator that localizes the population in the acceptor eigenstate directly from the bridge eigenstate, but only after first making a donor to bridge jump, L_{BA} and L_{DB}, which offers the usual barrier crossing interpretation resulting from bath fluctuations.

With these characterizations, we can now directly test how each mechanism contributes to the dynamics of the density matrix over a range of η. Figure 3.3 shows the fraction of superexchange trajectories, f_{SE}, and the corresponding fraction of hopping trajectories, $f_{\mathrm{H}} = 1 - f_{\mathrm{SE}}$, that occur in the reaction path ensemble. At weak system-bath coupling the majority of transfer events occurs via the superexchange mechanism, while at strong system-bath coupling the hopping mechanism is dominant. The decay of the fraction of superexchange jumps is exponential in the system bath coupling, which can be predicted by superexchange theory, due to the exponential decay of the inter-site coupling with increasing system-bath coupling in the polaron-transformed Hamiltonian. However, for all values of η considered, the average rate of energy transfer is a combination of superexchange and hopping. While superexchange theory predicts a monotonically decreasing rate, the rate of transfer via hopping is nonmonotonic, which is implied by the continued decrease in the overall rate in Fig. 3.1(b), in the strong coupling regime where the mechanism is dominated by hopping transitions. This nonmonotonic behavior is the result of self-trapping, which decreases the rate at large values of η.

3.4 Committor Analysis

In the context of photo-induced nonadiabatic dynamics, the rate of an event is often less important than its associated yield. The yield of such a process depends on how the dynamics of a specific chemical system favors forming the product state over relaxing back to the reactant state. In the context of chemical reactions this manifests itself in the chemical selectivity. In this section, we show how path ensembles can be used to understand this selectivity by studying the dynamics of a proton-coupled electron transfer (PCET) model developed by Hammes-Schiffer and co-workers[267]. In particular, we show how stochastic unraveling can be used to interrogate the relaxation mechanisms that determine quantum yield following photoexcitation using a generalization of commitment analysis incorporating the commitment to different potential product states. Understanding the mechanism of yields is of broad importance to understanding a number of chemical reactions in photochemistry such as photoisomerization reactions [15, 98] and other relaxation phenomena like hot carrier generation [56].

The model we study (model A from Ref. describes the photoinduced PCET for a system with electronic energy bias coupled to a bath. The system is composed of two harmonic oscillators, depicted in Fig. 3.4, coupled to a harmonic oscillator bath. The system is strongly coupled to this bath, so the small polaron transform is again utilized to ensure the accuracy of a weak coupling perturbation theory. In this polaron-transformed frame, the system Hamiltonian is,

$$H_S = -\frac{\hbar^2}{2m}\frac{\partial^2}{\partial \hat{q}^2} + \sum_{l=0,1} U_l(q)|l\rangle\langle l| \tag{3.34}$$

where $\hat{q}$ is the proton coordinate with mass m, l labels the donor, $|1\rangle\langle 1|$, and acceptor, $|0\rangle\langle 0|$, electronic states, each with an associated harmonic potential energy, $U_l(q)$

$$U_l(q) = \frac{1}{2}m\omega_l^2(q-q_l)^2 + \epsilon_l$$

where, ϵ_l is the potential energy minimum, q_l its equilibrium position, and ω_l its characteristic frequency. In this model, the system-bath coupling is treated in the electronic coupling, so that the bath serves to localize the excited electron and reduce the rate of electronic oscillation arising from off-diagonal coupling in the original system Hamiltonian. The electronic coupling can then be treated perturbatively with secular Redfield theory. Thus in this model electron transfer occurs because of bath fluctuations that temporarily permit the coherent electron transfer.

The resulting Lindblad operators are population transfer operators between the vibrational states on different electronic states,

$$L_{ln,l'n'} = |l\rangle|n\rangle\langle n'|\langle l'|, \quad \Gamma_{li,1j} = \mathcal{R}_{ln,l'n'} \tag{3.35}$$

where the pair ln, label the electronic state $l = |0\rangle, |1\rangle$ and n, the vibrational eigenstate. There is one dephasing operator that is just the unit operator for the donor state

$$L_{\mathrm{d}} = \sum_n \sqrt{G_{1n}} |1\rangle |n\rangle \langle n| \langle 1|. \tag{3.36}$$

weighted by the rate $\sqrt{G_{1n}}$, so that $\Gamma_{\mathrm{d}} = 1$. The population transfer rates are given by a Fourier-transform of the bath-correlation function formally expressed for acceptor to donor transitions and donor to acceptor transitions, respectively, as

$$\mathcal{R}_{ln,l'n'} = \frac{1}{\hbar^2} |V_{ll'}|^2 |F_{nn'}|^2 \int_{-\infty}^{\infty} dt\, e^{i(E_n^l - E_{n'}^{l'})t/\hbar} M(t) \tag{3.37}$$

where $V_{ll'}$ is the electronic coupling matrix element which is nonzero only for $l \neq l'$, $F_{nn'}$ is the Franck-Condon overlap factor between the vibrational states on different electronic states, $F_{nn'} = \langle 0| \langle n|n' \rangle |1\rangle$, and E_n^l is the energy of the nth vibrational state of the lth electronic state, and $M(t)$ is the thermally averaged, polaron transformed, bath correlation function. The elements of this tensor give the rate of transfer between the vibrational states of each electronic state. The dephasing rates are given by

$$G_{1n} = \sum_{n'} \mathcal{R}_{1n,0n'} \tag{3.38}$$

as the bath is only coupled to the donor electronic state, only the coherences of the donor state undergo dephasing. Following Ref. the bath correlation function is computed using a high-temperature approximation,

$$M(t) \approx \exp\left(-\frac{\lambda_s t^2}{\hbar^2 \beta} - \frac{it\lambda_s}{\hbar} \right), \tag{3.39}$$

where λ_s is the reorganization energy. Given the form of the Lindblad operators and their associated rates, population transfer only occurs between vibrational states of different electronic states, with an average dissipation roughly given by λ_s. As the original dynamics were simulated with the secular approximation, the Lindblad master equation we employ gives equivalent dynamics, just in a different representation.

We consider dynamics following a vertical excitation of the ground vibrational eigenstate of the acceptor into the donor electronic state. The subsequent initial condition, $|\psi_0^v\rangle$, is illustrated in Fig. 3.4 and is given by

$$|\psi_0^v\rangle = \sum_i c_n |i\rangle |1\rangle \tag{3.40}$$

where the coefficient $c_n = \langle 0| \langle 0|n \rangle |1\rangle$ is the vibrational overlap factor of the 0th vibrational state of electronic state 0, with the ith vibrational state of electronic state 1. Throughout this section we use $\Delta\epsilon = \epsilon_1 - \epsilon_0 = 1$ eV, so that the acceptor state is energetically preferred,

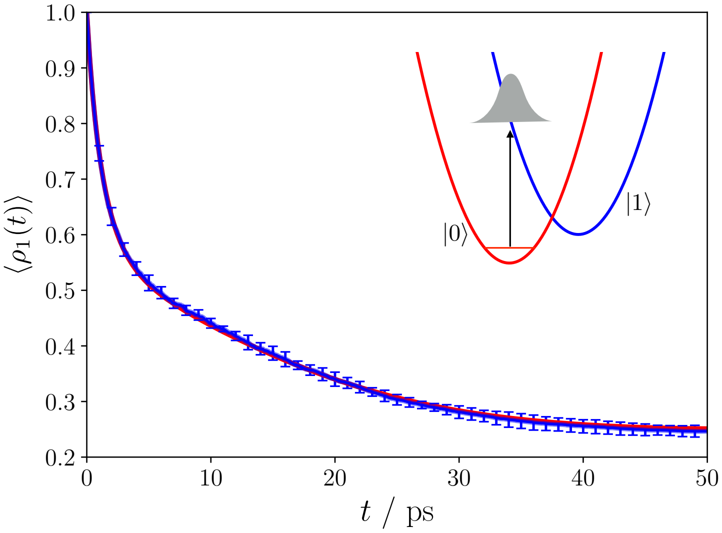

Figure 3.4: Population dynamics of PCET model from RDM simulation (red) and from stochastic unraveling (blue). Error bars are computed from block averaging and represent a 95 percent confidence interval. The inset shows the potential energy surfaces of the acceptor (red parabola) and the donor (blue parabola) states.

$\omega_0 = \omega_1 = 3000$ cm^{-1}, and $q_0 = -0.5$ Å, $q_1 = 0$ Å, The electronic coupling is taken to be $V_{01} = 0.03$ eV, $m = 1$ amu, the mass of a hydrogen atom, the temperature is $T = 300$ K and the reorganization energy is $\lambda_s = 0.892$ eV. For these parameters and initial condition, we find we can truncate the Hilbert space to include only the lowest 30 vibrational levels in each electronic state. The population dynamics in the donor state, $\langle \rho_1(t) \rangle$ where $\rho_1 = \sum_n |1\rangle|n\rangle\langle n|\langle 1|$, following this vertical excitation are compared between the reduced density matrix formalism and simulation with stochastic unraveling in Fig. 3.4. With 40,000 trajectories the population dynamics are well-converged and exhibit the same dynamical features. With these choices of parameters, following a fast initial relaxation aided by the large Franck-Condon overlap for high energy states, a metastable population forms at intermediate times relative to the equilibrium distribution in which the donor-state population is negligible. This metastable state is due to a branching process that occurs during the vibrational relaxation that splits population into the donor and acceptor states, resulting in an enhancement of population in the donor state, 0.3, over its equilibrium value, essentially 0.0. Using trajectory analysis we can clarify the mechanism by which this branching occurs and thus understand what bath fluctuations give rise to a preferential population of the donor state over the acceptor state.

To study the mechanism of preferential relaxation into the donor state, we define the reactive path ensemble for this model as

$$h_A = |\psi_0^v\rangle\langle\psi_0^v| \quad \text{and} \quad h_B = |1\rangle|0\rangle\langle 0|\langle 1| \tag{3.41}$$

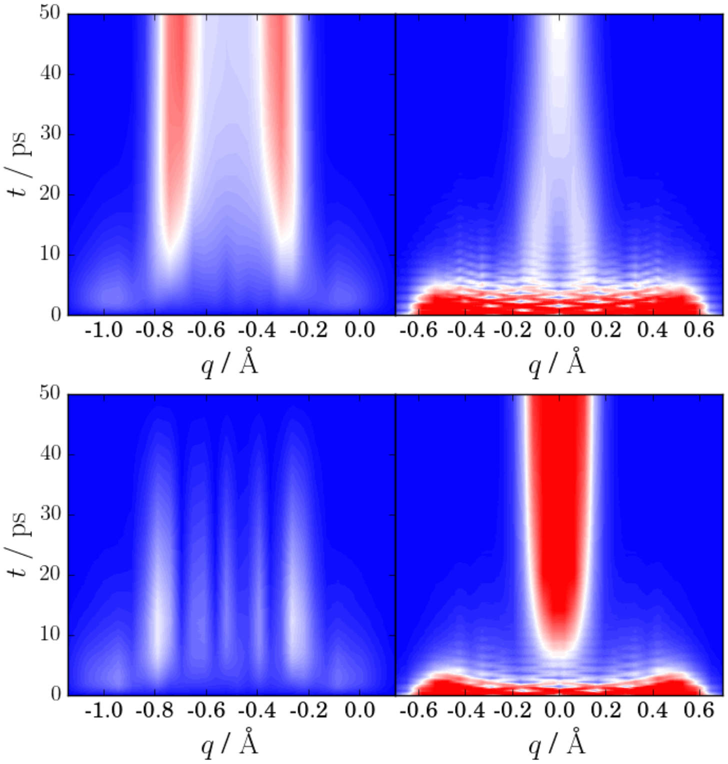

Figure 3.5: Projections of the wavepackets onto the position basis (q) in the acceptor state (left column) and the donor state (right column) for the unconditioned path ensemble (top row) and the conditioned path ensemble (bottom row) as described in the text. Positions of high wavepacket probability are in red and near zero are blue. All plots use a single color range.

where the vertically excited initial condition is taken as the reactant and ground vibrational level of the donor as the product, and consider $t_{\text{obs}} = 50$ ps which is long enough to observe initial relaxation to the ground vibrational state of the donor, but shorter than the characteristic time to thermally transfer population from the donor, over the potential barrier to the acceptor state. As was noted in Ref. the projections of the wavepacket onto the coordinate basis shows the relaxation into each minima. We have computed analogous wavepacket projections which are constructed by $\chi(q,t) = \langle q|\psi_t\rangle$ where $|q\rangle$ is an eigenvector of the position operator q and compared them with those averaged in the reactive path ensemble $\langle|\chi(q)|^2\rangle_{AB}$ to those in unconditioned ensemble, $\langle|\chi(q)|^2\rangle$. These are shown in Fig. 3.5, where the normalization is computed for the both ensembles by ensuring wavefunction normalization at $t = 0$. Figure 3.5 shows how the conditioned wavepacket begins branching from the unconditioned wavepacket, at roughly 10 ps seemingly commiting to either the donor and acceptor state after undergoing an initial dephasing which damped the oscillations in the donor state.

While the averaged dynamics illustrate correlations between early time wavepacket motion and eventual localization in the donor or acceptor states, specific causal relationships and mechanistic information cannot be determined from them alone. In order to clarify the specific mechanism by which relaxation preferentially localizes in the donor state we have performed a committor analysis [26, 55, 190]. For each trajectory within the reactive path ensemble, we compute the probability, $p_B(t)$, that a given state of the system at some intermediate time $0 < t < t_{\text{obs}}$ commits to the donor state. This is computed by averaging the fraction of trajectories that localizes in the donor state, integrated from the common intermediate state.

Figure 3.6(a) shows the commitment probabilities along all of the reactive trajectories taken from the unconditioned ensemble. At the initial time of each trajectory the commitment probability is the same and equal to the unconditioned yield of the reaction. which in this case is 0.3. Over the trajectory time, $p_B(t)$ changes as each trajectory begins to jump into different vibrational eigenstates that are more or less likely to localize in the donor state. At long times, $p_B(t)$ approaches 1, as required for a member of the reactive path ensemble. For each trajectory there is a unique time, $t_{1/2}$, where the commitment probability jumps above 1/2. The ensemble of configurations defined by the state of the system at $t = t_{1/2}$ are members of a transition state ensemble. By understanding the commonalities of trajectories in this ensemble, we can identify the required dynamical fluctuation for ending in the donor

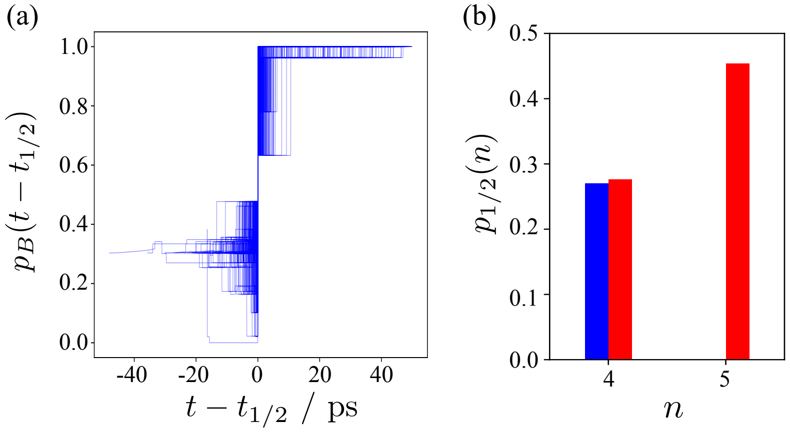

Figure 3.6: Commitment probabilities as a function of time along each trajectory are shown in a). Each probability is shifted in time by $t_{1/2}$ the time when the commitment probability jumps to greater than 1/2. The fraction ($p_{1/2}(n)$) of configurations at $t_{1/2}$ in the n^{th} vibrational state of the acceptor state (red bars) and the donor state (blue bars) is shown in b).

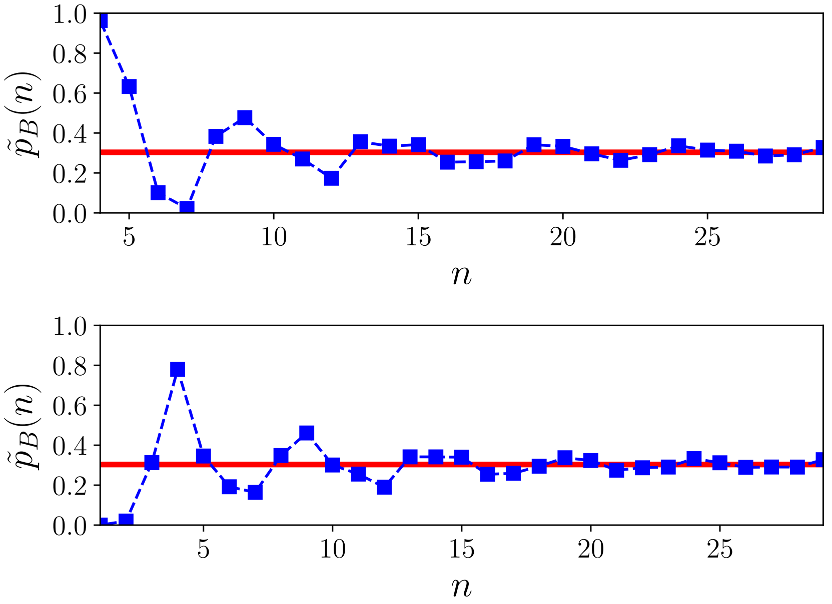

Figure 3.7: Commitment probabilities for initialization in each vibrational state of the acceptor (top panel) and the donor (bottom panel). The red line is the commitment probability from the unconditioned path ensemble.

state.

By analyzing the transition state ensemble, we have found that there are specific vibrational relaxation pathways that contribute the yield of the donor state. We have identified these pathways by computing the probability, $p_{1/2}(n)$, that members of the transition state ensemble reside in a particular vibrational state of the donor or acceptor,

$$p_{1/2}(n) = \int \mathcal{D}[\Psi(t_{\text{obs}})] P_{AB}[\Psi(t_{\text{obs}})] \delta(n - \langle \psi_{t_{1/2}} | n | \psi_{t_{1/2}} \rangle) \tag{3.42}$$

where the average is over the reactive ensemble, $n = \sum_l |l\rangle|n\rangle\langle n|\langle l|$ and the time is taken as the commitment time. Figure 3.6 (b) shows the fraction of vibrational states in the transition state ensemble, which has support over only 3 states, the 4th and 5th vibrational state of the acceptor and the 4th vibrational state of the donor. These states are greater in energy than the ground vibrational state of the donor state by either twice the solvent reorganization energy in the case of the donor state or just the solvent reorganization energy in the acceptor state.

To understand the importance of the reorganization energy in determining the commitment probability we computed the commitment probability, $\tilde{p}_B(n)$, for starting in a given vibrational state on either electronic states, unconditioned on being a member of the reactive path ensemble. This is shown in shown in Fig. 3.7. As a function of the vibrational state, the commitment probability oscillates around the unconditioned value of 0.3. The oscillations in these commitment probabilities have a period of nearly 2 times the reorganization energy. Comparing this to the transition rates computed from the Γ_{ij}'s it is clear that the average dissipation incurred by a jump is given by the solvent reorganization energy, and the bottleneck to localizing in the donor state is passing through specific vibration levels whose energy the bath can most effectively dissipate. Hence, the statistics of the dissipation for each jump has a determining impact on the commitment probability and subsequently the quantum yield. Within this small polaron framework, this result suggests that engineering the reorganization energy by changing the solvent could be used to enhance the yield of photo-induced PCET.

3.5 Evaluation of Rate Constants

Computing rate constants can often be a challenging endeavor, especially for systems with rare events that control the rate process. In those systems, simple rate theories like Transition State Theory[69, 280] (TST) are relied upon due to their ease of implementation, however, such theories often break down for systems in condensed phases due to entropic effects and recrossing events that are excluded in the theory. Furthermore the application of many simple theories requires *a priori* detailed knowledge of the mechanism, which can be elusive in complex condensed-phase systems. In this section, we utilize the path ensemble formalism to compute a rate constant in a model system with rare barrier crossing transitions.

The model in question has a system Hamiltonian

$$\hat{H}_s = -\frac{\hbar^2}{2m}\frac{\partial^2}{\partial q^2} + U(q). \tag{3.43}$$

The potential (depicted in Fig. 3.8), $U(q)$, has a quartic polynomial form

$$U(q) = aq^4 - bq^2 + \epsilon q, \tag{3.44}$$

where q is the position operator. The first two terms in the potential are necessary for producing a symmetric double-well potential, while the linear term induces a bias to one well that breaks the symmetry, a requirement for obtaining eigenstates that are localized to each well. In units of $\hbar = 1$ we have taken the mass of the particle to be $m = 1$ and $\beta = 2\times10^3$ with dimensionless potential parameters $a = 0.02\ k_{\mathrm{B}}T$, $b = -1.0\ 1k_{\mathrm{B}}T$, and $\epsilon = 0.2\ k_{\mathrm{B}}T$. The eigenstates are found using the sinc-function discrete variable representation (DVR) basis of Colbert and Miller[50]. The DVR grid was uniformly spaced over a range $q \in [-8, 8]$ with a distance $\Delta q = 0.05$ Å. Despite the large basis set required for converging the eigenstates, only the lowest 10 eigenstates, which are labeled in energy-ascending order from 0 to 9, were needed in propagating the dynamics.

We construct the Lindblad operators using a weak coupling secular Redfield theory where for each energy eigenstate pair $|\phi_i\rangle$ and $|\phi_j\rangle$ we have population transfer operators given by

$$L_{ij} = |\phi_i\rangle\langle\phi_j| \tag{3.45}$$

and rates, Γ_{ij}, given by

$$\Gamma_{ij} = \frac{1}{\pi}\int_0^\infty dt e^{-i\omega_{ij}t}\int_0^\infty d\omega J(\omega)[\coth(\beta\hbar\omega/2)\cos(\omega t) - i\sin(\omega t)] \tag{3.46}$$

where the spectral density, $J(\omega)$, has an Ohmic form with an exponential cutoff

$$J(\omega) = \eta\omega e^{-\omega/\omega_c}$$

with a coupling strength of $\eta = 0.01$ and cutoff frequency $\omega_c = (E_2 - E_0)/\hbar$. With these parameters the system is very weakly coupled to the bath, so secular Redfield theory is accurate, and the cutoff frequency is chosen to induce vibrational relaxation in each well of the quartic potential. Transitions between the wells will primarily occur as a result of barrier crossing, as is shown in the average wave-packet dynamics in the reactive ensemble in Fig. 3.8(b). This trajectory illustrates directly the importance of tunneling in the model, as an initially localized wavepacket in the reactant state transfers to the product state without having much support present in the barrier region. Since within the secular approximation, populations and coherences are decoupled, for simplicity we neglect dephasing operations without loss of generality.

We define a reactive path ensemble for transitions between the left and right well, as defined by

$$\hat{h}_A = |\phi_0\rangle\langle\phi_0| + |\phi_2\rangle\langle\phi_2| \quad \hat{h}_B = |\phi_1\rangle\langle\phi_1|, \tag{3.47}$$

which represent projectors for the lowest two eigenstates of the left well and the lowest eigenstate of the right well. The initial condition was a thermal distribution restricted to the reactant region,

$$\psi_0 = \sqrt{\frac{e^{-\beta E_0}}{Z}}|\phi_0\rangle + \sqrt{\frac{e^{-\beta E_2}}{Z}}|\phi_2\rangle \tag{3.48}$$

where $Z = e^{-\beta E_0} + e^{-\beta E_2}$. The rate constant from population dynamics, k^{pop}, is given by the time-derivative of the population in the product state,

$$k^{\mathrm{pop}} = \frac{d\langle h_B(t)\rangle}{dt}\,, \tag{3.49}$$

and when evaluated in the steady-state regime, the rate of the transition is estimated to be $k^{\mathrm{pop}} = 0.0106\ \mathrm{ns}^{-1}$.

The rate constant was also computed via TPS, as outlined in Sec. 6.2 C. Specifically, the ratio of path partition functions was estimated using umbrella sampling [262]. We

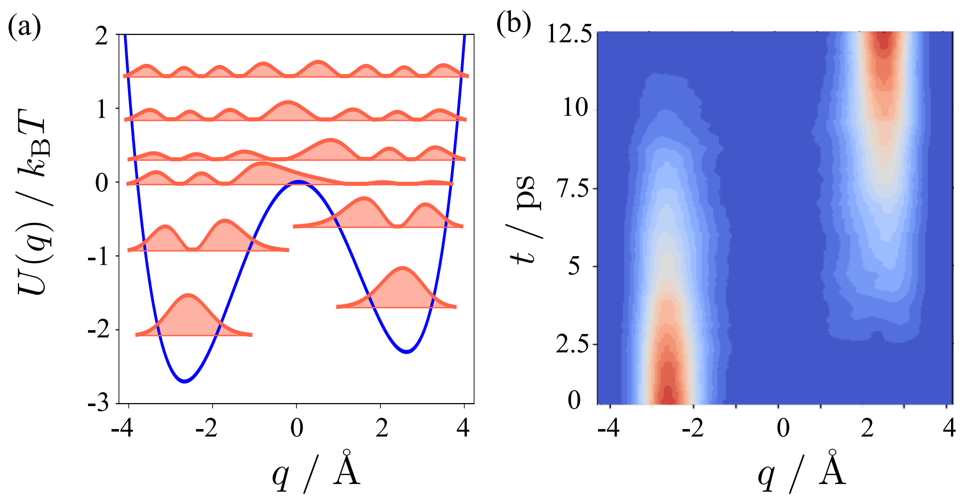

Figure 3.8: Model for thermally activated barrier crossing. (a)The quartic potential used as a function of the position (blue) with its associated eigenstate wavefunctions (red filled curves). (b) The average wavepacket conditioned on beginning in the left well and evolving to the right.

employed umbrella potentials of the form of hard walls to constrain the B-region of the trajectories using overlapping indicator functions of different eigenstates, denoted by h_λ, that were observed along typical transition paths. These umbrella potentials constrained the final wavefunction to be projected into an eigenstate contained in λ and by using overlapping indicator functions. The full path partition function could be reconstructed as a function of λ using histogram reweighted techniques [144, 238].

Specifically, umbrella sampling was performed using overlapping indicator functions, h_λ, ranging from eigenstates 0-10, with at least one indicator function equal to $h_A = |0\rangle\langle 0| + |2\rangle\langle 2|$ and one equal to $h_B = |1\rangle\langle 1|$. For each window 16,000 trajectories were harvested for every Monte Carlo sweep over an entire trajectory and the expectation value of the position operator $\langle q\rangle_{t_{\mathrm{obs}}}$ corresponding to the eigenstate of the wavefunction at $t = t_{\mathrm{obs}}$ was computed. The statistics of $\langle\psi_{t_{\mathrm{obs}}}|q|\psi_{t_{\mathrm{obs}}}\rangle$ obtained from this procedure were reweighted using the WHAM procedure [144], which given the discrete outcomes of the observables is a simple optimization routine. This procedure was repeated for a range of values for t_{obs} from 24 ps to 60 ps. An example of the resulting path partition function ratios for $t_{\mathrm{obs}} = 24$ ps. is shown in Fig. 3.9.

These path partition function ratios provide details about the transition rate. First, the ratio divided by t_{obs} precisely gives the rate of transitions between the reactant state and an intermediate λ-region provided t_{obs} is in the linear regime of population transfer. Hence, the rate constant is given in the same thermodynamic language from path ensembles in both the quantum and classical regimes. Finally, the ratio of path partition functions at different

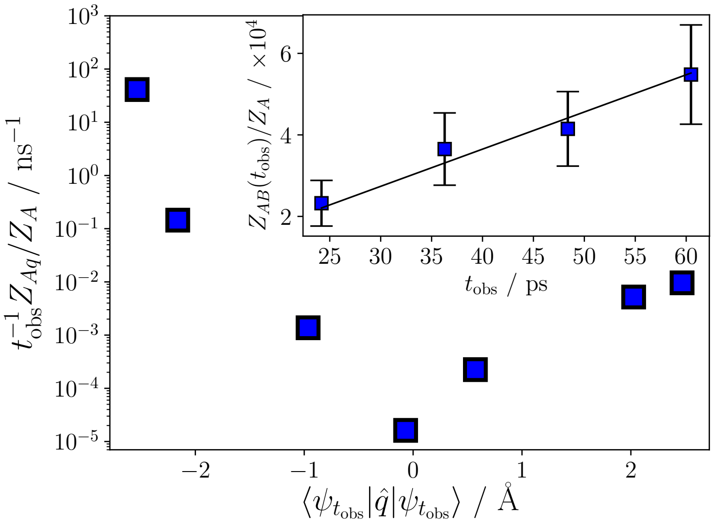

Figure 3.9: Evaluation of the rate using TPS. Ratio of path partition functions computed with $t_{\text{obs}} = 24$ ps along the reversible work path. The rightmost point is the rate constant computed from TPS at the observation time. (inset) Ratio of path partition function as a function of t_{obs}. Error bars represent a 95 percent confidence interval computed from block averaging. The black line is a linear fit $k^{\text{TPS}} t_{\text{obs}}$.

values of λ offer insight about the mechanism. As λ is tuned from eigenstates near the reactant state to the product state the ratio of path free partition functions, as in Fig. 3.9, decreases indicating a more rare and hence slower rate process, but for eigenstates that are energetically higher than the potential energy barrier, the path partition function ratio is very small, smaller than the ratio for the product state. Hence, states energetically above the potential energy barrier rarely contribute to the predominant transition paths and the typical transitions between the wells are tunneling events.

The resulting rate constant obtained from this umbrella sampling procedure is $k^{\text{TPS}} = 0.010 \pm 0.002$ ns^{-1}, which agrees quantitatively with the rate obtained from the population dynamics. Of important note is the short length of trajectories required for computing the rate constant with TPS compared to the population dynamics. Given many accurate quantum dynamics methods have exponential scaling in time, these results suggest that TPS can provide a practical alternative to computing a rate constant to population dynamics.

For comparison, the rate was also computed from transition state theory (TST) using

$$k^{\text{TST}} = \frac{\omega_0}{2\pi} e^{-\beta \Delta E^{\ddagger}} \tag{3.50}$$

where ω_0 is the frequency of the reactant well, $\Delta E^{\ddagger}$ is the activation energy [69, 280, 44]. The rate obtained by classical TST is 0.0019 ns^{-1}, which largely deviates from our result.

A temperature-dependent tunneling correction, $\kappa(\beta)$, can also be added, $k = \kappa(\beta)k^{\mathrm{TST}}$ to account for the tunneling transitions that are predicted by our trajectory analysis. For a parabolic barrier this correction is [170, 253],

$$\kappa(\beta) = \frac{\hbar\beta\omega_b/2}{\sin(\hbar\beta\omega_b/2)}, \tag{3.51}$$

here ω_b is the frequency of the parabolic barrier and corrects the overall rate constant to be 0.011 ns^{-1}, which now adds quantitative agreement with the rate obtained from TPS. Such agreement should be expected at low temperature with an approximately parabolic well and barrier as is the case for the quartic potential used here [253]. However, in the TPS calculation no assumption about the mechanism was required.

3.6 Conclusion

We have presented a path ensemble formalism useful for the study of quantum dynamics in condensed phases. The formalism enables the computation of conditioned ensembles for typical applications of TPS. To formalize a reactive path ensemble, we required an equation of motion that satisfies detailed balance, the complete positivity of the overall density matrix, and is stochastic. These conditions are satisfied by unravelling a Lindblad master equation into a quantum jump equation. The path ensemble formalism was applied to three systems, for each of which we devised a mapping from the original quantum master equation into a Lindblad form without loss of accuracy. This included developing a stochastic polaronic quantum master, illustrating an ability to invoke weak coupling approximations on transformed Hamiltonians in order to study systems that in the untransformed case were in the strong system-bath coupling regime. The use of conditioned ensembles showed the built-in correlations that can be obtained by sampling biased trajectories. These sorts of correlations could, in principle, be sampled by multi-time correlation functions [7], which can be difficult to compute and often require high-level methods due to violations of the quantum regression theorem [72]. Trajectory analysis also enables the identification of transport mechanisms in these systems by sampling the sequence of quantum jumps that occur along trajectories.

We also illustrated how TPS could be used to compute a rate constant. TPS was found to be efficient for sampling rare barrier-crossing trajectories and accurately reproduces the rate constant computed from population dynamics of the reduced density matrix. The necessary trajectory length for quantitative agreement was multiple orders of magnitude less than the reduced density matrix simulation. Other dynamics methods that satisfy properties enabling the path ensemble formalism, especially those that drastically improve the accuracy of weak-coupling quantum master equations, are applicable [106, 113, 173, 269] and for those methods with a computational complexity that scales with simulation time, TPS may be a key alternative to permit the calculation of rate constants. While the examples used here are relatively small systems with few degrees of freedom, we expect the utility of the present framework to be clear for large, multidimensional systems. Not only will the calculations be made possible by the reduced scaling of stochastic unraveling, the physical insight gained will become useful in detecting relevant reaction coordinates as the number of potential pathways increase.

Chapter 4

Hybrid Quantum Master Equations

> *"In the moment when I truly understand my enemy, understand him well enough to defeat him, then in that very moment I also love him."*
>
> — Ender Wiggin [38]

4.1 Introduction

The ultrafast excited-state relaxation dynamics of polyatomic systems are nearly universally mediated by motion through conical intersections[227, 285]. Advanced time-dependent spectroscopies have made the identification of such molecular motions possible in principle[41, 61, 139, 181, 185], elucidating their role in many photochemical reactions[57, 134, 286]. Theory and simulation are useful tools to interpret and elucidate the microscopic motions associated with the degrees of freedom probable with experiment. However, the ability to accurately and efficiently simulate such nonadiabatic dynamics in the condensed phase is challenging[107, 108, 265]. Nonadiabatic systems by definition contain many strongly coupled nuclear and electronic degrees of freedom, blurring the separation of time scales between their motion, and demanding a quantum description of both. In the condensed phase, the ability to correctly describe dissipation requires that a bath is represented either implicitly or explicitly, complicating approximations that make such calculations tractable in the gas phase. Here, we describe a framework to leverage a separation of energy and time scales to arrive at a hybrid method to study the dynamics of molecules through conical intersections. The method we employ treats the most strongly coupled modes explicitly, and develops a

---

This chapter is based on work that has been published in *The Journal of Chemical Physics* [221] hybrid reduced description for the remaining modes by identifying some as slow and others as fast relative to the nonadiabatic dynamics. This methodology enables us to study photochemical quantum yields in widely different environments.

Existing approaches to study motion through conical intersections in condensed phases fall into two broad categories. One way is to represent all of the interacting degrees of freedom and compute the dynamics of a closed system, albiet one with a large enough number of states to approximate the environment. These sorts of approaches can range from numerically exact methodologies such as the Multiconfigurational Time-Dependent Hartree (MCTDH) method[18, 274], the Quasiadiabatic Path Integral method[260, 261], and multiple spawning techniques[19, 151] to more approximate methods such as mixed-quantum classical theories like Ehrenfest[127] and surface hopping[132, 147, 264], and semiclassical theories as obtained from the mapping approaches.[166, 244, 254] Exactly representing the degrees of freedom has the advantage that arbitrary degrees of freedom can be represented provided a large enough basis. While these tools have shown promise in a variety of systems, they still can be limited by severe exponential scaling in numerically exact approaches or by invoking uncontrolled approximations that can break fundamental symmetries like detailed balance, complicating the description of a thermalizing bath.

An alternate approach relies on the master equation approach of open quantum systems[32, 179, 296], in which the dynamics of only a few relevant degrees of freedom are represented explicitly in a reduced density matrix that is coupled implicitly a set of environmental degrees of freedom. Often the environment is taken as an infinite bath of harmonic degrees of freedom, though this is not required. When a harmonic bath is used, these methods assume that a linear response relationship between the system and bath holds and thus the bath represents a set of degrees of freedom that obey gaussian statistics. When this approximation is valid, these methods also have a range of accuracy from the numerically exact Hierarchical Equation of Motion (HEOM)[248] to perturbative treatments such as Redfield theory.[204] By construction, most of these approaches accurately describe dissipation to the environment. However, they suffer from pitfalls in computational complexity, as HEOM scales roughly factorially in the system-bath coupling strength, or accuracy, as many perturbative theories have known issues with preserving the trace and positivity of the reduced density matrix.

In this chapter, we propose the use of a hybrid methodology, in the spirit of previous work[21, 22, 256], in which both approaches are utilized in regimes where they are valid. The most strongly coupled, anharmonic degrees of freedom are evolved directly and the remaining degrees of freedom are treated with different approximate theories, whose applicability rests in identifying relevant separations of time and energy scales. This approach has the advantage of a reduced computational cost compared to the most demanding numerically exact methods, while retaining both flexibility and accuracy and relies heavily on recent work in applying the so-called frozen mode approximation to quantum master equations.[173] The present chapter is organized in four remaining sections. In Sec. 4.2, the general framework for developing a hybrid method in the context of conical intersection models is outlined. In Sec. 4.3, this methodology is benchmarked in models of internal conversion of pyrazine and photoisomerization of rhodopsin by comparing to existing numerically exact results. In Sec. 4.4 we apply the framework to address the dependence of the quantum yield on the environment. Some concluding remarks are given in Sec. 4.5.

4.2 Theory

In this section we describe the framework on which a hybrid methodology can be built. This framework can begin from an *ab initio* molecular Hamiltonian, provided a diabatic basis can be constructed that minimizes the nonadiabatic coupling from the kinetic energy derivatives.[138, 266] In the diabatic basis we can write the Hamiltonian as,

$$H = \sum_{i,j} |i\rangle \left[T(\mathbf{Q})\delta_{ij} + V_{ij}(\mathbf{Q})\right] \langle j|, \tag{4.1}$$

where $T(\mathbf{Q})$ is the kinetic energy operator, which is diagonal, $V_{ii}(\mathbf{Q})$ is the potential energy surface of the ith diabatic electronic state and $V_{i\neq j}(\mathbf{Q})$ is the diabatic coupling between states i and j with $\mathbf{Q} = \{Q_1, Q_2, \ldots, Q_N\}$ the vector of displacements of each N nuclear degree of freedom from a reference geometry, $\mathbf{Q}_0$, or generalized modes. In principle, the full system can be completely described at all times by its density matrix, $\rho(t)$, whose time evolution is given by the Liouville-von Neumann equation

$$\partial_t \rho(t) = -i[H, \rho(t)] \tag{4.2}$$

where $[\cdot,\cdot]$ is the commutator. Due to exponential scaling of standard basis set treatments, this description becomes intractable for systems beyond only a few degrees of freedom, and in the condensed phase reduced descriptions are required. Throughout we will set $\hbar = 1$ and use mass weighted coordinates unless otherwise explicitly stated.

Mode expansion

To build a reduced description of the dynamics, we first impose some structure on the many body potential $V_{ij}(\mathbf{Q})$ appropriate for a molecule in a surrounding environment with a conical intersection. Within a general mode expansion[138], $V_{ij}(\mathbf{Q})$ can be approximated as,

$$V_{ij}(\mathbf{Q}) = V_{ij}^{(0)} + \sum_{k} V_{ij}^{(1)}(Q_k) + \sum_{k<l} V_{ij}^{(2)}(Q_k, Q_l) + \ldots \tag{4.3}$$

where $V_{ij}^{(n)}$ is a potential function that couples n modes of the system, truncated here to second order. Generally, each order potential could be a distinct function of its arguments, whose repeated indices we suppress for clarity.

As we are interested in motion in the vicinity of a conical intersection, we will isolate two orthogonal coordinates, the tuning mode, q_t, and a coupling mode, q_c, which define a surface of points where the two potential energy surfaces i and j intersect, giving rise to large non-adiabatic coupling. In the following, these are the modes we will consider strongly coupled. In principle, additional modes with coupling constants large relative to the bare electronic energy gap, or modes with large amplitude motion, should be included in this description. For the models we study only these two coordinates are included.

We will assume that only the tuning mode undergoes large amplitude motion away from the reference geometry. Under such assumption, which could be relaxed, we have a potential for the tuning mode of the form,

$$V_{ij}^{(1)}(q_t) = \delta_{ij}\left(v_i(q_t) + \kappa_t^{(i)} q_t\right) \tag{4.4}$$

where $v_i(q_t)$ is in general anharmonic. We assume the coupling mode is harmonic,

$$V_{ij}^{(1)}(q_c) = \delta_{ij}\left(\frac{1}{2}\Omega_c q_c^2 + \kappa_c^{(i)} q_c\right) + (1-\delta_{ij})\lambda^{(ij)} q_c \tag{4.5}$$

with frequency, Ω_c, is given by,

$$\Omega_c = \left(\frac{\partial^2 V_{ii}}{\partial q_c^2}\right)_{\mathbf{Q}_0}, \tag{4.6}$$

where the constants $V_{ij}^{(0)}$ are defined by the reference geometry $\mathbf{Q}_0$. We pull out the linear portions of the potentials, parameterized by $\kappa_k^{(i)}$, for clarity, which are Holstein-like coupling coefficients given by,

$$\kappa_k^{(i)} = \left(\frac{\partial V_{ii}(\mathbf{Q})}{\partial q_k}\right)_{\mathbf{Q}_0}, \tag{4.7}$$

and $\lambda^{(ij)}$ is a Peierls-like coupling coefficient, given by

$$\lambda^{(ij)} = \left(\frac{\partial V_{ij}}{\partial q_c}\right)_{\mathbf{Q}_0} \tag{4.8}$$

which is the only off-diagonal term in the diabatic state basis we consider and due to hermiticity, $\lambda^{(ij)} = \lambda^{(ji)}$. The existence of both $\lambda^{(ij)}$ and the $\kappa_k^{(i)}$'s reflect that at a conical intersection, both the electronic gap as well as the electronic coupling are modulated by nuclear degrees of freedom. The remaining modes are assumed to be harmonic,

$$V_{ij}^{(1)}(Q_k) = \frac{1}{2}\omega_k Q_k^2 + c_k^{(i)} Q_k \tag{4.9}$$

with frequencies,

$$\omega_k = \left(\frac{\partial^2 V_{ii}}{\partial Q_k^2}\right)_{\mathbf{Q}_0}, \tag{4.10}$$

and additional Holstein couplings,

$$c_{0,k}^{(i)} = \left(\frac{\partial V_{ii}(\mathbf{Q})}{\partial Q_k}\right)_{\mathbf{Q}_0}, \tag{4.11}$$

for each ith electronic state.

Provided the linear response form for all of the modes not including q_t, the highest-order mode coupling potential we consider that is consistent with this choice is bilinear in the modes. Specifically, we take

$$V_{ij}^{(2)}(Q_k, Q_l) = c_{k,l}^{(i)} Q_k Q_l \delta_{ij}(1 - \delta_{lk}) \tag{4.12}$$

where $c_{k,l}^{(i)}$ is the coupling coefficient that transfers vibrational energy between the kth and lth modes,

$$c_{k,l}^{(i)} = \left(\frac{\partial^2 V_{ii}}{\partial Q_k \partial Q_l} \right)_{\mathbf{Q}_0}, \tag{4.13}$$

which we take as diagonal in the diabatic states. By construction this is zero between the tuning and coupling modes, as these are chosen to be orthogonal. With the exception of the tuning mode, the remaining coordinates are all harmonic, so we can in principle orthogonalize the remaining $N-2$ subspace defined outside of q_t and q_c. The enables us to set $c_{k,l}^{(i)}$ to zero for all l and k that do not include q_c or q_t.

The resultant potential has a simple approximate form. The diabatic coupling is given by

$$V_{i \neq j}(\mathbf{Q}) = \lambda^{(ij)} q_c \tag{4.14}$$

containing only the coupling mode with Peierls constant, where here we have taken $V_{i \neq j}^{(0)} = 0$. The diabatic potentials are given by

$$\begin{aligned} V_{ii}(\mathbf{Q}) = {} & V_{ii}^{(0)} + v_i(q_t) + \kappa_t^{(i)} q_t + \frac{1}{2}\Omega_c q_c^2 + \kappa_c^{(i)} q_c \\ & + q_t \sum_k c_{t,k}^{(i)} Q_k + q_c \sum_k c_{c,k}^{(i)} Q_k + \sum_k c_{0,k}^{(i)} Q_k \\ & + \sum_k \frac{1}{2} \omega_k Q_k^2 \end{aligned} \tag{4.15}$$

where the tuning and coupling coordinates can exchange energy with the remaining $N-2$ modes, in such a way as to renormalize the effective Holstein and Peierls couplings. This potential is envisioned as including only the minimal ingredients required to describe a conical intersection with a surrounding environment, as additional complexity could be added if any of the approximations above were found invalid.[138]

System bath partitioning

For an isolated system, the N mode diabatic potential described above can be simulated directly using compact basis set techniques like MCTDH and multiple spawning. [18, 19, 151, 274] However, in a condensed phase, in order to correctly describe dissipation and relaxation, we require that the number of modes goes to infinity, such that the ω_k's will form a continuous band of frequencies. While basis set techniques can approximate this continuous band, doing so typically results in algorithms that scale exponentially in time[28]. As the remaining environment modes are expected to be less strongly coupled to the electronic degrees of freedom, we can consider ways to integrate them out and arrive at a reduced description of the dynamics of the system. In this way, we will define the total Hamiltonian, $H = H_S + H_{SB} + H_B$, as a partitioning between a system, bath and coupling terms. To determine an effective partitioning, we can leverage the identification of the relevant coupling constants and their expected scales.

Since we expect the coupling and tuning modes to be strongly coupled to the electronic states, we will treat their dynamics in the absence of additional coupling exactly. Restricting ourselves to two diabatic states, we refer to them, along with the electronic states, as the system Hamiltonian, H_S,

$$\begin{aligned} H_S &= \sum_{i,j=1,2} |i\rangle h_i \delta_{ij} + \lambda q_c (1-\delta_{ij}) \langle j| \\ h_i &= T + V_{ii}^{(0)} + v_i(q_t) + \kappa_t^{(i)} q_t + \frac{1}{2}\Omega_c q_c^2 + \kappa_c^{(i)} q_c \end{aligned} \tag{4.16}$$

where T is the kinetic energy of the tuning and coupling modes and we have removed the electronic state dependence from λ. In the case that both coordinates are harmonic, this Hamiltonian reduces to the so-called linear vibronic model[138]. The remaining degrees of freedom, the Q_k's, will make up a bath portion of the Hamiltonian. The coupling between the bath degrees of freedom and the system will be denoted by the system-bath coupling Hamiltonian, H_{SB}. This term can be written in the direct product form,

$$H_{SB} = \sum_{n=0,c,t} S_n \sum_k c_{n,k}^i Q_k \tag{4.17}$$

$$s_{(c,t)} = \sum_i |i\rangle q_{(c,t)} \langle i| \,, \qquad S_0 = \sum_i |i\rangle\langle i| \,,$$

where S_n in general includes both direct coupling to the electronic system and vibrational relaxation through coupling to the tuning or coupling modes. To describe the system-bath coupling strengths, it is useful to define the spectral densities, $J_n(\omega)$, for each system bath operator,

$$J_n(\omega) = \frac{\pi}{2} \sum_k \frac{c_{n,k}^2}{\omega_k} \delta(\omega - \omega_k). \tag{4.18}$$

and are parameterized by a reorganization energy, $E_{r,n}$,

$$E_{r,n} = \frac{1}{\pi} \int_0^\infty d\omega \, \frac{J_n(\omega)}{\omega}, \tag{4.19}$$

and a characteristic frequency, $\omega_{c,n}$. The reorganization energy reflects the overall strength of the coupling of the system to the bath, and the characteristic frequency determines the decay of the spectral density at infinite frequency. In order to treat the bath perturbatively, the dimensionless coupling parameter, η, given by

$$\eta = \max_n \left[\frac{2}{\pi^2 \omega_{c,n}} \int_0^\infty d\omega \frac{J_n(\omega)}{\omega} \right] \tag{4.20}$$

must be small on an absolute scale, $\eta \ll 1$. This parameter reflects the competing effects of the reorganization energy and characteristic frequency on the decay of higher-order correlation functions used in a perturbative expansion, and can be derived explicitly for simple models.[145, 173] For fixed $E_{r,n}$, η increases as $\omega_{c,n}$ gets smaller, generally violating the criteria for perturbation theory. This scaling of η with $\omega_{c,n}$ makes it difficult to use standard quantum master equation approaches for studying motion through conical intersections, as the relevant scale of the system dynamics is ultrafast, rendering typical bath relaxation times comparatively long[87, 88]. To remedy this requires confronting non-Markovian effects directly.

The remaining terms in the Hamiltonian are labeled as the bath, H_B, and are given by a set of noninteracting harmonic oscillators,

$$\begin{aligned} H_B = & \frac{1}{2} \sum_{k \in \text{slow}} \omega_k \left(P_k^2 + Q_k^2 \right) \\ & + \frac{1}{2} \sum_{k \in \text{fast}} \omega_k \left(P_k^2 + Q_k^2 \right) , \end{aligned} \tag{4.21}$$

which we will partition into a group labeled *fast* and a group labeled *slow*, depending on the oscillator's frequency, ω_k relative to a parameter ω^*. Here ω^* is a frequency that delineates between the fast and slow modes of the bath relative to a characteristic time scale of the system. As motion through a conical intersection is mediated by the nonadiabatic coupling, we assume the characteristic time scale of the system to be given by the Peierls coupling, λ, and consider slow modes to be those with $\omega_k < \lambda$.

Hybrid dynamical approach

Given the system-bath partitioning proposed above, we can develop an approximate way to evolve a reduced system dynamics that is capable of correctly describing dissipation even when some of the bath degrees of freedom are non-Markovian owing to the large separation of timescales between non-adiabatic system dynamics and slow environmental motions. To this aim we follow the procedure outlined in Ref. Specifically, we consider the time dependent reduced density matrix, $\sigma(t)$, as

$$\sigma(t) = \mathrm{Tr}_B\{\rho(t)\} \tag{4.22}$$

where the trace is taken over all $\mathbf{Q}$ defined in the bath part of the Hamiltonian. In order to obtain a closed evolution equation for $\sigma(t)$, we leverage the expected separation of timescales between evolution in the fast part of the bath and those in the slow part of the bath.

Following the partitioning in H_B, we can similarly partition a given spectral density into the slow and fast portions,[21, 22, 173]

$$J_n(\omega) = J_{n,\text{slow}}(\omega) + J_{n,\text{fast}}(\omega). \tag{4.23}$$

where

$$J_{n,\text{slow}}(\omega) = S(\omega) J_n(\omega) \tag{4.24}$$

delineates the slow portion and

$$J_{n,\text{fast}}(\omega) = [1 - S(\omega)] J_n(\omega) \tag{4.25}$$

the fast portion where

$$S(\omega) = \begin{cases} (1 - (\omega/\omega^*)^2)^2 & \omega < \omega^* \\ 0 \quad \omega \geq \omega^* \end{cases} \tag{4.26}$$

is a splitting function, parameterized by ω^*. In the limit that $\omega^* \ll \lambda$, we can consider the slow modes as static over the course of system dynamics. In such a limit, the total time-dependent density matrix factorizes into an initial piece from the slow modes and a time dependent remainder in which the fast modes of the bath and the system degrees of freedom evolve, $\rho(t) \approx \rho_{\boldsymbol{Q} \in \text{slow}}(0) \rho_{\boldsymbol{Q} \in \text{fast},S}(t)$. In such a case, the slow modes contribute only as a source of quenched disorder to the system Hamiltonian, and induces an inhomogeneous broadening due to different realizations of initial conditions. We include this part of the system-bath coupling directly into the Hamiltonian as,

$$\tilde{H}_S = H_S + \sum_n s_n \sum_{k \in \text{slow}} c_{n,k} \tilde{Q}_k, \tag{4.27}$$

where $\tilde{Q}_k$ is a classical variable, not an operator. Since these modes are incorporated into the system Hamiltonian, provided the assumed separation of time scales holds, they are treated to all orders in their coupling strength.

The reduced density matrix is obtained by averaging over different realizations of the reduced density matrix corresponding to different realizations of initial conditions,

$$\sigma(t) = \int d\tilde{\mathbf{Q}}\, p(\tilde{\mathbf{Q}}) \tilde{\sigma}(t), \tag{4.28}$$

where

$$\tilde{\sigma}(t) = \text{Tr}_{\mathbf{Q} \in \text{fast}}\{\rho(t)\} \tag{4.29}$$

is the reduced density matrix computed by tracing over only the fast degrees of freedom, which depends parametrically on the slow bath degrees of freedom. The initial conditions of the slow modes are drawn from the distribution $p(\tilde{\mathbf{Q}})$. Depending on the temperature relative to the characteristic frequency of the slow bath modes, $p(\tilde{\mathbf{Q}})$ may be a Wigner distribution or a Boltzmann distribution.

The remaining modes in the bath now have a smaller overall reorganization energy. Since by construction, these modes relax on a timescale faster than the system, they induce Markovian or nearly-Markovian dissipation and decoherence. For this reason, we can treat these degrees of freedom with time-dependent Redfield theory, also known as the 2nd-order Time Convolutionless master equation[45, 235] (TCL2). In the TCL2 formalism, the dynamics of the each realization of the reduced density matrix are given by,[194]

$$\begin{aligned}\partial_t \tilde{\sigma}(t) = -i[\tilde{H}_S, \tilde{\sigma}(t)] &+ \\ \sum_n [\Theta_n(t)\tilde{\sigma}(t), s_n] &+ [s_n, \tilde{\sigma}(t)\Theta_n^\dagger(t)],\end{aligned} \tag{4.30}$$

where $\Theta_n(t)$ is the system operator dressed by the time-dependent rates given by the bath correlation function. In the eigenstate basis of $\tilde{H}_S$, each element is given by

$$\left(\Theta_n\right)_{ij}(t) = \left(s_n\right)_{ij} \int_0^t d\tau e^{-i\omega_{ij}\tau} C_n(\tau) \tag{4.31}$$

where $\omega_{ij} = (\epsilon_i - \epsilon_j)$ are the dimensionless frequencies of the system given by scaled differences in the eigenvalues, ϵ_i, of $\tilde{H}_S$. The bath correlation function, $C_n(t)$ is given by

$$\begin{aligned}C_n(t) = \frac{1}{\pi} \int_0^\infty d\omega\, J_{n,\mathrm{fast}}(\omega) \left[\coth(\beta\omega/2)\cos(\omega t)\right. \\ \left. - i\sin(\omega t)\,\right].\end{aligned} \tag{4.32}$$

where β is inverse temperature times Boltzmann's constant. Since TCL2 stems from second-order perturbation theory, we expect for it to be accurate when $\eta \ll 1$, where the dimensionless coupling is computed over only the fast modes, $J_{n,\mathrm{fast}}$, with a characteristic frequency given by ω^*. Together, this hybrid formulation, denoted TCL2-FM, due to Montoya-Castillo, Berkelbach and Reichman,[173] offers a potentially computationally efficient and accurate[72, 251] way to study motion through conical intersections under our physically motivated assumptions of scale separation.

4.3 Comparison with exact results

Non-markovian bath limit

To understand the effectiveness of this approach, we first consider the case where the characteristic electronic timescale, λ, is well separated by the characteristic bath frequency, ω_c, such that $\omega_c/\lambda \ll 1$. This is expected to hold when the remaining bath degrees of freedom are described by long wavelength solvent modes, either from slow dipolar or density fluctuations.[73, 241] We explore this regime in the relaxation of the $S_2(\pi\pi^*) - S_1(n\pi^*)$ conical intersection of pyrazine, following a model developed by Kuhl and Domcke.[142, 143] The

Hamiltonian has the form of a linear vibronic model, with an additional ground electronic state. In dimensionless harmonic-oscillator coordinates it is given by,

$$\begin{aligned} H_S &= |0\rangle h_0 \langle 0| + \sum_{i,j=1,2} |i\rangle h_i \delta_{ij} + \lambda q_c (1-\delta_{ij}) \langle j| \\ h_i &= h_g + V_i^{(0)} + \kappa_t^{(i)} q_t \\ h_0 &= \sum_{n=c,t} \frac{\Omega_k}{2} \left(p_k + q_k^2 \right) \end{aligned} \tag{4.33}$$

where $\Omega_{t(c)}$ is the frequency of the tuning (coupling) mode, $\kappa_t^{(i)}$ denotes the Holstein-like coupling of the tuning mode to each electronic state i, h_0 denotes the Hamiltonian of the ground electronic state, and the vertical energy shifts from the ground state are $V_i^{(0)}$'s. There are no other Holstein-like couplings, so the system-bath coupling is given by

$$H_{SB} = (|1\rangle\langle 1| + |2\rangle\langle 2|) \sum_{n=c,t} q_n \sum_k c_{n,k} Q_{n,k}. \tag{4.34}$$

with spectral densities of the Debye form,

$$J_n(\omega) = 2E_{r,n}\omega_{c,n} \frac{\omega}{\omega^2 + \omega_{c,n}^2}, \quad n = c, t, \tag{4.35}$$

which results from an exponentially decaying bath correlation function. The form of system bath coupling induces vibrational relaxation in each of the electronic states. The specific parameters for the system are $\Omega_c = 0.118$, $\Omega_t = 0.074$, $\kappa_t^{(1)} = -0.105$, $\kappa_t^{(2)} = 0.149$, $\lambda = 0.262$, $V_1^{(0)} = 3.94$, and $V_2^{(0)} = 4.84$, all in eV, while the temperature of the bath was taken to be 300 K. The initial condition is generated by vertical excitation from the ground electronic state $|0\rangle$ into the diabatic electronic state $|2\rangle$ by

$$\sigma(0) = |2\rangle|\chi_{02}\rangle\langle\chi_{02}|\langle 2|, \tag{4.36}$$

where $|\chi_{02}\rangle$ denotes the vibrationally-coherent wavepacket obtained from Frank-Condon overlaps between the ground electronic state $|0\rangle$ and electronic state $|2\rangle$. The system was expanded in a direct product basis of 20 harmonic oscillator eigenstates for each mode, making the system size 800 total states. The dynamics were propagated in a truncated basis, which with this initial condition is converged by considering only the lowest 500 energy eigenstates. A sketch of the system is shown in Fig. 4.1(a).

We compare the validity of the dynamics obtained from TCL2 and the hybrid TCL2-FM, to the dynamics obtained from the numerically exact hierarchy equations of motion (HEOM) method by Chen *et al.*[46] These calculations were converged using the same basis with a hierarchy depth of 12. Since the system was at high temperature, no Matsubara terms were included. We first compute the time-dependent diabatic population in electronic state $|2\rangle$,

$$P_2(t) = \mathrm{Tr}\{|2\rangle\langle 2|\sigma(t)\}. \tag{4.37}$$

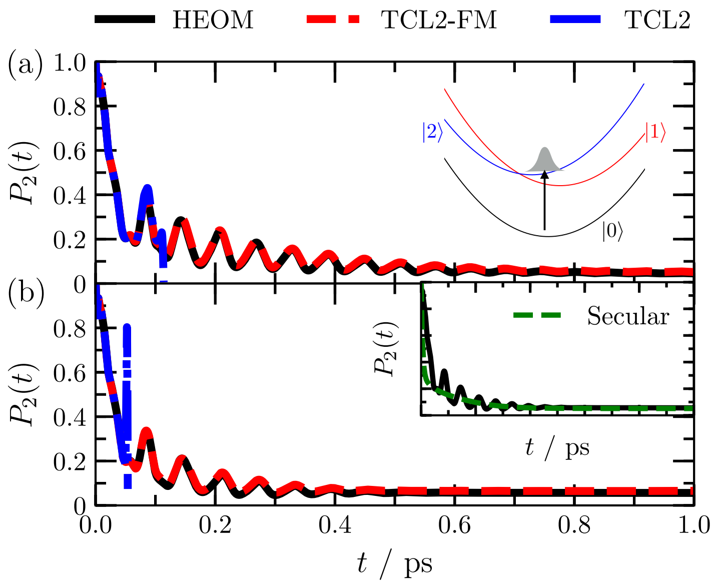

Figure 4.1: Diabatic populations given by Eq. 4.37 for a bath with $\omega_c = 0.0132$ eV with values of the reorganization energy $E_r = 0.006571$ eV (a) and $E_r = 0.01314$ eV (b). Shown in the inset of (a) are the potential energies for each electronic state along the coordinate q_t. In the inset of (b) is shown the results for secular Redfield theory with frozen modes. HEOM data was taken from Ref.

from a trace over all vibronic states. Two different characteristic frequencies of the bath are compared, a fast bath in which both the tuning and coupling modes are $\omega_{c,(c,t)} = 0.0132$ eV and a slower bath in which $\omega_{c,(c,t)} = 0.00397$ eV. Thus, in both cases the bath relaxes on a timescale of at least an order of magnitude slower compared to the Peierls coupling, $\omega/\lambda \ll 1$, and we can choose a large value of ω^* to treat the slow degrees of freedom. Details on the sensitivity of the results to the specific choice of ω^* are reported in Appendix B, but over the range from $\omega^* = [0.0165, 0.0329]$ we obtain nearly indistinguishable population dynamics. For both baths studied, we choose $\omega^* = 0.0219$ eV. Only 50 initial conditions are needed to obtain well-converged populations, which are drawn from a Boltzmann distribution with 1000 modes for each bath using the discretization procedure outlined in Ref.

The populations obtained in the case of the faster bath are compared in Fig. 4.1. Ultrafast relaxation from state $|2\rangle$ into state $|1\rangle$ occurs within 50 fs, as the initial wavepacket proceeds through the conical intersection. This is followed by a prolonged period of coherent wavepacket motion that persists up to 0.5 ps, before decohering. At weaker system-bath couplings than the ones presented here, TCL2 exhibits quantitative accuracy compared to HEOM. At larger system bath coupling strengths, $E_r = 0.006571$ and 0.01314 eV, TCL2 exhibits positivity violations of the density matrix, which for fixed time step leads to insta-

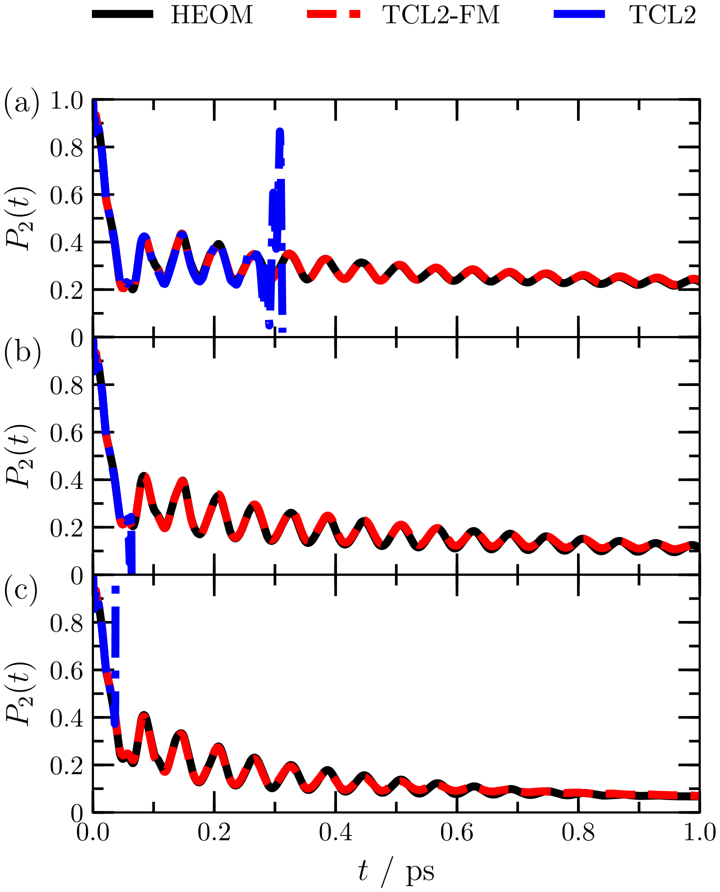

Figure 4.2: Diabatic populations for a bath with $\omega_c = 0.00397$ eV with values of the reorganization energy $E_r = 0.001314$ eV (a), $E_r = 0.006571$ eV (b), and $E_r = 0.01314$ eV (c). HEOM data was taken from Ref.

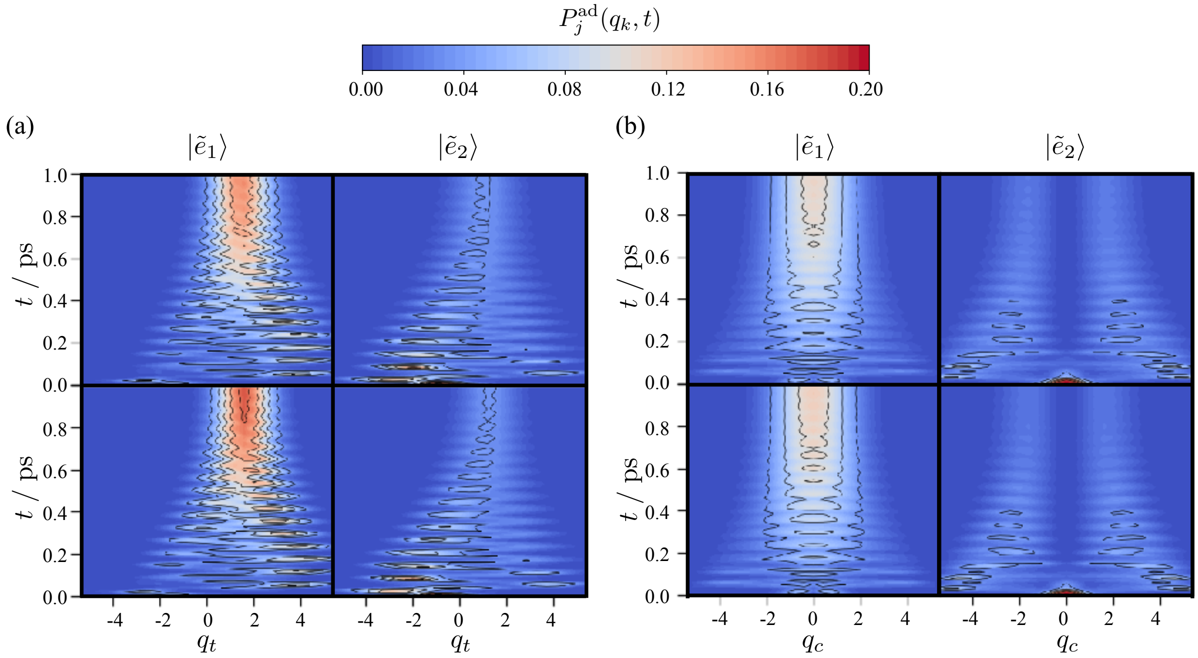

Figure 4.3: Projections onto the adiabatic ground- (left column) and excited-state (right column) surfaces for the dimensionless coordinate q_t (a) and for q_c (b) for the pyrazine system with $\omega_c = 0.0132$ eV and $E_r = 0.006571$. The top row shows results from TCL2 -FM while the bottom row shows results from HEOM from Ref.

bilities in the dynamics. This failure is due to the breakdown of perturbation theory and requires contributions from higher-order correlation functions, as multiphonon processes become important. This is evident by noting that the dimensionless couplings are $\eta = 0.317$ and 0.634, which are not much less the 1 as required by perturbation theory.

The hybrid approach, TCL2-FM, removes all positivity violations from TCL2 and achieves quantitative accuracy at all values of the reorganization energy studied, as compared to HEOM. The stability of the dynamics is a consequence of the frozen modes reducing the dimensionless couplings by nearly an order of magnitude, to $\eta = 0.055$ and 0.086, returning the treatment of the bath into the perturbative regime. The accuracy is a consequence of the small effect of the slow modes on the dynamics, acting only to further decohere vibrational oscillations but not significantly dissipate energy, due to the large separation of timescales between system and bath relaxation.

By invoking both the Markovian approximation, which takes the time integral in Eq. 4.31 to infinity, and the secular approximation, which decouples the dynamics of the populations from coherences in the energy eigenbasis[32], we get an equation of motion that is guaranteed to preserve positivity of the density matrix.[93, 158] These approximations fail to exhibit the extended vibrational coherence and over-estimates the rate of relaxation. Neither effects are improved by the addition of frozen modes. The lack of vibrational dephasing is due to the neglect of coherence-coherence couplings in the relaxation tensor within the secular approximation[143] and the over-estimation of the rate is due to the Markovian approximation. As shown in the inset to Fig. 4.1b), they do, however, obtain the correct long-time of the populations as thermalization with the environment is accurately modeled.

Shown in Fig. 4.2 are the populations for the case of the slower bath, where non-Markovian effects are more pronounced. As expected, TCL2 fails at an even smaller reorganization energy than in the fast bath regime due to the violation of the 2nd-order cumulant approximation. TCL2-FM remedies this failing and recovers quantitative accuracy for all reorganization energies studied. Again the stability is a consequence of reducing the dimensionless coupling by an order of magnitude. In this case the original couplings are $\eta = 0.210$, 1.05 and 2.10, and are reduced to $\eta = 0.021$, 0.106 and 0.213 by freezing the slow modes. As has been noted previously,[173] the inclusion of the slow modes as static disorder effectively incorporates all-order effects from those bath modes, albeit only their influence on the altered eigen-structure of the Hamiltonian. When the timescales of system and bath relaxation are well separated, as is expected to hold generally in systems with conical intersections where electronic relaxation is ultrafast, this frozen mode approximation allows for an accurate low order quantum master equation description of the dynamics.

A rigorous test of the accuracy of frozen modes can be obtained by comparing the projection of the wavepackets in the adiabatic basis obtained from,

$$P_j^{\mathrm{ad}}(q_t, t) = \int dq_c \langle q_c | \langle q_t | \langle \tilde{e}_j | \sigma(t) | \tilde{e}_j \rangle | q_t \rangle | q_c \rangle \tag{4.38}$$

$$P_j^{\mathrm{ad}}(q_c, t) = \int dq_t \langle q_c | \langle q_t | \langle \tilde{e}_j | \sigma(t) | \tilde{e}_j \rangle | q_t \rangle | q_c \rangle \tag{4.39}$$

where $|\tilde{e}_{j=1,2}\rangle$ are the adiabatic electronic wavefunctions given by the diabatic-to-adiabatic transformation[161]

$$|\tilde{e}_j\rangle = \sum_{j'} S(q_c, q_t) |j'\rangle \tag{4.40}$$

where $S(q_c, q_t)$ is the rotation matrix given by

$$S(q_c, q_t) = \begin{pmatrix} \cos\alpha(q_c, q_t) & -\sin\alpha(q_c, q_t) \\ \sin\alpha(q_c, q_t) & \cos\alpha(q_c, q_t) \end{pmatrix} \tag{4.41}$$

and $\alpha(q_c, q_t)$ is the diabatic-to-adiabatic mixing angle. These projections record information about the entire density matrix since it requires unitary transformations acting on both populations and coherences. Figure 4.3 (a) shows the projection of the wavepacket along the tuning mode obtained from TCL2-FM compared to those obtained from HEOM. The results from the TCL2-FM approach are virtually indistinguishable from the HEOM results at all times. This implies that the full density matrix is accurately computed with TCL2-FM. Projections along the coupling mode are shown in Fig. 4.3 (b). Again, TCL2-FM exhibits quantitative accuracy. That the full density matrix is accurately obtained also implies that arbitrary observables, including spectroscopic signals[72] might be reliably computed.

Markovian bath limit

To understand the limits of this approach, we next consider the case where the characteristic electronic timescale, λ, is not separated by the characteristic bath frequency, ω_c, such that $\omega_c/\lambda \sim 1$. This limit is expected when the remaining bath degrees of freedom couple directly to the electronic states through optical solvent modes or to high frequency vibrations. We study this case in a model for the photoisomerization dynamics of retinal rhodopsin, shown in the inset of Fig. 4.4 (a). This model has been studied by Thoss and Wang using the numerically exact multilayer formulation of MCDTH, ML-MCTDH.[255] The model describes the dynamics along a periodic isomerization coordinate, ϕ, which plays the role of the tuning mode, and a harmonic coupling coordinate, q_c.

The system Hamiltonian has the following form,

$$H_S = \sum_{i,j=0,1} |i\rangle (T + V_i)\delta_{ij} + \lambda q_c (1 - \delta_{ij}) \langle j|, \tag{4.42}$$

where T is the total kinetic energy operator,

$$T = \frac{1}{2I} p_\phi + \frac{\Omega_c}{2} p_c^2, \tag{4.43}$$

where I is the moment of inertia for the tuning mode. The potential energies for each electronic state, V_i, are

$$V_i = V_i^{(0)} + (-1)^i \frac{1}{2} W_i (1 - \cos\phi) + \frac{\Omega_c}{2} q_c^2 + \delta_{1i}\kappa_c q_c \tag{4.44}$$

where W_n are the energy amplitudes of the isomerization potential, and $V_i^{(0)}$ are the energy shifts of each diabatic state relative to the energy in the *cis* state. The coupling mode is described by the frequency Ω_c and Holstein coupling κ_c. The specific parameters for this model are $I^{-1} = 1.43 \times 10^{-3}$, $V_0^{(0)} = 0.0$, $V_1^{(0)} = 2.0$, $W_0 = 2.3$, $W_1 = 1.5$, $\Omega_c = 0.19$, $\lambda = 0.19$, and $\kappa_c = 0.095$, all in eV. The system was expanded in a basis of plane waves for the isomerization mode and harmonic oscillator eigen- states for the coupling mode with a basis set size of 301 and 24, respectively. This choice gave a Hilbert space size of 14448 states, but the dynamics were converged using only the lowest 1000 energy eigenstates.

The form of the system-bath coupling is given by

$$H_{SB} = |1\rangle\langle 1| \sum_k c_k Q_k, \tag{4.45}$$

which describes the response of a polar solvent to an instantaneous change in the charge distribution of the molecule. The spectral density used is Ohmic with an exponential cutoff,

$$J(\omega) = \frac{\pi E_r}{\omega_c} \omega e^{-\omega/\omega_c}, \tag{4.46}$$

and the value of this cutoff frequency used was $\omega_c = 0.2$ eV. The temperature was taken to be 0 K. The initial condition was a vertical excitation of the ground vibrational state of electronic state $|0\rangle$ into electronic state $|1\rangle$, given by

$$\sigma(0) = |1\rangle|\chi_{01}\rangle\langle\chi_{01}|\langle 1|, \tag{4.47}$$

where again $|\chi_{01}\rangle$ denotes the vibrationally-coherent wavepacket obtained from Frank-Condon overlaps between the two electronic states.

To test the validity of the TCL2 with frozen mode approach, we simulated the dynamics up to 2 ps and compared to the exact result obtained from ML-MCTDH for a range of reorganization energies, which represented the system degrees of freedom and a discretized bath of ~ 40 modes explicitly. We specifically compute the time-dependent population of the *trans* state,

$$P_{\text{trans}}(t) = \text{Tr}\{\theta(|\phi| - \pi/2)\}, \tag{4.48}$$

where $\theta(x)$ is the Heaviside step function and the trace implies integration over the ϕ and q_c coordinates, following initial excitation. For this model, the electronic timescale inferred from the Peierls coupling, λ is nearly the same as the characteristic frequency of the bath, ω_c, or $\omega_c/\lambda \sim 1$. Since the electronic and bath timescales are not well separated, we expect that while choosing to freeze some modes of the bath will reduce the system-bath coupling and stabilize the perturbation theory description of the fast bath modes, this will come at a cost of incorrectly describing the time-dependent dissipation as modes that are being held frozen should contribute. We first consider the consequences of choosing $\omega^* = \omega_c$, which will reduce the strength of coupling from modes that have frequencies smaller than the position of the peak in the spectral density, while treating the peak and modes with higher frequency with perturbation theory. We discretized the bath using 1000 modes and sampled over the Wigner transform of the Boltzmann distribution. Only five trajectories were averaged over due to the negligible effect of the frozen modes to TCL2 dynamics as discussed below.

Figure 4.4 shows the time dependent population in the *trans* state. At the smallest value of the reorganization energy used, $E_r = 0.0159$ eV, shown in Fig. 4.4(a), the dynamics are characterized by relaxation of the population after 0.1 ps and highly damped decay of vibrational coherences on a similar timescale. For this case, Markovian Redfield theory and TCL2 are nearly indistinguishable. This is a consequence of being well within the weak coupling limit, with $\eta = 0.050$. The dynamics are in quantitative agreement with available numerically exact ML-MCTDH results.[1] Adding frozen modes has no real effect on the dynamics, which might be expected at a small value of system-bath coupling.

At a reorganization energy that is a factor of ten larger, $E_r = 0.159$ eV, Redfield theory exhibits positivity violations that render the dynamics unstable after 1.5 ps. These results are shown in Fig. 4.4(b). These violations are corrected by TCL2, over short times, but at longer times TCL2 also becomes unstable. Using frozen modes stabilizes the dynamics

---

[1] We discovered a typographical error in the parameters from Ref. [255] for the reorganization $E_r = 0.0159$ eV results. One of the authors generously computed the dynamics up to 1 ps for us to compare, which is shown in Fig. 4.4 (a).

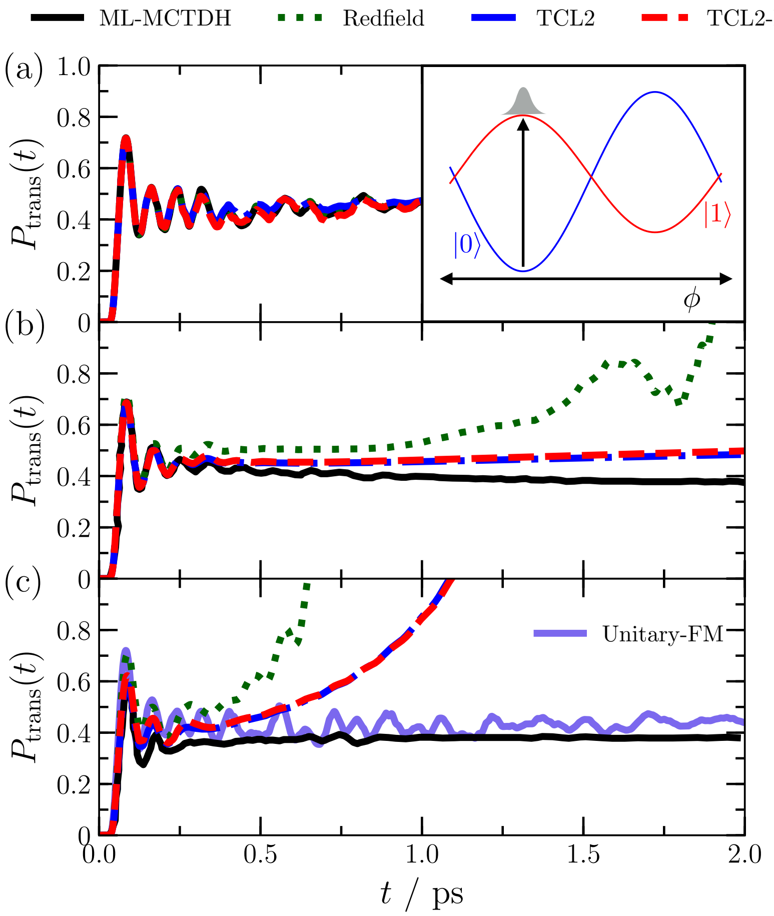

Figure 4.4: Shown are the results for the population in the trans state at different reorganization energies: $E_r = 0.0159$ eV (a), $E_r = 0.159$ eV (b), and $E_r = 0.318$ eV (c). Numerically exact ML-MCTDH results from Ref.are shown in dashed black lines, Redfield theory in green dotted, TCL2 in blue dashed-dotted lines, and TCL2 -FM in dashed red. The inset of (a) shows a figure of the periodic system along the ϕ coordinate. In (c) we also show the results when the entire bath is discretized and frozen (solid purple) giving rise to a purely unitary dynamics for each realization of bath modes. The unitary-FM dynamics were obtained by sampling over 100 trajectories.

at longer times, but has no effect at intermediate times. In all three descriptions the early qualitative features are correct, but the population in the *trans* state is too large for TCL2 and TCL2-FM at 2 ps and it does not decrease at long times as the exact ML-MCTDH results do. Under these conditions, the coupling to the bath is reduced from $\eta = 0.495$ to $\eta = 0.177$ using frozen modes, which are still larger than should be expected to yield

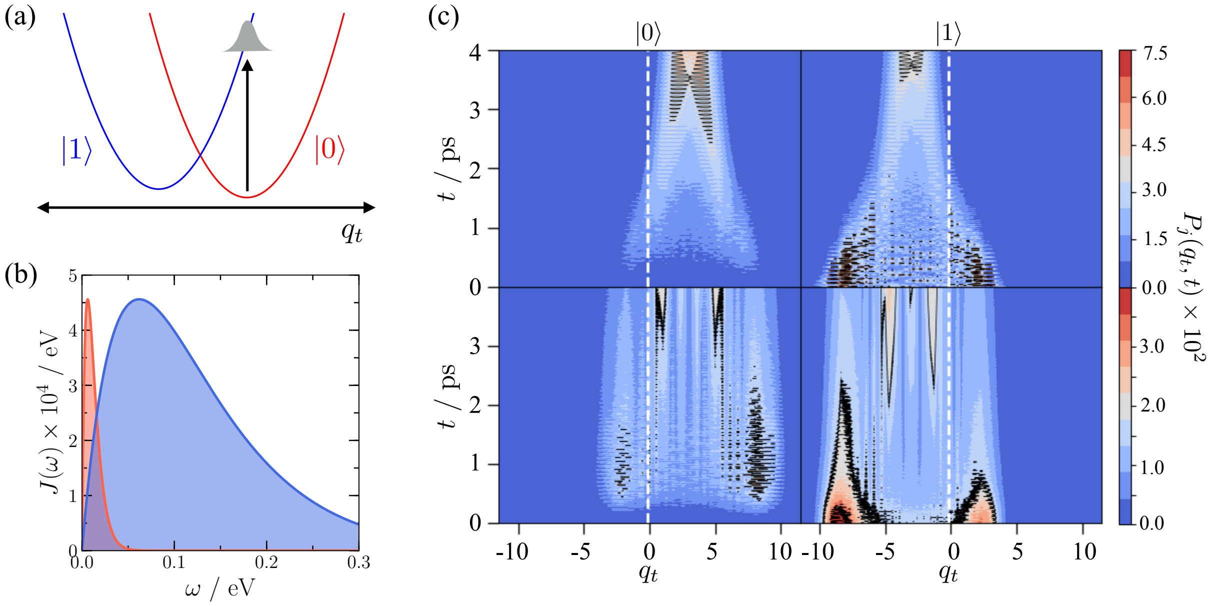

Figure 4.5: Shown in (a) is the harmonic oscillator model with initial condition. The spectral densities used are shown in (b) with $\omega_c = \Omega_t$ in blue and $\omega_c = \Omega_t/10$ in red. Projections onto the diabatic electronic surfaces in the dimensionless coordinate q_t are shown in (c) for $E_{r,t} = 0.2$ with $\omega_c = \Omega_t$ (top) and $\omega_c = \Omega_t/10$ (bottom).

accurate results. Thus, there are expected multi-phonon processes that are missed by the perturbative treatment in TCL2.

At even larger reorganization energies, both TCL2 and TCL2-FM show positivity violations and result in unstable dynamics past 1 ps. These results are shown in Fig. 4.4(c). At this value of the reorganization energy, the couplings to the bath both without and with frozen modes are $\eta = 1.01$ and $\eta = 0.372$ respectively, are too large to self-consistently truncate the cumulant expansion at second order. By taking ω^* to be larger, we can sufficiently reduce the coupling to the remaining bath degrees of freedom that the dynamics are stable, but still dissipative within a TCL2 description. However, the dynamics deviate from the numerically exact result, as the approximation that degrees of freedom with $\omega < \omega^*$ are static, is not valid as $\lambda < \omega^*$, leading to a description of the dynamics that is not consistent. While in the pyrazine model the large separation of time scales allowed a large range of ω^* to be selected without disrupting the subsequent relaxation dynamics, this separation is not present for the rhodopsin model studied.

To formulate a correct description of the system dynamics in the limit of strong system-bath coupling when motion in the system and bath are on similar time scales requires that the reorganization energy be reduced without freezing fast bath modes. This could be done by adding an additional effective bath mode into the description of the system, whose dynamics would be treated exactly. While including additional modes into the system Hamiltonian dramatically increases the Hilbert space, using unravelling techniques that reduce the scaling of master equation propagation[135, 268], adding a few additional modes is possible. This is an active area of research, though beyond the scope of the present study.

4.4 Application to Photoisomerization Quantum Yields

With the limitations of our approach mapped out, we now study the dependence of the photoisomerization quantum yield on the bath. We consider the nonadiabatic relaxation through a conical intersection of a linear vibronic model constructed to have features similar to those in a molecular photoisomerization processes.[96, 110] Specifically, we construct a model where a conical intersection lies above two adjacent basins, one metastable with respect to the other. Our approach enables us to study a wide range of system-bath coupling strengths in the Markovian and non-Markovian regimes and understand the impact of the yield on these parameters. Describing the dynamical features arising in such complex environments are paramount to describing the yields, as they are completely determined by relaxation rates rather than being constrained by thermodynamic considerations.[294]

The Hamiltonian we consider has the form,

$$\begin{aligned} H_S &= \sum_{i,j=0,1} |i\rangle h_i \delta_{ij} + \lambda q_c (1-\delta_{ij}) \langle j| \qquad (4.49) \\ h_i &= \sum_{k=c,t} \frac{\Omega_k}{2}\left(p_k^2 + q_k^2\right) + \kappa_t^{(i)} q_t + V_i^{(0)} \end{aligned}$$

with a system-bath coupling,

$$H_{SB} = (|0\rangle\langle 0| + |1\rangle\langle 1|) \sum_{n=c,t} q_n \sum_k c_{k,n} Q_k, \qquad (4.50)$$

meant to model vibrational relaxation and an Ohmic spectral density with exponential cutoff,

$$J_n(\omega) = \frac{\pi E_{r,n}}{\omega_{c,n}} \omega e^{-\omega/\omega_{c,n}}, \quad n = c, t. \qquad (4.51)$$

for both the coupling and tuning modes. The model described here, shown in Fig. 4.5 (a), is similar to a model studied by Thorwart and co-workers[197, 65]. We set the parameters to be $\Omega_c = 0.112$, $\Omega_t = 0.0620$, $\kappa_t^{(0)} = -0.186$, $\kappa_t^{(1)} = 0.186$, $\lambda = 0.0248$, $V_1^{(0)} = -0.031$, and $V_2^{(0)} = 0.031$ in eV, while the temperature of the bath is taken to be 300 K. The Hamiltonian was expanded in a basis of harmonic oscillator eigenstates with 75 states used for the tuning mode and 5 states for the coupling mode. The dynamics were propagated in the energy eigenbasis with a truncated basis of 400 states, which shows convergence to the full Hilbert space.

We have tuned the system Hamiltonian parameters to include a metastable well in the higher-energy electronic state. The barrier to transferring population along the ground adiabatic state is ~ 0.129 eV, so there will be a separation of timescales between initial relaxation into the minima of the two diabatic states and subsequent barrier crossings. We consider the dynamics following a vertical excitation into state $|1\rangle$ from the ground vibrational state of $|0\rangle$,

$$\sigma(0) = |1\rangle|\chi_{01}\rangle\langle\chi_{01}|\langle 1|. \tag{4.52}$$

and are interested in the quantum yield into state $|1\rangle$ following subsequent relaxation over times long relative to vibrational relaxation, but short relative to relaxation into a thermal state.

We have studied the dynamics of this model with two different environments, one in the Markovian regime where $\omega_c \sim \lambda$, and one in the non-Markovian regime where $\omega_c \ll \lambda$. These two regimes are illustrated by their spectral densities in Fig. 4.5 (b). For both baths, we have studied the dynamics over a range of reorganization energies. The fast bath we study has a cutoff frequency of $\omega_{c,t} = 0.062$ eV for the tuning mode and $\omega_{c,c} = 0.112$ eV for the coupling mode. Since the bath is moderately fast relative to the timescale induced by the electronic coupling and the reorganization energies used are small, the largest has a coupling constant of $\eta < 0.1$, these populations are accurately obtained from TCL2 without the use of frozen modes. The slow bath we study has cutoff frequencies for the tuning mode $\omega_{c,t} = 0.0062$ eV with the coupling mode held fixed. Since this system is in a more non-Markovian regime, the dynamics using TCL2 alone exhibit positivity violations at significantly smaller values of the reorganization energy relative to the fast bath, and we thus use the frozen mode approach. However, we found it necessary to only freeze modes in the bath associated with the tuning mode. For each value of the reorganization energy we used $\omega^* = 0.00868$ eV, decreasing the largest value of the coupling to $\eta = 0.05$. We find that choosing ω^* between 0.008 eV and 0.014 eV results in quantitatively similar population dynamics for all system bath coupling strengths considered. We simulated the dynamics with 50 trajectories, by discretizing the slow bath into 1000 modes for the tuning mode.

Shown in Fig. 4.5(c) are the projections of the wavepacket onto the position basis of the tuning mode for each diabatic state, given by,

$$P_j(q_t, t) = \int dq_c \langle q_c|\langle q_t|\langle j|\sigma(t)|j\rangle|q_t\rangle|q_c\rangle\,, \tag{4.53}$$

for both baths. In the fast bath case, the wavepacket starts in electronic state $|1\rangle$ and coherently oscillates with enough energy to put it back in the Franck-Condon region at short times. The bath dissipates energy from this wavepacket, which reduces the vibrational coherence until the wavepacket can no longer reach the Franck-Condon region. In the slow bath case, the wavepacket dynamics are markedly different, showing an extended lifetime in higher-energy vibrational states. The rate of decoherence appears to be much faster as the oscillations of the wavepacket are damped out almost instantly, which is a reflection of the role of slow bath being a source of inhomogeneous broadening.

These different relaxation mechanisms result in different quantum yields, and strikingly different dependence on the bath reorganization energy. We define the quantum yield as the diabatic population in state $|1\rangle$ in the quasi-steady-state limit,

$$P_1(t_{\mathrm{ss}}) = \mathrm{Tr}\{|1\rangle\langle 1|\sigma(t_{\mathrm{ss}})\}, \tag{4.54}$$

where t_{ss} is the time taken for the diabatic populations to be nearly time invariant, which for the parameters studied is around 4 ps. In the case of the fast bath, we find the yield increases monotonically with the reorganization energy. This is shown in Fig. 4.6, where η is proportional to the reorganization energy with ω_c fixed and we take η and E_r from the total spectral density, not the reduced values from just the fast modes. The increase in the yield with reorganization energy in the fast bath is attributable to the fact that with increasing E_r, the wavepacket spends less time in the Franck-Condon region where population can transfer between the two diabatic states through electronic coupling. As is evident from the wavepacket dynamics, increasing the reorganization energy will increase the rate of vibrational dissipation and hence the localization of the wavepacket into the minima of the diabatic states. In the case of the slow bath, we find the opposite trend. Increasing the reorganization energy results in a decreasing the quantum yield. This decrease is attributable to the increased rate of decoherence and slower rate of dissipation due to the lag in the bath's ability to remove energy from the system.

These results are in contrast to some other observations on related linear vibronic models. Previously, Thorwart and coworkers have found that the lifetime of vibrational coherence could be tuned by the reorganization energy or characteristic frequency of the bath and the persistence of this coherence had large impact on the photoisomerization yield.[62, 65, 197] While we note that the former of these claims is verified by our simulations, we note that the diabatic potentials they studied do not have metastability as the zero point energy in the higher-energy electronic state is on the order of the barrier height for population transfer along the ground adiabatic state. Having a well-defined quantum yield, in which there is a long-lived metastable state, requires a separation of timescales between the initial relaxation and eventual thermalization. If the barrier height is not sufficiently large, as in their previous work,[62, 65, 197] then there will not be a separation of timescales, and thus there will not be a uniquely defined quantum yield. Nevertheless, the complex dependence of the quantum yield on the parameters of the bath that we have found illustrates the rich chemical dynamics of conical intersection models that can be interrogated efficiently.

4.5 Conclusion

In this chapter, we have developed a strategy for simulating nonadiabatic relaxation through conical intersections in the condensed phase. The framework leverages the separation of

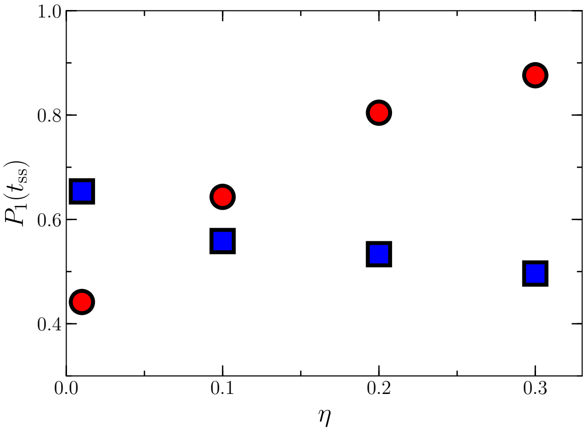

Figure 4.6: Yields of $P_1(t)$ taken in the quasi-steady-state limit for $\omega_{c,t} = \Omega_c/10$ (blue squares) and $\omega_{c,t} = \Omega_t$ (red circles), as a function of the coupling strength, η computed from the total spectral density.

timescales between the ultrafast dynamics of a few strongly coupled nuclear degrees of freedom, and the remaining weakly coupled degrees of freedom. In cases where the characteristic timescales of these two motions are well separated, when the nonadiabatic coupling is much larger than the characteristic frequency of the bath, we can consider the slowest of those modes frozen and treat the remaining with perturbation theory. Freezing the slowest modes produces a source of static disorder, and acts to decohere the resultant dynamics. Weak coupling perturbation theory, in the form of TCL2, correctly describes the time dependent dissipation to the environment and without the low frequency modes has a large domain of applicability. This is consistent with what has been previously observed in the context of the spin boson model.[173]

When applicable, the strategy we have presented represents a computationally efficient framework for simulating dynamics in condensed phase environments. This efficiency is due to the optimal representation of subsets of degrees of freedom. The hybrid method used in this chapter formally scales as $\mathcal{O}(tN_{\text{traj}}N_{\text{bath}}N^3)$ where N_{traj} is the number of trajectories used that can be trivially parallelized, N_{bath} is the number of baths and N is the number of states in the system, and is linear in time, t.[194] Wavefunction based methods like ML-MCTDH suffer from an exponential scaling in the size of the system that must be represented, albeit with a reduced scaling than naive direct product wavefunctions. This scaling arises in condensed phase models through the representation of explicit bath degrees of freedom, which causes super-linear scaling in the number of baths and causes exponential scaling in time due to the difficulty in avoiding Poincare recurrences. While exact quantum master equations, like HEOM, do not suffer from exponential scaling in time, they offer little benefit to the overall scaling as they scale factorially in in the number of auxiliary degrees of freedom that must be represented. This scaling causes significant memory requirements and also has super-linear scaling in the number of baths. This makes low temperature, and non-Markovian systems particularly difficult to study. As this approach extends the limitations of weak-coupling theories, it can be combined with importance sampling tools developed at weak-coupling to study reaction mechisms.[222] In molecular systems, when the number of degrees of freedom as well as anharmonicities in the system increases, we thus expect the hybrid approach of this chapter to be useful in providing numerically accurate results.

Chapter 5

Azobenzene Photoisomerization

"Mordor. The one place in Middle-earth we don't want to see any closer, and the one place we're trying to get to."

— Samwise Gamgee [259]

5.1 Introduction

The study of *trans*-to-*cis* azobenzene photoisomerization has long been fraught with debate over its complex gas-phase reaction mechanism. Experimental observations have shown that excitations at different wavelengths exhibit different quantum yields in violation of Kasha's rule—excitation with UV light to the $S2$ state has a nearly factor of two smaller yield than excitation with blue light to the $S1$ state,[16] however, the origin of this discrepancy was not widely understood.[76, 77, 78, 198, 203, 202, 218, 219, 226] Understanding the reaction mechanism was seen as key to understanding origin of this violation. The gas-phase reaction mechanism has, however, been elucidated through the use of advanced numerical techniques and time-resolved spectroscopy within the past few years.[180, 292] In particular, it has been shown that isomerization after both $S1$ and $S2$ excitation occurs through an "inversion-assisted" rotation rather than pure inversion or rotation, but that an additional relaxation pathway to the *trans* state is open to the $S2$ state only due to its additional excitation energy. In building off of this recent understanding, we aim to uncover the minimal ingredients that describe the photoisomerization process through a the development of a descriptive model.

While the gas-phase dynamics are becoming clearer, the generic understanding of azobenzene photoisomerization in condensed phases is still a mystery in which the photoisomerization yield obtains a strong dependence on the details of the environment in addition to the excitation wavelength. The solvent polarity induces an apparent linear increase in the quantum yield for $S1$ excitation, but has no effect on excitation to the $S2$ state.[174] The solvent viscosity, however, has little to no effect on the yield in either case, which is in strong contrast to stillbene photoisomerization, which is entirely rotational.[83, 240] Experiments performed on an extreme case of confinement in which rotation is almost entirely restricted showed this same behavior for stillbene, but the yield for azobenzene remarkably increased.[186] In this case of confinement, it was argued that the inversion pathway available to azobenzene became favored, which highlights the need to understand the favorability of reaction mechanisms in the condensed phase. The generic understanding behind these phenomena is, however, lacking and an understanding of the mechanistic changes in condensed phases is needed.

Furthermore, condensed phase environments are the home to applications of azobenzene photoisomerization. Azobenzene derivatives have been demonstrated as useful optical switches that can be used for optical storage,[112] solar thermal fuels for energy storage,[99, 136, 155] and can drive peptide and protein folding.[29, 205, 242] In each of these contexts, the photoisomerization is embedded in some condensed phase framework or is used to perform work on its broader environment and its dynamics will thus be influenced by the interactions with these surroundings and understanding these influences can aid in advancements of such technologies.

It is in describing these condensed phase phenomena of azobenzene photoisomerization that a minimal model will shine. Understanding the quantum dynamics of condensed phases are particularly challenging due to the computational workload—despite recent successes [156]—as well as the difficulty with understanding reaction coordinates in an expanded coordinate space. Having a minimal model in which the effects from the condensed phase can be incorporated we suspect will make great stride in understanding the general physics associated with azobenzene photoisomerization in these systems and applications.

In this chapter, we apply a recently developed hybrid quantum master equation framework[221] to develop a minimal model of azobenzene photoisomerization. The utility of this framework is in its significant reduction of the relevant degrees-of-freedom through systematic comparison of the relevant system energy scales as well as its straightforward extension to condensed phase environments through quantum master equations approaches. The chapter is organized in five remaining sections. In Section 5.2, we outline the hybrid framework as it applies to azobenzene photoisomerization. In Section 5.3 we discuss the computational approaches we use to develop the model and the model itself is introduced in Section 5.4. Photoisomerization dynamics simulations using the model are discuessed in Section 5.5. Some concluding remarks are offered in Section 5.6

5.2 Hybrid Framework for Azobenzene Hamiltonian

We herin apply the hybrid framework of Chapter 4 to azobenzene photoisomerization in the gas phase. To this end we use the Hamiltonian, H, in the diabatic picture as our starting point

$$H = \sum_{ij} |i\rangle \left[T\delta_{ij} + V(\mathbf{\Theta}_S, \{q_k\})\right] \langle j|, \tag{5.1}$$

where the set $\{|i\rangle\}$ are the diabatic electronic states, T is the kinetic energy, which is diagonal with respect to the electronic states in this picture, and V is the potential energy, which we take to be a function of the nuclear degrees-of-freedom. We distinguish the nuclear degrees-of-freedom as a set of system coordinates, $\mathbf{\Theta}_S$ and a set of bath modes, q_k. The system coordinates are internal coordinates of the molecule that strongly couple to the electronic states and/or undergo large amplitude motion in the chemical process in which we are describing. The external coordinates are the set of remaining internal coordinates that have been orthogonalized with respect to one another, but not with respect to the system coordinates, and undergo small amplitude motion. The potential can be written as an expansion about some reference geometry, which we take to be the zero of our potential,

$$\begin{aligned} V(\mathbf{\Theta}_S, \{q_k\}) &= \sum_{n=1}^{\infty} \frac{1}{n!} \nabla_S^n V(\mathbf{\Theta}_S, \{q_k\}) \delta\mathbf{\Theta}_S^n + \sum_k \frac{1}{2} m_k \omega_k^2 q_k \\ &+ \sum_k q_k \frac{\partial}{\partial q_k} \left(V(\mathbf{\Theta}_S, \{q_k\}) + \sum_{n=1}^{\infty} \frac{1}{n!} \nabla_S^n V(\mathbf{\Theta}_S, \{q_k\}) \delta\mathbf{\Theta}_S^n \right), \end{aligned} \tag{5.2}$$

where we have identified the frequencies, ω_k^2, as the values of the diagonal part of the Hessian with respect to the bath modes. Here we have explicitly truncated the expansion in the bath modes to first order, but have left all orders of the expansion for the system coordinates due to strong coupling.

The first term in Eq. 5.2, which includes all ordered derivatives of the potential with respect to the system coordinates, can be considered as the potential of system modes and can take on a complicated functional form, $V_S(\mathbf{\Theta}_S)$. This identification then makes clear the separation in the third term as a sum of the electron-nuclear coupling of the bath modes,

$$V_{eB}(\{q_k\}) = \sum_k q_k \frac{\partial}{\partial q_k} V(\mathbf{\Theta}_S, \{q_k\}), \tag{5.3}$$

which is evaluated at the reference geometry, and the mode-mode coupling between the system coordinates and the bath modes,

$$V_{SB}(\mathbf{\Theta}_S, \{q_k\}) = \sum_k q_k \frac{\partial}{\partial q_k} V_S(\mathbf{\Theta}_S), \tag{5.4}$$

which is evaluated across the entire system coordinate space. The former of these terms is directly related to the spectral density taken from linear absorption measurements via the Huang-Rhys factor, that is, defining the value of the derivative as

$$c_k = \frac{\partial}{\partial q_k} V(\mathbf{\Theta}_S, \{q_k\}), \tag{5.5}$$

the spectral density can be expressed as

$$J(\omega) = \frac{\pi}{2} \sum_k \frac{c_k^2}{m_k \omega_k} \delta(\omega - \omega_k), \tag{5.6}$$

and the Huang-Rhys factors are

$$S_k = \frac{c_k^2 m_k \omega_k}{2\hbar}. \tag{5.7}$$

The system-bath mode couplings, which are related to the gradients of the system potential in Eq. 5.2 evaluated at each point in the system coordinate space, can then be taken as some nonlinear function in the system coordinates linear coupled to the bath coordinates, that is,

$$V_{SB}(\mathbf{\Theta}_S, \{q_k\}) = \sum_k q_k g_k(\mathbf{\Theta}_S), \tag{5.8}$$

where

$$g_k(\mathbf{\Theta}_S) = \frac{\partial}{\partial q_k} V_S(\mathbf{\Theta}_S). \tag{5.9}$$

The cutoff for partitioning the system coordinates and the bath coordinates is then made by comparing the relative magnitude of these gradient terms and their associated timescales (see the discussion in Chapter 4).

The dependence of these potential terms on the electronic states, enters in as an inner product, *e.g.*,

$$V_S^{(ij)}(\mathbf{\Theta}_S) \equiv \langle i | V_S(\mathbf{\Theta}_S) | j \rangle, \tag{5.10}$$

is the potential of the system coordinates for diabatic states $|i\rangle$ and $|j\rangle$. Terms with gradients are then related, via a spatially-dependent unitary transformation, to the derivative couplings and energy gradients of the adiabatic electronic states, which are readily available in standard quantum chemistry packages. These gradients (and Hessians) are typically given in Cartesian coordinates, which are transformed to internal coordinate gradients through a procedure described in Appendix C.

5.3 Electronic Structure of Azobenzene

In this section we describe all aspects of the electronic structure calculations performed in developing the reduced model. These calculations include the optimization of various critical point geometries, benchmark comparisons of more computationally efficient approaches to high-level multireference methods, and the specific calculations that were performed to evaluate the potential energy surface and additional couplings. Unless otherwise specified we have utilized the spin-flip time-dependent density functional theory (SF-TDDFT)[231] method, which has been shown to provide quantitatively accurate results,[51, 100, 171, 283] to compute the energies and nonadiabatic couplings used in the development of a diabatic potential for the three lowest singlet states, $S0$, $S1$, and $S2$. All SF-TDDFT calculations were performed using the BHHLYP functional with a 6-31G** basis as implemented in the Q-Chem software.[232]

Benchmarking of Approximate Methods

To accurately describe the electronic structure of azobenzene it has been widely found that methods that incorporate much static and dynamical correlation are required.[4, 39, 40, 80, 114, 291, 292] This requirement necessitates calculations using active space methods, such as the Complete Active Space Self-Consistent Field (CASSCF) method,[212] with exceedingly large active spaces and incorporation of dynamic correlation through perturbation theory such as CASPT2[8] with various flavors of including multiple states such as state averaging (SA)[278] or extended multistate methods (XMS).[94, 237] Such calculations have historically been restricted to a small number of critical point geometries or one-dimensional studies along judiciously chosen reaction coordinates and even then calculation of nonadiabatic coupling vectors are prohibitively expensive. Subsequent approximations to CASSCF that restrict the configurations in the active space used in the SCF cycles to reduce the overall computational cost, such as RASSCF and RASPT2 and multistate extensions, have been shown to quantitatively represent the multidimensional potential energy surface.[4] Analytical nonadiabatic couplings are, however, not generically available, which prohibits the generation of a diabatic model as the energies *and* nonadiabatic couplings are required at all geometries. Recent work has shown that approximate methods based on the linear response formalism of time-dependent density functional theory (TDDFT) with initial wavefunctions that differ from the signlet ground state, namely the hole-hole Tamm-Dancoff approximated DFT (hh-TDA) and SF-TDDFT, can accurately describe the electronic structure of azobenzene throughout the photoisomerization process as based on on-the-fly dynamics simulations,[291, 292, 293] which motivates their use in this study.

To assess the accuracy of SF-TDDFT for the development of a diabatic model we have performed a number of benchmark calculations. These first included optimizing the configuration of a variety of important critical point geometries and computing the lowest three adiabatic energies. The optimized geometries, depicted in Fig. 5.1, and energies are listed in Table 5.1. The ground state minima and the two $S0/S1$ conical intersections are optimized without constraint while the $S1$ and $S2$ minima are optimized with the CNNC dihedral angle constrained to 180°. The geometries and energies found are in largely excellent agreement with previous calculations as well as experiment.[292] Critical points of the $S2$ state are difficult to generically optimize as SF-TDDFT suffers from spin contamination in the Franck-Condon regions of *trans* and *cis* azobenzene, which is resolved in the twisted region (50°-130°). We later show that this spin contamination, while likely important in the describing the precise details of the electronic structure has a negligible effect on the coarse-grained dynamical observables with which we are concerned.

As a more direct comparison to higher-level methods we have compared electronic structure calculations of the $S0$, $S1$, and $S2$ states at geometries along one-dimensional coordinates. In Fig. 5.2 a, we compare SF-TDDFT calculations at the geometries along a relaxed scan of the CNNC dihedral developed in Ref. [39] with the resulting energies from hh-TDA.[291, 292] As can be seen SF-TDDFT gives a quantitatively accurate description of the vertical excitation energies as well as the shape of the potential energy surfaces across a

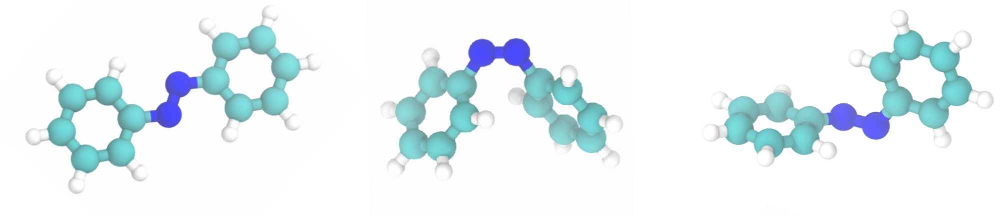

trans minimum *cis* minimum S0/S1 twisted conical intersection

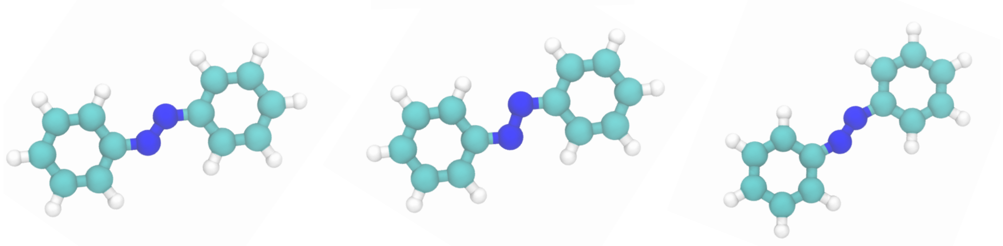

S1 *trans* minimum S2 *trans* minimum S0/S1 planar conical intersection

Figure 5.1: Optimized geometries used for benchmark comparisons. Geometries were optimized at the SFTDDFT level of theory with BHHLYP functional in a 6-31G** basis.

Critical Point	θ (deg)	φ_1	φ_2	r_{NN} (Å)	E_{S0} (eV)	E_{S1}	E_{S2}
trans minimum	180	115	115	1.24	0.00	3.04	3.92
cis minimum	7	124	124	1.23	0.69	3.53	3.93
$S1$ *trans* minimum	180	129	129	1.24	0.72	2.49	4.39
$S2$ *trans* minimum	180	113	113	1.31	0.40	2.49	3.92
$S0/S1$ twisted conical intersection	92	119	138	1.25	2.34	2.34	3.49
$S0/S1$ planar conical intersection	179	151	151	1.20	3.14	3.14	4.32

Table 5.1: Relevant internal coordinates and energies of critical points optimized and computed at SF-TDDFT level of theory as described in the text.

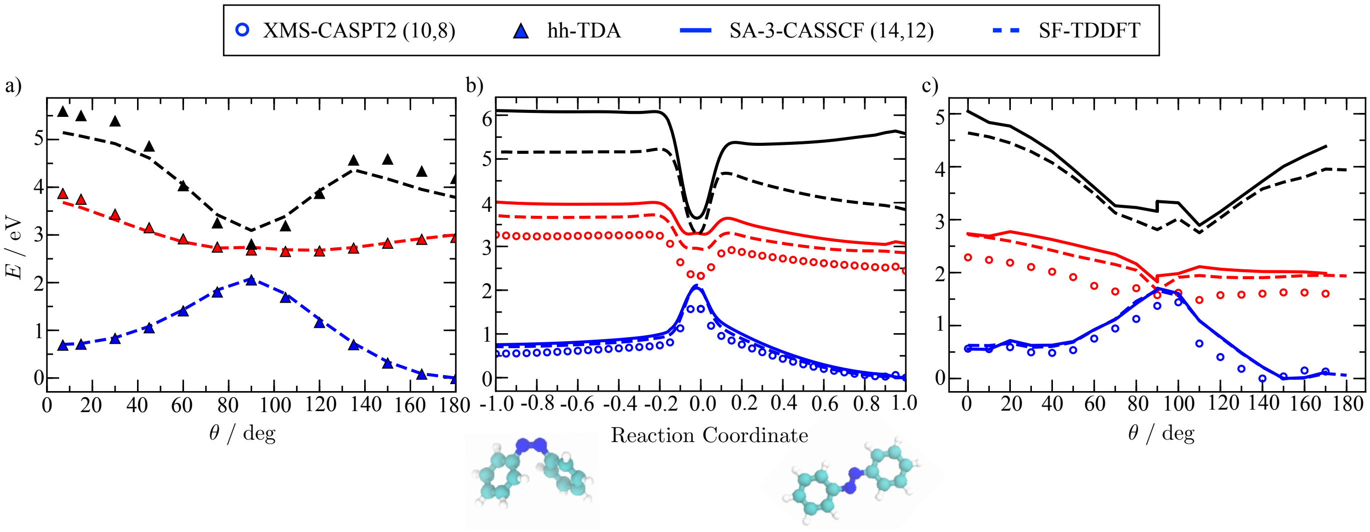

Figure 5.2: Comparison of adiabatic energies from various electronic structure methods. Energies computed along ground state reaction pathways are shown in a) and b) and an excited pathway is shown in c). The reaction coordinate in b) starts in the *cis* configureation (left, -1) and goes to the *trans* configuration (right, 1).

variety of geometries. We have also generated a one-dimensional reaction pathway in both the ground singlet state and first singlet excited state for comparison of SF-TDDFT with SA-CASSCF, and XMS-CASPT2. We note that these reaction pathways are not used to infer the importance of particular degrees-of-freedom in the photoisomerization process, but due to the procedures through which they are generated they represent typical configurations that are visited by a wavepacket in ground- and excited-state simulations and thus represent an appropriate test set for benchmarking the approximate methods used here.

The ground-state reaction pathway was generated using CASSCF with an active space consisting of 6 electrons and 6 orbitals. An initial transition state optimization was performed with a seed geometry near the $\theta = 90°$. Once the transition state geometry intermediate between the *trans* and *cis* ground state minimua was reached the reaction path was constructed by perturbing the transition state geometry along the positive and negative direction of the negative frequency mode and then gradients were followed down to the ground-state minima with geometries generated along the path from the small changes along the gradients. The energies were then computed with SA-CASSCF with equal weighting on the lowest three singlet states with a (14e,12o) active space, XMS-CASPT2 with a (10e,8o) active space for only the $S0$ and $S1$ states, and SF-TDDFT. The multiconfigurational wavefunctional calculations were performed using the MOLPRO[277, 279] and BAGEL software.[236] Since this calculation does not account for changes to the potential in the excited state the pathway is mostly rotational, with some small changes in the geometries along other degrees-of-freedom.

The resulting energies along the ground state pathway are shown in Fig. 5.2 b. SF-TDDFT exhibits qualitative accuracy for the $S0$ and $S1$ states compared to the multiconfigurational methods and is nearly quantitatively accurate (< 1 mHa) for the ground state at all geometries. Clearly dynamical correlation serves to lower the energy of the $S1$ state and somewhat change the shape at geometries near $\theta = 90^\circ$, which is flatter in the SA-CASSCF and SF-TDDFT calculations. Interestingly, SF-TDDFT and CASSCF qualitatively deviate in the $S2$ energies in the *trans* configuration—SF-TDDFT shows an increase in energy along the rotational path from *trans* to *cis*, but SA-CASSCF shows a decrease. We suspect that the SF-TDDFT calculations are more trustworthy—due to the agreement in Fig. 5.2a—in this region due to the potential inclusion of, albeit not systematic, dynamic correlation in the choice of functional.

The excited-state reaction pathway was generated by choosing, from the set of configurations calculated through constrained geometry optimizations as outlined in the next section, the lowest $S1$ energy configuration at a particular value of the CNNC dihedral angle, θ, and the optimized conical intersection geometry. This pathway thus constitutes a representative set of configurations that are visited along the minimum energy pathway upon excitation to the $S1$ excited state, but is not a smooth pathway, which is the origin of the jagged potentials. The resulting energies are shown in Figure 5.2c. Despite the significant deviation from the symmetrically constrained reaction pathway, SF-TDDFT still retains quantitative accuracy in all three electronic states computed here.

Generation of the Potential Energy Surface

To generate the diabatic potential energy surface used in the simulations we first computed the adiabatic energies of and nonadiabatic couplings between the $S0$, $S1$, and $S2$ states at enumerated values of the internal coordinates, which are taken to be the CNNC dihedral angle, θ, and the two CNN bending angles, φ_1 and φ_2, for which the latter two are represented by their symmetric, $\overline{\varphi} = \frac{1}{2}(\varphi_1 + \varphi_2)$, and antisymmetric, $\hat{\varphi} = \frac{1}{2}(\varphi_1 - \varphi_2)$, components. The geometries at the *trans* and *cis* minima exhibit stark differences in the CCNN dihedral angles owing to the degree of steric hindrance between the benzene rings at their respective θ configurations. Rather than fixing all other degrees-of-freedom and smoothly transforming between each value of the internal coordinates, we relax the geometries by performing a series of ground state geometry optimizations constrained at particular values of θ, $\overline{\varphi}$, and $\hat{\varphi}$. This procedure, while not strictly guaranteeing a smooth surface, avoids artificial barriers and potentially large discontinuities from the use of different starting geometries.

The constrained geometry optimizations were performed using ground state DFT with the B3LYP[243] functional and a 6-31G** basis. A one-dimensional path along the dihedral angle from 180° to 0° in 5° increments was found through this procedure. From these geometries further constrained geometry optimizations were performed along $\overline{\varphi}$ with fixed θ and $\hat{\varphi}$ fixed at 0° from 105° to 175° in 5° increments. Finally these symmetric geometries were then used to scan $\hat{\varphi}$ from 0° to a maximum $\hat{\varphi}$ such that $\overline{\varphi} + \hat{\varphi} \leq 175$ with increments of 2.5°. This grid extends over the relevant physical space that is seen by a wavepacket from previous

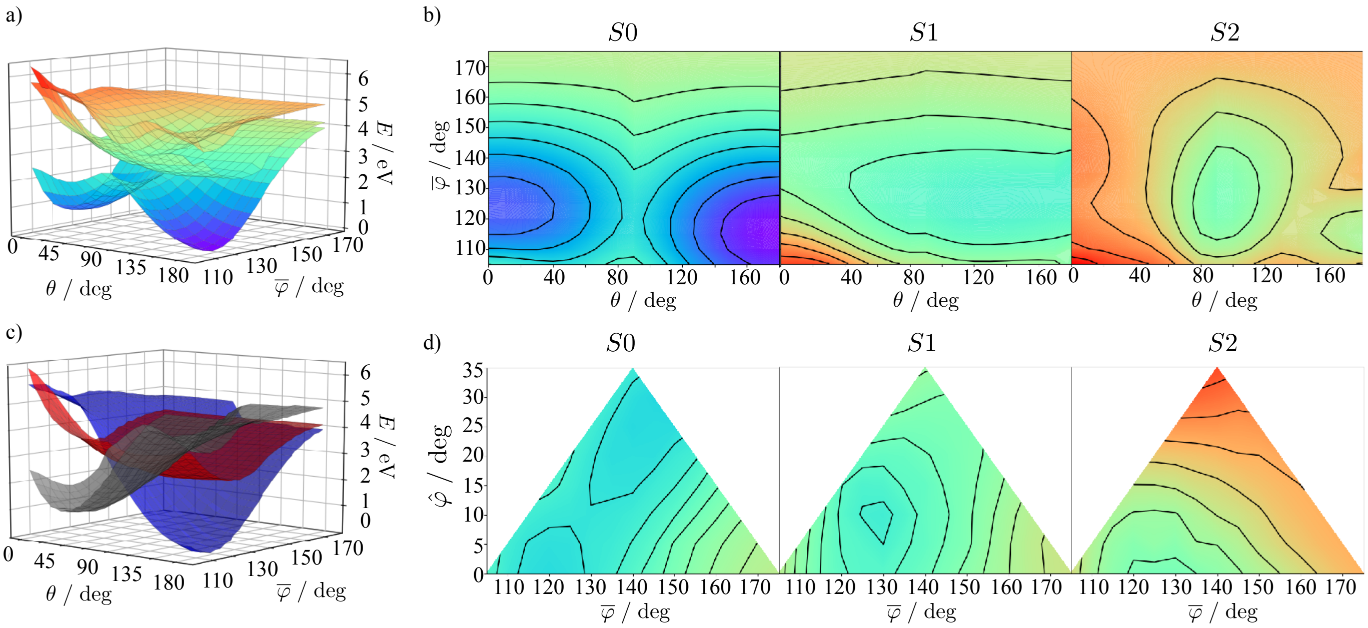

Figure 5.3: *Ab initio* potential energy surfaces in the adiabatic picture—a), b), and d)—and diabatic picture, c), from propagation diabatization. Potential energy surfaces on the symmetric ($\hat{\varphi} = 0°$) surface are shown in a)-c) and the antisymmetric surface at $\theta = 90°$ is shown in d).

numerical simulations. Due to the choice of electronic structure method, there are select geometries with which the constrained geometry optimizations fail to converge, however the number of geometries for which this failure is present is small relative to the density of the grid. At each of the optimized geometries SF-TDDFT calculations are performed. The $S0$, $S1$, and $S2$ states are taken to be the lowest three singlet states with a total spin cutoff of $\langle S^2 \rangle < 1.2$. This generally picks out three singlet states with $\langle S^2 \rangle < 0.4$, but as previously mentioned takes a $S2$ state that contains some degree of spin contamination, which appears only in the Franck-Condon regions at the *trans* and *cis* ground state minima.

A depiction of the adiabatic potential energy surface along the symmetrically constrained ($\hat{\varphi} = 0°$) is shown in Fig. 5.3 a and b. The $S0$ surface is characterized by two deep potential wells in the *trans* and *cis* configurations that are separated by a barrier (relative to the *trans* minimum) of $\sim$2 eV, which is in agreement with previous calculations. The $S1$ state has a diffuse landscape along the *trans* to *cis* rotational pathway, but has a much steeper force along the *cis* to *trans* rotational pathway, which is likely the origin of the substantially reduced excited-state lifetime in the *cis* to *trans* photoisomerization process.[218, 219, 247] Along the symmetric bending coordinate in the *trans* configuration, the $S1$ and $S0$ states come quite close in energy, but never quite form a conical intersection on the symmetric bending surface from these geometries. In the $S2$ state there are two relative minima, one near the twisted conical intersection at $\theta = 90°$ and one in the Franck-Condon region of the *trans* configuration. The latter of these is encapsulated by a ~ 1 eV barrier that restricts rotation. Instead the local minimum is somewhat constricted along $\overline{\varphi}$, which brings the $S1$ and $S2$ states near in energy and forms a supposed conical intersection,[180, 292] the details of which are not perfectly characterized by SF-TDDFT due to spin contamination.

The role of the antisymmetric bending coordinate is then to couple the $S0$ and $S1$ states, which have different symmetry. The adiabatic potential energy surface along $\overline{\varphi}$ and $\hat{\varphi}$ at a fixed value of $\theta = 90°$ is shown in Fig. 5.3 d. While the $S2$ state remains somewhat higher in energy, the $S0$ and $S1$ states meet forming a conical intersection. Specifically, at the conical intersection the $S0$ state exhibits an unstable critical point with a corresponding stable critical point in $S1$ that are extremely close in energy, which become degenerate (within numerical convergence) due to small perturbations to the conical intersection geometry shown in Fig. 5.1.

As was previously noted, along $\overline{\varphi}$ in the *trans* configuration the $S0$ and $S1$ energies do trend closer together, but do not quite meet to form a conical intersection. The role of such a conical intersection—or conical seam as was found in Ref. [4]—has been recently elucidated as a major source of the observed Kasha's rule violation in azobenzene photoisomerization.[180, 292] As was shown in Ref. [292], geometry optimization with respect to the $S1$ state is important for capturing this feature in the potential energy surface. We have thus performed additional constrained geometry optimization calculations of the $S1$ state at $\theta = 180°$ and $\hat{\varphi} = 0°$ along $\overline{\varphi}$ using SF-TDDFT. A more detailed discussion of the results is, however, saved for a later section.

With this database, in which we also include the critical points mentioned above, of energies and nonadiabatic couplings on a fixed grid of the system internal coordinates we constructed the diabatic states. For this construction we utilized the propagation diabatization method,[208] which is a generic method that can transform the adiabatic states to diabatic states with the minimal information from which we have obtained. We used the *cis* ground state minimum geometry as our starting geometry, which we found much more closely preserves the symmetry between the adiabatic states. This symmetry connects only the $S0$ and $S2$ states along the symmetric surface ($\hat{\varphi} = 0$) and thus gives a diabatic state which largely mimics the $S1$ adiabatic state and two diabatic states that interpolate between the $S0$ and $S2$ states along a one-dimensional cut of θ.

Coupling to Additional Degrees-of-Freedom

Additional terms beyond the system coordinates chosen may be potentially needed in the Hamiltonian to observe the correct quantitative trend in the *trans*-to-*cis* quantum yield. While not used in the present set of calculations, we show how additional degrees-of-freedom may be included as explicit modes in the Hamiltonian or through a system-bath interaction with a high-frequency environment.

The coupling term used in the Hamiltonian requires a costly evaluation of a gradient of a Hessian, which necessitates the use of analytical Hessians to avoid overhead. These

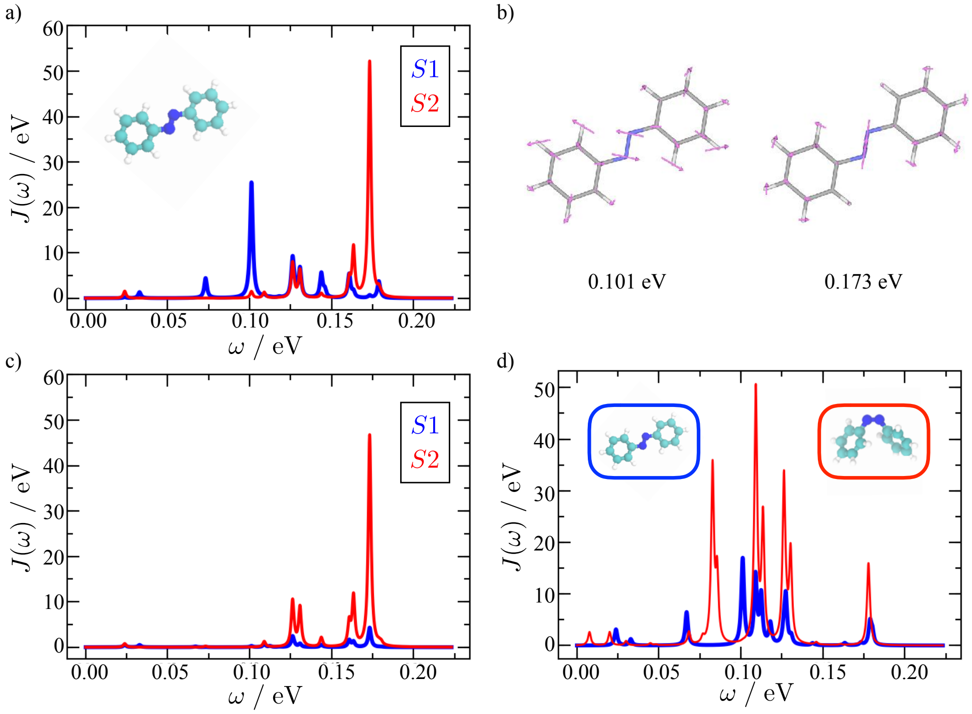

Figure 5.4: Spectral density calculations from TDDFT with ωB97X-D. Full electronic spectral density is shown in a). Normal modes for the main peaks are shown in b) for the $S1$ (left) and $S2$ (right) states. Projected electronic spectral density is given in c). Vibrational spectral density is shown in d) for the *trans* (blue) and *cis* (red) configurations.

are unavailable with SF-TDDFT so we utilize DFT with the ω-B97X-D functional[42] with a 6-31G** basis. This method is known to give reasonable values for excitation energies and vibrational frequencies and thus gives a healthy balance between cost and accuracy in computing these gradients. Nevertheless we have computed the electronic spectral density for the $S1$ and $S2$ states at the *trans* minimum geometry to compare with experimental and literature values for the frequencies and energy gradients. We first performed a ground vibrational frequency calculation from which we can extract the normal modes and then computed the energy gradient in the $S1$ and $S2$ excited states. This cartesian gradient was then projected onto the normal modes (see Appendix C) to give energy gradients along the normal modes. This quantity can be related to the spectral density by

$$J(\omega) = \frac{\pi}{2} \sum_k \frac{c_k^2}{m_k \omega_k} \delta(\omega - \omega_k), \tag{5.11}$$

where $J(\omega)$ is the spectral density, m_k and ω_k are the reduced mass and frequency of the kth normal mode, and c_k is the energy gradient with respect to the normal mode. In practice we broaden the spectral density using a Lorentzian broadening

$$J(\omega) = \frac{1}{2\gamma} \sum_k \frac{c_k^2}{m_k \omega_k} \frac{1}{(\omega - \omega_k)^2 + \gamma^2} \tag{5.12}$$

with a broadening factor of $\gamma = 0.001$ eV. The broadened spectral densities are shown in Fig. 5.4 a and the normal modes of the dominant peaks for the $S1$ and $S2$ states are shown in Fig. 5.4 b. These peaks and the associated modes are consistent with both experiment and other literature quantities[180] suggesting that the method chosen for this procedure will give accurate results. In this calculation, we have scaled the frequencies by a factor such that the dominant peak in the $S2$ spectral density, associated with a NN stretch mode is equal to a previously found value of 1397 cm^{-1}.[67, 78, 180] To avoid overcounting energy gradients of the incorporated system coordinates, we projected out the components of the normal mode gradients along the cartesian vector of the system coordinates (see Appendix C), which are shown in Fig. 5.4 c. The dramatic change in the $S1$ spectral density suggests that the reorganization energy in $S1$ is predominantly accounted for by the chosen system coordinates—specifically $\overline{\varphi}$—while the dominant peak in the $S2$ spectral density is unaccounted and could be included to improve the overall model.

The complete calculation to incorporate the additional couplings between the system coordinates and the bath modes is performed by taking a numerical gradient of the ground state Hessian with respect to the normal modes. The numerical gradient is taken by use of a central difference, that is, the reference geometry is displaced half forward and half backward along the mass- and frequency-weighted normal mode at which the analytical Hessian is computed. This finite difference gradient Hessian is then projected onto the internal coordinates θ, $\overline{\varphi}$, and $\hat{\varphi}$, which gives the coupling term for, *e.g.*, θ, as

$$g_{k,\theta} \equiv \frac{1}{3!} \left(\frac{\partial H_\theta}{\partial q_k} \right)_0 \approx \frac{1}{3!} \left[H_\theta(\delta q_k/2) - H_\theta(-\delta q_k/2) \right], \tag{5.13}$$

where $H_\theta(\delta q_k/2)$ denotes the Hessian projected onto the θ coordinate (see Appendix C for details of this projection) evaluated at a geometry positively displace by half the kth normal mode. These coefficients can then be used to construct a spectral density as in Eq. 5.11 but replacing c_k with g_k. This calculation is performed using both the *trans* and *cis* ground state geometries to get local spectral densities and we assume that this coupling acts identically to the electronic states, which can be verified through the use of numerical Hessians in the excited states. This vibrational spectral density is shown in Fig. 5.4 d and is only shown for coupling to θ as the other coordinates have negligible couplings. As can be seen from the scale of the spectral density, these couplings are sizeable relative to the electronic spectral density and its inclusion may be needed to induce additional vibrational relaxation in the reduced system.

5.4 Developing a Minimal Model

In this section, we discuss the methods we use in developing models to be used in the dynamics simulations. We focus on two particular strategies—one which attempts to directly fit the potential energy surface and one that emphasizes model simplicity for ease of numerical simulations and subsequent analysis. Recognizing the limitations—discontinuities from the geometry optimizations and high-frequency oscillations in the diabatization to name a few—of the procedure through which we generate the potential energy further warrants the use of our procedures for direct fitting and model building.

Numerical Fit of the Diabatic Potential

To directly fit the resulting diabatic potential energy surface we utilize the POTFIT method,[117] which provides a Tucker decomposition or Higher-Order Singular Value Decomposition of the potential energy tensor on a grid.[189] Each potential energy element (diagonal and off-diagonal) can be fit using this method, however, given the data we have obtained from quantum chemistry we have to perform a few manipulations. First, the resulting potential energies from the geometry optimizations and propagation diabatization are not perfectly smooth, which can induce artificial behavior in the quantum dynamics. To avoid this scenario we have used a fourth-power Shepherd interpolation to obtain a smoothed potential energy surface for each diabatic state and coupling as well as to provide energies at configurations where the quantum chemistry failed.

The second manipulation is an extrapolation of the potentials to a wider grid in the bending angle coordinates. This extrapolation is required to give a potential energy elements on the grid for convergence of the dynamics. For the diabatic potentials we extrapolate the nearest energy in the coordinate space with and exponential rise in the distance from the nearest coordinate on the quantum chemistry grid. This extrapolation also ensures that the potential is bounded within the defined grid. Extrapolation of the diabatic couplings is achieved through Shephered interpolation, which essentially flattens out the surface to the potential of the nearest geometry.

POTFIT is performed on the resulting data, which was extrapolated to give a grid of $\overline{\varphi} \in [90, 180]$ and $\hat{\varphi} \in [-50, 50]$ with 2.5° intervals while the θ grid was unchanged due to its periodicity. The potential was expanded in a natural potential basis of 3 terms for the $\hat{\varphi}$ coordinate and 7 terms for the $\overline{\varphi}$ coordinate while the θ coordinate was used for contraction. Further interpolation to the fine grid used in dynamics was performed via cubic spline interpolation. All calculations were performed using the Heidelberg MCTDH code.[17]

Parametrization of a Model Diabatic Potential

As an initial attempt for developing a simplified model, we have imposed a phenomenological ansatz for the form of the potential based on qualitative observations of the electronic structure calculations. The ansatz we have chosen assumes that the system degrees-of-freedom are uncoupled and thus have a separable potential for both the diabatic potentials and couplings, that is,

$$V_S^{(ij)}(\mathbf{\Theta}_S) = V_{S,\theta}^{(ij)}(\theta) + V_{S,\overline{\varphi}}^{(ij)}(\overline{\varphi}) + V_{S,\hat{\varphi}}^{(ij)}(\hat{\varphi}), \tag{5.14}$$

where, *e.g.*, $V_{S,\theta}^{(ij)}(\theta)$ is the ij diabatic potential (coupling if $i \neq j$) for θ. Supposing that this ansatz is close to the true potential it is straightforward to systematically improve by adding mode-mode coupling terms, also phenomenologically.

To fit the diabatic potentials we utilize only the adiabatic energies obtained from the $S0$-optimized geometries as we impose potentials that only require information from the adiabatic limits of the diabatic potentials. The diabatic potentials for θ are expanded in a cosine series, which imposes the even symmetry of the molecule with θ. For the $|0\rangle$ and $|2\rangle$ diabatic states, we limit this series to first order obtaining the form, similar to that of Ref. [15, 98, 229],

$$V_{S,\theta}^{(00)}(\theta) = E_0 + \frac{1}{2}(W_0 - E_0)(1 - \cos\theta) \tag{5.15}$$

$$V_{S,\theta}^{(22)}(\theta) = E_2 + \frac{1}{2}(W_2 - E_2)(1 + \cos\theta) \tag{5.16}$$

where $E_{0(2)}$ is the energy minimum for the $|0\rangle$ ($|2\rangle$) state, and $W_{0(2)}$ is the energy taken in the opposite configuration (*trans* or *cis*) at the same value of $\overline{\varphi}$ and $\hat{\varphi} = 0°$. The parameters $E_{0(2)}$ are thus the adiabatic energies in the *trans* (*cis*) minima and $W_{0(2)}$ are the adiabatic energies at the *cis* (*trans*) configurations in the opposite adiabatic limit of $E_{0(2)}$. The form of this potential has a smooth variation over θ which is qualitatively ill-suited to describe the flat landscape of the $|1\rangle$ diabatic state along θ. We thus fit a more general sixth-order cosine expansion

$$V_{S,\theta}^{(11)}(\theta) = E_1 + \sum_{n=1}^{6} W_{1,n} \cos n\theta, \tag{5.17}$$

to the potential with fixed $\overline{\varphi} = 130°$ and $\hat{\varphi} = 0°$, which corresponds to the $|1\rangle$ minimum in the *trans* confiugration. The resulting diabatic potentials are compared with the diabatic potential from the diabatization procedure in Fig. 5.5a. The $|1\rangle$ state is in near perfect agreement due to the order of cosine expansion in the fit. Despite the minimal information taken from the adiabatic states, the $|0\rangle$ and $|2\rangle$ states are also qualitatively well fit in the region of their minima, however, the Franck-Condon region of the $|2\rangle$ state is qualitatively incorrect. This discrepancy is likely due to the cross-over in the character of the adiabatic states along rotation from a $n \to \pi^*$ state to a $n^2 \to \pi^{*2}$ state,[80] which would require an additional state in the diabatic representation to fully characterize.

To describe the potential for $\overline{\varphi}$ we used a Morse potential

$$V_{S,\overline{\varphi}}^{(ii)}(\overline{\varphi}) = D_i(1 - e^{-\alpha_i(\overline{\varphi} - \overline{\varphi}_{i,0})})^2, \tag{5.18}$$

where $\overline{\varphi}_{ii,0}$ is the value of $\overline{\varphi}$ at the energy minimum along the torsional path taken in the fit ($\overline{\varphi}_{0,0} = 115°$, $\overline{\varphi}_{1,0} = 130°$, $\overline{\varphi}_{2,0} = 125°$), and D_i and α_i are the usual parameters of

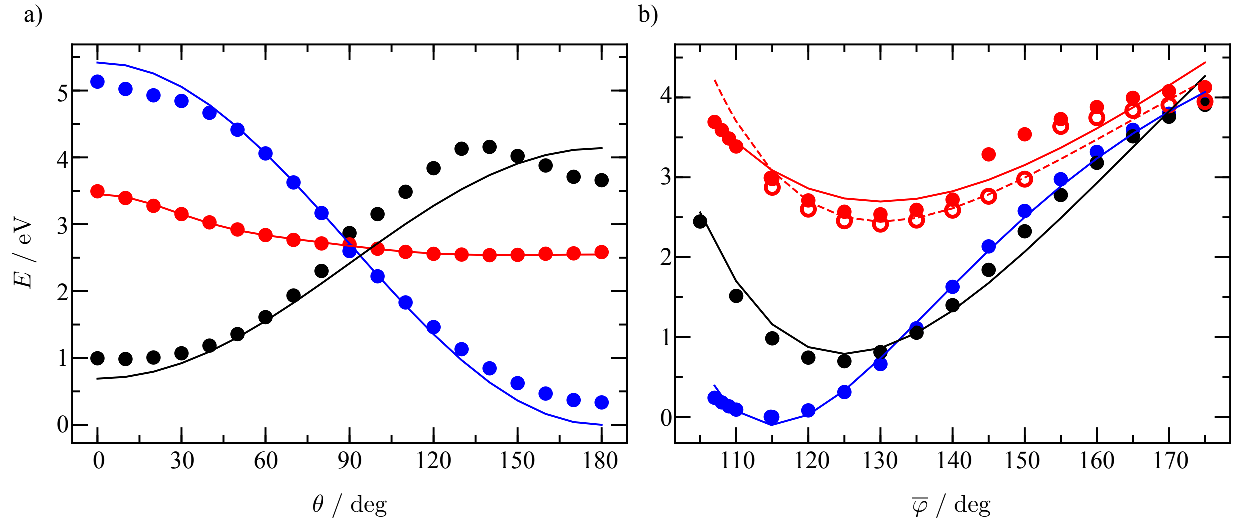

Figure 5.5: Diabatic model fits compared to the *ab initio* potentials. Comparison between the model potential (solid curves) along the dihedral angle, θ, compared to the diabatic potential from propagation diabatization (solid circles) is shown in a) for the $|0\rangle$ (blue), $|1\rangle$ (red), and $|2\rangle$ (black) states. In b), a comparison between the adiabatic potentials (solid circles) of the $S0$ *trans* (blue), $S1$ *trans* (red), and $S0$ *cis* (black) states and the diabatic potentials (solid curves) of the $|0\rangle$ *trans* (blue), $|1\rangle$ *trans* (red), and $|2\rangle$ *cis* (black) states is shown along the symmetric bending angle, $\overline{\varphi}$. Open circles are adiabatic energies obtained from $S1$-optimized geometries compared to the diabatic model fit with a dashed curve.

the Morse potential. This form of potential ensures that no additional energy is added at the minimum points taken in the torsional fit. The $|0\rangle$ and $|2\rangle$ energies are taken from the adiabatic database in which geometries were optimized with respect to the $S0$ state. For the $|1\rangle$ state, we have fit parameters using both this $S0$ database, but also energies that were obtained by performing constrained geometry optimizations with respect to the $S1$ state. Comparison of these fits to the adiabatic energies are shown in Fig. 5.5b. Optimization on the $S1$ state tends to lower the energy with respect to $S0$ optimization. This energy relaxation may serve to bring the $S1$ and $S0$ states closer in energy to truly form a conical intersection.

The antisymmetric bending potential is taken for simplicity to be a harmonic potential

$$V^{(ii)}_{S,\hat{\varphi}}(\hat{\varphi}) = \omega^2_{i,\hat{\varphi}}\hat{\varphi}^2, \tag{5.19}$$

where $\omega_{i,\hat{\varphi}}$ is the frequency of this coordinate found by fitting the $\hat{\varphi}$ dependence at the respective minima as described above. While the adiabatic potential energy surface suggests dynamics along this coordinate will be important, we expect this only to come about because of the diabatic coupling due to variation $\hat{\varphi}$ that couples electronic states of different symmetries. This reasoning follows from previous attempts at modeling photoisomerization in which the linear vibronic framework was used with tuning and coupling coordinates distinct from the isomerization coordinate were imposed by considering symmetries of the electronic states and harmonic modes.[15, 98, 229]

We now turn our attention to the form of the diabatic couplings. As has been noted elsewhere[180] and found in the diabatization, the symmetry of the electronic states determines, to a large degree, the form of the diabatic coupling. The $S0$ and $S2$ states, having the same symmetry, can thus be coupled along symmetric, $\hat{\varphi} = 0°$, coordinates. For simplicity we suppose the form of the diabatic coupling between the $|0\rangle$ and $|2\rangle$ states is given by

$$V_{S,\theta}^{(02)}(\theta) = \frac{\lambda_\theta}{2}(1 - \cos 2\theta), \tag{5.20}$$

which qualitatively mimics the resulting diabatic coupling obtained from propagation diabatization. The parameter λ_θ is taken as the value of the diabatic coupling between the $|0\rangle$ and $|2\rangle$ states at $\theta = 90°$, $\overline{\varphi} = 130°$, and $\hat{\varphi} = 0°$. The diabatic coupling between the $|1\rangle$ state and the $|0\rangle$ and $|2\rangle$ states must then be through antisymmetric coordinates due to the different symmetry of the $S1$ state

$$V_{S,\theta}^{(01)}(\hat{\varphi}) = V_{S,\theta}^{(12)}(\hat{\varphi}) = \lambda_{\hat{\varphi}}|\hat{\varphi}|, \tag{5.21}$$

where $\lambda_{\hat{\varphi}}$ is taken as the slope of the diabatic coupling along $\hat{\varphi}$ at fixed $\theta = 90°$ and $\overline{\varphi} = 130°$ between the $|1\rangle$ and $|0\rangle/|2\rangle$ states, which encompasses the conical intersection geometry. The absolute value ensures both that the symmetry of the adiabatic potential about $\hat{\varphi}$ is preserved and that the correct topology of a conical intersection is obtained. The simplicity with which we have chosen this coupling arises from the lack of qualitatively large amplitude motion in this degree-of-freedom outside of the symmetry breaking associated with the twisted $S0/S1$ conical intersection.[180, 292, 293] We thus expect the linear vibronic coupling framework, as imposed here, to capture the relevant features of the adiabatic potential to replicate the nonadiabatic dynamics.

The parameters used for the diabatic model are listed in Table 5.2. The adiabatic and diabatic potentials along the symmetric and a set of antisymmetric coordinates are shown in Fig. 5.6. We have proposed a simple form for the diabatic potential and we thus do not expect the adiabatic potential to be quantitatively reproduced by the model. There are, however, a number of features that are qualitatively inaccurate that are worth mentioning. Due to symmetry there should not be a conical intersection along the symmetric surface, though there is an apparent crossing point near $\theta = 90°$ and $\overline{\varphi} = 110°$ as can be seen in Fig. 5.6a. Additionally, there is a sharp barrier along θ at large $\overline{\varphi}$ ($\overline{\varphi} \geq 140°$), which is not present in the calculated adiabatic potential of Fig. 5.3a and b. We also note that the $S0/S1$ conical intersection topology is not faithfully reproduced. While the adiabatic potentials displayed in Fig. 5.6d come near in energy they do not touch to form a degeneracy. Moreover, the $S0$ state does not exhibit a saddle point topology nor does the $S1$ state show a local minimum at $\hat{\varphi} \neq 0°$. Despite the limitations with the model here, we see a qualitatively accurate potential for the $|1\rangle$ state on which a majority of the dynamics are

Parameter	Value (eV)
E_0	0
E_1	2.7944
E_2	0.6905
W_0	5.4186
$W_{1,1}$	0.3729
$W_{1,2}$	0.1561
$W_{1,3}$	0.05999
$W_{1,4}$	0.04429
$W_{1,5}$	0.01958
$W_{1,6}$	0.005224
W_2	3.4484
D_0	5.7086
D_1	9.8480
D_1	4.8625 ($S1$ opt)
D_2	10.3943
α_0	0.03211 (dimensionless)
α_1	0.01212 (dimensionless)
α_1	0.02056 ($S1$ opt, dimensionless)
α_2	0.01727 (dimensionless)
$\omega_{0,\hat{\varphi}}$	0.003520
$\omega_{1,\hat{\varphi}}$	0.001355
$\omega_{2,\hat{\varphi}}$	0.002153
λ_θ	0.4
$\lambda_{\hat{\varphi}}$	-0.024

Table 5.2: Parameters for the diabatic model outlined in the text. The parameters with the designation "$S1$ opt" are fit to energies obtained from $S1$-optimized geometries.

run. This state has a flat landscape along θ at its minimum in $\overline{\varphi} = 130°$. These features will dominate the short-time dynamics, which have been shown to contain the key aspects that determine the Kasha's rule violations.[180, 292] While not explicitly done in the current study, an extension of the proposed model that incorporates additional terms such mode couplings between the symmetric degrees-of-freedom is straightforward and we expect such an extension to achieve marked improvement in the representation of the adiabatic potential and subsequent dynamics. For example, incorporating these mode couplings would flatten the diabatic potentials at large $\overline{\varphi}$ and bring the adiabatic potentials close to quantitative accuracy. This improvement combined with the addition of mode couplings for the diabatic potential $V_S^{(02)}$ may resolve the anomalous conical intersection on the symmetric surface. We reserve implementation of these improvements to a future study.

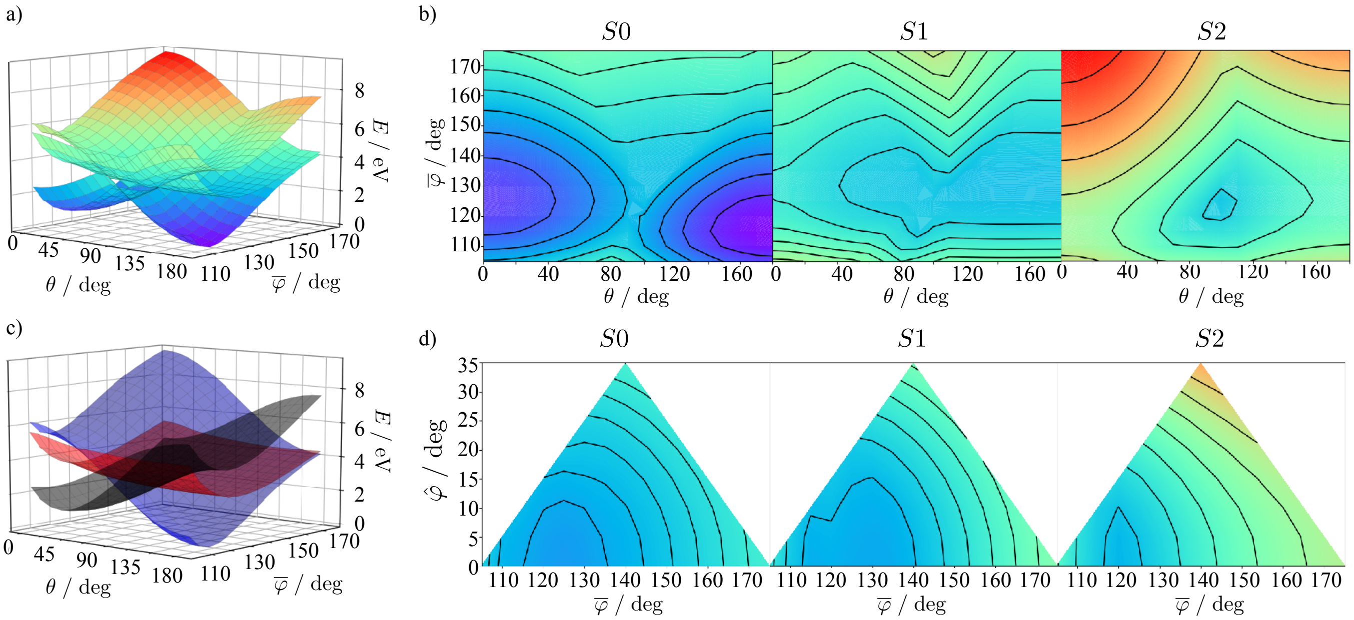

Figure 5.6: Same as Fig. 5.3, but with energies generated from the model functions and parameters. The parameters for $V^{(11)}_{S,\overline{\varphi}}$ are found by fitting to the $S1$-optimized geometries.

Numerical Kinetic Energy Operator

Up to this point, we have ignored an entire half of the Hamiltonian—the kinetic energy operator, which in generalized coordinates $\{Q\}$ has the form

$$T = -\frac{\hbar}{2}\sum_{ij}\frac{\partial}{\partial Q_i}\left(G_{ij}(\mathbf{Q})\frac{\partial}{\partial Q_j}\right), \tag{5.22}$$

where $G_{ij}(\mathbf{Q})$ is the G-tensor characterizing the reduced mass of the generalized coordinates. Specification of a coordinate system and the G-tensor then determines the kinetic energy operator. Obtaining the exact kinetic energy operator for polyatomic molecules is generally rather complicated and involves a calculated choice of coordinate system, which is inconsistent with the coordinate system we have chosen for the potential. To overcome this complication, we utilize a numerical procedure (described in Appendix C) to obtain the values of the G-tensor in the chosen coordinate system at all values of the internal coordinates.

Armed with the numerical values of the G-tensor, we then require a functional representation so as to efficiently calculate the matrix elements of the kinetic energy operator. We propose two approaches: one which fixes the values of the G-tensor at a reference geometry and assumes a diagonal (with respect to the internal coordinates) form of the kinetic energy operator and one which represents the full G-tensor on the underlying grid of internal co-

Parameter	Value (au)
$G_{\theta\theta}$	2.868e-5
$G_{\overline{\varphi}\overline{\varphi}}$	0.08166
$G_{\hat{\varphi}\hat{\varphi}}$	0.01939

Table 5.3: Parameters used for the fixed representation of the G tensor. The parameter for $G_{\theta\theta}$ here assumes θ is given in radians, which is naturally used in the Heidelberg MCTDH code.

ordinates. In the first approach, the G-tensor is calculated at the trans minimum geometry and the kinetic energy operator has the form

$$T = -\frac{\hbar}{2} \sum_{Q \in (\theta, \overline{\varphi}, \hat{\varphi})} G_{QQ} \frac{\partial^2}{\partial Q^2}. \tag{5.23}$$

The calculated values are listed in Table 5.3.

To retain the computational efficiency of grid-based dynamics methods (see the discussion on sum-of-product Hamiltonians in Chapter 2) in the second kinetic energy approach, we assume that the G-tensor elements can be represented by functions having sum-of-products forms just as the potential counterparts do. These functions were then fit to the calculated elements of the G-tensor at all geometries in the data set. The diagonal elements of the G-tensor have the following forms (subscripts denote the corresponding degrees-of-freedom for the matrix element),

$$G_{\theta\theta} = G_{\theta\theta}^{(0)} + u_{\theta\theta} \cos\theta + \left(s_{\theta\theta}^{(t)} f_t(\theta) + s_{\theta\theta}^{(c)} f_c(\theta) \right) \frac{1}{(\overline{\varphi} - 180)^2} \tag{5.24}$$

$$G_{xx} = G_{xx}^{(0)} + u_{xx} \cos\theta + \left(s_{xx}^{(t)} f_t(\theta) + s_{xx}^{(c)} f_c(\theta) \right) (\overline{\varphi} - 180)^2, \tag{5.25}$$

where $x = \overline{\varphi}, \hat{\varphi}$ and $f_{t/c}(\theta) = \frac{1}{2}(1 \mp \cos\theta)$. Each component in these forms are fit to one-dimensional cuts along the potential, that is, the θ-dependent terms are fit to data at a fixed $\overline{\varphi} = 115$ and $\hat{\varphi} = 0$, while the $\overline{\varphi}$-dependent terms are fit to data at a fixed $\theta = 180$ ($\theta = 0$) and $\hat{\varphi} = 0$ for the *trans* (*cis*) parameters, denoted by the superscript t (c).

The off-diagonal terms have the following form

$$G_{\theta\overline{\varphi}} = g(\theta) \left(G_{\theta\overline{\varphi}}^{(0)} + \frac{s_{\theta\overline{\varphi}}}{\overline{\varphi} - 180} \right) \tag{5.26}$$

$$G_{\overline{\varphi}\hat{\varphi}} = s_{\overline{\varphi}\hat{\varphi}} |\hat{\varphi}| \tag{5.27}$$

where $g(\theta) = \frac{1}{2}(1 - \cos 2\theta)$ and we have assumed $G_{\theta\hat{\varphi}} = 0$ since those values are consistently an order of magnitude smaller than $G_{\theta\overline{\varphi}}$ or $G_{\overline{\varphi}\hat{\varphi}}$. The coupling between θ and $\overline{\varphi}$ is fit at a fixed $\theta = 90$ and $\hat{\varphi} = 0$ while the coupling between $\hat{\varphi}$ and $\hat{\varphi}$ is fit at fixed $\theta = 180$. We note

Parameter	Value (au)
$G^{(0)}_{\theta\theta}$	-2.790e-5
$G^{(0)}_{\overline{\varphi\varphi}}$	0.06860
$G^{(0)}_{\hat{\varphi}\hat{\varphi}}$	0.06812
$G^{(0)}_{\theta\overline{\varphi}}$	0.00061942
$u_{\theta\theta}$	-3.397e-5
$u_{\overline{\varphi\varphi}}$	-0.04735
$u_{\hat{\varphi}\hat{\varphi}}$	0.04634
$s^{(t)}_{\theta\theta}$	0.08836
$s^{(c)}_{\theta\theta}$	0.4726
$s^{(t)}_{\overline{\varphi\varphi}}$	-8.135e-5
$s^{(c)}_{\overline{\varphi\varphi}}$	-7.058e-7
$s^{(t)}_{\hat{\varphi}\hat{\varphi}}$	-5.922e-7
$s^{(c)}_{\hat{\varphi}\hat{\varphi}}$	-8.469e-6
$s_{\theta\overline{\varphi}}$	0.09986
$s_{\overline{\varphi}\hat{\varphi}}$	-0.0003055

Table 5.4: Parameters used for the full representation of the G tensor. The same unit convention is used as in Table 5.3.

that derivatives of the G matrix elements with respect to θ and $\overline{\varphi}$ are computed in matrix form rather than analytically, which preserves boundary conditions of the underlying grid and guarantees the system's even symmetry in θ. The derivative with respect to $\hat{\varphi}$, however, is treated approximately and analytically to smooth the discontinuity in the derivative numerically as

$$\frac{\partial}{\partial\hat{\varphi}}|\hat{\varphi}| \approx \tanh(\hat{\varphi}). \tag{5.28}$$

The specific parameters used in this work are listed in Table 5.4, which not only reasonably approximate the elements of the G-tensor, but also give strictly positive eigenvalues at all points on the grid use in the MCTDH simulations.

5.5 Photoisomerization Dynamics

We have simulated the photoisomerization dynamics of azobenzene using the model outlined in the previous section with the fixed G-tensor approach. Initial wavepackets were prepared in the excited state positions that mimic the excitations to the $S1$ and $S2$ states as observed in experiments. We utilized a grid-based approach to describe the system degrees-of-freedom, which provides a numerically exact description of all vibronic effects within the current

Mode	N_{SPF}	N_{PBF}	PBF min (degrees)	PBF max
θ	45	151	0	360
$\overline{\varphi}$	40	93	90	180
$\hat{\varphi}$	35	87	-40	40

Table 5.5: Parameters used for the MCTDH wavefunction with the simplified model.

Mode	N_{SPF}	N_{PBF}	PBF min (degrees)	PBF max
θ	50	151	0	360
$\overline{\varphi}$	40	75	95	170
$\hat{\varphi}$	35	75	-40	40

Table 5.6: Parameters used for the MCTDH wavefunction with the POTFIT model.

model. The efficiency of such calculations were aided by the use of the MCTDH method to represent the system degrees-of-freedom.

Details of the MCTDH calculations

The MCTDH wavefunction used here is expanded in a set of electronic states and SPFs for each system degree-of-freedom

$$|\Psi(t)\rangle = \sum_{\alpha} \sum_{j_\theta} \sum_{j_{\overline{\varphi}}} \sum_{j_{\hat{\varphi}}} A_{\alpha,j_\theta j_{\overline{\varphi}} j_{\hat{\varphi}}}(t)|\phi_\alpha\rangle|\phi^{\theta}_{\alpha,j_\theta}(t)\rangle|\phi^{\overline{\varphi}}_{j_{\alpha,\overline{\varphi}}}(t)\rangle|\phi^{\hat{\varphi}}_{\alpha,j_{\hat{\varphi}}}(t)\rangle \tag{5.29}$$

The SPFs were expanded in a primitive basis using an exponential or plane-wave grid, which are further described in Tables 5.5 and 5.6. All dynamics were performed using the Constant Mean Field integrator with variable step sizes and an accuracy of 10^{-5}. The coefficients were propagated using the Short Iterated Lanczos algorithm and the SPFs were propagated using the Bulirsch-Stoer algorithm both with an accuracy of 10^{-6}. All calculations were performed using the Heidelberg MCTDH code.[17]

Two initial conditions were needed to describe the $S1$ and $S2$ excitation dynamics. For the $S1$ initial condition, the ground vibrational eigenstates from the model diabatic potential of the $|0\rangle$ state was projected into the $|1\rangle$ state, representing a vertical excitation initial condition into the $S1$ state due to the adiabatic limit in which the potential was fit. The initial condition for the $S2$ dynamics was taken as the same for the $S1$ initial condition, except the initial diabatic potential for the $|0\rangle$ state was fictitiously taken to have a minimum $\overline{\varphi} = 108$ degrees. This initial condition mimics the wavepacket that rapidly transitions to the $S1$ state from the $S2$ state,[78, 180] but is required within the model due to the limitations of describing the Franck-Condon region of the $S2$ state.

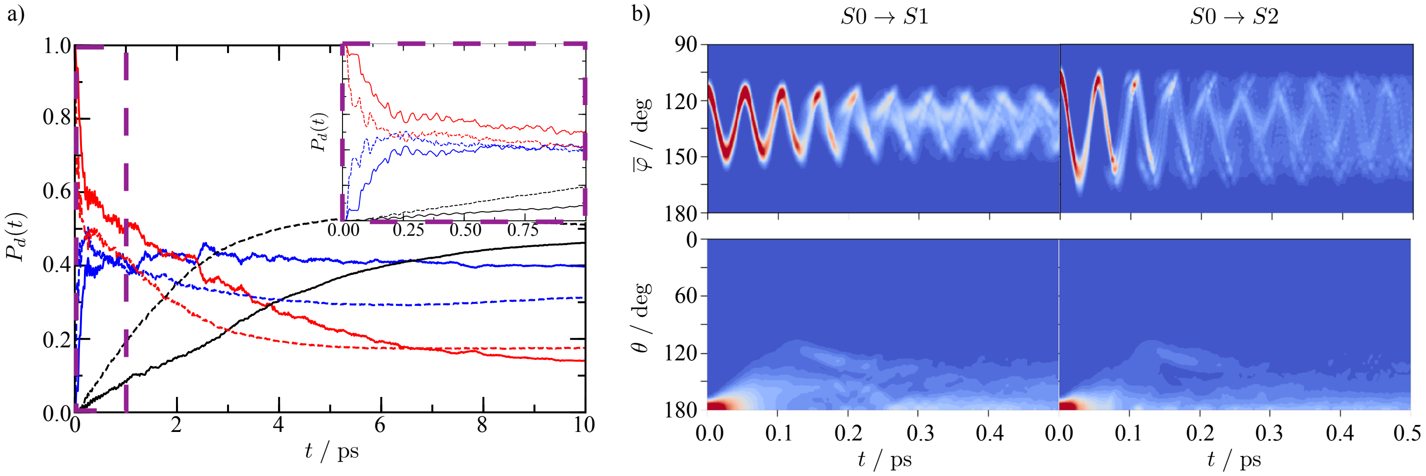

Figure 5.7: Results of the photoisomerization dynamics. Diabatic populations of the $|0\rangle$ state (blue), $|1\rangle$ state (red), and $|2\rangle$ state (black) are shown in a) for the $S1$ excitation (solid) and $S2$ excitation (dashed). The inset shows the diabatic populations up to 1 ps. Projections of the wavepacket are shown in b) as given by Eq. 5.32 (top row) and 5.33 (bottom row) for $S1$ excitation (left) and $S2$ excitation (right).

Description of Kasha's Rule Violation

We simulated the dynamics from $S1$ and $S2$ excitation using parameters obtained by fitting parameters to energies obtained from $S0$-optimized geometries. The dynamics of the electronic states can be characterized by the diabatic populations

$$P_{d,i}(t) = \int d\theta \int d\overline{\varphi} \int d\hat{\varphi} \langle \overline{\varphi} | \langle \theta | \langle \hat{\varphi} | \langle \phi_i || \Psi(t) \rangle, \tag{5.30}$$

which are depicted in Fig. 5.7a. In the case of $S1$ excitation, the population of $|1\rangle$ has a rapid (< 1 ps) population decay, which is transferred to the $|0\rangle$ state followed by onset of population decay at a slower rate, which primarily transfers to the $|2\rangle$ state en route to isomerization. The former of these population relaxation dynamics are qualitatively accurate albeit much faster than was found previously, but the latter dynamics are unfortunately in disagreement with previous simulations, which found near 50% population transfer at longer times associated with the rotational mechanism. This population transfer continues on a much slower timescale, extending out to beyond 10 ps, which is in agreement with previous simulations and experiments, but due to the increased relative transfer to the $|2\rangle$ state the quantum yield in the steady-state limit ($t \rightarrow t_{SS}$, where t_{SS}),

$$\text{Yield}(t) = \frac{P_{d,2}(t)}{P_{d,0}(t) + P_{d,2}(t)} \times 100\%, \tag{5.31}$$

is too large giving a value at 10 ps of 53.7%.

We have also computed the projection of the wavepacket onto different coordinates in the diabatic states

$$P_{d,i}^{(\overline{\varphi})}(\overline{\varphi})(t) = \int d\theta \int d\hat{\varphi} \langle \overline{\varphi} | \langle \theta | \langle \hat{\varphi} | \langle \phi_i || \Psi(t) \rangle, \tag{5.32}$$

$$P_{d,i}^{(\theta)}(\theta)(t) = \int d\overline{\varphi} \int d\hat{\varphi} \langle \theta | \langle \overline{\varphi} | \langle \hat{\varphi} | \langle \phi_i || \Psi(t) \rangle, \tag{5.33}$$

which roughly shows the motion of the internal coordinates in the different electronic states and are shown in Fig. 5.7b. The dynamics along $\overline{\varphi}$ show oscillations as the wavepacket begins motion in the $|1\rangle$ state that has a different minimum than the vertical excitation conditions. These oscillations are noticeably faster than apparent motion along θ exhibiting nearly two full periods before the system begins rotation, which is due to the significantly smaller moment of inertia of θ compared to the reduced mass of $\overline{\varphi}$ as well as the flat landscape of the potential along θ in the $|1\rangle$ state.

The dynamics following $S2$ excitation show similar features—there is a fast population transfer from $|1\rangle$ to $|0\rangle$ followed by transfer from $|1\rangle$ to $|2\rangle$ on a slower timescale. In contrast, however, there is some additional population transfer to the $|2\rangle$ state from the $|0\rangle$ state and the population relaxation from $|1\rangle$ occurs on a faster timescale reaching a steady-state by ~5 ps. The dynamics are notably different in $\overline{\varphi}$ as shown in Fig. 5.7b. Due to the higher-energy initial condition—mimicking excitation to the ~1 eV difference between $S2$ and $S1$ states in the Franck-Condon region—the wavepacket can move to larger $\overline{\varphi}$ where the $S0$ and $S1$ adiabatic states come closer in energy and more population can transfer as is clear from the inset of Fig. 5.7a. Dynamics in θ do not appear markedly different, which is expected as the isomerization mechanism is known to still be rotational, but at a lower yield. Unfortunately, the quantum yield is larger for $S2$ excitation, 61.9%, than $S1$ excitation, which is the opposite result as found in previous simulations and, importantly, experiments.

This incorrect qualitative behavior of the model dynamics is likely a result of two inadequacies with the model we have developed. As was noted, the population transfer occurring on a slower timescale dramatically favors isomerization to the *cis* configuration (transfer to the $|2\rangle$ state) rather than relaxation back to the *trans* state in disagreement with previous simulations. Since this population transfer requires an accurate description of the potential in the vicinity of the twisted conical intersection, which the model does not qualitatively represent well, incorporation of additional terms in the potential—such as symmetric mode couplings as was discussed—are needed to obtain a more faithful representation of this portion of the potential. Specifically, much of the population transfer that results in relaxation to the *trans* state occurs at large $\overline{\varphi}$ near the twisted conical intersection and hence terms that tend to flatten the $|0\rangle$ and $|2\rangle$ diabatic potentials rather than favor the adiabatic limits along $\overline{\varphi}$ we expect to lead to an improvement.

Finally, the model proposed here ignores much of the vibrational energy redistribution that can occur to help relax the molecule. Additional vibrational energy redistribution would be introduced through mode-couplings as well as the expanded kinetic energy operator, however, there may be a significant effect from the environmental modes that may be

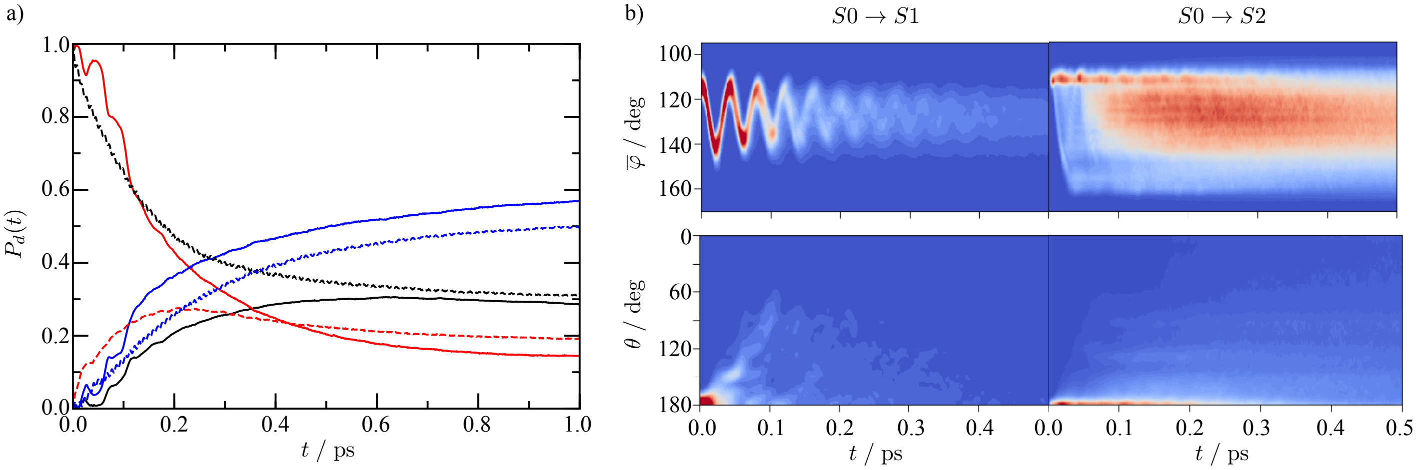

Figure 5.8: Results of the photoisomerization dynamics obtained from the POTFIT model. Diabatic populations of the $|0\rangle$ state (blue), $|1\rangle$ state (red), and $|2\rangle$ state (black) are shown in a) for the $S1$ excitation (solid) and $S2$ excitation (dashed). Projections of the wavepacket are shown in b) as given by Eq. 5.32 (top row) and 5.33 (bottom row) for $S1$ excitation (left) and $S2$ excitation (right).

incorporated through the calculated spectral densities. In particular, this enhanced vibrational relaxation may be needed to distribute the additional energy from $S2$ excitation to ensure relaxation to the *trans* state after transfer to the $|0\rangle$ state unlike what was found in the population dynamics of Fig. 5.7a.

Environmental Effects

We have also performed MCTDH simulations using the aforementioned POTFIT model from both $S1$ and $S2$ excitation initial conditions with and without additional degrees-of-freedom to test environmental effects. In this model, we also utilized the more complex form of the kinetic energy operator that includes coordinate-dependence and couplings to the G-tensor. Due to the flexibility of the POTFIT model for fitting potentials, we have explicitly used the $|2\rangle$ state when considering the $S2$ excitation initial condition—that is we have projected the ground ($|0\rangle$) vibrational eigenstates into the $|2\rangle$ diabatic state—which differs from the calculations using the simplified model.

The diabatic population dynamics are depicted in Fig. 5.8a for both the $S1$ and $S2$ excitations. There are some notable differences between these dynamics and the dynamics of the simplified model notwithstanding the different initial condition for the $S2$ excitation. The population dynamics in both initial conditions have a shortened coherence lifetime and much faster population relaxation. These features can likely both be explained by the description of the potential energy surface in the POTFIT model, which gives a much

Parameter	Value (eV)
ω_0	0.1670
ω_1	0.1564
ω_2	0.1640
$\kappa_0^{(t)}$	0.0
$\kappa_0^{(c)}$	0.3203
$\kappa_1^{(t)}$	0.1541
$\kappa_1^{(c)}$	0.1335
$\kappa_2^{(t)}$	0.4092
$\kappa_2^{(c)}$	0.0
N_{SPF}	15
N_{PBF}	40

Table 5.7: Parameters used for the additional mode with electron-phonon coupling. All parameters are given in units of eV except for the parameters of the basis functions.

more accurate representation of the diabatic potential in the regions where the potential has not been extrapolated. This description includes additional terms that couple all the modes together and would thus induce additional vibrational decoherence relative to the simplified model. This vibrational decoherence is also aided by more terms in the kinetic energy operator used in this model.

The faster population relaxation can also be attributed to the accuracy of the potential representation. As was noted in the adiabatic potential resulting from the simplified model (see Fig. 5.6a), the real adiabatic potential along the symmetric surface does not have a barrier in the $S1$ state along the dihedral angle at large symmetric bending angle. This region is an area where the adiabatic states come close—though not close enough to form a conical intersection exactly—in energy and where much faster population transfer can occur. As this region is entirely avoided in the simplified model we would expect a much slower population transfer such that population transfer along the rotational mechanism only occurs at or near the conical intersection geometry.

Interestingly, however, the qualitative features of the short-time dynamics are rather similar. The projection of the wavepacket onto the θ and $\overline{\varphi}$ degrees-of-freedom for both initial conditions with the POTFIT model are shown in Fig. 5.8b. As can be seen, the oscillations in $\overline{\varphi}$ are still faster than the rotational motion of θ such that the additional energy in the $S2$ excitation should take the wavepacket to a region of fast population transfer prior to significant rotation. Unfortunately, even in this case of a more accurate potential representation we have still not uncovered the correct Kasha's rule violation obtaining quantum yields of 30.1% for $S1$ excitation and 35.3% for $S2$ excitation.

Having tested the dependence of the quantum yield on the accuracy of the potential

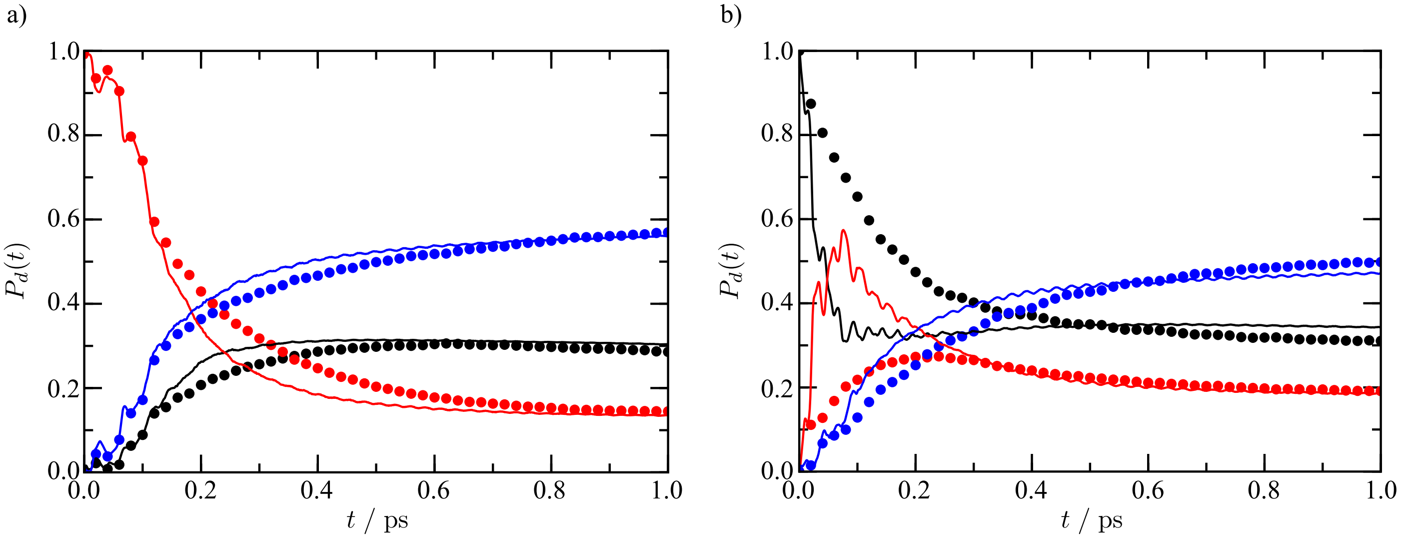

Figure 5.9: Comparison of the diabatic populations between the POTFIT model without (dots) and with (solid lines) an additional mode with electron-phonon coupling. Results for the $S1$ excitation are shown in a) and for the $S2$ excitation are shown in b). Colors have the same correspondence as in Fig. 5.8.

representation, we can now turn our attention to the effect from "environmental" degrees-of-freedom that are not included in the system potential. We have added an electron-phonon coupling in the form of Eq. 5.3 parametrized by the spectral density calculations shown in Fig. 5.4c. As the main peak in the spectral density is due to NN stretch mode and significantly dominates over the remaining modes we have included only a single mode (herein refered to as Q), which was obtained by performing a single iteration of the effective mode transformation of Burghardt and co-workers (see Ref. [107, 108, 273]) on the spectral densities shown in Fig. 5.4c and a similar spectral density calculated using the *cis* geometry. The additional terms are given by

$$V(Q) + V_{eB}(Q) = \sum_I |I\rangle\langle I| \left(\frac{1}{2}\omega_I Q^2 + \frac{\kappa_I^{(t)}}{2}(1 - \cos\theta)Q + \frac{\kappa_I^{(c)}}{2}(1 + \cos\theta)Q \right) \tag{5.34}$$

where ω_I is the frequency of the mode in the Ith diabatic state, $\kappa_I^{(t)}$ ($\kappa_I^{(c)}$) is the coupling coefficient due to coupling from the *trans* (*cis*) state geometry in the Ith diabatic state, and we have excluded the mass due to our use of dimensionless harmonic oscillator coordinates and primitive basis in the simulation. The values of the simulation parameters are listed in Table 5.7.

The diabatic populations with the electron-phonon coupling included is compared to the diabatic populations without the extra mode in Fig. 5.9. In the case of the $S1$ excitation the additional mode has negligible effect on the overall dynamics and gives similar yield to the case without this environmental mode. This result could have been expected as the modes not included in the original potential have little contribution to the $S1$ spectral density and thus the predominant nuclear effects are already included in the system potential. In the $S2$ excitation, the short-time (<300 fs) are dramatically different exhibiting a significantly faster population transfer from the $|2\rangle$ to $|1\rangle$ state before additional transfer to the $|0\rangle$ state. The NN stretch mode clearly has a significant effect on the dynamics in this regime due to the large electron-phonon coupling exhibited in Fig. 5.4c. Also contributing to this effect is the fact that the optimized geometries in the region of the $S1/S2$ conical intersection show little change in the NN distance, which clearly contributes to the coupling between the two states through energy fluctuations. Despite this significant change in the population dynamics at early times, the yield is nearly unchanged yet again and this effect does not appear to contribute to the Kasha's rule violation in azobenzene.

As was noted earlier, additional vibrational relaxation may be necessary to enhance the population transfer in particular regions of the potential that may contribute to the Kasha's rule violation. Another effect from the nuclear degrees-of-freedom may be a nonlinear effect arising from the geometry optimization procedure used in obtaining the potential energy surface. If the entire potential were instead optimized with respect to the $S1$ state at each constrained geometry faster population transfer may be observed due to the changes in the relative adiabatic energy differences. An initial investigation into this effect has been shown in Fig. 5.5b, where it was shown that optimization with respect to the $S1$ state significantly lowers the adiabtic energy of this state, but (not shown) leaves the other states' energies invariant. As SF-TDDFT is not well-suited for calculations of this type when there is spin contamination, we expect a different flavor of TDDFT or higher-level method may prove more fruitful along these lines.

5.6 Conclusion

In this chapter, we have utilized the hybrid formalism of Chapter 4 to develop a reduced model for azobenzene photoisomerization. This model incorporates the minimal information needed to characterize the known reaction pathways and was parametrized by *ab initio* electronic structure calculations as well direct calculation of the kinetic energy operator. The dynamics with the model can be simulated with numerically exact wavepacket propagation methods such as the MCTDH calculations that were performed in this work. The qualitative behavior of the short-time dynamics were found to be in agreement with previous simulations noted by fast oscillations in $\overline{\varphi}$ and an increase of the early population transfer upon $S2$ excitation compared to the $S1$ excitation. The quantum yield, however, was found to be qualitatively incorrect being above 50% for $S1$ excitation and increasing upon $S2$ excitation in disagreement with previous simulations and experimental observations.

We have noted the limitations of the currently proposed model, which when addressed may improve the results toward quantitative accuracy. Unfortunately directly improving the representation of the potential and more accurate fits as well as adding electron-phonon coupling may not provide the solution, which was shown through MCTDH calculations with a POTFIT model. As this is the first diabatic potential developed for azobenzene, however, this work will pave the way for developing a more accurate model and enhancing the description of the reaction mechanism. Future tests of this model may also compare spectroscopic observables to help describe novel experiments on conical intersetion dynamics.[131] Furthermore, once an accurate diabatic model is achieved, simulations incorporating the effects from condensed phase environments can begin and the complete picture regarding complex dynamics of azobenzene photoisomerization can be elucidated through the used of advanced simulation techniques.[222]

Chapter 6

Two-Dimensional Electronic Vibrational Spectroscopy

> *"There's always another secret."*
>
> — Kelsier [216]

6.1 Introduction

Elucidating the mechanisms of quantum mechanical energy transfer has fundamental implications for the way we understand natural light-harvesting and develop artificial analogs.[224] Previous experimental studies on natural systems[35, 68, 178] have been unable, however, to clearly establish the mechanism of energy transfer that leads to quantum efficiencies approaching unity[25] and have launched long-standing debates obfuscating the role of observed electronically and/or vibrationally coherent phenomena in the transfer process.[1, 12, 34, 47, 48, 54, 79, 103, 124, 160, 184, 187, 191, 195, 209, 211, 250, 257] It has been postulated that these coherent processes may not actually serve any purpose in the overall energy transfer mechanism.[37, 75] This ambiguity largely surrounds the lack of consistent treatment of electronic-vibrational coupling in energy transfer models, which we address through a simplified heterodimer model in this chapter. It has been shown that explicit details of the vibronic coupling mechanism can have a large influence on the overall dynamics.[64, 66, 288, 295] Also contributing to the uncertainty is that the distinguishing features between vibronic mixing mechanisms in coupled systems can be subtle in electronic spectroscopies[196, 228, 295]—and are only further obscured in the complex, congested spectra of experimental realizations.

This chapter is based on work that has been submitted to *The Journal of Chemical Physics.*[11]

Recently, two-dimensional electronic-vibrational (2DEV) spectroscopy has emerged as a candidate experimental technique that can directly observe the correlated motion of electronic and nuclear degrees-of-freedom and their role in energy transfer.[185] Indeed, initial studies on photosynthetic complexes, such as light-harvesting complex II (LHCII), showed promise in utilizing this technique to unravel the dynamics of energy transfer between different chromophores owing to the improved spectral resolution and structural details afforded via probing vibrational modes.[154] Subsequent 2DEV measurements have shown evidence of vibronic mixing in and its facilitation of ultrafast energy transfer in LHCII.[12] In the latter, the 2DEV spectra showed rich vibrational structure corresponding to the dominant electronic excitations which exhibited oscillatory dynamics reminiscent of non-Condon effects found in previous transient absorption measurements.[126, 196, 290] These oscillations were also found to be present at slightly higher-energy excitations to vibronically mixed states. In this case, the clear similarity in the quantum beating patterns between these higher-lying states and the dominant, more electronically mixed excitations, was speculated to be indicative of rapid energy relaxation due to vibronic mixing. Here we develop a strategy to simulate these general effects in 2DEV spectra and connect them to vibronic coupling mechanisms of energy transfer. Further 2DEV studies on LHCII, involving excitation well-beyond the dominant absorption bands, showed the same rapid energy relaxation, but with a significant polarization-dependence.[10] With polarization control, the dynamics of vibronic excitations, exhibiting much more rapid energy transfer, were disentangled from purely electronic excitations with significantly slower energy transfer. Not only does this polarization-dependence isolate the role of vibronic mixing on the rate of energy transfer, it potentially rules out the role the protein environment has on enhancing rapid energy transfer and suggests a predominant contribution from *intra*molecular modes to the underlying energy transfer mechanism.

To date, theoretical work regarding the 2DEV signals of coupled systems, while informative, has been restricted to systems that have a only have a single vibrational mode per monomeric unit.[24, 153, 286] An interpretation of the origin of the vibronic coupling observed in these recent findings is, therefore, lacking. Particularly, the relative infancy of 2DEV spectroscopy makes assigning vibronic mixing to direct electron-nuclear coupling or non-Condon effects in the experiments difficult as this requires the development of multimode models. In this chapter, we bridge this gap between vibronic coupling mechanisms and analysis of the experimental measurements by directly simulating the 2DEV spectra of a minimal model vibronically coupled heterodimer while controlling various vibronic coupling mechanisms. By utilizing a model system, we are able to isolate the role that different vibronic coupling mechanisms have on the structure of the excitonic states that are electronically excited in typical experiments and show how that structure is identifiable in 2DEV spectroscopy both statically and dynamically. We further compare these signatures to the population dynamics, which demonstrates the ability to directly link the mechanism of energy transfer with spectral observables and connects model systems to potential *ab initio* simulations for which only simple observables like the populations are available.

The remainder of this chapter is organized as follows. In Section 6.2, we introduce a model vibronic heterodimer and the formalism we use for computing linear absorption and

2DEV spectra. We analyze the static and dynamical signatures of vibronic coupling in the spectra in Sections 6.3 and 6.4, respectively. Concluding remarks and directions for future work are provided in Section 6.5.

6.2 Theory

In this section, we introduce a minimal vibronically coupled heterodimer model and the theoretical formalism by which we simulate spectra. We utilize an open quantum system approach to describe the heterodimer in contact with a thermal bath given by the total Hamiltonian, $H = H_S + H_B + H_{SB}$, where H_S is the system Hamiltonian of the heterodimer, H_B is the bath Hamiltonian, and H_{SB} is the system-bath Hamiltonian describing their interactions. This approach offers an exact description of the most strongly-coupled system degrees-of-freedom with a simple treatment of relevant environmental effects that induce dissipation and dephasing in the system.

Model Hamiltonian

The system (depicted in Fig. 6.1a) is comprised of two chromophores (herein referred to as sites A and B) each consisting of a local ground and excited electronic state and local intramolecular modes. These chromophores, in the context of natural light-harvesting, could be considered distinct pigments in a protein or two of the same pigments with different protein binding properties that statically change the characteristics of the local Hamiltonians. We restrict the system Hamiltonian to the ground state (G) and singly-excited state manifold, thus containing three electronic states of the form,

$$\begin{aligned} H_S = {} & (h_A^g + h_B^g)|G\rangle\langle G| + (h_A^e + h_B^g + \epsilon)|A\rangle\langle A| \\ & + (h_A^g + h_B^e + \Delta E + \epsilon)|B\rangle\langle B| + J(|A\rangle\langle B| + \text{h.c.}), \end{aligned} \tag{6.1}$$

where we have implied the Kronecker product structure of the A and B local Hamiltonians applying on their local vibrational subspace. The electronic state $|A\rangle$ ($|B\rangle$) refers to the state when site A (B) is excited and site B (A) is in its ground state. Here, the ground state is uncoupled to and energetically separated from the excited states by an excitation energy, ϵ, which may be removed without loss of generality. The excited states comprise a two-level system in the electronic subspace that has an energy difference denoted by ΔE and an electronic coupling denoted by J. In this two-level subsystem it is useful to consider the excitonic gap, which is equivalent to a Rabi frequency given by $\hbar\Omega_R = \sqrt{\Delta E^2 + 4J^2}$ that determines the timescale of electronic oscillations between the excited states.

Each site has a ground (g) and excited (e) state where the local Hamiltonians acting on

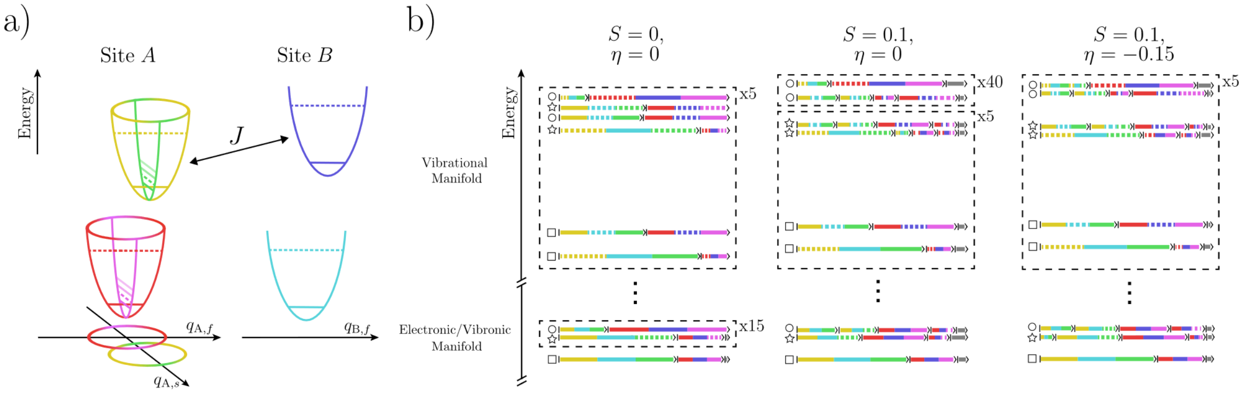

Figure 6.1: a) Schematic of the model consisting of two sites, A and B, each with one electronic degree-of-freedom and one high-frequency vibrational mode. For site A (B), the high-frequency mode is shown in red (light blue) in the ground state and yellow (dark blue) in the excited state. Horizontal lines in each harmonic potential indicate vibrational levels where dashed lines, specifically, indicate one vibrational quantum. Site A includes an additional low-frequency mode, shown in pink in the ground state and green in the excited state with line-markings corresponding to different vibrational excited states. b) Simplified eigenenergy level diagram arising from electronic coupling, J, between the excited state manifolds of sites A and B for each of the three models considered here. For simplicity, the ground state manifold has been omitted and only the three lowest excitonic states in the excited electronic/vibronic manifold as well as the corresponding vibrational levels have been illustrated. The relative site contributions for these levels are also shown by the length of each ket, "$|\,\rangle$", with site-specific color-coding following a). Dashed lines indicate a vibrational excitation. Site contributions of $< 5\%$ are grouped together and denoted in gray. Shapes on the left hand side of the energy levels in the electronic/vibrational denote the main excited state absorption (ESA) transitions while shapes in the vibrational manifold denote the states to which the main ESA excitations are excited by vibrational pulses.

the site vibrational subspaces have the form

$$h_I^i = \frac{\hbar\omega_{I,i,f}}{2}\left(p_{I,f}^2 + (q_{I,f} - \delta_{ie}\sqrt{2S_f})^2\right) + \delta_{IA}\frac{\hbar\omega_{I,s}}{2}\left(p_{I,s}^2 + (q_{I,s} - \delta_{ie}\sqrt{2S})^2\right) \tag{6.2}$$

where $I = A, B$ denotes the chromophore site, $i = g, e$ denotes the electronic state of the site, δ_{ij} denotes the Kronecker delta, and the q and p are the position and momentum operators, respectively of high-frequency, f, and low-frequency, s, modes. Each site contains one high-frequency ($\omega_{I,i,f}/\Omega_R \gg 1$) local intramolecular modes with a distinct site- and electronic-state-dependent frequency. These high-frequency modes are slightly displaced in the excited states and thus have a small, but non-zero Huang-Rhys factor, S_f, which we will consider fixed throughout this study. Vertical excitations and electronic transitions are, however, still dominated by transitions that leave the vibrational states of these modes unchanged. Coupled to site A only is also a low-frequency mode that is nearly-degenerate with the excitonic gap, $\omega_{A,s} \approx \Omega_R$. In practice, this mode could be considered an intramolecular mode with significant local site electron-phonon coupling. This mode is also shifted in the excited state of the A chromophore with a non-zero Huang-Rhys factor, S, however due to the resonance with the excitonic gap, this displacement induces significant vibronic mixing by coupling different vibrational states in vertical excitations from the ground state or electronic transitions between the A and B sites. Thus, S can be varied to tune the strength of the vibronic coupling mechanism through what we herein refer to as Franck-Condon (FC) activity. We note that in this work, two vibrational levels per high-frequency mode and four vibrational levels for the low-frequency mode were required for convergence. Additionally, we have restricted the model to the ground- and singly- excited vibrational state manifold with respect to the subspace of the high-frequency modes for a total system Hilbert space dimension of 36.

The electronic coupling is considered to arise from a dipole-dipole interaction between the excited states of the two chromophores,

$$J = \frac{\kappa}{r^3}\mu_A\mu_B, \tag{6.3}$$

where $\mu_{A(B)}$ is the magnitude of the transition dipole moment (TDM) for the A (B) site, r is the distance between the two chromophores, and κ is a factor accounting for the relative orientation of the chromophores. We assume here that the distance, relative orientation, and TDM of the B chromophore are fixed ($r = r_0$, $\kappa = \kappa_0$, and $\mu_B = \mu_{B0}$, respectively), while the TDM of the A chromophore depends linearly on the low-frequency mode,

$$\mu_A(q_{A,s}) = \mu_{A0}\left(1 + \sqrt{2}\eta q_{A,s}\right), \tag{6.4}$$

where μ_{A0} is the static contribution to the dipole moment. The mode-dependence arises as a non-Condon effect, that is,

$$\sqrt{2}\mu_{A0}\eta = \left(\frac{\partial\mu_A}{\partial q_{A,s}}\right), \tag{6.5}$$

where η is a dimensionless parameter controlling the strength of this effect. We note that because the electronic states have the same symmetry there is no strict symmetry requirement here for the HT active mode.[3] Under this assumption, the electronic coupling obtains the form

$$J(q_{A,s}) = J_0 \left(1 + \sqrt{2}\eta q_{A,s}\right), \tag{6.6}$$

where J_0 is the electronic coupling arising from the static contributions of the TDM at a fixed distance and orientation, $J_0 = \kappa_0 \mu_{A0} \mu_{B0} / r_0^3$, and the non-Condon effect is given by $\sqrt{2} J_0 \eta q_{A,s}$. We consider here a system in the electronically coherent regime ($\Delta E = J_0$), which is typical for energy transfer dynamics in these chromophoric systems. Since η is a dimensionless parameter and it enters directly in the TDM, it can be varied to systematically study Herzberg-Teller (HT) activity in this system.

The chromophoric system here is assumed to be weakly coupled to a set of environmental modes that describe the short- and long-range fluctuations of the environment. In particular we consider two sets of baths, an electronic set and a vibrational set, which are assumed to be independent due to disparity of the frequency of modes that couple to the separate electronic or vibrational degrees-of-freedom. The electronic baths independently couple to the electronically excited states through a dipolar coupling

$$(H_B + H_{SB})_{\text{el}} = \sum_{I,n} \frac{\hbar\omega_{I,n}^{\text{el}}}{2} \left[\left(p_{I,n}^{\text{el}}\right)^2 + \left(q_{I,n}^{\text{el}} - \frac{g_{I,n}^{\text{el}}}{\sqrt{2}} V_I \right)^2 \right], \tag{6.7}$$

where V_I ($I = A, B$) are the dimensionless system dipole operators and the vibrational baths independently couple to the nuclear modes of the system

$$\begin{aligned}(H_B + H_{SB})_{\text{vib}} = \sum_{I,n} \Bigg\{ & \frac{\hbar\omega_{I,n}^{f}}{2} \left[\left(p_{I,n}^{f}\right)^2 + \left(q_{I,n}^{f} - g_{I,n}^{f} q_{I,f} \right)^2 \right] \\ & + \delta_{IA} \frac{\hbar\omega_{I,n}^{s}}{2} \left[\left(p_{I,n}^{s}\right)^2 + \left(q_{I,n}^{s} - g_{I,n}^{s} q_{I,s} \right)^2 \right] \Bigg\}. \end{aligned} \tag{6.8}$$

Here we have included the system-bath couplings as system-dependent shifts in the minima of the bath oscillators, which ensures translational invariance of the bath with respect to the system. The g coefficients in the above expressions are the bilinear coupling coefficients with the form,

$$g_{k,n} = \frac{\sqrt{2} c_{k,n}}{\hbar\omega_{k,n}}, \tag{6.9}$$

which comprise the spectral density function,

$$J_{m,k}(\omega) = \frac{\pi}{2} \sum_n \frac{c_{k,n}^2}{\hbar\omega_{k,n}} \delta(\omega - \omega_{k,n}). \tag{6.10}$$

Parameter	Value (cm^{-1})
$\hbar\omega_{A,g,f}$	1650
$\hbar\omega_{B,g,f}$	1660
$\hbar\omega_{A,e,f}$	1545
$\hbar\omega_{B,e,f}$	1540
$\hbar\omega_{A,s}$	200
ΔE	100
J_0	100
λ_{el}	35
λ_{vib}	17.5
$\hbar\gamma_{el}$, $\hbar\gamma_{vib}$	$\sim$ 106
$1/\beta$	$\sim$ 105
S_f	0.005 (dimensionless)
μ_{A0}/μ_{B0}	-4 (dimensionless)

Table 6.1: Fixed parameters used in the model heterodimer. All parameters are in units of cm^{-1} unless otherwise specified.

Here m = el,vib denotes whether the spectral density corresponds to an electronically- or vibrationally-coupled environment and k serves here as a composite index ($k = I$ for the electronic bath and $k = I, f/s$ for the vibrational bath) describing the environmental modes that are coupled to the different system degrees-of-freedom in Eqs. 6.7 and 6.8. The spectral densities are all assumed to have the Debye form,

$$J_{m,k}(\omega) = 2\lambda_m\gamma_m\omega\frac{1}{\gamma_m^2 + \omega^2}, \tag{6.11}$$

where λ_m is the reorganization energy and γ_m is the bath relaxation timescale and each m, k environment. These parameters are chosen such that the bath represents a weakly-coupled, Markovian bath so that the use of multilevel Redfield theory is justified in treating the dynamics of the total system-bath Hamiltonian.[173, 221] We note here that while this form is consistent with much of the underlying physics of the total system, it is primarily phenomenologically included to induce weak dissipation and dephasing for ease of numerical simulations and a further study that considers the effects a more systematically imposed system-bath coupling is warranted. A detailed list of the model parameters used in this study can be found in Table 6.1.

Linear Absorption and 2DEV Spectroscopy from Quantum Master Equations

To calculate spectroscopic observables we utilize the response function formalism, which has been described elsewhere[176], so we restrict our discussion to the key aspects of our simulation. In this formalism, linear and nonlinear spectra can be related via Fourier Transforms of correlation functions. Specifically, for a linear absorption spectrum in the impulsive limit, the relevant response function is

$$R(t) = \left(\frac{i}{\hbar}\right) \theta(t) \mathrm{Tr}\left\{\mu_{el} G(t) \mu_{el}^{\times} \rho_{eq}\right\}, \tag{6.12}$$

where $\mu^{\times}\cdot = [\mu, \cdot]$, $\mathrm{Tr}\{\cdot\}$ is the quantum mechanical trace over the full system plus bath Hilbert space, $\theta(t)$ is the Heaviside step function, and ρ_{eq} is the thermal equilibrium density matrix given by

$$\rho_{eq} = \frac{e^{-\beta H}}{\mathrm{Tr}\left\{e^{-\beta H}\right\}}, \tag{6.13}$$

where β is inverse thermal energy. This response function is a dipole-dipole autocorrelation function of the electronic dipole given by

$$\mu_{el} = \mu_A + \mu_B \tag{6.14}$$

where

$$\mu_I = \mu_{I0}\left(1 + \delta_{IA}\sqrt{2}\eta q_{A,s}\right)\left(|I\rangle\langle G| + |G\rangle\langle I|\right). \tag{6.15}$$

The time-dependence is given by action of the propagator $G(t)\cdot = e^{-iHt/\hbar} \cdot e^{iHt/\hbar}$, which is the unitary evolution in the full Hilbert space. This unitary evolution is prohibitively expensive, so we utilize the quantum master equation (QME) technique whereby we take a partial trace over the bath degrees-of-freedom and compute the response function from the dynamics of the reduced density matrix[72],

$$\mathrm{Tr}_B\left\{G(t)\mu_{el}^{\times}\rho_{eq}\right\} = \mathcal{G}(t)\rho_{\mu} \tag{6.16}$$

where ρ_{μ} is the reduced density matrix of the system after action of the dipole operator and $\mathcal{G}(t)$ is the reduced propagator defined by our QME. The Redfield theory approach taken here uses a double perturbation theory in both the light-matter interaction and system-bath interaction, where the light-matter interaction is assumed to be even weaker than the weak system-bath coupling.[2, 152] In this representation the response function is,

$$R(t) = \left(\frac{i}{\hbar}\right) \theta(t) \mathrm{Tr}_S\left\{\mu_{el}\mathcal{G}(t)\rho_{\mu}\right\}. \tag{6.17}$$

Here we also invoke the rotating wave approximation (RWA), which reduces the terms allowed in the expansion of the commutators. Denoting the dipole operators as a sum of raising and lowering dipole operators, respectively,

$$\mu_{el}^{+} = \mu_A^{+} + \mu_B^{+} = \mu_{A0}\left(1 + \sqrt{2}\eta q_{A,s}\right)|A\rangle\langle G| + \mu_{B0}|B\rangle\langle G| \tag{6.18}$$

$$\mu_{el}^{-} = \left(\mu_{el}^{+}\right)^{\dagger}, \tag{6.19}$$

and ignoring the negative frequency contribution, the response function then becomes

$$R(t) = \left(\frac{i}{\hbar}\right) \theta(t) \mathrm{Tr}_S \left\{ \mu_{el}^{-} \mathcal{G}(t) \rho_{\mu^+} \right\}, \tag{6.20}$$

where $\mathcal{G}(t)\rho_{\mu^+} = \mathrm{Tr}_B \left\{ G(t) \mu_{el}^{+} \rho_{eq} \right\}$. The corresponding linear absorption spectrum is given by the imaginary part of the Fourier transform

$$S(\omega_{\text{exc.}}) = \mathrm{Im} \int dt \; e^{i\omega_{\text{exc.}} t} R(t), \tag{6.21}$$

where $\omega_{\text{exc.}}$ is the excitation frequency less the excitation energy ϵ.

2DEV spectroscopy is a cross-peak specific multidimensional spectroscopic technique where the signal arises from both visible and subsequent infrared light-matter interactions. Specifically, visible excitation pulses prepare an ensemble of electronic/vibronic states which evolve as a function of waiting time, T. The evolution of the ensemble is then tracked via an infrared detection pulse.

Within the same formalism, the response function for 2DEV spectroscopy can be written as

$$\begin{aligned} R_3(t_{\text{det.}}, T, t_{\text{exc.}}) = {} & \left(\frac{i}{\hbar}\right)^3 \theta(t_{\text{det.}}) \theta(T) \theta(t_{\text{exc.}}) \\ & \times \mathrm{Tr} \left\{ \mu_{vib} G(t_{\text{det.}}) \mu_{vib}^{\times} G(T) \mu_{el}^{\times} G(t_{\text{exc.}}) \mu_{el}^{\times} \rho_{eq} \right\}, \end{aligned} \tag{6.22}$$

where $t_{\text{exc.}}$ denotes the time between the two visible pulses, $t_{\text{det.}}$ denotes the time between the infrared pulses, and the vibrational dipole operator acting on the high-frequency modes is given by

$$\mu_{vib} = \mu_{A,f} + \mu_{B,f} \tag{6.23}$$

where $\mu_{I,f} = \sqrt{2} q_{I,f} \left| I \right\rangle \left\langle I \right|$ and we have ignored the vibrational TDM of the slow mode due to non-resonance with the infrared probe. We again utilize the QME technique to compute the response function, which in the weak-coupling ($\lambda_m \to 0$) and Markovian ($\gamma_m \to 0$) limits we have chosen here reduces to the expression obtained from the quantum regression theorem[5, 72],

$$\begin{aligned} R_3(t_{\text{det.}}, T, t_{\text{exc.}}) = {} & \left(\frac{i}{\hbar}\right)^3 \theta(t_{\text{det.}}) \theta(T) \theta(t_{\text{exc.}}) \\ & \times \mathrm{Tr}_S \left\{ \mu_{vib} \mathcal{G}(t_{\text{det.}}) \mu_{vib}^{\times} \mathcal{G}(T) \mu_{el}^{\times} \mathcal{G}(t_{\text{exc.}}) \rho_{\mu} \right\}. \end{aligned} \tag{6.24}$$

Working also with the RWA invokes further simplifications, specifically to the number of pathways[185], giving the response function as a sum of rephasing (RP) and non-rephasing (NR) pathways

$$R_3(t_{\text{det.}}, T, t_{\text{exc.}}) = R_3^{\text{RP}}(t_{\text{det.}}, T, t_{\text{exc.}}) + R_3^{\text{NR}}(t_{\text{det.}}, T, t_{\text{exc.}}), \tag{6.25}$$

where, denoting $K = \mathrm{NR}, \mathrm{RP}$,

$$R_3^K(t_{\mathrm{det.}}, T, t_{\mathrm{exc.}}) = R_{\mathrm{GSB}}^K(t_{\mathrm{det.}}, T, t_{\mathrm{exc.}}) - R_{\mathrm{ESA}}^K(t_{\mathrm{det.}}, T, t_{\mathrm{exc.}}) \tag{6.26}$$

where GSB denotes the ground-state bleach pathways given by

$$\begin{aligned} R_{\mathrm{GSB}}^{\mathrm{RP}}(t_{\mathrm{det.}}, T, t_{\mathrm{exc.}}) = &\left(\frac{i}{\hbar}\right)^3 \theta(t_{\mathrm{det.}})\theta(T)\theta(t_{\mathrm{exc.}}) \\ &\times \mathrm{Tr}_S \left\{\mu_{vib}^- \mathcal{G}(t_{\mathrm{det.}})\mu_{vib}^+ \mathcal{G}(T)\mu_{el}^- \mathcal{G}(t_{\mathrm{exc.}})\rho_{\mu^+}\right\} \end{aligned} \tag{6.27}$$

$$\begin{aligned} R_{\mathrm{GSB}}^{\mathrm{NR}}(t_{\mathrm{det.}}, T, t_{\mathrm{exc.}}) = &\left(\frac{i}{\hbar}\right)^3 \theta(t_{\mathrm{det.}})\theta(T)\theta(t_{\mathrm{exc.}}) \\ &\times \mathrm{Tr}_S \left\{\mu_{vib}^- \mathcal{G}(t_{\mathrm{det.}})\mu_{vib}^+ \mathcal{G}(T) \left(\mathcal{G}(t_{\mathrm{exc.}})\rho_{\mu^+}^\dagger\right) \mu_{el}^+\right\} \end{aligned} \tag{6.28}$$

and ESA denotes the excited state absorption pathways given by

$$\begin{aligned} R_{\mathrm{ESA}}^{\mathrm{RP}}(t_{\mathrm{det.}}, T, t_{\mathrm{exc.}}) = &\left(\frac{i}{\hbar}\right)^3 \theta(t_{\mathrm{det.}})\theta(T)\theta(t_{\mathrm{exc.}}) \\ &\times \mathrm{Tr}_S \left\{\mu_{vib}^- \mathcal{G}(t_{\mathrm{det.}})\mu_{vib}^+ \mathcal{G}(T) \left(\mathcal{G}(t_{\mathrm{exc.}})\rho_{\mu^+}\right) \mu_{el}^-\right\} \end{aligned} \tag{6.29}$$

$$\begin{aligned} R_{\mathrm{ESA}}^{\mathrm{NR}}(t_{\mathrm{det.}}, T, t_{\mathrm{exc.}}) = &\left(\frac{i}{\hbar}\right)^3 \theta(t_{\mathrm{det.}})\theta(T)\theta(t_{\mathrm{exc.}}) \\ &\times \mathrm{Tr}_S \left\{\mu_{vib}^- \mathcal{G}(t_{\mathrm{det.}})\mu_{vib}^+ \mathcal{G}(T)\mu_{el}^+ \mathcal{G}(t_{\mathrm{exc.}})\rho_{\mu^+}^\dagger\right\}. \end{aligned} \tag{6.30}$$

Here we have also used the raising and lowering operator representation of the vibrational dipole operator

$$\mu_{vib}^+ = \mu_{A,f} + \mu_{B,f} = a_{A,f}^\dagger \langle A|+\rangle a_{B,f}^\dagger \langle B|,\rangle \tag{6.31}$$

$$\mu_{vib}^- = \left(\mu_{vib}^+\right)^\dagger \tag{6.32}$$

where $a_{I,f}^\dagger$ denotes the bosonic creation operator of the fast mode of chromophore I. The signal observed experimentally is then the double Fourier transform over the excitation and detection times,

$$\chi(\omega_{\mathrm{det.}}, T, \omega_{\mathrm{exc.}}) = \mathrm{Re}\left\{\chi^{\mathrm{RP}}(\omega_{\mathrm{det.}}, T, \omega_{\mathrm{exc.}}) + \chi^{\mathrm{NR}}(-\omega_{\mathrm{det.}}, T, \omega_{\mathrm{exc.}})\right\}, \tag{6.33}$$

where,

$$\chi^{\mathrm{K}}(\omega_{\mathrm{det.}}, T, \omega_{\mathrm{exc.}}) = \int dt_{\mathrm{det.}} \int dt_{\mathrm{exc.}} e^{i(\omega_{\mathrm{det.}} t_{\mathrm{det.}} + \omega_{\mathrm{exc.}} t_{\mathrm{exc.}})} \times R_3^K(t_{\mathrm{det.}}, T, t_{\mathrm{exc.}}). \tag{6.34}$$

The visualization of the data is typically best presented in the form of excitation frequency ($\omega_{\mathrm{exc.}}$)-detection frequency ($\omega_{\mathrm{det.}}$) correlation plots of the total absorptive spectrum parameterized by T.

Eigenstate Structure of the Model Hamiltonian

The effects from the distinct vibronic coupling mecahnisms are displayed in the eigenenergy levels shown in Fig. 6.1b for which we will first focus on the electronic/vibronic manifold. In the case where there is no vibronic coupling ($S = 0$, $\eta = 0$) we see that the lowest energy eigenstates in the excited state manifold consist of two electronically mixed states with respect to the chromophore sites denoted by a square and circle. We note that, throughout this chapter, we will colloquially refer to excitonic states of particular electronic or vibronic mixing character in accordance with their assigned shapes in Fig. 6.1b. There is an additional state, denoted by a star, which is similar in its site character to the lowest-energy (square) eigenstate, but has a single quantum from the low-frequency mode on the A chromophore. This state is nearly degenerate with the higher-energy (circle) eigenstate, but is composed of sites that are virtually uncoupled to the aformentioned eigenstates due to the orthogonality of the vibrational states on different electronically excited states without any vibronic coupling.

When vibronic mixing is instigated through FC activity ($S = 0.1$, $\eta = 0$), the nearly degenerate energy eigenstates are strongly coupled and energetically split into the star state, which is a vibronically mixed state due to the additional character of multiple low-frequency vibrational states from a *single* electronically excited state, and the circle state, which is still primarily electronically coupled, but has additional character of multiple low-frequency vibrational states from *both* electronically excited states. We thus refer to the energy eigenstates denoted by a square and circle as electronically coupled states, while the state denoted by a star is referred to as a vibronically coupled state.

Although difficult to capture in the energy level diagram, the energetic splitting between the circle and star states increases in the HT active case (S=0.1, $\eta = -0.15$) versus FC active (S=0.1, $\eta = 0$). In either scenario, the vibronic coupling clearly serves to distribute site A character throughout the excited state manifold, therefore promoting additional possible relaxation pathways. HT activity, though, specifically results in the distribution of pure electronic character from site A to the vibronically coupled state (star) in contrast to FC activity which only distributes vibrational (low-frequency mode) character from site A. In this way, in the presence of HT activity, the circle state is nearly invariant, retaining its electronic-coupling character, but the star state gains pure electronic-coupling character, unlike in the FC active scenario. While not shown in Fig. 6.1b, the next set of excitonic states in the electronic/vibronic manifold are electronic replicas of the star and circle states with an additional quantum in each vibrational state of the slow mode. These unpictured states thus contribute to the intensity borrowing effect of HT activity in the absorption lineshape.

Currently, the discussion has been restricted to the electronic/vibronic manifold, however, a comparison of the site character of the excitonic states in the vibrational manifold reveals striking differences. In fact, the high-frequency excited state vibrational modes are clearly influenced by changes in relative site contributions, which makes them sensitive reporters of vibronic mixing mechanisms. The eigenstates in the vibrational manifold are also labelled by shapes denoting the predominant transitions from the electronic/vibronic manifold due to the vibrational transition dipole moment. In this manner, we note that excitonic states in the vibrational manifold with the same shape as those in the electronic/vibronic manifold have the same electronic/vibronic character. When S is nonzero, transitions between these manifolds can change the electronic/vibronic character due to changes in the vibrational transition dipole moment matrix elements. A focused discussion on the interpretation of vibronic coupling through a spectroscopic interrogation of the electronic/vibronic manifold versus both the electronic/vibronic and vibrational manifolds is reserved for Sec. 6.3.

6.3 Static Signatures of Vibronic Coupling

While 2DEV spectroscopy gives a time-dependent spectroscopic signal from which dynamical phenomena can be inferred, it is first useful to uncover the ways in which it can be utilized to unravel the detailed structure arising from the underlying system Hamiltonian. In particular, we compare the signal observed from electronic linear absorption spectroscopy and the signal observed from 2DEV spectroscopy at a waiting time of $T = 0$ fs. To show the specific effects arising from FC activity and HT activity we have computed both spectra with pair values of S and η at $(S, \eta) = (0, 0), (0.1, 0), (0.1, -0.15)$, which are shown in Fig. 6.2. When both parameters are set to zero, that is, there is neither FC nor HT activity, we expect to see coupling between the two chromophores that is purely electronic in nature. Indeed the linear absorption spectra (Fig. 6.2a) shows two peaks that are inhomogeneously broadened with respect to the stick spectra due to the weak coupling between the system and bath. These peaks are transitions to the two lowest excitonic states in the excited state manifold, with zero vibrational quanta in the low-frequency modes, which have an excitonic energy gap of $\hbar\Omega_R$. The 2DEV spectrum gives additional structural information in both the GSB (positive) or ESA (negative) signals from the quartet structure owing to the correlation of the excitonic states with the vibrational character of the fast modes for each chromophore in each electronic state populated. The two excitonic transitions are observable as bands along the excitation axis with splitting equal to $\hbar\Omega_R$, however, additional cross-correlation between these bands at various positions along the detection axis is observed (see Fig. 6.2a in the region spanning 1570∼1595 cm^{-1}) which shows that the excitonic states are comprised of sites that are electronically coupled. The peaks along each band report on the population of particular excitonic states in electronic/vibronic manifold. Since the high-frequency modes are local to each site, there are two vibrational peaks of the same electronic/vibronic character per band (denoted by the same shapes) that appear through coupling with excitonic states in the vibrational manifold (see Fig. 6.1b). This locality also provides some information about the relative populations in each site rather than purely excitonic populations, despite working in the electronically coherent regime. The 2DEV signal, even in this very simple case, goes well beyond the observable description obtainable by linear absorption—particularly because both the electronic/vibronic and vibrational manifolds are directly interrogated spectroscopically in the former. In this way, it is understandable how vibronic mixing mechanisms could be heavily obscured—even in other multidimensional

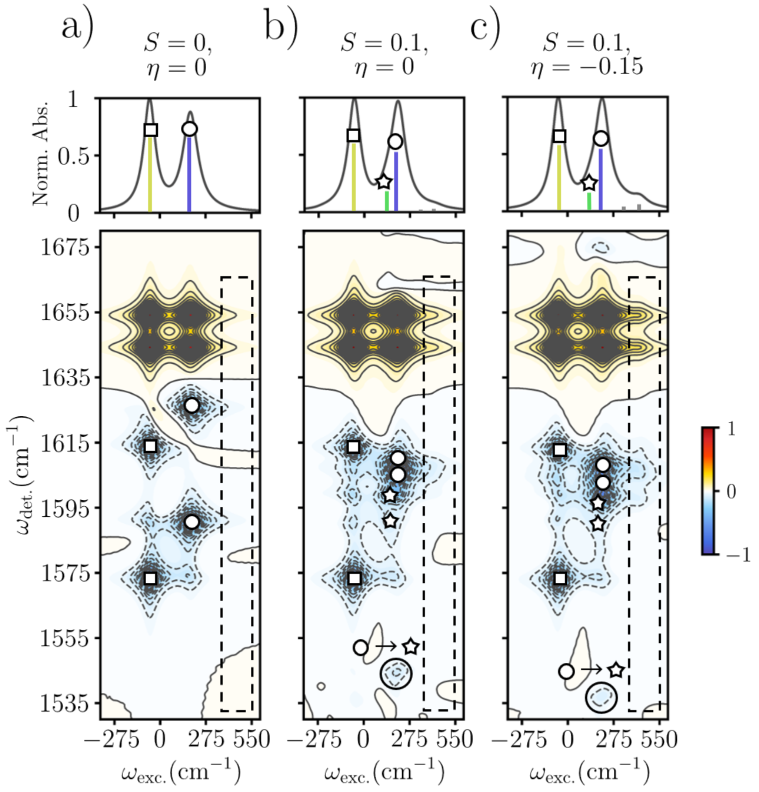

Figure 6.2: (Top row) Electronic linear absorption spectra for the three treatments of vibronic coupling—a) no coupling, b) FC activity, and c) HT activity. Stick spectra are also shown where yellow (square), green (star), and blue (circle) indicate the three lowest-energy excitonic transitions, explicitly described in Fig. 6.1, while gray sticks indicate higher-lying vibronic transitions. (Bottom row) Corresponding 2DEV spectra at $T = 0$ fs. Positive, red/yellow features indicate GSBs and negative, blue features indicate ESAs. Contour levels are drawn in 2% intervals. All spectra have been normalized to the maximum in each data set. ESA peaks are labeled by shapes according to transitions to the electronic/vibronic manifold as indicated in Fig. 6.1. The black, dashed box highlights the higher-excitation frequency portion of the spectra where vibronic transitions appear. In b) and c), the circled ESA transition at the bottom is assigned to a transition between states of different excitonic character through a vibrational pulse.

spectroscopies—that are limited only to interrogations of the electronic/vibronic manifold.

The stark contrast in detectable information between these spectroscopies arises in the presence of vibronic coupling activity. The linear absorption and 2DEV spectra for the FC active case (S=0.1, η=0) are shown in Fig. 6.2b. Despite a significant change in the structure of the excitonic states, the linear absorption spectrum is virtually indistinguishable from the vibronically inactive spectrum when accounting for broadening. As is shown in the stick spectrum, the new vibronic excitonic state (star) is excited, however, due to the relative weakness of the transition and the comparable excitonic gap between the vibronic and the higher-energy electronic excitonic states (star and circle, respectively) this state is masked under typical broadening. This excitonic state is, however, clearly shown in the 2DEV spectrum. As was expected from analysis of the excitonic states (see Sec. 6.2), the lowest-lying excitonic state remains largely unchanged in its excitation energy and vibrational structure, however, additional structure in the cross-coupling along the detection axis of this band is observed since this excitonic state now has site character that couples to the vibronic (star) state in addition to the higher-energy electronic (circle) state. In essence, detection via the vibrational manifold serves to disperse the spectroscopic signatures of the excitonic states along the detection axis where even slight changes due to various couplings can be readily observed.

The higher-energy excitation band retains this substructure from the additional vibronic excitonic state, however, it is notable that there is a small, but detectable, energy shift along this band corresponding to the different excitonic states—the vibronic (star) state is slightly lower in energy than the electronic (circle) state. An additional subtle feature arises along the higher-energy excitation band at a lower detection frequency. This feature is a unique consequence of FC activity and is a signature of the site mixing in both the vibronic/electronic (star/circle, respectively) states and newly allowed transitions in the vibrational TDM. Specifically, as a result of the mixing, vibrational transitions with lower energy difference (electronic circle to vibronic star transitions in Fig. 6.2b) can emerge—a transition that is expressly disallowed without FC activity due to the orthogonality of the excitonic states with respect to the low-frequency vibrational states. We also note that additional broadening in the higher-energy band is exhibited in both the GSB and ESA signals, which we attribute to coupling between the higher-energy (circle) excitonic state and other vibronic states, however, this effect is likely not distinguishable in practice.

In the final case, ($S = 0.1, \eta = -0.15$), we consider the simultaneous effect of both FC activity and HT activity on the structure of the spectra. While the vibronic state is still masked by broadening in the linear absorption spectrum, a new peak appears at an excitation energy nearly $\hbar\omega_{A,s}$ larger than the higher-energy excitonic (circle) state, which is due to the intensity borrowing effect of HT activity, i.e. there are even stronger dipole-allowed transitions to higher-lying excitonic states with additional vibrational quanta in the low-frequency mode. These additional transitions specifically build on the vibrational progression of the low-frequency mode in the circle and star states—rather than the square state—due to the near-resonance condition of the circle and star states in the FC inactive case. The 2DEV spectra expectedly picks up this feature along the excitation axis in both the GSB and ESA signals, however, it is interestingly correlated with IR transitions similar to the circle state rather than the star state or a combination of the circle and star state. This correlation is due to the relative intensities that can be borrowed from the circle and star states, that is, the HT activity induces transitions that are like the circle state plus one vibrational quantum in the low-frequency mode with a stronger signal than the star state. This correlation also indicates that 2DEV spectroscopy directly reports on HT activity if the side-bands exactly replicate, with lower intensity, the lower-energy excitonic states along the detection axis and if no additional IR transitions emerge at lower detection energies akin to the circle to star IR transition from FC activity described above.

A final point regarding the HT activity is that the observed signal here—the intensity borrowing from the dominant excitonic states along the excitation axis—is strictly due to the form of the non-Condon activity we have chosen, namely that the low-frequency mode changes the magnitude of the dipole moment and thus changes the electronic TDM directly. The same effect in the electronic coupling could arise, to first-order, from different modes that modulate the relative positions of the chromophores, but leave invariant the TDM. Since the structure of the excitonic states is apparently not influenced as much by HT activity as FC activity in the electronically coherent regime, this HT activity distinctly shows up as stronger side-band transitions along the excitation axis, which would not be present in other forms of mode-dependent electronic coupling terms.

6.4 Dynamical Signatures of Vibronic Coupling

With 2DEV spectroscopy established as a sensitive tool for witnessing vibronic effects, we turn to an analysis of how these effects manifest in the dynamics from the spectra. Rather than analyzing the complex dynamical signatures from the spectra in the time-domain, we convert to the frequency-domain to construct beat maps in the waiting time as a function of the excitation and detection frequencies. Specifically, these beat maps are formed by first filtering out the high-frequency oscillatory dynamics using a Savitzky-Golay filter[220], which produces a dynamical map of the excitonic population dynamics. These population dynamics are then subtracted from the total spectra yielding the remaining coherent dynamical components (denoted by $\tilde{\chi}$) from which the power spectrum is calculated as

$$S(\omega_{\text{det.}}, \omega_T, \omega_{\text{exc.}}) = |\Xi(\omega_{\text{det.}}, \omega_T, \omega_{\text{exc.}})|^2 \tag{6.35}$$

where

$$\Xi(\omega_{\text{det.}}, \omega_T, \omega_{\text{exc.}}) = \int dT e^{-i\omega_T T} \tilde{\chi}(\omega_{\text{det.}}, T, \omega_{\text{exc.}}). \tag{6.36}$$

In the following, we will show how these oscillatory components report directly on the interplay between excitonic states. Additionally, the conclusions drawn from this specific type of beat map analysis can be readily applied to more complex systems where the excitonic manifold as well as the dynamics are often highly congested.

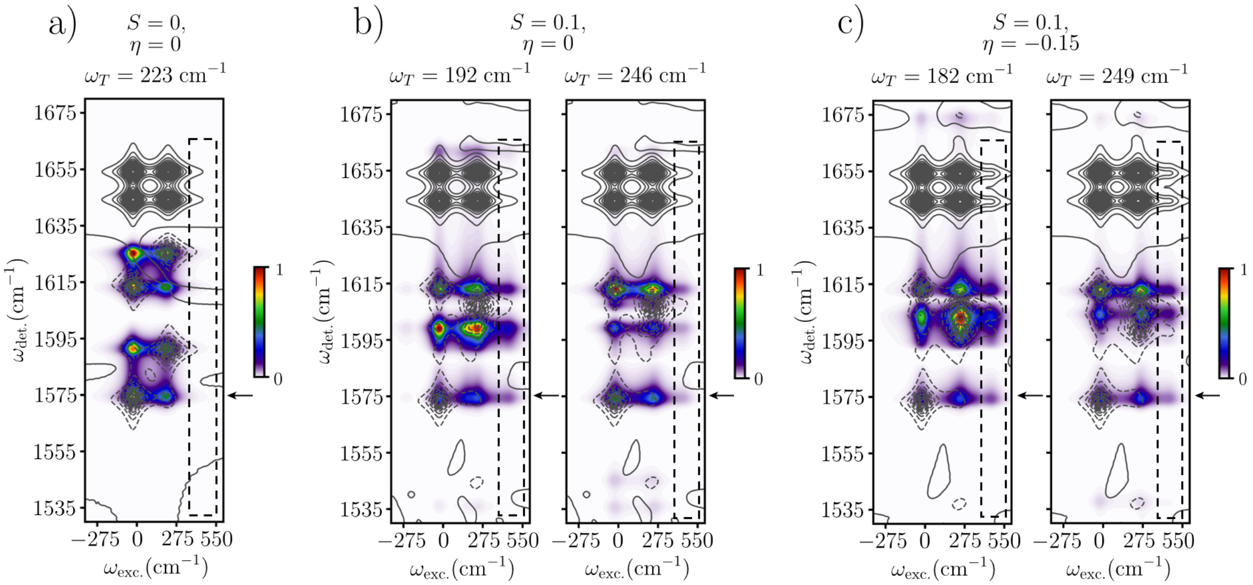

Figure 6.3: Beat maps at specific ω_T values corresponding to the excitonic energy gaps in the models where there is a) no vibronic coupling, b) FC activity, and c) HT activity. For each model, the plots are normalized to the maximum beat frequency amplitude. The colormap indicates spectral regions that oscillate at the given ω_T values with amplitudes ranging from zero (white) to one (red), the maximum value. Contour lines indicate the 2DEV spectra for each model at $T = 0$ fs. The black, dashed box highlights the higher-excitation frequency portion of the spectra where vibronic transitions appear. The black arrows indicate the spectral region of $\omega_{\mathrm{det.}}$ that is further analyzed in Fig. 6.5.

Population dynamics of the sites can also be inferred from these dynamical beat maps since 2DEV probes local intramolecular modes.[153] To illustrate this point, we compare the dynamical beat maps to the population dynamics starting from an initial vertical excitation to the B site given by,

$$\rho(0) = \mu_B \rho_{eq} \mu_B^{\dagger}. \tag{6.37}$$

This initial condition considers specifically the rapid population transfer from the higher-energy B site to the lower-energy A site to show the complex dynamical features observed in this ultrafast process comparable to realistic systems such as LHCII. While this initial condition is not entirely physically realizable as the chromophores are intrinsically coupled and cannot be isolated in this way, it is useful to show how the dynamical signatures in 2DEV spectra are exhibited in more idealistic simulations for drawing connections between future atomistic simulations for which corresponding spectral simulations are beyond computational capabilities.

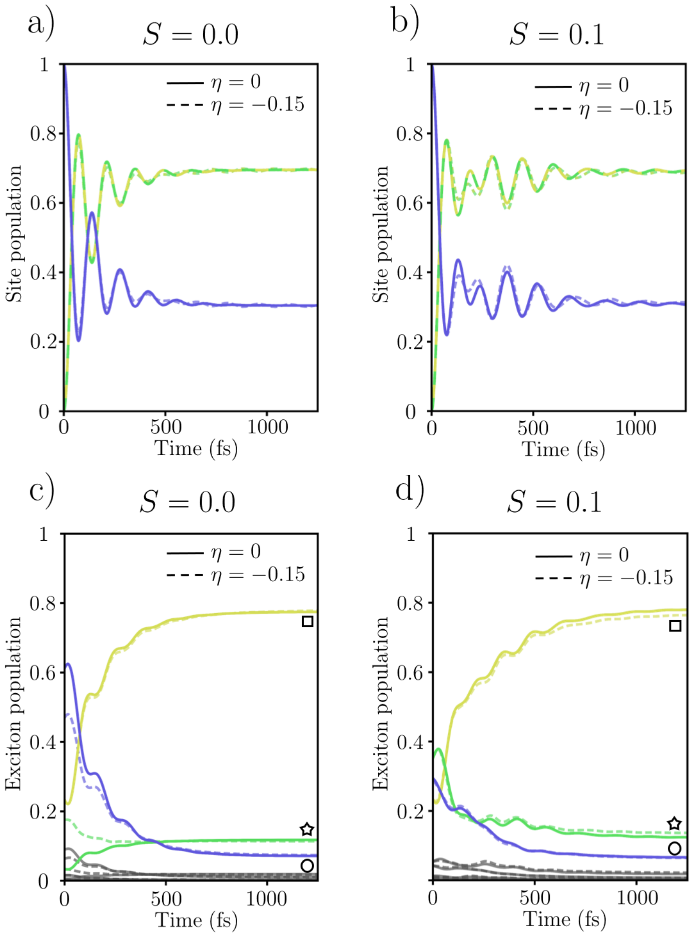

Figure 6.4: (Top row) Site populations for an initially, vertically excited wavepacket into the B site where a) $S = 0$ and b) $S = 0.1$. Yellow/green indicates the population of site A and blue indicates the population of site B. (Bottom row) Corresponding exciton populations where a) $S = 0$ and b) $S = 0.1$. Yellow (square), green (star), and blue (circle) indicate the populations of the three corresponding lowest-energy exciton levels, explicitly described in Fig. 6.1, while gray indicates the populations of all higher-lying levels. Throughout, solid lines indicate $\eta = 0$ and dashed lines indicate $\eta = -0.15$ (i.e. no HT activity versus HT activity).

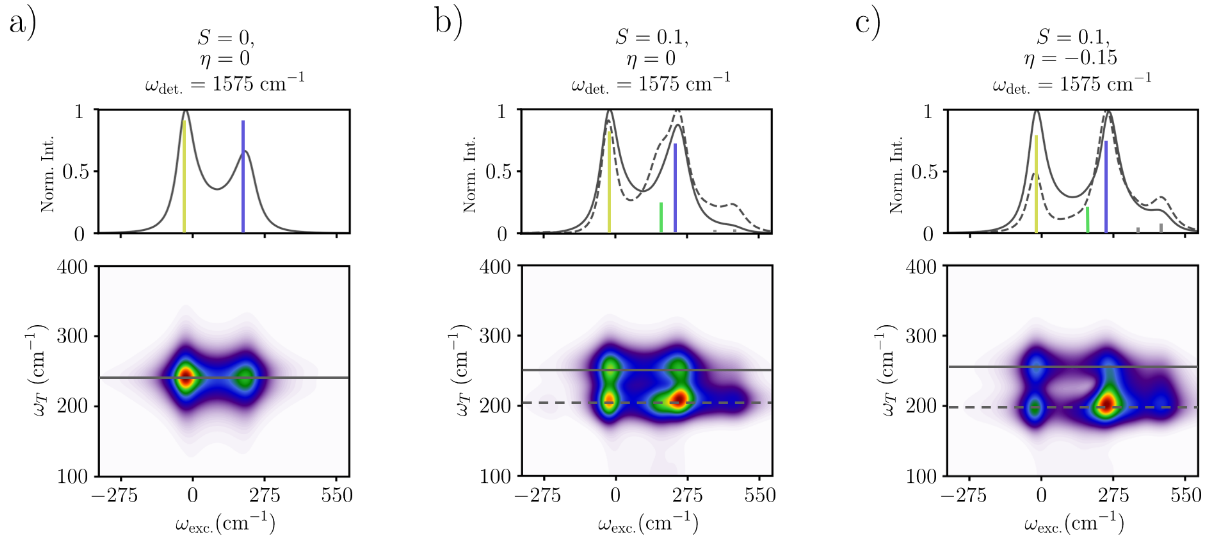

Figure 6.5: Beat maps at a fixed detection frequency, $\omega_{\mathrm{det.}}$ (indicated by the black arrows in Fig. 6.3), for the three models where there is a) no vibronic coupling, b) FC activity, and c) HT activity. The corresponding colormaps are identical to those in Fig. 6.3. Slices along the excitation axis at specific beat frequencies, corresponding to the exciton energy gaps in the model, are shown above each beat map. Also shown in these plots for comparison are the electronic linear absorption stick spectra as described in Fig. 6.2.

In the beat maps, we observe peaks in the dynamical frequency ω_T that correlate with the excitonic states at particular $\omega_{\mathrm{exc.}}$ and $\omega_{\mathrm{det.}}$. The correlations between the dynamical frequency and the excitonic states specifically show the contribution from certain states to a particular dynamical signature, that is, which states beat at which frequencies. We have analyzed these beat maps in each parameter set (S, η), which are shown in Fig. 6.3 as overlayed with the $T = 0$ fs 2DEV spectra for clearer identification. In the case $(S = 0, \eta = 0)$ we observe a single dynamical frequency corresponding to the bare excitonic gap $\hbar\Omega_R$. This signature is to be expected as there is negligible contribution of FC activity from the high-frequency modes and no vibronic contribution from the low-frequency mode. Thus, the state populations oscillate, at times shorter than the onset of thermalization, in accordance with the dynamics of a two-level system. This beat map is consistent with the population dynamics, shown in Fig. 6.4a and c, which show the site and excitonic populations, respectively. In particular, the site populations exhibit beating only at the excitonic gap between the chromophoric states with subsequent thermal relaxation. This same beating appears in the excitonic populations where it is convoluted with population transfer between the excitonic states. We have also computed the population dynamics considering only the HT activity, $(S = 0, \eta = -0.15)$, and found that there is little to no difference in the site population dynamics. Rather, the difference is in the initial excitation condition of the excitonic populations due to the aforementioned change in the structure of the excitonic states to which we are exciting.

With the addition of both cases of vibronic coupling comes an additional dynamical frequency associated with quantum beating at the excitonic gap between the square and star state, which is distinct from pure Rabi oscillations. While the Rabi frequency is slightly modified, this beating frequency is still associated predominantly with the excitonic state of mostly electronic character (circle), while the additional frequency is associated with the vibronic state (star). This distinction is emphasized when considering the correlation between the beat frequency and the excitonic state character as shown in Fig. 6.3b and c, which show the beat maps for the $S = 0.1$ and $\eta = 0, -0.15$ cases. In both cases, the modified Rabi frequency is slightly higher due to the additional coupling but in the FC-only active case, this frequency is specifically correlated with the circle state with a small contribution from the star state. This correlation is most notable when considering the lower detection frequency circle to star transition (1530∼1540 cm^{-1}) which has a weak signal at the modified Rabi frequency but no signal at the new vibronic frequency. The vibronic frequency has much more participation from the vibronic (star) state than does the modified Rabi frequency. At this new frequency, there is also notably more activity at higher-lying vibronic states along the excitation axis suggesting that these higher-lying vibronic states are relaxing mainly to the star state. These excitation side-band correlations become significantly more prevalent in the HT active case ($S = 0.1, \eta = -0.15$). Noticeably, however, there is enhanced activity of these higher-lying vibronic states in *both* frequency components. The main difference is that HT activity leads to borrowing of pure electronic character from the circle to the star state (see Fig. 6.1b). This activity, in turn, leads to more equal contributions from both states at the new vibronic frequency and the (further) modified Rabi frequency facilitating participation of the higher-lying vibronic states across all beat frequencies.

In both cases, $(S, \eta) = (0.1, 0), (0.1, -0.15)$, the population dynamics (shown in Fig. 6.4b and d) are virtually identical and we will thus consider them in unison. The site populations show a seemingly polychromatic beating pattern with initial electronic oscillations corresponding to the modified Rabi frequency crossing over to beating on the vibronic frequency. This pattern is also exhibited in the excitonic populations with an initial beat between the electronic (square and circle) states followed by correlated oscillations in the square and star states. In this instance, it appears as though population transfer between the chromophores is assisted by vibronic coupling, specifically FC activity, by protecting the transfer from back-oscillations. In particular, the crossover from purely electronic oscillations at short times (about one period of the modified Rabi frequency) to oscillations at the excitonic gap coupling the star state prohibits further population from transferring back to the B site after transferring to the A site. We emphasize, however, that this is only a weakly drawn conclusion with respect to energy transfer in realistic systems and requires further analysis in which we consider various regimes including the electronically incoherent regime. For example, the overall transfer between sites A and B in this case is largely dictated by the electronic coupling which distributes a reasonable amount of site B character in the lowest excitonic state—in direct competition with the vibronically-induced distribution of site A character among the higher-lying states. In the incoherent regime, the lowest excitonic state will almost completely resemble site A, however, vibronic mixing will still serve to distribute site A character throughout the higher-lying excitonic states in the same way as for the models considered here (see Fig. 6.1b). Therefore, we expect that vibronic effects will manifest more strongly in the incoherent regime where they are the dominant means for the distribution of site A character—without the competing effects of electronic coupling distributing site B character in the opposite, undesirable direction. The treatment of this regime in regards to 2DEV spectral simulations, though, is beyond the perturbative limit of Redfield theory used in this study. Nevertheless, vibronic coupling has a clear impact on the population dynamics that emerges in the dynamical signatures of the 2DEV spectra from these models.

We further note that in both cases of vibronic mixing there are congested signals in the beat maps. It is thus useful to consider a particular slice of these beat maps along the detection axis associate with the lowest-lying excitonic state. Since this state is mostly unchanged by vibronic coupling, it can serve as a sensitive reporter of the changes in the dynamical beat frequencies through which the effects from vibronic mixing emerge. These excitonic-state specific beat maps are shown in Fig. 6.5. Along with these two-dimensional beat maps we consider slices along the observed dynamical frequencies shown relative to the linear absorption stick spectrum. In the vibronically inactive case, we again observe a single dynamical frequency associated with the Rabi frequency to which both excitonic states contribute. This signature clearly identifies the connectivity between these states.[12] In systems with more complex excited state manifolds, i.e. with vibronic mixing, the implications of these maps are striking. For example, in the FC active case ($S = 0.1, \eta = 0$) (Fig. 6.5b) the additional peaks in the vibronic frequency band illustrate how energy flows within the excitonic manifold. By looking at slices along ω_T at the modified Rabi frequency, it is apparent that population primarily flows from the circle to square state. However, at ω_T specific to the vibronic frequency, there is an additional peak at the higher-lying vibronic side-band as well as at the star state. This distinction reveals how FC activity promotes a "vibronic funnel" whereby excitation flows from the higher-lying states through the circle and star states down to the lowest excitonic state (square)—clearly demonstrating the additional relaxation channel. In the HT active case ($S = 0.1, \eta = -0.15$) (Fig. 6.5c), we see a similar features along the lower ω_T frequency, however, in the higher ω_T value, there is amplified contribution from the higher-lying vibronic states as compared to ($S = 0.1, \eta = 0$) (Fig. 6.5b). This feature is perhaps a clearer demonstration of how HT activity results in additional mixing, i.e. additional vibronically-promoted relaxation pathways through the modified electronic coupling.

6.5 Conclusion

In this work, we have introduced a minimal model for an electronically/vibronically coupled heterodimer for which two distinct mechanisms of vibronic coupling can be systematically tuned. This model adequately describes the coupling of a low-frequency nuclear mode to site-exciton states in a multichromophoric system and introduces a set of local high-frequency modes to report on the vibronic coupling in 2DEV spectroscopy. This low-frequency mode can induce vibronic coupling through Franck-Condon activity, which couples the nuclear mode to the site energies, or through Herzberg-Teller activity, which introduces nuclear dependence of the electronic coupling through the TDM of a single chromophore.

Through the development of these heterodimer models, we have shown how different mechanisms of vibronic coupling, or lack thereof, manifest in both the composition of the resulting excitonic states as well as the 2DEV spectra through both static and dynamical contributions to the overall signal. In the absence of vibronic coupling, the system resembles that of a two-level model in which the dominant excitonic states are observable in the 2DEV spectra through excitation bands with vibrational structure of the chromophores and cross-peaks characterizing the electronic coupling. When the low-frequency mode is coupled to the electronic manifold, vibronic structure emerges due to an additional vibronically mixed state in the case of FC activity and an increased signal in the electronic side-band arising specifically from HT activity rather than mode-dependent electronic coupling. 2DEV spectroscopy also reports on the population dynamics due to the locality of the vibrational probe and can thus reveal nature of quantum beating patterns during energy transfer. Without vibronic coupling, the system beats at a single frequency associated with the electronic coupling while vibronic coupling introduces a new quantum beat frequency due to additional vibronically mixed excitonic states. These beat frequencies directly characterize the population dynamics and show the additional relaxation pathways vibronic coupling affords the energy transfer dynamics. Ultimately, the insight gained from this work provides a general framework for the interpretation of the underlying Hamiltonian of vibronically coupled systems. In fact, connections between previous experimental work and the present models, addressed elsewhere, have uncovered details about the vibronic coupling mechanisms in LHCII.[9]

Various aspects do, however, require further investigation. For example, we have only considered here the electronically coherent regime where HT activity has little effect on the overall energy transfer, a feature which we do not expect to generically hold true across all regimes. With regard still to the nuclear dependence of the electronic coupling, our treatment is specific to that which arises from nuclear dependence of the dipole moment, however, a similar effect in the electronic coupling due to the spatial/orientational changes from short- or long-range nuclear fluctuations could be expected. A more systematic understanding of the effect on the energy transfer and the signature in 2DEV spectroscopy from these separate coupling mechanisms warrants further study. While generalizations to the model presented here would be required, the way in which electronic-nuclear coupling mechanistically mediates dynamics through conical intersections[101, 213] or assists in charge transfer[70, 82, 289] and singlet fission[225] are similarly deserving of explicit theoretical treatment with respect to 2DEV spectroscopy.

Appendix A

Details of the MCTDH Equations of Motion

For the sake of clarity within this appendix we repeat here the MCTDH wavefunction,

$$|\Psi(t)\rangle = \sum_{\alpha} \sum_{j_1,j_2,\ldots,j_N} A_{\alpha,j_1,j_2,\ldots,j_N}(t)|\varphi_\alpha\rangle \prod_{m=1}^{N} |\phi^m_{\alpha,j_m}(t)\rangle, \tag{A.1}$$

which has the following equation of motion

$$i\dot{A}_J(t) = \sum_K \langle\Phi_J(t)|H|\Phi_K(t)\rangle A_K(t) \tag{A.2}$$

$$i|\dot{\phi}^m_{\alpha,j}(t)\rangle = (1 - P^{(m)}_\alpha) \sum_{\beta,k,l} (\rho^{-1}_{m,\alpha})_{jk} \langle H\rangle^{(m)}_{\alpha\beta,kl} |\phi^m_{\beta,l}(t)\rangle, \tag{A.3}$$

the former of which is the equation of motion for the coefficients and the latter the equation of motion for the SPFs. The equation of motion for the SPFs contains a number of complex terms, which we will discuss in order. The first of these terms is the projector, which ensures the orthonormality of the SPFs and projects out any of the propagation included in the propagation of the coefficients. The projector is given by the following equation

$$P^{(m)}_\alpha(t) = \sum_j^{n_m} |\phi^{(m)}_{\alpha,j}(t)\rangle\langle\phi^{(m)}_{\alpha,j}(t)|. \tag{A.4}$$

For the latter two terms, it is useful to introduce the single-hole form of the MCTDH wavefunction, which emphasizes a particular mode

$$|\Psi(t)\rangle = \sum_\alpha \sum_j |\phi^m_{\alpha,j}(t)\rangle |G^m_{\alpha,j}(t)\rangle, \tag{A.5}$$

and $|G^m_{\alpha,j}(t)\rangle$ is the single-hole function given by

$$|G^m_{\alpha,j}(t)\rangle = \sum_{j_p:p\neq m} A_{\alpha,j_1,\ldots,j_{m-1},j,j_{m+1}\ldots,j_N}(t)|\varphi_\alpha\rangle \prod_{p\neq m} |\phi^p_{\alpha,j_p}(t)\rangle. \tag{A.6}$$

The density matrices can now be defined as

$$(\rho_{m,\alpha})_{jk} = \langle G^m_{\alpha,j}(t)|G^m_{\alpha,k}(t)\rangle = \sum_{j_p:p\neq m} A^*_{\alpha,j_1,\ldots,j_{m-1},j,j_{m+1}\ldots,j_N} A_{\alpha,j_1,\ldots,j_{m-1},k,j_{m+1}\ldots,j_N}. \tag{A.7}$$

The interpretation of this matrix is comparable (though not the same) as the density matrix in quantum mechanics in that it describes to some degree the populations of the SPFs for a particular mode. As SPFs can be unpopulated, typically initially, during a calculation, this matrix is not generally invertible and is thus regularized in some way, often by adding a small, positive parameter ϵ to the diagonal elements. A deeper discussion on regularization schemes or alternative integrators that avoid inversion of the density matrices can be found in Ref. [159, 167, 272, 271].

The SPFs undergo action from the Hamiltonian through the mean-field matrices, which are defined as

$$\langle H\rangle^{(m)}_{\alpha\beta,kl} = \langle G^m_{\alpha,k}(t)|H|G^m_{\beta,l}(t)\rangle. \tag{A.8}$$

Using the sum-of-products form of the Hamiltonian

$$H = \sum_r^s d_r h_r^{(\mathrm{el})} \prod_{m=1}^N h_r^{(m)} \tag{A.9}$$

gives the mean-field matrices as

$$\langle H\rangle^{(m)}_{\alpha\beta,kl} = \sum_{r=1}^s d_r \mathcal{H}^{(m,r)}_{\alpha\beta,kl} h_r^{(m)} \tag{A.10}$$

where

$$\mathcal{H}^{(m,r)}_{\alpha\beta,kl} = \sum_{k_p l_p:p\neq m} A^*_{\alpha,k_1,\ldots,k_{m-1},k,k_{m+1},\ldots,k_N} A_{\beta,l_1,\ldots,l_{m-1},l,l_{m+1},\ldots,l_N} \langle\varphi_\alpha|h_r^{(\mathrm{el})}|\varphi_\beta\rangle \prod_{p\neq m} \langle\phi^p_{\alpha,k_p}|h_r^{(p)}|\phi^p_{\beta,l_p}\rangle. \tag{A.11}$$

The final component of the full equation of motion is the matrix elements for propagating the coefficients, which are given by—using Eq. A.10 for the Hamiltonian—

$$\langle\Phi_J(t)|H|\Phi_K(t)\rangle = \sum_{r=1}^s d_r \langle\varphi_\alpha|h_r^{(\mathrm{el})}|\varphi_\beta\rangle \prod_{m=1}^N \langle\phi^m_{\alpha,j_m}|h_r^{(m)}|\phi^m_{\beta,k_m}\rangle. \tag{A.12}$$

For a further discussion on different numerical schemes for propagating the equations of motion, we refer the reader to Refs. [18]. Since the MCTDH algorithm utilizes the sum-of-products Hamiltonian and the SPFs are expanded in a DVR basis it is only necessary to compute the matrix elements (from the perspective of the PBFs) of the kinetic energy and position operators and the SPF matrix elements are then efficient element-wise products of functions of pre-computed operators. For propagation of the MCTDH wavefunction, efficient tensor contraction libraries can be utilized, which due to recent development and computational advances are well suited to parallel supercomputing architectures and specialized computing units such as graphical processing units (GPU) and tensor processing units (TPU).

Appendix B

Choosing ω^* for Hybrid Quantum Master Equations

Here we consider the choice of the parameter ω^* in the TCL2-FM method for conical intersection models. We note that for site-exciton models an efficient choice has been found that partitions the bath based on the comparison of the Rabi frequencies and the characteristic frequency of the bath.[173] Our discussion on this choice for conical intersection models will be *ad hoc*, in that there will be no rigorously derived equation, but will provide a physically motivated procedure using the pyrazine model as an example.

Fig. B.1 (a) shows the dynamics of the pyrazine model without the presence of a bath. Within the first 30 fs, there is significant population transfer from electronic state $|2\rangle$ to state $|1\rangle$ followed by electronic beating that is modulated by the vibrational levels. These observations match those of Krčmár *et al*, who compute two-dimensional electronic spectra in the two-mode pyrazine model with phenomenological dephasing.[140] The spectra showed rapid population transfer between the two electronic states within 50 fs in addition to a complicated vibronic structure. The complex structure of this beating makes choosing a characteristic timescale of the system that can delineate between the slow and fast portions of the bath difficult. Despite this complexity, we infer that this first population transfer determines the splitting frequency for the bath.

This hypothesis can be numerically tested by varying ω^* to treat less and less of the bath with TCL2 and incorporate more of the bath into the frozen modes description. Example diabatic populations are shown in Fig. B.1 (b) for a range of values of ω^* compared to the HEOM result and the TCL2-FM result from Fig. 4.2 (b). For very small values of ω^* positivity violations are observed. As ω^* is increased these positivity violations become delayed until eventually they are washed out entirely. At values of ω^* corresponding to the range [0.0165,0.0329] eV, the numerically exact result is essentially reproduced, however, as ω^* is increased to infinity, so that the entire bath is treated as static, the results exhibit deviations due to the lack of dissipation in the completely static bath limit.

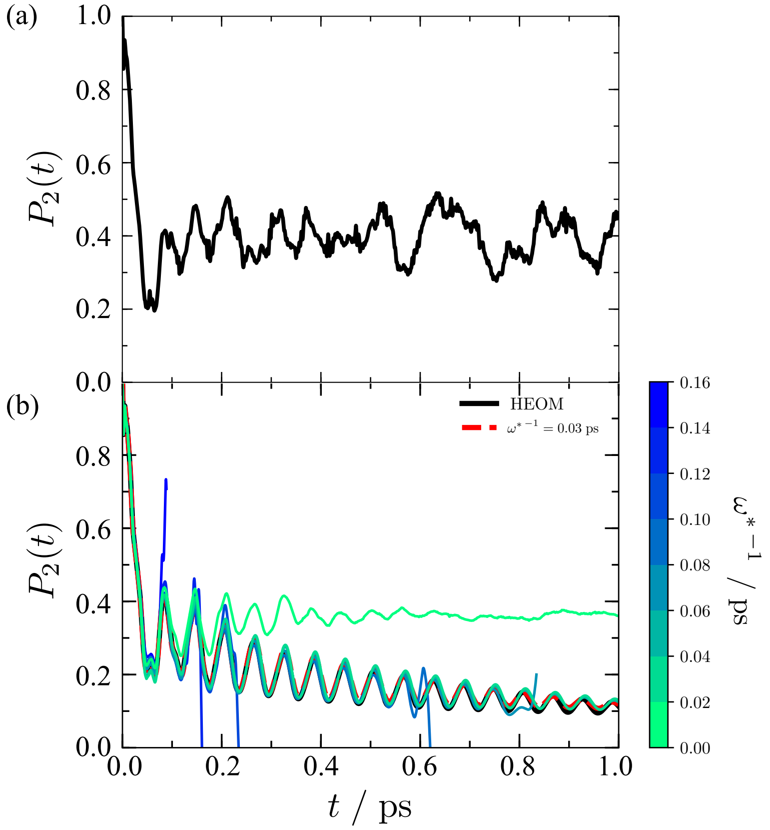

Figure B.1: Shown are the population dynamics for the pyrazine model without the presence of a bath (a). TCL2-FM with different values of ω^* corresponding to a timescale given in the colorbar are shown in (b). Also shown in (b) are exact HEOM (solid black) and TCL2-FM (dashed red) results with $\omega^* = 0.0219$ eV from the main text. The bath parameters used were $\omega_c = 0.00397$ eV and $E_r = 0.006571$ eV.

Appendix C

Numerical Gradients of Generalized Coordinates

C.1 Transformation of Cartesian Gradients to Internal Coordinate Gradients

Here we derive the relations for transforming Cartesian gradients, which are readily accessible from quantum chemistry calculations, to gradient with respects to the internal coordinates used in the representation of the system. We denote the Cartesian coordinates as $\mathbf{R}$, which are the standard (x, y, z) coordinates for each nuclei, and the Cartesian gradient as

$$\nabla_{\mathbf{R}} = \begin{pmatrix} \frac{\partial}{\partial R_1} \\ \frac{\partial}{\partial R_2} \\ \vdots \\ \frac{\partial}{\partial R_{3N}} \end{pmatrix}, \tag{C.1}$$

where the indices run over all $3N$ Cartesian coordinates for the atoms. For brevity, we denote the generic ith internal coordinate as Q_i. We are interested in obtaining quantities of the form

$$\frac{\partial f(\mathbf{R})}{\partial Q_i}, \tag{C.2}$$

where $f(\mathbf{R})$ is some function that depends on the nuclear coordinates, *e.g.*, the energy of an electronic state, $\langle i|H|i\rangle$. Naively inserting the chain rule is, however, problematic as the Jacobian of the Cartesian coordinates with respect to the internal coordinates is not uniquely defined, that is, we cannot simply use the inverse of the an element of the Cartesian Jacobian as the internal coordinate Jacobian,

$$\frac{\partial R_i}{\partial Qa_j} \neq \left(\frac{\partial Q_j}{\partial R_i}\right)^{-1}. \tag{C.3}$$

We hence require a specification of the full Jacobian in a set of $3N - 6$ internal coordinates and invert the resulting Jacobian to obtain the correct change-of-variable factor,

$$\frac{\partial Q_i}{\partial R_j} = \left(J^{-1}\right)_{ij}, \tag{C.4}$$

where J is the Cartesian Jacobian with elements,

$$J_{ij} = \frac{\partial Q_i}{\partial R_j}, \tag{C.5}$$

which can be easily calculated numerically through finite differences. Now performing the multivariate chain rule on $f(\mathbf{R})$,

$$\begin{aligned} \frac{\partial f(\mathbf{R})}{\partial Q_i} &= \sum_j \frac{\partial R_j}{\partial Q_i} \frac{\partial f(\mathbf{R})}{\partial R_j} \\ &= J_i^{-1} \cdot \nabla_{\mathbf{R}} f(\mathbf{R}), \end{aligned} \tag{C.6}$$

where J_i^{-1} is the ith *column* of the inverted Cartesian Jacobian. The internal coordinates are chosen to be the set of bond lengths, angles, and dihedrals that specify the connectivity of the molecule in the so-called Z-matrix form and due to the independence of these coordinates from center-of-mass translations and rotations Eq. C.6 projects out any of these artifacts.

Transforming the Hessian follows a similar procedure, but now includes two instances of the chain rule. The Hessian using internal coordinates, H^{int} can be related to the Hessian in Cartesian coordinates, H, as

$$\begin{aligned} H_{ij}^{\text{int}} &= \frac{\partial^2 V}{\partial Q_i \partial Q_j} \\ &= \sum_{kl} \frac{\partial R_k}{\partial \theta_i} \frac{\partial R_l}{\partial \theta_j} H_{ij}. \end{aligned} \tag{C.7}$$

Using our relations for the Jacobians we see that the Hessian in internal coordinates is given by

$$H^{\text{int}} = J^{-T} H J^{-1}. \tag{C.8}$$

We also note that using gradients and Hessians with mass-weighted Cartesian coordinates and/or center-of-mass translations and rotations projected out give the same results, however, in the gradient transformation of Eq. C.6 is modified to

$$\frac{\partial f(\mathbf{R})}{\partial Q_i} = J_i^{-1} \cdot \mathbf{M}^{1/2} \nabla_{\tilde{\mathbf{R}}} f(\mathbf{R}), \tag{C.9}$$

and the Hessian transformation of Eq. C.8 is modified to

$$H^{\text{int}} = J^{-T} \mathbf{M}^{1/2} \tilde{H} \mathbf{M}^{1/2} J^{-1}, \tag{C.10}$$

where $\mathbf{M}$ is the diagonal mass matrix, $\nabla_{\tilde{\mathbf{R}}}$ is the gradient of the mass-weighted Cartesian coordinates $\tilde{\mathbf{R}}$, and $\tilde{H}$ is the mass-weighted Hessian with center-of-mass translations and rotations projected out.

It is sometimes more natural to use the set of normal mode coordiantes, $\{\tilde{Q}_k\}$ for the gradient transformations as is the case with the spectral density, which has a frequency dependence. These normal mode coordinates, however, can mix contributions from system and bath coordinates, which would lead us to double counting energy gradient terms in the potential expansion of Chapter 5. To project out the contributions from specific internal coordinates we define the following projector of some internal coordinate Q,

$$P_Q = |Q\rangle\langle Q|, \tag{C.11}$$

where

$$|Q\rangle = \frac{\partial Q}{\partial \tilde{\mathbf{Q}}}, \tag{C.12}$$

which is simply a Jacobian vector defining the transformation between normal mode coordinates and the internal coordinate Q. This Jacobian vector is, however, complicated to find and thus we rely on the Cartesian Jacobian vectors as intermediats

$$\begin{aligned}\frac{\partial Q}{\partial \tilde{\mathbf{Q}}} &= \frac{\partial Q}{\partial \mathbf{R}}\frac{\partial \mathbf{R}}{\partial \tilde{\mathbf{Q}}} \\ &= J_Q \mathbf{W},\end{aligned} \tag{C.13}$$

where $\mathbf{W}$ is the matrix of normal mode vectors in Cartesian coordinates. The weights of the spectral density are given by the vector

$$\mathbf{c} = \left(\frac{\partial H}{\partial \mathbf{R}}\right)_0, \tag{C.14}$$

and the weights with the system internal coordinates projected out are given by

$$\tilde{\mathbf{c}} = \left(1 - \sum_{Q\in S} P_Q\right)\mathbf{c}, \tag{C.15}$$

where $Q \in S$ denotes that the coordinates Q are taken from the set of system coordinates.

C.2 Numerical Procedure for Generating the Kinetic Energy

The kinetic energy operator in Cartesian coordinates has a simple, separable form given by the mass-weighted Cartesian Laplacian

$$T_{\mathbf{R}} = -\frac{\hbar^2}{2}\left(\mathbf{M}^{-1/2}\nabla_{\mathbf{R}}\right)^2. \tag{C.16}$$

We seek here a simple expression for the kinetic energy operator in a set of internal coordinates. The completely specified Jacobian of Eq. C.5 gives a coordinate transformation from the Cartesian to internal coordinates

$$Q_i = \sum_{j=1}^{3N} J_{ij} R_j, \tag{C.17}$$

which upon insert into Eq. C.16 gives the kinetic energy operator in internal coordinates[282],

$$T = -\frac{\hbar^2}{2} \sum_{k=1}^{3N-6} \sum_{l=1}^{3N-6} j^{-1/2} \frac{\partial}{\partial Q_k} \left[j G_{kl}(\mathbf{Q}) \frac{\partial}{\partial Q_l} j^{-1/2} \right], \tag{C.18}$$

where $j = \det |J|$ is the Jacobian determinant and G_{kl} are the elements of the G-tensor,

$$G_{kl}(\mathbf{Q}) = \sum_{i=1}^{3N} \frac{1}{M_i} J_{ki} J_{li}. \tag{C.19}$$

Assuming that the change in j is small [252] we obtain an approximate form for the kinetic energy operator,

$$T = -\frac{\hbar^2}{2} \sum_{kl} \frac{\partial}{\partial Q_k} \left[G_{kl}(\mathbf{Q}) \frac{\partial}{\partial Q_l} \right]. \tag{C.20}$$

As the elements of the G-tensor are dependent on the internal coordinates and an analytical expression is often intractable, these can be computed numerically using the finite difference procedure described above.

The G-tensor characterizes the reduced masses and the kinetic couplings of all the internal coordinates, which can be written as

$$G = \begin{pmatrix} G_{\text{system}} & G_{\text{system,bath}} \\ G_{\text{system,bath}} & G_{\text{bath}} \end{pmatrix}. \tag{C.21}$$

If the motion of the bath coordinates is small and there is negeligible couplings between the system and bath degrees-of-freedom, we can focus solely on the system block of this matrix for describing the kinetic energy operator of the system.

Bibliography

[1] Darius Abramavicius and Shaul Mukamel. “Quantum oscillatory exciton migration in photosynthetic reaction centers”. In: *The Journal of Chemical Physics* 133.6 (2010), p. 064510.

[2] Victor V Albert et al. “Geometry and response of Lindbladians”. In: *Physical Review X* 6.4 (2016), p. 041031.

[3] Andreas C Albrecht. ““Forbidden” Character in Allowed Electronic Transitions”. In: *The Journal of Chemical Physics* 33.1 (1960), pp. 156–169.

[4] Flavia Aleotti et al. “Multidimensional potential energy surfaces resolved at the RASPT2 level for accurate photoinduced isomerization dynamics of azobenzene”. In: *Journal of chemical theory and computation* 15.12 (2019), pp. 6813–6823.

[5] Daniel Alonso and Inés de Vega. “Multiple-time correlation functions for non-Markovian interaction: beyond the quantum regression theorem”. In: *Physical review letters* 94.20 (2005), p. 200403.

[6] Nandini Ananth. “Mapping variable ring polymer molecular dynamics: A path-integral based method for nonadiabatic processes”. In: *The Journal of chemical physics* 139.12 (2013), p. 124102.

[7] Nandini Ananth and Thomas F Miller III. “Flux-correlation approach to characterizing reaction pathways in quantum systems: a study of condensed-phase proton-coupled electron transfer”. In: *Molecular Physics* 110.9-10 (2012), pp. 1009–1015.

[8] Kerstin Andersson et al. “Second-order perturbation theory with a CASSCF reference function”. In: *Journal of Physical Chemistry* 94.14 (1990), pp. 5483–5488.

[9] Eric A Arsenault et al. “Note: Vibronic coupling in light-harvesting complex II revisited”. In: (Submitted).

[10] Eric A Arsenault et al. “The role of mixed vibronic $\mathrm{Q_y}$-$\mathrm{Q_x}$ states in green light absorption of light-harvesting complex II”. In: *Nature Communications* 11.1 (2020), p. 6011.

[11] Eric A Arsenault et al. “Vibronic coupling in energy transfer dynamics and two-dimensional electronic-vibrational spectra”. In: (Submitted).

[12] Eric A Arsenault et al. “Vibronic mixing enables ultrafast energy flow in light-harvesting complex II”. In: *Nature Communications* 11.1 (2020), p. 1460.

[13] Cenap Ates et al. “Dynamical phases and intermittency of the dissipative quantum Ising model”. In: *Physical Review A* 85.4 (2012), p. 043620.

[14] Michael Baer. “Adiabatic and diabatic representations for atom-molecule collisions: Treatment of the collinear arrangement”. In: *Chemical Physics Letters* 35.1 (1975), pp. 112–118.

[15] Birgit Balzer and Gerhard Stock. “Modeling of decoherence and dissipation in nonadiabatic photoreactions by an effective-scaling nonsecular Redfield algorithm”. In: *Chemical physics* 310.1-3 (2005), pp. 33–41.

[16] HM Dhammika Bandara and Shawn C Burdette. “Photoisomerization in different classes of azobenzene”. In: *Chemical Society Reviews* 41.5 (2012), pp. 1809–1825.

[17] Michael Beck et al. *The Heidelberg MCTDH Package: A set of programs for multidimensional quantum dynamics*.

[18] Michael H Beck et al. “The multiconfiguration time-dependent Hartree (MCTDH) method: a highly efficient algorithm for propagating wavepackets”. In: *Physics reports* 324.1 (2000), pp. 1–105.

[19] M Ben-Nun and Todd J Martınez. “Nonadiabatic molecular dynamics: Validation of the multiple spawning method for a multidimensional problem”. In: *The Journal of chemical physics* 108.17 (1998), pp. 7244–7257.

[20] Timothy C Berkelbach, Mark S Hybertsen, and David R Reichman. “Microscopic theory of singlet exciton fission. I. General formulation”. In: *The Journal of Chemical Physics* 138.11 (2013), p. 114102.

[21] Timothy C Berkelbach, Thomas E Markland, and David R Reichman. “Reduced density matrix hybrid approach: Application to electronic energy transfer”. In: *The Journal of chemical physics* 136.8 (2012), p. 084104.

[22] Timothy C Berkelbach, David R Reichman, and Thomas E Markland. “Reduced density matrix hybrid approach: An efficient and accurate method for adiabatic and non-adiabatic quantum dynamics”. In: *The Journal of chemical physics* 136.3 (2012), p. 034113.

[23] Robert B Best and Gerhard Hummer. “Reaction coordinates and rates from transition paths”. In: *Proceedings of the National Academy of Sciences* 102.19 (2005), pp. 6732–6737.

[24] Pallavi Bhattacharyya and Graham R Fleming. “Two-dimensional electronic–vibrational spectroscopy of coupled molecular complexes: A near-analytical approach”. In: *The Journal of Physical Chemistry Letters* 10.9 (2019), pp. 2081–2089.

[25] Robert E Blankenship. *Molecular mechanisms of photosynthesis*. John Wiley & Sons, 2014.

[26] Peter G Bolhuis et al. "Transition path sampling: Throwing ropes over rough mountain passes, in the dark". In: *Annual Review of Physical Chemistry* 53.1 (2002), pp. 291–318.

[27] Sara Bonella, Daniel Montemayor, and David F Coker. "Linearized path integral approach for calculating nonadiabatic time correlation functions". In: *Proceedings of the National Academy of Sciences* 102.19 (2005), pp. 6715–6719.

[28] M Bonfanti et al. "Compact MCTDH wave functions for high-dimensional system-bath quantum dynamics". In: *The Journal of Physical Chemistry A* 116.46 (2012), pp. 11406–11413.

[29] Olga Bozovic, Brankica Jankovic, and Peter Hamm. "Using Azobenzene Photocontrol to Set Proteins in Motion". In: *arXiv preprint arXiv:2106.06289* (2021).

[30] Heinz-Peter Breuer. "Genuine quantum trajectories for non-Markovian processes". In: *Physical Review A* 70.1 (2004), p. 012106.

[31] Heinz-Peter Breuer and Francesco Petruccione. "Stochastic dynamics of quantum jumps". In: *Physical Review E* 52.1 (1995), p. 428.

[32] Heinz-Peter Breuer, Francesco Petruccione, et al. *The theory of open quantum systems*. Oxford University Press on Demand, 2002.

[33] Adrián A Budini, Robert M Turner, and Juan P Garrahan. "Fluctuating observation time ensembles in the thermodynamics of trajectories". In: *Journal of Statistical Mechanics: Theory and Experiment* 2014.3 (2014), P03012.

[34] Vytautas Butkus, Leonas Valkunas, and Darius Abramavicius. "Vibronic phenomena and exciton–vibrational interference in two-dimensional spectra of molecular aggregates". In: *The Journal of Chemical Physics* 140.3 (2014), p. 034306.

[35] Tessa R Calhoun et al. "Quantum coherence enabled determination of the energy landscape in light-harvesting complex II". In: *The Journal of Physical Chemistry B* 113.51 (2009), pp. 16291–16295.

[36] Herbert B Callen and Theodore A Welton. "Irreversibility and generalized noise". In: *Physical Review* 83.1 (1951), p. 34.

[37] Jianshu Cao et al. "Quantum biology revisited". In: *Science Advances* 6.14 (2020), eaaz4888.

[38] Orson Scott Card. *Ender's Game*. Tor Books, 1985.

[39] Josep Casellas, Michael J Bearpark, and Mar Reguero. "Excited-state decay in the photoisomerisation of azobenzene: a new balance between mechanisms". In: (2016).

[40] Alessandro Cembran et al. "On the mechanism of the cis- trans isomerization in the lowest electronic states of azobenzene: S0, S1, and T1". In: *Journal of the American Chemical Society* 126.10 (2004), pp. 3234–3243.

[41] Mirianas Chachisvilis and Ahmed H Zewail. "Femtosecond dynamics of pyridine in the condensed phase: Valence isomerization by conical intersections". In: *The Journal of Physical Chemistry A* 103.37 (1999), pp. 7408–7418.

[42] Jeng-Da Chai and Martin Head-Gordon. "Long-range corrected hybrid density functionals with damped atom–atom dispersion corrections". In: *Physical Chemistry Chemical Physics* 10.44 (2008), pp. 6615–6620.

[43] David Chandler. "Introduction to modern statistical". In: *Mechanics. Oxford University Press, Oxford, UK* 40 (1987).

[44] David Chandler. "Statistical mechanics of isomerization dynamics in liquids and the transition state approximation". In: *The Journal of Chemical Physics* 68.6 (1978), pp. 2959–2970.

[45] S Chaturvedi and F Shibata. "Time-convolutionless projection operator formalism for elimination of fast variables. Applications to Brownian motion". In: *Zeitschrift für Physik B Condensed Matter* 35.3 (1979), pp. 297–308.

[46] Lipeng Chen et al. "Dissipative dynamics at conical intersections: simulations with the hierarchy equations of motion method". In: *Faraday discussions* 194 (2016), pp. 61–80.

[47] Niklas Christensson et al. "Origin of long-lived coherences in light-harvesting complexes". In: *The Journal of Physical Chemistry B* 116.25 (2012), pp. 7449–7454.

[48] Jeffrey A Cina and Graham R Fleming. "Vibrational coherence transfer and trapping as sources for long-lived quantum beats in polarized emission from energy transfer complexes". In: *The Journal of Physical Chemistry A* 108.51 (2004), pp. 11196–11208.

[49] Guy Cohen and Eran Rabani. "Memory effects in nonequilibrium quantum impurity models". In: *Physical Review B* 84.7 (2011), p. 075150.

[50] Daniel T Colbert and William H Miller. "A novel discrete variable representation for quantum mechanical reactive scattering via the S-matrix Kohn method". In: *The Journal of Chemical Physics* 96.3 (1992), pp. 1982–1991.

[51] Irene Conti, Marco Garavelli, and Giorgio Orlandi. "The different photoisomerization efficiency of azobenzene in the lowest nπ^* and $\pi\pi^*$ singlets: the role of a phantom state". In: *Journal of the American Chemical Society* 130.15 (2008), pp. 5216–5230.

[52] Gavin E Crooks. "Entropy production fluctuation theorem and the nonequilibrium work relation for free energy differences". In: *Physical Review E* 60.3 (1999), p. 2721.

[53] Sajjad Dadashi-Silab, Sean Doran, and Yusuf Yagci. "Photoinduced Electron Transfer Reactions for Macromolecular Syntheses". In: *Chemical Reviews* 116.17 (2016). PMID: 26745441, pp. 10212–10275. DOI: `10.1021/acs.chemrev.5b00586`. eprint: `https://doi.org/10.1021/acs.chemrev.5b00586`. URL: `https://doi.org/10.1021/acs.chemrev.5b00586`.

[54] Jacob C Dean et al. “Vibronic enhancement of algae light harvesting”. In: *Chem* 1.6 (2016), pp. 858–872.

[55] Christoph Dellago, Peter G Bolhuis, and Phillip L Geissler. “Transition path sampling”. In: *Advances in Chemical Physics* 123 (2002), pp. 1–78.

[56] PB Deotare et al. “Nanoscale transport of charge-transfer states in organic donor–acceptor blends”. In: *Nature materials* 14.11 (2015), p. 1130.

[57] Jessalyn A DeVine et al. “Non-adiabatic effects on excited states of vinylidene observed with slow photoelectron velocity-map imaging”. In: *Journal of the American Chemical Society* 138.50 (2016), pp. 16417–16425.

[58] PAM Dirac. “Proc. Cambridge Philos. Soc.” In: (1930).

[59] Amro Dodin and Adam P Willard. “Approaching quantum dynamics from a classical perspective: dynamical flow, trajectory ensembles and state-space distributions for closed and open quantum systems”. In: *arXiv preprint arXiv:1805.09756* (2018).

[60] Wolfgang Domcke, David Yarkony, et al. *Conical intersections: electronic structure, dynamics & spectroscopy*. Vol. 15. World Scientific, 2004.

[61] Wolfgang Domcke and David R Yarkony. “Role of conical intersections in molecular spectroscopy and photoinduced chemical dynamics”. In: *Annual review of physical chemistry* 63 (2012), pp. 325–352.

[62] Hong-Guang Duan, RJ Dwayne Miller, and Michael Thorwart. “Impact of vibrational coherence on the quantum yield at a conical intersection”. In: *The Journal of Physical Chemistry Letters* 7.17 (2016), pp. 3491–3496.

[63] Hong-Guang Duan and Michael Thorwart. “Quantum Mechanical Wave Packet Dynamics at a Conical Intersection with Strong Vibrational Dissipation”. In: *The Journal of Physical Chemistry Letters* 7.3 (2016), pp. 382–386.

[64] Hong-Guang Duan et al. “Intramolecular vibrations enhance the quantum efficiency of excitonic energy transfer”. In: *Photosynthesis research* 144.2 (2020), pp. 137–145.

[65] Hong-Guang Duan et al. “Signature of the geometric phase in the wave packet dynamics on hypersurfaces”. In: *Chemical Physics* 515 (2018), pp. 21–27.

[66] Hong-Guang Duan et al. “Ultrafast energy transfer in excitonically coupled molecules induced by a nonlocal Peierls phonon”. In: *The journal of physical chemistry letters* 10.6 (2019), pp. 1206–1211.

[67] Rudolph H Dyck and Donald S McClure. “Ultraviolet spectra of stilbene, p-monohalogen stilbenes, and azobenzene and the trans to cis photoisomerization process”. In: *The Journal of Chemical Physics* 36.9 (1962), pp. 2326–2345.

[68] Gregory S Engel et al. “Evidence for wavelike energy transfer through quantum coherence in photosynthetic systems”. In: *Nature* 446.7137 (2007), pp. 782–786.

[69] Henry Eyring. “The activated complex in chemical reactions”. In: *The Journal of Chemical Physics* 3.2 (1935), pp. 107–115.

[70] Sarah Maria Falke et al. “Coherent ultrafast charge transfer in an organic photovoltaic blend”. In: *Science* 344.6187 (2014), pp. 1001–1005.

[71] MD Fayer. “Dynamics of liquids, molecules, and proteins measured with ultrafast 2D IR vibrational echo chemical exchange spectroscopy”. In: *Annual review of physical chemistry* 60 (2009), pp. 21–38.

[72] Jonathan H Fetherolf and Timothy C Berkelbach. “Linear and nonlinear spectroscopy from quantum master equations”. In: *The Journal of Chemical Physics* 147.24 (2017), p. 244109.

[73] Graham R Fleming, Scott H Courtney, and Michael W Balk. “Activated barrier crossing: Comparison of experiment and theory”. In: *Journal of Statistical Physics* 42.1-2 (1986), pp. 83–104.

[74] IA Frenkel et al. “Wave mechanics; advanced general theory”. In: (1934).

[75] Yuta Fujihashi, Graham R Fleming, and Akihito Ishizaki. “Impact of environmentally induced fluctuations on quantum mechanically mixed electronic and vibrational pigment states in photosynthetic energy transfer and 2D electronic spectra”. In: *The Journal of Chemical Physics* 142.21 (2015), p. 212403.

[76] Tatsuya Fujino, Sergei Yu Arzhantsev, and Tahei Tahara. “Femtosecond time-resolved fluorescence study of photoisomerization of trans-azobenzene”. In: *The Journal of Physical Chemistry A* 105.35 (2001), pp. 8123–8129.

[77] Tatsuya Fujino, Sergei Yu Arzhantsev, and Tahei Tahara. “Femtosecond/Picosecond Time-Resolved Spectroscopy of trans-Azobenzene: Isomerization Mechanism Following S2 ($\pi\pi^*$)← S0Photoexcitation”. In: *Bulletin of the Chemical Society of Japan* 75.5 (2002), pp. 1031–1040.

[78] Tatsuya Fujino and Tahei Tahara. “Picosecond time-resolved Raman study of trans-azobenzene”. In: *The Journal of Physical Chemistry A* 104.18 (2000), pp. 4203–4210.

[79] Franklin D Fuller et al. “Vibronic coherence in oxygenic photosynthesis”. In: *Nature Chemistry* 6.8 (2014), pp. 706–711.

[80] Laura Gagliardi et al. “A theoretical study of the lowest electronic states of azobenzene: the role of torsion coordinate in the cis–trans photoisomerization”. In: *Theoretical Chemistry Accounts* 111.2 (2004), pp. 363–372.

[81] Juan P Garrahan and Igor Lesanovsky. “Thermodynamics of quantum jump trajectories”. In: *Physical Review Letters* 104.16 (2010), p. 160601.

[82] James D Gaynor, Jason Sandwisch, and Munira Khalil. “Vibronic coherence evolution in multidimensional ultrafast photochemical processes”. In: *Nature Communications* 10.1 (2019), p. 5621.

[83] Dina Gegiou, KA Muszkat, and Ernst Fischer. “Temperature dependence of photoisomerization. VI. Viscosity effect”. In: *Journal of the American Chemical Society* 90.1 (1968), pp. 12–18.

[84] Phillip L Geissler, Christoph Dellago, and David Chandler. “Kinetic pathways of ion pair dissociation in water”. In: *The Journal of Physical Chemistry B* 103.18 (1999), pp. 3706–3710.

[85] Phillip L Geissler et al. “Autoionization in liquid water”. In: *Science* 291.5511 (2001), pp. 2121–2124.

[86] Rami Gherib et al. “On the inclusion of the diagonal Born-Oppenheimer correction in surface hopping methods”. In: *The Journal of chemical physics* 144.15 (2016), p. 154103.

[87] Etienne Gindensperger, Irene Burghardt, and Lorenz S Cederbaum. “Short-time dynamics through conical intersections in macrosystems. I. Theory: Effective-mode formulation”. In: *The Journal of chemical physics* 124.14 (2006), p. 144103.

[88] Etienne Gindensperger, Irene Burghardt, and Lorenz S Cederbaum. “Short-time dynamics through conical intersections in macrosystems. II. Applications”. In: *The Journal of chemical physics* 124.14 (2006), p. 144104.

[89] N Gisin and I C Percival. “Quantum state diffusion, localization and quantum dispersion entropy”. In: 26.9 (1993), pp. 2233–2243.

[90] N Gisin and I C Percival. “The quantum state diffusion picture of physical processes”. In: 26.9 (1993), pp. 2245–2260.

[91] N Gisin and I C Percival. “The quantum-state diffusion model applied to open systems”. In: 25.21 (1992), pp. 5677–5691.

[92] Hsi-Sheng Goan et al. “Continuous quantum measurement of two coupled quantum dots using a point contact: A quantum trajectory approach”. In: *Physical Review B* 63.12 (2001), p. 125326.

[93] Vittorio Gorini, Andrzej Kossakowski, and Ennackal Chandy George Sudarshan. “Completely positive dynamical semigroups of N-level systems”. In: *Journal of Mathematical Physics* 17.5 (1976), pp. 821–825.

[94] Alexander A Granovsky. “Extended multi-configuration quasi-degenerate perturbation theory: The new approach to multi-state multi-reference perturbation theory”. In: *The Journal of chemical physics* 134.21 (2011), p. 214113.

[95] Richard F. Grote and James T. Hynes. “The stable states picture of chemical reactions. II. Rate constants for condensed and gas phase reaction models”. In: *The Journal of Chemical Physics* 73.6 (2021/06/24 1980), pp. 2715–2732.

[96] Elisabeth Gruber et al. “Action-spectroscopy studies of positively charge-tagged azobenzene in solution and in the gas-phase”. In: *The Journal of chemical physics* 150.8 (2019), p. 084303.

[97] Scott Habershon et al. “Ring-polymer molecular dynamics: Quantum effects in chemical dynamics from classical trajectories in an extended phase space”. In: *Annual review of physical chemistry* 64 (2013), pp. 387–413.

[98] Susanne Hahn and Gerhard Stock. “Ultrafast cis-trans photoswitching: A model study”. In: *The Journal of Chemical Physics* 116.3 (2002), pp. 1085–1091.

[99] Ggoch Ddeul Han et al. “Photon energy storage materials with high energy densities based on diacetylene–azobenzene derivatives”. In: *Journal of Materials Chemistry A* 4.41 (2016), pp. 16157–16165.

[100] Yu Harabuchi et al. “Dynamics simulations with spin-flip time-dependent density functional theory: Photoisomerization and photocyclization mechanisms of cis-stilbene in $\pi\pi^*$ states”. In: *The Journal of Physical Chemistry A* 118.51 (2014), pp. 11987–11998.

[101] Stephanie M Hart et al. “Identification of nonradiative decay pathways in Cy3”. In: *The Journal of Physical Chemistry Letters* 11.13 (2020), pp. 5000–5007.

[102] Frank Herbert. *Dune*. Chilton Books, 1965.

[103] Jacob S Higgins et al. “Photosynthesis tunes quantum-mechanical mixing of electronic and vibrational states to steer exciton energy transfer”. In: *Proceedings of the National Academy of Sciences* 118.11 (2021).

[104] Jordan M Horowitz. “Quantum-trajectory approach to the stochastic thermodynamics of a forced harmonic oscillator”. In: *Physical Review E* 85.3 (2012), p. 031110.

[105] Jordan M Horowitz and Juan MR Parrondo. “Entropy production along nonequilibrium quantum jump trajectories”. In: *New Journal of Physics* 15.8 (2013), p. 085028.

[106] Keith H Hughes, Clara D Christ, and Irene Burghardt. “Effective-mode representation of non-Markovian dynamics: A hierarchical approximation of the spectral density. I. Application to single surface dynamics”. In: *The Journal of chemical physics* 131.2 (2009), p. 024109.

[107] Keith H Hughes, Clara D Christ, and Irene Burghardt. “Effective-mode representation of non-Markovian dynamics: A hierarchical approximation of the spectral density. I. Application to single surface dynamics”. In: *The Journal of chemical physics* 131.2 (2009), p. 024109.

[108] Keith H Hughes, Clara D Christ, and Irene Burghardt. “Effective-mode representation of non-Markovian dynamics: A hierarchical approximation of the spectral density. II. Application to environment-induced nonadiabatic dynamics”. In: *The Journal of chemical physics* 131.12 (2009), 09B622.

[109] Gerhard Hummer. “From transition paths to transition states and rate coefficients”. In: *The Journal of chemical physics* 120.2 (2004), pp. 516–523.

[110] Tatsushi Ikeda, Arend G Dijkstra, and Yoshitaka Tanimura. “Modeling and analyzing a photo-driven molecular motor system: Ratchet dynamics and non-linear optical spectra”. In: *The Journal of chemical physics* 150.11 (2019), p. 114103.

[111] Tatsushi Ikeda and Yoshitaka Tanimura. “Probing photoisomerization processes by means of multi-dimensional electronic spectroscopy: The multi-state quantum hierarchical Fokker-Planck equation approach”. In: *The Journal of Chemical Physics* 147.1 (2017), p. 014102.

[112] Tomiki Ikeda and Osamu Tsutsumi. “Optical switching and image storage by means of azobenzene liquid-crystal films”. In: *Science* 268.5219 (1995), pp. 1873–1875.

[113] Jake Iles-Smith, Neill Lambert, and Ahsan Nazir. “Environmental dynamics, correlations, and the emergence of noncanonical equilibrium states in open quantum systems”. In: *Physical Review A* 90.3 (2014), p. 032114.

[114] Takeshi Ishikawa, Takeshi Noro, and Takayuki Shoda. “Theoretical study on the photoisomerization of azobenzene”. In: *The Journal of Chemical Physics* 115.16 (2001), pp. 7503–7512.

[115] Akihito Ishizaki and Graham R Fleming. “Quantum coherence in photosynthetic light harvesting”. In: *Annu. Rev. Condens. Matter Phys.* 3.1 (2012), pp. 333–361.

[116] Akihito Ishizaki and Graham R Fleming. “Theoretical examination of quantum coherence in a photosynthetic system at physiological temperature”. In: *Proceedings of the National Academy of Sciences* (2009), pnas–0908989106.

[117] A Jäckle and H-D Meyer. “Product representation of potential energy surfaces”. In: *The Journal of Chemical Physics* 104.20 (1996), pp. 7974–7984.

[118] Seogjoo Jang. “Theory of multichromophoric coherent resonance energy transfer: A polaronic quantum master equation approach”. In: *The Journal of Chemical Physics* 135.3 (2011), p. 034105.

[119] Seogjoo Jang, Timothy C Berkelbach, and David R Reichman. “Coherent quantum dynamics in donor–bridge–acceptor systems: beyond the hopping and super-exchange mechanisms”. In: *New Journal of Physics* 15.10 (2013), p. 105020.

[120] Seogjoo Jang et al. “Theory of coherent resonance energy transfer”. In: *The Journal of Chemical Physics* (2008).

[121] Seogjoo J Jang and Benedetta Mennucci. “Delocalized excitons in natural light harvesting complexes”. In: *Reviews of Modern Physics* 90.3 (2018), p. 035003.

[122] Christopher Jarzynski. “Nonequilibrium equality for free energy differences”. In: *Physical Review Letters* 78.14 (1997), p. 2690.

[123] Jan Jeske and Jared H Cole. “Derivation of Markovian master equations for spatially correlated decoherence”. In: *Physical Review A* 87.5 (2013), p. 052138.

[124] David M Jonas. “Vibrational and Nonadiabatic Coherence in 2D Electronic Spectroscopy, the Jahn–Teller Effect, and Energy Transfer”. In: *Annual review of physical chemistry* 69 (2018), pp. 327–352.

[125] Chanelle C Jumper et al. “From coherent to vibronic light harvesting in photosynthesis”. In: *Current Opinion in Chemical Biology* 47 (2018). Energy / Mechanistic Biology, pp. 39–46. ISSN: 1367-5931. DOI: `https://doi.org/10.1016/j.cbpa.2018.07.023`. URL: `https://www.sciencedirect.com/science/article/pii/S1367593118300711`.

[126] Hideaki Kano, Takashi Saito, and Takayoshi Kobayashi. “Observation of Herzberg-Teller-type Wave Packet Motion in Porphyrin J-Aggregates Studied by Sub-5-fs Spectroscopy”. In: *The Journal of Physical Chemistry A* 106.14 (2002), pp. 3445–3453.

[127] Raymond Kapral. “Progress in the theory of mixed quantum-classical dynamics”. In: *Annu. Rev. Phys. Chem.* 57 (2006), pp. 129–157.

[128] Raymond Kapral. “Quantum dynamics in open quantum-classical systems”. In: *Journal of Physics: Condensed Matter* 27.7 (2015), p. 073201.

[129] Raymond Kapral and Giovanni Ciccotti. “Mixed quantum-classical dynamics”. In: *The Journal of chemical physics* 110.18 (1999), pp. 8919–8929.

[130] John A Kattirtzi, David T Limmer, and Adam P Willard. “Microscopic dynamics of charge separation at the aqueous electrochemical interface”. In: *Proceedings of the National Academy of Sciences* 114.51 (2017), pp. 13374–13379.

[131] Daniel Keefer et al. “Imaging conical intersection dynamics during azobenzene photoisomerization by ultrafast X-ray diffraction”. In: *Proceedings of the National Academy of Sciences* 118.3 (2021).

[132] Aaron Kelly and Thomas E Markland. “Efficient and accurate surface hopping for long time nonadiabatic quantum dynamics”. In: *The Journal of chemical physics* 139.1 (2013), p. 014104.

[133] Lyran Kidon et al. “On the memory kernel and the reduced system propagator”. In: *The Journal of chemical physics* 149.10 (2018), p. 104105.

[134] Katherine A Kitney-Hayes et al. “Two-dimensional Fourier transform electronic spectroscopy at a conical intersection”. In: *The Journal of chemical physics* 140.12 (2014), p. 124312.

[135] Ulrich Kleinekathöfer, Ivan Kondov, and Michael Schreiber. “Stochastic unraveling of time-local quantum master equations beyond the Lindblad class”. In: *Physical Review E* 66.3 (2002), p. 037701.

[136] Alexie M Kolpak and Jeffrey C Grossman. “Azobenzene-functionalized carbon nanotubes as high-energy density solar thermal fuels”. In: *Nano letters* 11.8 (2011), pp. 3156–3162.

[137] Ivan Kondov, Ulrich Kleinekathöfer, and Michael Schreiber. "Stochastic unraveling of Redfield master equations and its application to electron transfer problems". In: *The Journal of Chemical Physics* 119.13 (2003), pp. 6635–6646.

[138] H Köuppel, Wolfgang Domcke, and Lorenz S Cederbaum. "Multimode molecular dynamics beyond the Born-Oppenheimer approximation". In: *Advances in chemical physics* (1984), pp. 59–246.

[139] Markus Kowalewski et al. "Catching conical intersections in the act: Monitoring transient electronic coherences by attosecond stimulated X-ray Raman signals". In: *Physical review letters* 115.19 (2015), p. 193003.

[140] Jindřich Krčmář et al. "Signatures of conical intersections in two-dimensional electronic spectra". In: *Journal of Physics B: Atomic, Molecular and Optical Physics* 47.12 (2014), p. 124019.

[141] Ryogo Kubo, Morikazu Toda, and Natsuki Hashitsume. *Statistical physics II: nonequilibrium statistical mechanics.* Vol. 31. Springer Science & Business Media, 2012.

[142] Axel Kühl and Wolfgang Domcke. "Effect of a dissipative environment on the dynamics at a conical intersection". In: *Chemical Physics* 259.2-3 (2000), pp. 227–236.

[143] Axel Kühl and Wolfgang Domcke. "Multilevel Redfield description of the dissipative dynamics at conical intersections". In: *The Journal of chemical physics* 116.1 (2002), pp. 263–274.

[144] Shankar Kumar et al. "The weighted histogram analysis method for free-energy calculations on biomolecules. I. The method". In: *Journal of Computational Chemistry* 13.8 (1992), pp. 1011–1021.

[145] Brian B Laird, Jane Budimir, and James L Skinner. "Quantum-mechanical derivation of the Bloch equations: Beyond the weak-coupling limit". In: *The Journal of chemical physics* 94.6 (1991), pp. 4391–4404.

[146] Zhihao Lan et al. "Quantum slow relaxation and metastability due to dynamical constraints". In: *Physical review letters* 121.4 (2018), p. 040603.

[147] Brian R Landry and Joseph E Subotnik. "How to recover Marcus theory with fewest switches surface hopping: Add just a touch of decoherence". In: *The Journal of chemical physics* 137.22 (2012), 22A513.

[148] Mi Kyung Lee and David F Coker. "Modeling electronic-nuclear interactions for excitation energy transfer processes in light-harvesting complexes". In: *The Journal of Physical Chemistry Letters* 7.16 (2016), pp. 3171–3178.

[149] Mi Kyung Lee, Pengfei Huo, and David F Coker. "Semiclassical path integral dynamics: photosynthetic energy transfer with realistic environment interactions". In: *Annual review of physical chemistry* 67 (2016), pp. 639–668.

[150] Emanuele Levi et al. "Robustness of many-body localization in the presence of dissipation". In: *Physical review letters* 116.23 (2016), p. 237203.

[151] Benjamin G Levine and Todd J Martınez. “Isomerization through conical intersections”. In: *Annu. Rev. Phys. Chem.* 58 (2007), pp. 613–634.

[152] Amikam Levy, Eran Rabani, and David T Limmer. “Response theory for nonequilibrium steady-states of open quantum systems”. In: *arXiv preprint arXiv:2010.03929* (2020).

[153] Nicholas HC Lewis et al. “A method for the direct measurement of electronic site populations in a molecular aggregate using two-dimensional electronic-vibrational spectroscopy”. In: *The Journal of Chemical Physics* 143.12 (2015), p. 124203.

[154] Nicholas HC Lewis et al. “Observation of electronic excitation transfer through light harvesting complex II using two-dimensional electronic–vibrational spectroscopy”. In: *The Journal of Physical Chemistry Letters* 7.20 (2016), pp. 4197–4206.

[155] Shuwei Li et al. “Photo-isomerization energy storage using azobenzene and nanoscale templates: a topical review”. In: *Journal of Thermal Science* 29.2 (2020), pp. 280–297.

[156] Ruibin Liang. “First-Principles Nonadiabatic Dynamics Simulation of Azobenzene Photodynamics in Solutions”. In: *Journal of Chemical Theory and Computation* 17.5 (2021), pp. 3019–3030.

[157] JC Light, IP Hamilton, and JV Lill. “Generalized discrete variable approximation in quantum mechanics”. In: *The Journal of chemical physics* 82.3 (1985), pp. 1400–1409.

[158] Goran Lindblad. “On the generators of quantum dynamical semigroups”. In: *Communications in Mathematical Physics* 48.2 (1976), pp. 119–130.

[159] Christian Lubich. “Time integration in the multiconfiguration time-dependent Hartree method of molecular quantum dynamics”. In: *Applied Mathematics Research eXpress* 2015.2 (2015), pp. 311–328.

[160] Fei Ma et al. “Vibronic coherence in the charge separation process of the Rhodobacter sphaeroides reaction center”. In: *The Journal of Physical Chemistry Letters* 9.8 (2018), pp. 1827–1832.

[161] Uwe Manthe and H Köppel. “Dynamics on potential energy surfaces with a conical intersection: Adiabatic, intermediate, and diabatic behavior”. In: *The Journal of Chemical Physics* 93.3 (1990), pp. 1658–1669.

[162] George R. R. Martin. *A Game of Thrones*. Bantam Books, 1996.

[163] AD McLachlan. “A variational solution of the time-dependent Schrodinger equation”. In: *Molecular Physics* 8.1 (1964), pp. 39–44.

[164] Garrett A Meek and Benjamin G Levine. “Wave function continuity and the diagonal Born-Oppenheimer correction at conical intersections”. In: *The Journal of chemical physics* 144.18 (2016), p. 184109.

[165] Artur R Menzeleev, Franziska Bell, and Thomas F Miller III. “Kinetically constrained ring-polymer molecular dynamics for non-adiabatic chemical reactions”. In: *The Journal of Chemical Physics* 140.6 (2014), p. 064103.

[166] Hans-Dieter Meyer and William H Miller. “A classical analog for electronic degrees of freedom in nonadiabatic collision processes”. In: *The Journal of Chemical Physics* 70.7 (1979), pp. 3214–3223.

[167] Hans-Dieter Meyer and Haobin Wang. “On regularizing the MCTDH equations of motion”. In: *The Journal of chemical physics* 148.12 (2018), p. 124105.

[168] David A Micha. “Density matrix treatment of non-adiabatic photoinduced electron transfer at a semiconductor surface”. In: *The Journal of chemical physics* 137.22 (2012), 22A521.

[169] William H Miller. “Classical S matrix: Numerical application to inelastic collisions”. In: *The Journal of Chemical Physics* 53.9 (1970), pp. 3578–3587.

[170] William H Miller, Steven D Schwartz, and John W Tromp. “Quantum mechanical rate constants for bimolecular reactions”. In: *The Journal of Chemical Physics* 79.10 (1983), pp. 4889–4898.

[171] Noriyuki Minezawa and Mark S Gordon. “Optimizing Conical Intersections by Spin-Flip Density Functional Theory: Application to Ethylene”. In: *The Journal of Physical Chemistry A* 113.46 (2009), pp. 12749–12753.

[172] Daniele M Monahan et al. “Room-temperature coherent optical phonon in 2D electronic spectra of CH3NH3PbI3 perovskite as a possible cooling bottleneck”. In: *The Journal of Physical Chemistry Letters* 8.14 (2017), pp. 3211–3215.

[173] Andrés Montoya-Castillo, Timothy C Berkelbach, and David R Reichman. “Extending the applicability of Redfield theories into highly non-Markovian regimes”. In: *The Journal of Chemical Physics* 143.19 (2015), p. 194108.

[174] Hazime Mori. “A continued-fraction representation of the time-correlation functions”. In: *Progress of Theoretical Physics* 34.3 (1965), pp. 399–416.

[175] Shaul Mukamel. “Multidimensional femtosecond correlation spectroscopies of electronic and vibrational excitations”. In: *Annual review of physical chemistry* 51.1 (2000), pp. 691–729.

[176] Shaul Mukamel. *Principles of nonlinear optical spectroscopy*. 6. Oxford University Press on Demand, 1999.

[177] KW Murch et al. “Observing single quantum trajectories of a superconducting quantum bit”. In: *Nature* 502.7470 (2013), p. 211.

[178] Jeffrey A Myers et al. “Two-dimensional electronic spectroscopy of the D1-D2-cyt b559 photosystem II reaction center complex”. In: *The Journal of Physical Chemistry Letters* 1.19 (2010), pp. 2774–2780.

[179] Sadao Nakajima. “On quantum theory of transport phenomena: steady diffusion”. In: *Progress of Theoretical Physics* 20.6 (1958), pp. 948–959.

[180] Artur Nenov et al. “UV-light-induced vibrational coherences: the key to understand Kasha rule violation in trans-azobenzene”. In: *The journal of physical chemistry letters* 9.7 (2018), pp. 1534–1541.

[181] Daniel M Neumark. “Slow electron velocity-map imaging of negative ions: applications to spectroscopy and dynamics”. In: *The Journal of Physical Chemistry A* 112.51 (2008), pp. 13287–13301.

[182] Abraham Nitzan. *Chemical dynamics in condensed phases: relaxation, transfer and reactions in condensed molecular systems.* Oxford university press, 2006.

[183] Scott H. Northrup and James T. Hynes. “The stable states picture of chemical reactions. I. Formulation for rate constants and initial condition effects”. In: *The Journal of Chemical Physics* 73.6 (2021/06/24 1980), pp. 2700–2714.

[184] Vladimir I Novoderezhkin et al. “Exciton-vibrational resonance and dynamics of charge separation in the photosystem II reaction center”. In: *Physical Chemistry Chemical Physics* 19.7 (2017), pp. 5195–5208.

[185] Thomas AA Oliver, Nicholas HC Lewis, and Graham R Fleming. “Correlating the motion of electrons and nuclei with two-dimensional electronic–vibrational spectroscopy”. In: *Proceedings of the National Academy of Sciences* 111.28 (2014), pp. 10061–10066.

[186] Christopher J Otolski et al. “Ultrafast Dynamics of Encapsulated Molecules Reveals New Insight on the Photoisomerization Mechanism for Azobenzenes”. In: *The journal of physical chemistry letters* 10.1 (2018), pp. 121–127.

[187] Gitt Panitchayangkoon et al. “Direct evidence of quantum transport in photosynthetic light-harvesting complexes”. In: *Proceedings of the National Academy of Sciences* 108.52 (2011), pp. 20908–20912.

[188] Tae Jun Park and JC Light. “Unitary quantum time evolution by iterative Lanczos reduction”. In: *The Journal of chemical physics* 85.10 (1986), pp. 5870–5876.

[189] Daniel Peláez and Hans-Dieter Meyer. “The multigrid POTFIT (MGPF) method: Grid representations of potentials for quantum dynamics of large systems”. In: *The Journal of Chemical Physics* 138.1 (2013), p. 014108.

[190] Baron Peters. “Reaction coordinates and mechanistic hypothesis tests”. In: *Annual Review of Physical Chemistry* 67 (2016), pp. 669–690.

[191] Martin B Plenio, J Almeida, and Susana F Huelga. “Origin of long-lived oscillations in 2D-spectra of a quantum vibronic model: electronic versus vibrational coherence”. In: *The Journal of Chemical Physics* 139.23 (2013), p. 235102.

[192] MB Plenio and PL Knight. “The quantum-jump approach to dissipative dynamics in quantum optics”. In: *Reviews of Modern Physics* 70.1 (1998), p. 101.

[193] Eli Pollak. “Theory of activated rate processes: A new derivation of Kramers’expression”. In: *The Journal of Chemical Physics* 85.2 (2021/06/24 1986), pp. 865–867.

[194] W Thomas Pollard and Richard A Friesner. “Solution of the Redfield equation for the dissipative quantum dynamics of multilevel systems”. In: *The Journal of Chemical Physics* 100.7 (1994), pp. 5054–5065.

[195] Sergey Polyutov, Oliver Kühn, and Tõnu Pullerits. “Exciton-vibrational coupling in molecular aggregates: Electronic versus vibronic dimer”. In: *Chemical Physics* 394.1 (2012), pp. 21–28.

[196] Bradley S Prall et al. “Anti-correlated spectral motion in bisphthalocyanines: Evidence for vibrational modulation of electronic mixing”. In: *The Journal of Physical Chemistry A* 109.48 (2005), pp. 10870–10879.

[197] Da-Long Qi et al. “Tracking an electronic wave packet in the vicinity of a conical intersection”. In: *The Journal of chemical physics* 147.7 (2017), p. 074101.

[198] M Quick et al. “Photoisomerization dynamics and pathways of trans-and cis-azobenzene in solution from broadband femtosecond spectroscopies and calculations”. In: *The Journal of Physical Chemistry B* 118.29 (2014), pp. 8756–8771.

[199] A Raab. “On the Dirac–Frenkel/McLachlan variational principle”. In: *Chemical physics letters* 319.5-6 (2000), pp. 674–678.

[200] A. Raab, I. Burghardt, and H.âD. Meyer. “The multiconfiguration time-dependent Hartree method generalized to the propagation of density operators”. In: *The Journal of Chemical Physics* 111.19 (1999), pp. 8759–8772. DOI: `10.1063/1.480334`. eprint: `https://doi.org/10.1063/1.480334`. URL: `https://doi.org/10.1063/1.480334`.

[201] Shahnawaz Rafiq and Gregory D. Scholes. “From Fundamental Theories to Quantum Coherences in Electron Transfer”. In: *Journal of the American Chemical Society* 141.2 (2019). PMID: 30412671, pp. 708–722. DOI: `10.1021/jacs.8b09059`. eprint: `https://doi.org/10.1021/jacs.8b09059`. URL: `https://doi.org/10.1021/jacs.8b09059`.

[202] Hermann Rau. “Further evidence for rotation in the π, π^* and inversion in the n, π^* photoisomerization of azobenzenes”. In: *Journal of photochemistry* 26.2-3 (1984), pp. 221–225.

[203] Hermann Rau and Erik Lueddecke. “On the rotation-inversion controversy on photoisomerization of azobenzenes. Experimental proof of inversion”. In: *Journal of the American Chemical Society* 104.6 (1982), pp. 1616–1620.

[204] Alfred G Redfield. “On the theory of relaxation processes”. In: *IBM Journal of Research and Development* 1.1 (1957), pp. 19–31.

[205] Christian Renner and Luis Moroder. “Azobenzene as conformational switch in model peptides”. In: *ChemBioChem* 7.6 (2006), pp. 868–878.

[206] Jeremy O Richardson and Michael Thoss. “Communication: Nonadiabatic ring-polymer molecular dynamics”. In: *The Journal of chemical physics* (2013).

[207] Gareth W Richings and Scott Habershon. “A new diabatization scheme for direct quantum dynamics: Procrustes diabatization”. In: *The Journal of chemical physics* 152.15 (2020), p. 154108.

[208] Gareth W Richings and Graham A Worth. “A practical diabatisation scheme for use with the direct-dynamics variational multi-configuration Gaussian method”. In: *The Journal of Physical Chemistry A* 119.50 (2015), pp. 12457–12470.

[209] Brian S Rolczynski et al. “Correlated protein environments drive quantum coherence lifetimes in photosynthetic pigment-protein complexes”. In: *Chem* 4.1 (2018), pp. 138–149.

[210] Elisabet Romero, Vladimir I. Novoderezhkin, and Rienk van Grondelle. “Quantum design of photosynthesis for bio-inspired solar-energy conversion”. In: *Nature* 543.7645 (2017), pp. 355–365.

[211] Elisabet Romero et al. “Quantum coherence in photosynthesis for efficient solar-energy conversion”. In: *Nature Physics* 10.9 (2014), pp. 676–682.

[212] Björn O Roos, Peter R Taylor, and Per EM Sigbahn. “A complete active space SCF method (CASSCF) using a density matrix formulated super-CI approach”. In: *Chemical Physics* 48.2 (1980), pp. 157–173.

[213] Partha Pratim Roy et al. “Solvent mediated excited state proton transfer in Indigo Carmine”. In: *The Journal of Physical Chemistry Letters* 11.10 (2020), pp. 4156–4162.

[214] Ilya G Ryabinkin and Artur F Izmaylov. “Geometric phase effects in dynamics near conical intersections: Symmetry breaking and spatial localization”. In: *Physical review letters* 111.22 (2013), p. 220406.

[215] Ilya G Ryabinkin, Loıc Joubert-Doriol, and Artur F Izmaylov. “Geometric phase effects in nonadiabatic dynamics near conical intersections”. In: *Accounts of chemical research* 50.7 (2017), pp. 1785–1793.

[216] Brandon Sanderson. *Mistborn: The Final Empire*. Tor Books, 2006.

[217] Brandon Sanderson. *The Way of Kings*. Tor Books, 2010.

[218] H Satzger, C Root, and M Braun. “Excited-state dynamics of trans-and cis-azobenzene after UV excitation in the $\pi\pi^*$ band”. In: *The Journal of Physical Chemistry A* 108.30 (2004), pp. 6265–6271.

[219] H Satzger et al. “Fluorescence spectra of trans-and cis-azobenzene–emission from the Franck–Condon state”. In: *Chemical physics letters* 372.1-2 (2003), pp. 216–223.

[220] Abraham Savitzky and Marcel JE Golay. “Smoothing and differentiation of data by simplified least squares procedures.” In: *Analytical Chemistry* 36.8 (1964), pp. 1627–1639.

[221] Addison J Schile and David T Limmer. “Simulating conical intersection dynamics in the condensed phase with hybrid quantum master equations”. In: *The Journal of Chemical Physics* 151.1 (2019), p. 014106.

[222] Addison J Schile and David T Limmer. “Studying rare nonadiabatic dynamics with transition path sampling quantum jump trajectories”. In: *The Journal of chemical physics* 149.21 (2018), p. 214109.

[223] RW Schoenlein et al. “The first step in vision: femtosecond isomerization of rhodopsin”. In: *Science* 254.5030 (1991), pp. 412–415.

[224] Gregory D Scholes et al. “Lessons from nature about solar light harvesting”. In: *Nature Chemistry* 3.10 (2011), pp. 763–774.

[225] Jonathan D Schultz et al. “Influence of Vibronic Coupling on Ultrafast Singlet Fission in a Linear Terrylenediimide Dimer”. In: *Journal of the American Chemical Society* 143.4 (2021), pp. 2049–2058.

[226] Thomas Schultz et al. “Mechanism and dynamics of azobenzene photoisomerization”. In: *Journal of the American Chemical Society* 125.27 (2003), pp. 8098–8099.

[227] Michael S Schuurman and Albert Stolow. “Dynamics at conical intersections”. In: *Annual review of physical chemistry* 69 (2018), pp. 427–450.

[228] Joachim Seibt and Tomáš Mančal. “Treatment of Herzberg-Teller and non-Condon effects in optical spectra with Hierarchical Equations of Motion”. In: *Chemical Physics* 515 (2018), pp. 129–140.

[229] Luis Seidner and Wolfgang Domcke. “Microscopic modelling of photoisomerization and internal-conversion dynamics”. In: *Chemical physics* 186.1 (1994), pp. 27–40.

[230] Udo Seifert and Thomas Speck. “Fluctuation-dissipation theorem in nonequilibrium steady states”. In: *EPL (Europhysics Letters)* 89.1 (2010), p. 10007.

[231] Yihan Shao, Martin Head-Gordon, and Anna I Krylov. “The spin–flip approach within time-dependent density functional theory: Theory and applications to diradicals”. In: *The Journal of chemical physics* 118.11 (2003), pp. 4807–4818.

[232] Yihan Shao et al. “Advances in molecular quantum chemistry contained in the Q-Chem 4 program package”. In: *Molecular Physics* 113.2 (2015), pp. 184–215.

[233] MC Sherman and SA Corcelli. “Nonadiabatic transition path sampling”. In: *The Journal of chemical physics* 145.3 (2016), p. 034110.

[234] Qiang Shi and Eitan Geva. “A new approach to calculating the memory kernel of the generalized quantum master equation for an arbitrary system–bath coupling”. In: *The Journal of chemical physics* 119.23 (2003), pp. 12063–12076.

[235] Fumiaki Shibata, Yoshinori Takahashi, and Natsuki Hashitsume. “A generalized stochastic liouville equation. Non-Markovian versus memoryless master equations”. In: *Journal of Statistical Physics* 17.4 (1977), pp. 171–187.

[236] Toru Shiozaki. “BAGEL: Brilliantly advanced general electronic-structure library”. In: *Wiley Interdisciplinary Reviews: Computational Molecular Science* 8.1 (2018), e1331.

[237] Toru Shiozaki et al. *Communication: Extended multi-state complete active space second-order perturbation theory: Energy and nuclear gradients.* 2011.

[238] Michael R Shirts and John D Chodera. “Statistically optimal analysis of samples from multiple equilibrium states”. In: *The Journal of Chemical Physics* 129.12 (2008), p. 124105.

[239] Philip Shushkov, Richard Li, and John C Tully. “Ring polymer molecular dynamics with surface hopping”. In: *The Journal of Chemical Physics* 137.22 (2012), 22A549.

[240] Narcisse Siampiringue et al. “The cis→ trans photoisomerization of azobenzene: an experimental re-examination”. In: *Journal of photochemistry* 37.1 (1987), pp. 185–188.

[241] Xueyu Song, David Chandler, and RA Marcus. “Gaussian field model of dielectric solvation dynamics”. In: *The Journal of Physical Chemistry* 100.29 (1996), pp. 11954–11959.

[242] Sebastian Spörlein et al. “Ultrafast spectroscopy reveals subnanosecond peptide conformational dynamics and validates molecular dynamics simulation”. In: *Proceedings of the National Academy of Sciences* 99.12 (2002), pp. 7998–8002.

[243] Philip J Stephens et al. “Ab initio calculation of vibrational absorption and circular dichroism spectra using density functional force fields”. In: *The Journal of physical chemistry* 98.45 (1994), pp. 11623–11627.

[244] Gerhard Stock and Michael Thoss. “Semiclassical description of nonadiabatic quantum dynamics”. In: *Physical review letters* 78.4 (1997), p. 578.

[245] Attila Szabo and Neil S Ostlund. *Modern quantum chemistry: introduction to advanced electronic structure theory.* Dover Publications, 1996.

[246] Satoshi Takeuchi et al. “Spectroscopic Tracking of Structural Evolution in Ultrafast Stilbene Photoisomerization”. In: *Science* 322.5904 (2008), pp. 1073–1077.

[247] Eric MM Tan et al. “Fast photodynamics of azobenzene probed by scanning excited-state potential energy surfaces using slow spectroscopy”. In: *Nature communications* 6.1 (2015), pp. 1–7.

[248] Yoshitaka Tanimura and Ryogo Kubo. “Time evolution of a quantum system in contact with a nearly Gaussian-Markoffian noise bath”. In: *Journal of the Physical Society of Japan* 58.1 (1989), pp. 101–114.

[249] Xuecheng Tao, Philip Shushkov, and Thomas F Miller III. “Path-integral isomorphic Hamiltonian for including nuclear quantum effects in non-adiabatic dynamics”. In: *The Journal of chemical physics* 148.10 (2018), p. 102327.

[250] Roel Tempelaar, Thomas LC Jansen, and Jasper Knoester. “Vibrational beatings conceal evidence of electronic coherence in the FMO light-harvesting complex”. In: *The Journal of Physical Chemistry B* 118.45 (2014), pp. 12865–12872.

[251] Roel Tempelaar and David R Reichman. “Vibronic exciton theory of singlet fission. III. How vibronic coupling and thermodynamics promote rapid triplet generation in pentacene crystals”. In: *The Journal of Chemical Physics* 148.24 (2018), p. 244701.

[252] Sebastian Thallmair, Matthias K Roos, and Regina de Vivie-Riedle. “Design of specially adapted reactive coordinates to economically compute potential and kinetic energy operators including geometry relaxation”. In: *The Journal of Chemical Physics* 144.23 (2016), p. 234104.

[253] Ward H Thompson. “Quantum mechanical transition state theory and tunneling corrections”. In: *The Journal of Chemical Physics* 110.9 (1999), pp. 4221–4228.

[254] Michael Thoss and Gerhard Stock. “Mapping approach to the semiclassical description of nonadiabatic quantum dynamics”. In: *Physical Review A* 59.1 (1999), p. 64.

[255] Michael Thoss and Haobin Wang. “Quantum dynamical simulation of ultrafast molecular processes in the condensed phase”. In: *Chemical physics* 322.1-2 (2006), pp. 210–222.

[256] Michael Thoss, Haobin Wang, and William H Miller. “Self-consistent hybrid approach for complex systems: Application to the spin-boson model with Debye spectral density”. In: *The Journal of Chemical Physics* 115.7 (2001), pp. 2991–3005.

[257] Erling Thyrhaug et al. “Identification and characterization of diverse coherences in the Fenna–Matthews–Olson complex”. In: *Nature Chemistry* 10.7 (2018), pp. 780–786.

[258] Michio Tokuyama and Hazime Mori. “Statistical-mechanical theory of random frequency modulations and generalized Brownian motions”. In: *Progress of Theoretical Physics* 55.2 (1976), pp. 411–429.

[259] J. R. R. Tolkien. *The Lord of the Rings: The Two Towers*. George Allen & Unwin, 1954.

[260] Maria Topaler and Nancy Makri. “Path integral calculation of quantum nonadiabatic rates in model condensed phase reactions”. In: *The Journal of Physical Chemistry* 100.11 (1996), pp. 4430–4436.

[261] Maria Topaler and Nancy Makri. “Quasi-adiabatic propagator path integral methods. Exact quantum rate constants for condensed phase reactions”. In: *Chemical Physics Letters* 210.1-3 (1993), pp. 285–293.

[262] Glenn M Torrie and John P Valleau. “Nonphysical sampling distributions in Monte Carlo free-energy estimation: Umbrella sampling”. In: *Journal of Computational Physics* 23.2 (1977), pp. 187–199.

[263] Hugo Touchette. “The large deviation approach to statistical mechanics”. In: *Physics Reports* 478.1-3 (2009), pp. 1–69.

[264] John C Tully. “Molecular dynamics with electronic transitions”. In: *The Journal of Chemical Physics* 93.2 (1990), pp. 1061–1071.

[265] John C Tully. “Perspective: Nonadiabatic dynamics theory”. In: *The Journal of chemical physics* 137.22 (2012), 22A301.

[266] Troy Van Voorhis et al. “The diabatic picture of electron transfer, reaction barriers, and molecular dynamics”. In: *Annual review of physical chemistry* 61 (2010), pp. 149–170.

[267] Charulatha Venkataraman, Alexander V Soudackov, and Sharon Hammes-Schiffer. “Photoinduced homogeneous proton-coupled electron transfer: Model study of isotope effects on reaction dynamics”. In: *The Journal of Chemical Physics* 131.15 (2009), p. 154502.

[268] Nicolas Vogt, Jan Jeske, and Jared H Cole. “Stochastic Bloch-Redfield theory: Quantum jumps in a solid-state environment”. In: *Physical Review B* 88.17 (2013), p. 174514.

[269] Peter L Walters and Nancy Makri. “Iterative quantum-classical path integral with dynamically consistent state hopping”. In: *The Journal of Chemical Physics* 144.4 (2016), p. 044108.

[270] Haobin Wang. “Multilayer multiconfiguration time-dependent Hartree theory”. In: *The Journal of Physical Chemistry A* 119.29 (2015), pp. 7951–7965.

[271] Haobin Wang and Hans-Dieter Meyer. “Importance of Appropriately Regularizing the ML-MCTDH Equations of Motion”. In: *The Journal of Physical Chemistry A* 125.15 (2021), pp. 3077–3087.

[272] Haobin Wang and Hans-Dieter Meyer. “On regularizing the ML-MCTDH equations of motion”. In: *The Journal of chemical physics* 149.4 (2018), p. 044119.

[273] Haobin Wang and Michael Thoss. “A multilayer multiconfiguration time-dependent Hartree simulation of the reaction-coordinate spin-boson model employing an interaction picture”. In: *The Journal of chemical physics* 146.12 (2017), p. 124112.

[274] Haobin Wang and Michael Thoss. “Multilayer formulation of the multiconfiguration time-dependent Hartree theory”. In: *The Journal of chemical physics* 119.3 (2003), pp. 1289–1299.

[275] Arieh Warshel. “Bicycle-pedal model for the first step in the vision process”. In: *Nature* 260.5553 (1976), pp. 679–683.

[276] Michael R. Wasielewski. “Photoinduced electron transfer in supramolecular systems for artificial photosynthesis”. In: *Chemical Reviews* 92.3 (May 1992), pp. 435–461.

[277] H.-J. Werner et al. *MOLPRO, version , a package of ab initio programs*. see.

[278] Hans-Joachim Werner and Wilfried Meyer. “A quadratically convergent MCSCF method for the simultaneous optimization of several states”. In: *The Journal of Chemical Physics* 74.10 (1981), pp. 5794–5801.

[279] Hans-Joachim Werner et al. “The Molpro quantum chemistry package”. In: *The Journal of chemical physics* 152.14 (2020), p. 144107.

[280] Eugene Wigner. “The transition state method”. In: *Transactions of the Faraday Society* 34 (1938), pp. 29–41.

[281] David MG Williams and Wolfgang Eisfeld. “Neural network diabatization: A new ansatz for accurate high-dimensional coupled potential energy surfaces”. In: *The Journal of chemical physics* 149.20 (2018), p. 204106.

[282] Edgar Bright Wilson, John Courtney Decius, and Paul C Cross. *Molecular vibrations: the theory of infrared and Raman vibrational spectra.* Courier Corporation, 1980.

[283] Max Winslow, Warren B Cross, and David Robinson. “Comparison of Spin-Flip TDDFT-Based Conical Intersection Approaches with XMS-CASPT2”. In: *Journal of chemical theory and computation* 16.5 (2020), pp. 3253–3263.

[284] HM Wiseman and GJ Milburn. “Interpretation of quantum jump and diffusion processes illustrated on the Bloch sphere”. In: *Physical Review A* 47.3 (1993), p. 1652.

[285] Graham A Worth and Lorenz S Cederbaum. “Beyond Born-Oppenheimer: molecular dynamics through a conical intersection”. In: *Annu. Rev. Phys. Chem.* 55 (2004), pp. 127–158.

[286] Eric C Wu et al. “Two-dimensional electronic-vibrational spectroscopic study of conical intersection dynamics: an experimental and electronic structure study”. In: *Physical Chemistry Chemical Physics* (2019).

[287] David R Yarkony. “Diabolical conical intersections”. In: *Reviews of Modern Physics* 68.4 (1996), p. 985.

[288] Shu-Hao Yeh et al. “Elucidation of near-resonance vibronic coherence lifetimes by nonadiabatic electronic-vibrational state character mixing”. In: *Proceedings of the National Academy of Sciences* 116.37 (2019), pp. 18263–18268.

[289] Yusuke Yoneda et al. “Electron–Nuclear Dynamics Accompanying Proton-Coupled Electron Transfer”. In: *Journal of the American Chemical Society* 143.8 (2021), pp. 3104–3112.

[290] Yusuke Yoneda et al. “Non-condon effect on ultrafast excited-state intramolecular proton transfer”. In: *The Journal of Physical Chemistry A* 124.2 (2019), pp. 265–271.

[291] Jimmy K Yu et al. “Ab Initio Nonadiabatic Molecular Dynamics with Hole–Hole Tamm–Dancoff Approximated Density Functional Theory”. In: *Journal of Chemical Theory and Computation* 16.9 (2020), pp. 5499–5511.

[292] Jimmy K Yu et al. “Nonadiabatic Dynamics Simulation of the Wavelength-Dependent Photochemistry of Azobenzene Excited to the nπ^* and $\pi\pi^*$ Excited States”. In: *Journal of the American Chemical Society* 142.49 (2020), pp. 20680–20690.

[293] Ling Yue, Yajun Liu, and Chaoyuan Zhu. “Performance of TDDFT with and without spin-flip in trajectory surface hopping dynamics: cis–trans azobenzene photoisomerization”. In: *Physical Chemistry Chemical Physics* 20.37 (2018), pp. 24123–24139.

[294] Nicole Yunger Halpern and David T Limmer. “Fundamental limitations on photoisomerization from thermodynamic resource theories”. In: *arXiv* (2018).

[295] Hou-Dao Zhang et al. “Effects of Herzberg–Teller vibronic coupling on coherent excitation energy transfer”. In: *The Journal of Chemical Physics* 145.20 (2016), p. 204109.

[296] Robert Zwanzig. “Ensemble method in the theory of irreversibility”. In: *The Journal of Chemical Physics* 33.5 (1960), pp. 1338–1341.